IDENTIFICATION OF IN VIVO MATERIAL PROPERTIES OF ASCENDING THORACIC AORTIC ANEURYSM: TOWARDS NONINVASIVE RISK ASSESSMENT

A Dissertation
Presented to
The Academic Faculty

by

Minliang Liu

In Partial Fulfillment
of the Requirements for the Degree
Doctor of Philosophy in the
School of Mechanical Engineering

Georgia Institute of Technology
December 2020

COPYRIGHT © 2020 BY MINLIANG LIU

IDENTIFICATION OF IN VIVO MATERIAL PROPERTIES OF ASCENDING THORACIC AORTIC ANEURYSM: TOWARDS NONINVASIVE RISK ASSESSMENT

Approved by:

Dr. Wei Sun
Department of Biomedical Engineering
Georgia Institute of Technology

Dr. Rudolph L. Gleason
School of Mechanical Engineering
Georgia Institute of Technology

Dr. H. Jerry Qi
School of Mechanical Engineering
Georgia Institute of Technology

Dr. John N. Oshinski
School of Medicine
Emory University

Dr. Bradley G. Leshnower
School of Medicine
Emory University

Date Approved: 11/02/2020

To my grandparents Xinzhi Liu and Chunyu Li.

ACKNOWLEDGEMENTS

Froemost, I would like to express my sincerest gratitude to my advisor, Dr. Wei Sun for his generous guidance and continuous support. I would also like to thank him for giving me the opportunity to pursue a Ph.D and work on many interesting topics, which allowed me to expand my skill set. I would also like to express gratitude to my thesis committee members Dr. Brad Leshnower, Dr. Jerry Qi, Dr. Rudy Gleason and Dr. John Oshinski for their guidance and support.

I would like to acknowledge the funding support of AHA pre-doctoral fellowship 19PRE34430060. I would also like to thank Dr. Brad Leshnower for serving as co-sponsor on my AHA pre-doctoral fellowship.

I would like to thank current members and alumni of the Tissue Mechanics Laboratory, especially Dr. Liang Liang for mentorship, support and patience. I must also thank Dr. Xiaoying Lou for providing clinical insights. I would like to thank Dr. Caitlin Martin, Dr. Wenbin Mao, Dr. Thuy Pham, Fatiesa Sulejmani, Dr. Andres Caballero, Dr. Hai Dong and Dr. Tongran Qin for their guidance and support on my research. I would also like to thank Qing Zou, Yasmeen Ismail, M. Subhi Al Jabi, Parikirt Oggu, Ahdil Gill, and Clarisse Gieowarsingh for assistance in collecting experimetanl data, Vishal Shah for assistance in data analysis, and Daksha Jadhav, Ibrahima Diallo, Yilin Xu and Isha Bhatia for assistance in creating computational models.

Last but not leaset, I would like to thank my family and friends for their unwavering support.

TABLE OF CONTENTS

ACKNOWLEDGEMENTS **iv**

LIST OF TABLES **ix**

LIST OF FIGURES **xii**

SUMMARY **xxi**

CHAPTER 1. Introduction **1**
1.1 Ascending Thoracic Aortic Aneurysm (ATAA) **1**
1.1.1 Diagnosis and Treatment 3
1.1.2 The Current Diameter Criterion is not a Perfect Predictor of ATAA Risk 4
1.2 Biomechanical Testing of Aortic Tissues **5**
1.2.1 Uniaxial Testing 5
1.2.2 Planar Biaxial Testing 6
1.2.3 Bulge Inflation Testing 11
1.3 Hyperelastic and Failure Modeling of Aortic Tissues **12**
1.3.1 Hyperelastic Modelling 12
1.3.2 Failure Modelling 16
1.4 Biomechanical Assessment of ATAA Risk **20**
1.4.1 Biomechanical Risk Assessment is Promising 20
1.4.2 In Vivo Hyperelastic Properties are the Biggest Unknown 22
1.4.3 Failure Metric Plays a Critical Role in Biomechanical Assessment 23
1.5 Existing Methods for Mechanical Property Identification **25**
1.5.1 Methods to Identify Ex Vivo Material Properties 25
1.5.2 In Vivo Identification Methods using Simplified Geometries or Material Models 25
1.5.3 FE Updating Methods for In Vivo Material Property Identification 26
1.6 Application of Machine Learning (ML) in Biomechanics **28**
1.6.1 ML Models as Nonlinear Function Approximators 28
1.6.2 ML Models as Surrogates for Computational Biomechanical Analysis 30
1.7 Motivation of the Study **32**
1.7.1 Objectives of This Study 32
1.7.2 Significance of This Study 34

CHAPTER 2. Static Determinacy of the Aortic Wall **36**
2.1 Background **37**
2.2 Theoretical and Analytical Arguments **38**
2.2.1 Different Opening Angles and Material Models 39
2.2.2 Layer-Specific Three-Dimensional Residual Deformation 43
2.3 Finite Element Analyses Incorporating Patient-Specific Material Properties and Residual Deformations **46**
2.3.1 The Forward Penalty Approach 46
2.3.2 Nonlinear FE Simulations with Patient-Specific Material Properties 47

2.3.3 Nonlinear FE Simulations Incorporating Different Opening Angles 50
2.3.4 Nonlinear FE Simulations Incorporating Layer-Specific Three-Dimensional Residual Deformations 57
2.4 Discussion 60
2.4.1 Comparison with Traditional Iterative Approach with Nonlinear Material Properties and Residual Deformations 60
2.4.2 The Transmural Mean Stress is Consistence with Homogenized Stress State 61
2.4.3 Static Determinacy of Axial/Longitudinal Stress 62
2.5 Summary 63

CHAPTER 3. Inverse Identification of In Vivo Hyperelastic Properties of the Aortic Wall 64
3.1 Background 65
3.2 The Inverse Method 67
3.2.1 Prerequisites and Assumptions 67
3.2.2 Constitutive Model 68
3.2.3 The Workflow for Constitutive Parameter Identification 68
3.2.4 “Almost-True” Stress Computation using the Forward Penalty Approach 70
3.2.5 Continuum Mechanics Framework for Systolic Stress Estimation 70
3.2.6 Implementation of the Inverse Method 74
***3.3* Numerical Validations 77**
3.3.1 Inverse Computation of Diastolic Left Stretch Tensor 78
3.3.2 Constitutive Parameters Identification 79
3.4 Experimental Validation 84
3.4.1 Image Data and Corresponding Tissue Specimens 84
3.4.2 Biaxial Testing Protocols 87
3.4.3 Wall Thickness and Blood Pressures 88
3.4.4 In Vivo-Identified and Ex Vivo-Fitted Material Properties 89
3.5 Discussion 91
3.5.1 Computational Cost 92
3.5.2 Discrepancies in Material Properties 93
3.5.3 Mesh Correspondence 95
3.5.4 Limitations 96
3.6 Summary 97

CHAPTER 4. Machine Learning Approach for Fast In Vivo Hyperelastic Properties Identification 98
4.1 Background 99
4.2 Statistical Shape Modeling of the Aorta 102
4.2.1 Image Data 102
4.2.2 Aorta Surface Remeshing and Shape Alignment 103
4.2.3 Statistical Shape Model Construction 104
4.2.4 Shape Decomposition and Shape Sampling 105
4.3 The ML-Based Inverse Method 107
4.3.1 Constitutive Model 107
4.3.2 Generating the Training/Validation Dataset and the Testing Dataset 107
4.3.3 The Machine Learning Model 112

4.3.4 Training, Adjusting and Testing the ML-Model 116
4.4 Validation and Testing Results 120
4.4.1 Actual and Predicted Material Parameters 120
4.4.2 Actual and Predicted Stress-Stretch Curves 122
4.5 Discussion 124
4.5.1 Support Vector Regression (SVR) for Nonlinear Mapping 125
4.5.2 Training and Testing Loss for Different Activation Functions 126
4.5.3 Limitations 127
4.6 Summary 129

CHAPTER 5. Probabilistic and Anisotropic Failure Metric 130
5.1 Background 131
5.2 Anisotropic Failure Criterion 131
5.2.1 The Tsai-Hill (TH) criterion 132
5.2.2 Off-Axis Tension Tests 133
5.2.3 Fitting TH Criterion to Off-Axis Testing Data 136
5.3 Failure Property Data 139
5.3.1 Uniaxial Testing in the Circumferential and Axial Directions 140
5.3.2 Anisotropic Failure Properties 141
5.4 Anisotropic and Probabilistic Failure Metric 142
5.4.1 Probability Distribution of Failure Properties 143
5.4.2 Failure Probability 145
5.5 ATAA Failure Metric under Elevated Pressure using In Vivo-Identified Hyperelastic Properties 148
5.6 Discussion 150
5.6.1 Probabilistic Metric and Uncertainty Quantification 151
5.6.2 Deterministic and Probabilistic Metrics 152
5.6.3 Limitations 153
5.7 Summary 154

CHAPTER 6. Comparsion of Risk Assessment Methods 155
6.1 Background 155
6.2 CT Image and Tissue Testing Data 157
6.2.1 Biaxal Testing 158
6.2.2 Uniaxial Testing 159
6.3 Reconstructing ATAA Risk using Patient-Specific CT Images and Tissue Testing Data 159
6.4 ATAA Risk Stratification Methods 161
6.5 Results 165
6.5.1 Comparison of Different Risk Stratification Methods 165
6.5.2 Comparison between Probabilistic and Deterministic metrics 167
6.6 Discussion 170
6.6.1 Discriminative Power of Different Risk Assessment Methods 170
6.6.2 Limitations 171
6.7 Summary 172

CHAPTER 7. Conclusions 173

7.1 Summary 173
7.2 Clinical Relevance 176
7.3 Future Directions 177
  7.3.1 Refinement of the Computational Framework for ATAA Risk Assessment 177
  7.3.2 Identification of In Vivo Heterogeneous Hyperelastic Properties 178
  7.3.3 Develop and Validate Tissue Failure Criteria with Distributed Fiber Orientations 179
  7.3.4 Evaluate ATAA Risk Assessment Methods using Clinical Data 180

APPENDIX A. Estimation of in vivo mechanical properties of the aortic wall: A multi-resolution direct search approach 182
A.1 Introduction 183
A.2 Methods 186
  A.2.1 Prerequisites and Assumptions 186
  A.2.2 Constitutive Model 186
  A.2.3 Workflow of Constitutive Parameter Estimation 187
  A.2.4 The MRDS Strategy 190
A.3 Results 200
  A.3.1 Numerical Validation 200
  A.3.2 Estimation of In Vivo Mechanical Properties of an Aged Human Healthy Aorta 203
A.4 Discussion 205
  A.4.1 Mesh Correspondence 207
  A.4.2 Limitations 208
A.5 Conclusion 210

APPENDIX B. A generic physics-informed neural network-based constitutive model for soft biological tissues 212
B.1 Introduction 213
B.2 Constitutive Modeling of Soft Biological Tissues 217
  B.2.1 Expert-Constructed Constitutive Equations 219
  B.2.2 ML-Based Constitutive Model 221
B.3 Cross Validation and Testing 228
  B.3.1 Planar Biaxial Testing Data 228
  B.3.2 Fitting and Testing of the Expert-Constructed Models 229
  B.3.3 Cross Validation and Testing of the ML-based Constitutive Model 230
B.4 Results 232
  B.4.1 Cross Validation 233
  B.4.2 Testing 235
  B.4.3 Parametric Study 238
B.5 Discussion 239
  B.5.1 Comparison to Traditional FFNN Models 241
  B.5.2 Standard Regularization Procedures 242
  B.5.3 The NNMat Model is Generic 243
B.6 Conclusions 243

REFERENCES 245

LIST OF TABLES

Table 2.1 - The parameters used in the opening angle method. 42

Table 2.2 - The inner and outer radii A and B of the stress-free configurations corresponding to various opening angles α. 42

Table 2.3 - GOH material parameters of the patient "BAV17" extracted from [58]. Coefficient of determination of the curve fitting is 0.9551. 43

Table 2.4 - Material and residual deformation parameters from [140, 143]. In addition, $\mathrm{l} = 2.48\mathrm{mm}$, $\mathrm{b}^{(\mathrm{I})} = \mathrm{a}^{(\mathrm{M})}$ and $\mathrm{b}^{(\mathrm{M})} = \mathrm{a}^{(\mathrm{A})}$ can be calculated according to [140]. 45

Table 2.5 - The mean values, standard deviations (SD), MAEs and MAPEs in terms of the in-plane mean stresses ($\overline{\sigma}_{\theta\theta}$ and $\overline{\sigma}_{\mathrm{zz}}$) and transmural mean von Mises stress ($\overline{\sigma}_{\mathrm{VM}}$). 56

Table 2.6 - Sensitivity of MAPE w.r.t. the thickness. 57

Table 2.7 - Layer-specific GOH material parameters from [52]. 58

Table 3.1 - Initial value, upper and lower bounds of constitutive parameters. 77

Table 3.2 - "True" and estimated constitutive parameters of the four patients. 81

Table 3.3 - Coefficient of determination in the stretch-stress curves for the four patients. 83

Table 3.4 - Time spent for the parameter estimation for each patient. 84

Table 3.5 - Measured wall thickness (mean ± standard deviation) from CT scans and surgically-resected tissue. 88

Table 3.6 - Diastolic and systolic blood pressure for the two patients. 88

Table 3.7 - In vivo-identified and ex vivo-fitted material parameters for the two patients. 89

Table 4.1 - Averaged NMAE (defined in Eqn. (4.11)) of the five material parameters w.r.t. network structure in LOO cross-validation (3,000 epochs). 118

Table 4.2 - Averaged NMAE (defined in Eqn. (4.11)) of the five material parameters w.r.t. network structure in ten-fold cross-validation (3,000 epochs). 119

Table 4.3 - NMAE and NSTAE of the five material parameters in testing set (10,000 epochs). 121

Table 4.4 - The actual and predicted material parameters for the best, median, worst cases. 123

Table 4.5 - NMAE and NSTAE of the five material parameters in testing set using support vector regression (SVR). 126

Table 5.1 - Failure model parameters and corresponding R^2 obtained from fitting off-axis testing data of the healthy porcine aortas. 137

Table 5.2 - Failure model parameters and corresponding R^2 obtained from fitting off-axis testing data of the human ATAA tissues. 139

Table 5.3 - Goodness-of-fit tests for the joint distribution and marginal distributions. Null hypothesis: the data comes from the KDE-estimated distribution; alternative hypothesis: the data does not come from such distribution. 145

Table 6.1 - Patient characteristics in Group 2 used for validation. The reconstructed failure pressure is obtained in Section 6.3. 157

Table 6.2 - Reconstructed risk (PRR) and failure metrics evaluated by different methods (Section 6.4). 163

Table A.1 - Upper, lower bounds and increment of constitutive parameters for sampling. 193

Table A.2 - Experimentally-derived and estimated constitutive parameters in the numerical validation. 202

Table A.3 - Estimated constitutive parameters for the healthy aorta. 204

Table B.1 - Fitting and validation results obtained from grid search with different α and β values. The number of training epochs was set to be 1000. 234

Table B.2 - Fitting and validation results obtained using different number of training epochs. 235

Table B.3 - Fitting and testing R2 predicted by the NNMat model and expert-constructed models using the testing dataset. 236

Table B.4 - Fitting and testing R^2 (mean ± standard deviation) obtained by the NNMat model and the expert-constructed models. The p-values are computed using Behrens-Fisher two-sample t-test with the null hypothesis that R^2 of the expert-constructed model is great than that of the NNMat model. The results indicate that performance of the NNMat model is much better than the HGO model. 237

LIST OF FIGURES

Figure 1.1 - Thoracic aortic aneurysm (TAA). Left: ascending thoracic aortic aneurysm (ATAA); right: descending thoracic aortic aneurysm (DTAA), adopted from uvahealth.com. 2

Figure 1.2 - ATAA before and after repair (adapted from www.healio.com) 4

Figure 1.3 - Uniaxial testing of aortic wall tissue. The specimen is quasi-statically stretched until failure. 6

Figure 1.4 - Setup of the planar biaxial test. The specimen is mounted on to the biaxial device using four suture attachments. 7

Figure 1.5 - DL model for estimation of nonlinear anisotropic stress-strain responses of chemically-treated collagenous tissues directly from noninvasive microscopy images [118]. 30

Figure 1.6 - Stress distributions computed from the FE model and DL model [120]. 31

Figure 2.1 - The transmural mean, thin-walled and thick-walled hoop stresses across the wall thickness. In the left figure, thick-walled hoop stresses were computed using neo-Hookean model, while in the right figure, GOH model was used. Transmural mean hoop stress remains the same for all scenarios, thus only one line is plotted. 43

Figure 2.2 - The transmural mean, thin-walled and layer-specific hoop stress distributions in the three layer composite wall when 0 and 80 mmHg pressures are applied. 46

Figure 2.3 - Comparison of von Mises stress computed using nonlinear FE with patient-specific material properties (a), (c), (e) and (g) and that computed from forward penalty approach (b), (d), (f) and (h). Pressure=120mmHg. Mean absolute percentage error (MAPE) for geometries ATAA1 ((a)&(b)), ATAA2 ((c)&(d)), ATAA3 ((e)&(f)) and ATAA4 ((g)&(h)) are obtained by taking the nonlinear FE computed stress as “true” value. 50

Figure 2.4 - Predicted results using the forward penalty approach and the GPA approach with different opening angles: (1) von Mises stress distribution in the dissected view (row 1 and row 4), (2) 54 the transmural mean von Mises stress (row 2 and row 5), and (3) the signed transmural percentage error (row 3 and row 6).

Figure 2.5 - von Mises stress distribution in an aortic hoop using the forward penalty approach and the iterative approach (GPA) with different opening angles. 55

Figure 2.6 - The probability density function (PDF) of the STPE is shown in the histogram and fitted using the Gaussian distribution (left) and fitted PDFs correspond to different opening angles (right). 57

Figure 2.7 - Predicted results using the forward penalty approach and the iterative approach (GPA) with layer-specific three-dimensional residual deformations: (1) the von Mises stress distribution in the dissected view (row 1), (2) the transmural mean stress (row 2). 59

Figure 2.8 - von Mises stress distribution in the aortic hoop using the forward approach, the GPA approach (α=180°) and the layer-specific 3D residual deformation. 59

Figure 2.9 - Longitudinal forces computed using the GPA approach (α=180°) and the forward penalty approach on the proximal (nodes 0~50) and distal (nodes 51~100) boundaries of the ATAA model. The longitudinal forces were summed across the wall thickness before plotting. Because longitudinal forces for various opening angles are almost identical, thus only when α=180° is plotted. 63

Figure 3.1 - The flowchart of the material parameter identification process. 69

Figure 3.2 - Deformation measures that map the unloaded configuration Ω_0, the corotated unloaded configuration $\Omega_0^{'}$, the diastolic configuration Ω_a and the systolic configuration Ω_b. 72

Figure 3.3 - Implementation of the constitutive parameter identification. 76

Figure 3.4 - Validation of the inverse computation of left stretch tensor $\widetilde{V}_a$ using the constitutive parameters of patient ATAA2 $(C_{10}, k_1, k_2, \kappa, \theta) = (29.91, 512.56, 0.00, 0.3190, 90.00)$. The error is calculated by comparing the estimated $\widetilde{V}_a^{est}$ with "true" $\widetilde{V}_a$, the error bars represent the standard deviations. 79

Figure 3.5 - Convergence of the optimization for ATAA2. The solid black line is the “true” curve, and the dashed curves correspond to the estimated parameters in each iteration. Stress in the circumferential direction is plotted. 80

Figure 3.6 - Stretch-stress curves in 3-protocol numerical stretch-controlled tensile experiments for (1) strip biaxial tension in the circumferential direction (a), (d), (g) and (j); (2) equi-biaxial tension (b), (e), (h) and (k); (3) strip biaxial tension in the axial direction (c) (f) (i) and (l). The comparison of “true” and estimated curves for one patient is in the same row, i.e., (a)(b)(c) for ATAA1, (d)(e)(f) for ATAA2, (g)(h)(i) for ATAA3, (j), (k)(l) for ATAA4. 82

Figure 3.7 - Comparison of “true”, “almost-true” (i.e. computed from the forward penalty approach), and estimated systolic stress from optimization for patient (a) ATAA1, (b) ATAA2, (c) ATAA3 and (d) ATAA4. The error bars represent the standard deviation. 83

Figure 3.8 - CT image segmentation of the aorta (red) and ATAA segment (yellow) for the two patients. 85

Figure 3.9 - Measuring wall thickness from CT scans. 86

Figure 3.10 - Surface registration and transform to establish mesh correspondence. (A) Diastolic geometry Ω_{dia} and systolic geometry Ω_{sys} from image segmentation. (B) A nonlinear transform T from diastolic to systolic phase was obtained using non-rigid ICP registration [172] and thin-plate spline (TPS) fitting [173] algorithms, and therefore the distance between Ω_{sys} and the transformed geometry $\mathrm{T}(\Omega_{\mathrm{dia}})$ is minimized. (C) Diastolic and systolic quad meshes of the ATAA with mesh correspondence. 87

Figure 3.11 - Stress-stretch curves determined from the in vivo-identified material parameters and ex vivo-fitted material parameters for Patient 1 ((A)~(F)) and Patient 2 ((G)~(L)). Left column: strip-biaxial protocol in the circumferential direction; middle column: equi-biaxial protocol; right column: strip-biaxial protocol in the longitudinal direction. First and third rows: circumferential stress, second and fourth rows: longitudinal stress. The average response is indicated by 'ex vivo all'. Q1 and Q3 denote the 25% and 75% interquartile of in vivo stress range. 91

Figure 4.1	- The proposed machine learning (ML) approach.	101
Figure 4.2	- (a) The aorta segmented from a 3D CT image. (b) Trimmed aorta surface in gold color.	103
Figure 4.3	- Systolic aorta shapes corresponding to some representative sets of SSM parameters. The shapes are color-coded with curvature values.	107
Figure 4.4	- Datasets projected in 3D material parameter subspaces. The convex hull is plotted in the 3D subspaces for illustrative purpose.]	109
Figure 4.5	- Sampling the SSM parameter spaces.	110
Figure 4.6	- The procedure to generate aorta geometries at systole and diastole. The number in the parenthesis indicates the testing dataset.	112
Figure 4.7	- The neural network for mapping the shape codes to the material parameters. The green dots represent the input layer, and the blue dots represent the softplus units in the hidden layers and the output layer of the neural network.	116
Figure 4.8	- Adjusting the network structure using the leave-one-out (LOO) cross-validation.	118
Figure 4.9	- Evaluating the accuracy using the testing dataset.	120
Figure 4.10	- The actual and predicted material parameters. Each point was plotted using its actual value as horizontal x-coordinate and the ML-predicted value as the vertical y-coordinate. A perfect straight line (y=x) indicates perfect prediction, and any deviation from the straight line indicates prediction errors.]	122
Figure 4.11	- The actual and predicted stress-stretch curves for the best ((a), (b) and (c)), median ((d), (e) and (f)) and worst cases ((g), (h) and (i)).]	124
Figure 4.12	- MSE loss function for training and testing using softplus and other units.	127
Figure 5.1	- Off-axis tension test of the healthy porcine (a) and human ATAA (b) aortic samples. (a) Outlines of bog-bone shape specimen geometries on a porcine aortic sample. (b) Outlines of bog- bone shape specimen geometries on a human ATAA aortic sample. The 65° and 80° specimens were only obtained	135

from two patients. (c) Screenshots shows the change of fiber direction during the uniaxial test. $\hat{\theta}$ denotes the undeformed fiber orientation and θ is the deformed fiber orientation. A and C represent axial and circumferential directions, respectively.

Figure 5.2 - Effect of axial position on the circumferential strength. Solid red line indicates the mean value of circumferential strength. Blue dashed lines indicate the mean ± standard deviation. 136

Figure 5.3 - Uniaxial strength obtained from off-axis tests and failure criteria fits for the healthy porcine aortas. (a) to (d) represent porcine individual 1 to 4, respectively. 137

Figure 5.4 - Boxplot of uniaxial strength of human ATAA tissues in off-axis tests. Undeformed mean fiber orientation $\hat{\theta}$ is plotted on the horizontal axis. The red mark indicates the median, and the bottom and top edges of the box indicate the 25th and 75th percentiles, respectively. The whiskers extend to the maximum and minimum of $X_{\theta\theta}$. **, ***, **** indicates statistical significance levels of $p \leq 0.01$, $p \leq 0.001$, $p \leq 0.0001$, respectively. 138

Figure 5.5 - Uniaxial strength obtained from off-axis tests and failure criteria fits for the human ATAA patients. (a) and (b) represent patient 1 and 2, respectively. 139

Figure 5.6 - Boxplot of uniaxial strengths of human ATAA tissues. The red mark indicates the median, and the bottom and top edges of the box indicate the 25th and 75th percentiles, respectively. The whiskers extend to the maximum and minimum. **** indicates statistical significance level $p \leq 0.0001$. 141

Figure 5.7 - Uniaxial strengths and failure envelopes. (a) Circumferential (X) and axial (Y) strengths of the 125 ATAA patients. Among them, 84 patients were used for developing the probabilistic metric (Group 1), 41 patients were used for validation (Group 2). (b) Tsai-Hill (TH) failure envelopes of the 84 patients in Group 1. $\tau_{\theta z} = 0$ when generating the failure envelopes. 142

Figure 5.8 - The KDE-estimated joint PDF f_{XY} and marginal PDFs f_X and f_Y. Histograms for marginal distributions are also visualized. 144

Figure 5.9 - The estimated pdf f_W with given $\sigma_{\theta\theta}$ and σ_{zz} values. 147

Figure 5.10 - 2D contour of FP in $\sigma_{\theta\theta}$-σ_{zz} plane using (a) $\tau_{\theta z} = 0$ and (b) $\tau_{\theta z} = 300\text{kPa}$. 148

Figure 5.11 - FP evaluated under elevated blood pressure ($1.5P_{sys}$) using *in vivo*-identified ((a) and (c)) and *ex vivo*-derived ((b) and (d)) hyperelastic properties. (a) and (b): Patient 1; (c) and (d): Patient 2. 150

Figure 6.1 - FE simulations to reconstruct ATAA risk. 161

Figure 6.2 - Distribution of failure metrics for high and low risk patients using different stratification methods (Section 6.4). The numerically-reconstructed PRR (Section 6.3) is used as the “ground-truth” risk displayed in the horizontal axis. (a) Method 1: maximum diameter; (b) Method 2: maximum FP evaluated at P_{sys}; (c) Method 3: maximum FP evaluated at $1.5P_{sys}$ using representative hyperelastic properties; and (d) Method 4: maximum FP evaluated at $1.5P_{sys}$ using patient-specific hyperelastic properties. “one mat” stands for representative hyperelastic properties; “P-S mat” stands for patient-specific hyperelastic properties. The red mark indicates the median, and the bottom and top edges of the box indicate the 25th and 75th percentiles, respectively. The whiskers extend to the maximum and minimum. *, **, **** indicates statistical significance levels of $p \leq 0.05$, $p \leq 0.01$, $p \leq 0.0001$, respectively. 166

Figure 6.3 - ROC curves of different risk stratification methods. The plots are generated using false positive rate (FPR) versus true positive rate (TPR). “one mat” stands for representative hyperelastic properties; “P-S mat” stands for patient-specific hyperelastic properties. AUC for the diameter (Method 1), FP at P_{sys} (Method 2), FP at $1.5P_{sys}$ using representative hyperelastic properties (Method 3), and FP at $1.5P_{sys}$ using patient-specific hyperelastic properties (Method 4) are 0.5489, 0.8448, 0.7644 and 0.8621, respectively. 167

Figure 6.4 - Distribution of probabilistic (FP) and deterministic (TH) failure metrics for high and low risk ATAA. The numerically-reconstructed PRR (Section 6.3) is used as the “ground-truth” risk displayed in the horizontal axis. (a) and (b) Method 2: FP and TH evaluated at P_{sys}; (c) and (d) Method 4: FP and TH evaluated at $1.5P_{sys}$ using patient-specific hyperelastic properties. “P-S mat” stands for patient- 169 specific hyperelastic properties. The red mark indicates the median, and the bottom and top edges of the box indicate the 25th and 75th percentiles, respectively. The whiskers extend to the maximum and minimum. *, **, **** indicates statistical significance levels of $p \leq 0.05$, $p \leq 0.01$, $p \leq 0.0001$, respectively.

Figure 6.5 - ROC curves of diameter criterion, probabilistic (FP) and deterministic (TH) failure metrics. The plots are generated using false positive rate (FPR) versus true positive rate (TPR). (a) Method 2: FP and TH evaluated at P_{sys}; (b) Method 4: FP and TH evaluated at $1.5P_{sys}$ using patient-specific hyperelastic properties. "P-S mat" stands for patient-specific hyperelastic properties. AUC for the diameter, FP at P_{sys}, TH at P_{sys}, FP at $1.5P_{sys}$ and TH at $1.5P_{sys}$ are 0.5489, 0.8448, 0.8017, 0.8621 and 0.8362, respectively. 170

Figure 7.1 - Failure envelopes in the σ_{11}-σ_{22} plane for the human ATAA patients. (a) and (b) represent patient 1 and 2, respectively. Failure parameters are obtained from fitting off-axis testing data. 180

Figure A.1 - Flow chart of the material parameter estimation process. The backward displacement iteration is set to be 10 according to [13] 188

Figure A.2 - Procedures to build resolutions and links. 188

Figure A.3 - Overlay plots of the 4 levels projected in (a) $PC_1 \sim PC_2$ and (b) $PC_2 \sim PC_3$ plane. 192

Figure A.4 - The stress-stretch curves in the circumferential strip biaxial protocol for the first and second levels. 196

Figure A.5 -The stress-stretch curves in the circumferential strip biaxial protocol obtained by randomly sampling 117 points from the material parameter space. 196

Figure A.6 - Links between the first 2 levels projected in the $PC_1 \sim PC_2 \sim PC_3$ space. 199

Figure A.7 - Convergence of estimated material parameters to the experimentally-derived material parameters using the MRDS method. The equi-biaxial stress-stretch curves are plotted in each level from (a) to (d). 202

Figure A.8 - Stretch-stress curves in the numerical validation for (a) strip biaxial tension in the circumferential direction; (b) equi-biaxial tension; (c) strip biaxial tension in the longitudinal direction. 203

Figure A.9 - Comparison of the "measured" and estimated geometries at the systolic phase in the numerical validation. ε_{sys} is the average of node-to-surface distances between the "measured" and estimated systolic geometries. The "measured" geometry is displayed in triangle mesh, estimated systolic geometry is displayed in quadrilateral shell mesh. 203

Figure A.10 - Estimated stress-stretch curves for the healthy aorta for (a) strip biaxial tension in the circumferential direction; (b) equi-biaxial tension; (c) strip biaxial tension in the longitudinal direction. 205

Figure A.11 - Comparison of the estimated systolic geometry and the systolic geometry from CT image for the healthy aorta. ε_{sys} is the average of node-to-surface distances between two geometries. The geometry from CT image is displayed in triangle mesh, estimated systolic geometry is displayed in quadrilateral shell mesh. 205

Figure B.1 - The proposed machine learning-based constitutive model. 217

Figure B.2 - The novel neural network material model (NNMat) with a physics constraint and two parameter-set structures: the class parameter set (blue) and the subject parameter set (red), dashed arrows indicate skip connections. The subject parameter set consist of three constitutive parameters: $\{m_1, m_2, \theta\}$. 222

Figure B.3 - Representative stress-stretch results of the seven-protocol planar biaxial testing of two ATAA tissues. Each row represents one patient. (a) and (d): seven successive nominal stress ratios. (b) and (e): circumferential stress-stretch data. (c) and (f): longitudinal stress-stretch data. 229

Figure B.4 - Cross validation of the NNMat model on patient level and stress protocol level. Ten-fold cross validation was performed for different patient groups. For each patient, leave-one-out cross validation was performed with different stress protocols. 231

Figure B.5 - Evaluating accuracy of the NNMat model using an additional testing dataset of 6 patients. 232

Figure B.6 - Representative Cauchy stress stretch results of the NNMat model and the Holzapfel-Gasser-Ogden model [9] (Section 2.1) in fitting and testing for patient 59. 236

Figure B.7 - Strain energy density function with respect to E_11 and E_22 with E_12=0. Four representative patients are plotted. (a): patient 58, (b): patient 59, (c): patient 60 and (d): patient 62. 238

Figure B.8 - Contour plots of tangent moduli in the subject parameter space (θ=0°, trained using patients 7~63). (a) and (b): circumferential; (c) and (d): longitudinal. (a) and (c): tangent modulus at high strain region (0.5); (d) and (d): tangent modulus at low strain region (0.1). Units of tangent moduli are in MPa. 239

SUMMARY

Advances in imaging techniques and numerical methods have made it possible to investigate the *in vivo* biomechanics of the cardiovascular system on a patient-specific level. For the four key components in a patient-specific biomechanical analysis (geometries, loading and boundary conditions, material hyperelastic properties and material failure properties), patient-specific geometries and physiological loading conditions can be obtained at a high level of spatial and temporal resolutions from clinical diagnostic imaging tools, such as CT scans, and blood pressure measurements, respectively. However, accurate identification of the unknown *in vivo* patient-specific hyperelastic properties, which are nonlinear and anisotropic, has been a challenging problem in the field of cardiovascular biomechanics for several decades. Furthermore, since patient-specific failure properties cannot be obtained noninvasively from clinical images, an accurate failure metric that incorporates uncertainties of failure properties, needs to be developed for patient-specific biomechanical assessment. Therefore, the objective of this thesis was to develop a novel computational framework to identify *in vivo* patient-specific hyperleastic properties for biomechanical risk assessment of ascending thoracic aortic aneurysm (ATAA). A novel inverse method was developed for *in vivo* hyperleastic property identification from clinical 3D CT images. A machine learning (ML) approach was investigated for fast *in vivo* material property identification (i.e., within seconds). To assess ATAA risk, a novel probabilistic and anisotropic failure metric was derived by using uniaxial failure testing data. For validation, risk assessment methods were compared using matching CT images and tissue samples of additional patients.

CHAPTER 1. INTRODUCTION

1.1 Ascending Thoracic Aortic Aneurysm (ATAA)

The aorta is the largest artery that is responsible for carrying oxygen-rich blood away from the heart to the rest of body. Aortic aneurysm occurs when the aortic wall becomes weakened and enlarges. Aortic aneurysm that occurs in the chest area is known as thoracic aortic aneurysm (TAA). TAA can involve aortic root, ascending aorta, aortic arch, or descending aorta. As shown in Figure 1, ascending thoracic aortic aneurysm (ATAA) and descending thoracic aortic aneurysm (DTAA) are two common types of TAA. TAA is a lethal disease, which may lead to aortic rupture or dissection. Aortic rupture is the rupture or breakage of the aorta, which is an extremely dangerous condition. Aortic dissection occurs when a tear in the inner layer of the aorta produces a crack that propagates between the layers in the aortic wall. This separation can weaken the aorta by creating a false lumen (FL) where blood can flow, increasing risk of aortic rupture [1]. In addition, the formation of a pressurized FL can compress the true lumen (TL) until collapse, resulting in malperfusion [2]. The five-year survival in TAA patients left untreated is 54% [3].

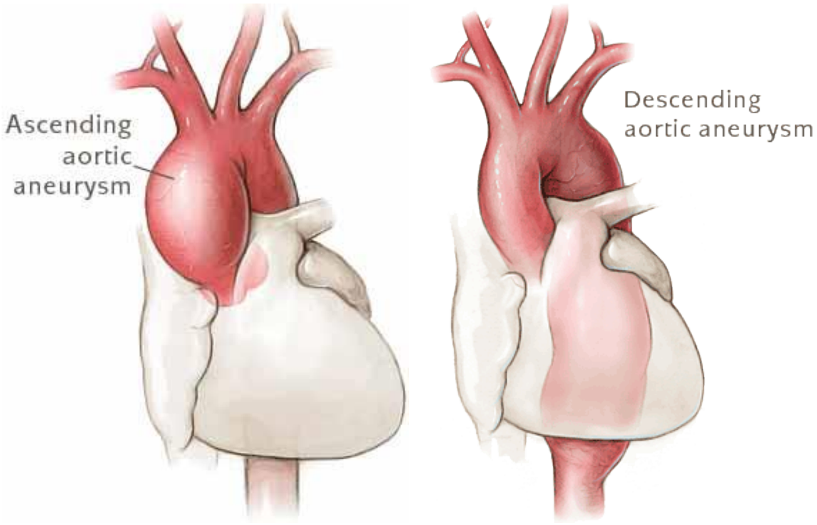

Figure 1.1 - Thoracic aortic aneurysm (TAA). Left: ascending thoracic aortic aneurysm (ATAA); right: descending thoracic aortic aneurysm (DTAA), adopted from uvahealth.com.

TAA grows on average at 0.10 cm per year. The descending aorta grows faster than the ascending aorta at 0.19 versus 0.07 cm per year. Also the larger the aorta the faster it grows [4]. Symptoms are rare with this disease: for about 95% of patients, the first symptom is often death [5]. Rupture and dissection can be avoided through elective surgical repair; however, identifying individuals at risk is challenging.

ATAA is also linked with familial inherited pattern [6]: aortic growth rate was highest for the familial group (0.21cm per year), intermediate for the sporadic group (0.16 cm per year), and lowest for the Marfan group (0.1 cm per year). Furthermore, familial ATAA patients tended to be younger at presentation than sporadic aneurysm patients.

ATAA had negative association with systemic atherosclerosis [7]. By scoring calcification of each coronary artery and aortic segment, aneurysms and dissection were found to be associated with decreased systemic atherosclerosis. But the mechanism behind the phenomena remained speculative. Aortic stenosis presented a significant added risk of rupture or dissection for patients with aneurysmal disease in the setting of bicuspid aortic valve (BAV) [8].

1.1.1 Diagnosis and Treatment

The diagnosis of an ascending aortic aneurysm is often made on computed tomography (CT) scans or magnetic resonance imaging (MRI). Strict blood pressure control can help prevent progression of the aneurysm in many patients with small ATAAs, which is frequently achieved by beta-blockers. Currently, the clinical decision whether to electively repair a TAA [9] is mainly based on the aortic size. Elective, preemptive surgical repair restored life expectancy to normal. In an open chest surgery, TAA is repaired by removing the aneurysmal section of the aorta and replacing it with a synthetic graft, which is sewn into place. For connective tissue disorders such as the Marfan syndrome, aortic root replacement is typically performed. The native aortic valve may be replaced by a mechanical or biological valve. In an endovascular surgery, the endovascular graft can reinforce the aneurysmal section of the aorta to prevent TAA rupture. Endovascular repair is promising [10], but long-term safety remains unproven [11].

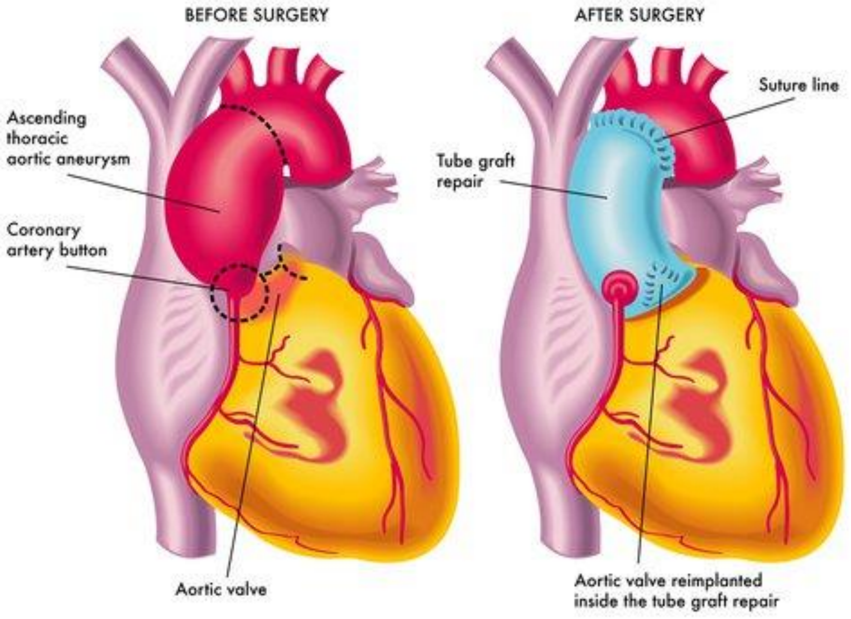
BEFORE SURGERY
AFTER SURGERY
Ascending thoracic aortic aneurysm
Coronary artery button
Aortic valve
Suture line
Tube graft repair
Aortic valve reimplanted inside the tube graft repair

Figure 1.2 - ATAA before and after repair (adapted from www.healio.com)

1.1.2 The Current Diameter Criterion is not a Perfect Predictor of ATAA Risk

The aortic size is a strong predictor of rupture, dissection, and mortality [3]. The incidence of dissection or rupture increased with aneurysm size [9]. Hinge points in the aortic size were identified at which rupture or dissection occurred. At size greater than 6.0 cm, the odds ratio for rupture or dissection increased sharply. Thus, intervention was recommended for the ascending aorta at the size of 5.5cm and for the descending aorta at 6.5cm [4]. A relative aortic size index (ASI) which was calculated as aortic diameter divided by body surface area was introduced to predict aneurysm rupture more accurately [12]. In risk/benefit analysis, the accumulated data strongly supported a policy of preemptive surgical extirpation of the asymptomatic aneurysmal thoracic aorta to prevent rupture and dissection [4].

Currently, the clinical surgery criterion is primarily based on the aortic size and classifies an ATAA as high risk if the (maximum) diameter is larger than 5.5cm [9, 12]. This diameter-based decision rule can be explained by mechanical analysis of a simplified aorta as a straight tube with a uniform diameter, where the hoop stress is proportional to the diameter, and it uses the simple rupture criterion: as the diameter increases, the hoop stress will eventually exceed the strength of the aorta tissue, resulting in tissue failure.

Not surprisingly, the aortic size-based criterion has been shown to be an unreliable indicator of patient risk [13, 14], which may not accurately reflect a patient's risk: some aneurysms at smaller diameters (e.g., < 4cm) can and do rupture [13].

1.2 Biomechanical Testing of Aortic Tissues

Biomechanical tests are typically performed to characterize aortic tissue properties, which usually include uniaxial testing, biaxial testing, and bulge inflation testing. In this thesis, uniaxial tests and planar biaxial tests were performed to obtain mechanical properties of human aortic tissues. Thus, their testing setups and methods are briefly summarized here.

1.2.1 Uniaxial Testing

In a typical uniaxial test, the sample is trimmed into dog bone-shaped specimen. Thickness values are measured at three locations in the narrow portion. An average thickness can be calculated for the undeformed cross-section area. The uniaxial tests can be conducted at room temperature. Optical markers are placed on the narrow portion of the specimens for optical strain measurements. The axial force can be measured using a load cell. During the test, fine grit sandpaper can be placed between the tissue and the clamps to avoid slippage. The specimen is quasi-statically stretched to failure at a constant displacement rate, which is shown in Figure 1.3. The specimen needs to be continuously hydrated with phosphate buffered normal saline (PBS) solution to allow for optimal tissue hydration during testing. Displacement between the markers can be obtained by tracking the optical markers using image analysis. The stress and strain can be calculated from the force and displacement measurements.

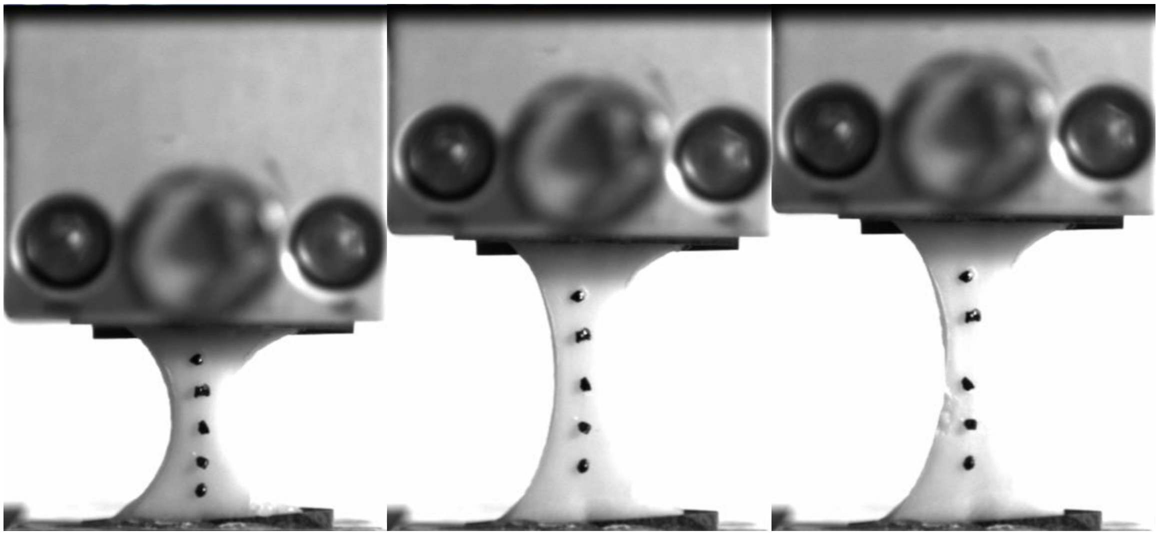

Figure 1.3 - Uniaxial testing of aortic wall tissue. The specimen is quasi-statically stretched until failure.

Uniaxial tests are typically performed to obtain hyperplastic responses and failure strengths of the aortic wall. Many aortic tissue rupture studies [15-24] revealed that hyperplastic and failure properties of the aortic wall are anisotropic. Significant difference was found between the circumferential and axial wall strengths [15-24].

1.2.2 Planar Biaxial Testing

Planar biaxial test is a technique to investigate mechanical behaviour of soft tissue. The tissue undergoes different paths of strain/stress in the planar biaxial test. Figure 1.4 illustrates a typical setup of biaxial testing. Planar biaxial tests are performed on a square specimen of planar soft tissue, which has a side length of about 10-25 mm. Optical markers are placed on the central region of the specimens for optical strain measurements. The specimen is mounted on to the biaxial device using suture attachments, which allows the edges to expand freely in the lateral direction [25]. During the planar biaxial tests, the specimen completely immersed in PBS (pH 7.4) at body (37 °C) temperature. The central testing region, where the optical markers are attached to, must be sufficiently small and located away from the outer edges to remove the boundary effects [25]. Thus, in the central testing region the stress and strain fields are generally considered homogeneous. The two-dimensional (2D) strain can be calculated from the displacement of the markers.

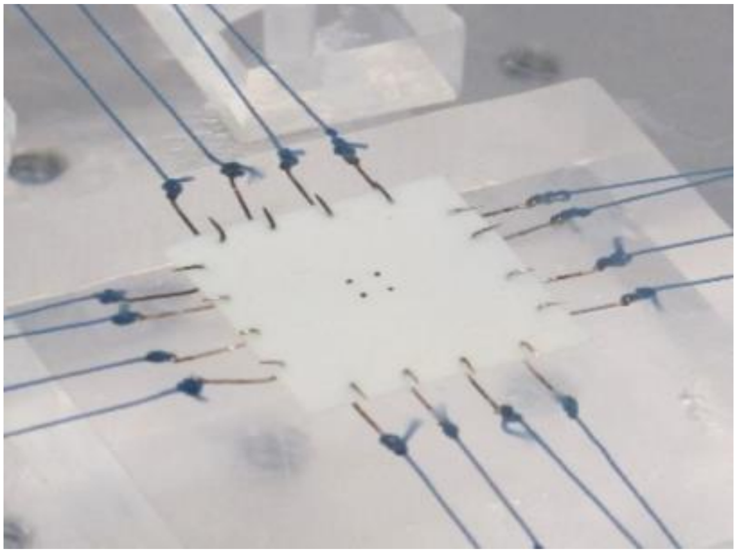

Figure 1.4 - Setup of the planar biaxial test. The specimen is mounted on to the biaxial device using four suture attachments.

2D strain field in the central testing region can be computed using finite element (FE) interpolation. Briefly, using linear shape/interpolation functions, the displacement and reference nodal positions can be interpolated to a continuous function. Next, the displacement gradient tensor can be obtained by taking derivatives of displacement with respect to reference nodal positions, Finally, the deformation gradient and Green strain tensors are computed.

For a 2D four node quadrilateral element, the shape functions map the reference configuration to a master element and interpolate the discrete reference coordinates. Considering counterclockwise order of the nodes, the shape functions for the four nodes are

$$\text{Node 1: } \phi_1(r,s) = \frac{1}{4}(1+r)(1+s)$$

$$\text{Node 2: } \phi_2(r,s) = \frac{1}{4}(1-r)(1+s)$$

$$\text{Node 3: } \phi_3(r,s) = \frac{1}{4}(1-r)(1-s)$$

$$\text{Node 4: } \phi_4(r,s) = \frac{1}{4}(1+r)(1-s) \tag{1.1}$$

where r and s are coordinates in the master element. Therefore, for any points inside the quadrilateral element, the coordinates X and Y of reference configuration are

$$X(r,s) = \phi_1(r,s)X_1 + \phi_2(r,s)X_2 + \phi_3(r,s)X_3 + \phi_4(r,s)X_4 \tag{1.2}$$

$$Y(r,s) = \phi_1(r,s)Y_1 + \phi_2(r,s)Y_2 + \phi_3(r,s)Y_3 + \phi_4(r,s)Y_4$$

where X_i and Y_i denotes the coordinates of ith node. Similar equations hold for displacement u and v are

$$u(r,s) = \phi_1(r,s)u_1 + \phi_2(r,s)u_2 + \phi_3(r,s)u_3 + \phi_4(r,s)u_4$$

$$v(r,s) = \phi_1(r,s)v_1 + \phi_2(r,s)v_2 + \phi_3(r,s)v_3 + \phi_4(r,s)v_4 \tag{1.3}$$

Apply the chain rule, one can compute a component of displacement gradient tensor using

$$\frac{\partial u}{\partial X} = \frac{\partial u}{\partial r}\frac{\partial r}{\partial X} + \frac{\partial u}{\partial s}\frac{\partial s}{\partial X}$$

$$\frac{\partial u}{\partial Y} = \frac{\partial u}{\partial r}\frac{\partial r}{\partial Y} + \frac{\partial u}{\partial s}\frac{\partial s}{\partial Y} \tag{1.4}$$

Similar equations exist for $\frac{\partial v}{\partial X}$ and $\frac{\partial v}{\partial Y}$, and the displacement gradient $\boldsymbol{H}$ in 2-D form can be obtained as

$$\boldsymbol{H} = \begin{bmatrix} \frac{\partial u}{\partial X} & \frac{\partial u}{\partial Y} \\ \frac{\partial v}{\partial X} & \frac{\partial v}{\partial Y} \end{bmatrix} = \begin{bmatrix} \frac{\partial u}{\partial r} & \frac{\partial u}{\partial s} \\ \frac{\partial v}{\partial r} & \frac{\partial v}{\partial s} \end{bmatrix} \begin{bmatrix} \frac{\partial r}{\partial X} & \frac{\partial r}{\partial Y} \\ \frac{\partial s}{\partial X} & \frac{\partial s}{\partial Y} \end{bmatrix} = \begin{bmatrix} \frac{\partial u}{\partial r} & \frac{\partial u}{\partial s} \\ \frac{\partial v}{\partial r} & \frac{\partial v}{\partial s} \end{bmatrix} \begin{bmatrix} \frac{\partial X}{\partial r} & \frac{\partial X}{\partial s} \\ \frac{\partial Y}{\partial r} & \frac{\partial Y}{\partial s} \end{bmatrix}^{-1} \tag{1.5}$$

For the derivatives in the matrix, considering that u_i, v_i, X_i and Y_i are constant, the derivatives are

$$\frac{\partial u}{\partial r} = \frac{1}{4}[(1+s)u_1 - (1+s)u_2 - (1-s)u_3 + (1-s)u_4]$$

$$\frac{\partial u}{\partial s} = \frac{1}{4}[(1+r)u_1 + (1-r)u_2 - (1-r)u_3 - (1+r)u_4]$$

$$\frac{\partial v}{\partial r} = \frac{1}{4}[(1+s)v_1 - (1+s)v_2 - (1-s)v_3 + (1-s)v_4]$$

$$\frac{\partial v}{\partial s} = \frac{1}{4}[(1+r)v_1 + (1-r)v_2 - (1-r)v_3 - (1+r)v_4]$$

$$\frac{\partial X}{\partial r} = \frac{1}{4}[(1+s)X_1 - (1+s)X_2 - (1-s)X_3 + (1-s)X_4]$$

$$\frac{\partial X}{\partial s} = \frac{1}{4}[(1+r)X_1 + (1-r)X_2 - (1-r)X_3 - (1+r)X_4]$$

$$\frac{\partial Y}{\partial r} = \frac{1}{4}[(1+s)Y_1 - (1+s)Y_2 - (1-s)Y_3 + (1-s)Y_4]$$

$$\frac{\partial Y}{\partial s} = \frac{1}{4}[(1+r)Y_1 + (1-r)Y_2 - (1-r)Y_3 - (1+r)Y_4] \tag{1.6}$$

By using above equations, the displacement gradient can be computed. The deformation gradient tensor $\boldsymbol{F}$ can be computed using

$$\boldsymbol{F} = \boldsymbol{H} + \boldsymbol{I} \tag{1.7}$$

where $\boldsymbol{I}$ is identity tensor. Using incompressibility condition, the three-dimensional (3D) deformation gradient tensor can be obtained. Since the nominal stress $\boldsymbol{N}$ can be directly calculated from the force measurements and tissue thickness, the second Piola-Kirchhoff stress $\boldsymbol{S}$ can be obtained using

$$\boldsymbol{S} = \boldsymbol{N}\boldsymbol{F}^{-T} \tag{1.8}$$

Planar biaxial tests have been used to study hyperleastic properties of aortic tissues. In a study [15], Planar biaxial tests were performed to investigate and compare the mechanical properties of aortic tissues from 55 ATAA patients with and without concomitant bicuspid aortic valve (BAV) or bovine aortic arch (BAA). It was found that the BAV samples were stiffer than both ATAA and BAA samples, and the BAA samples were similar to the ATAA samples. In another study [26], age-related biaxial biomechanical behavior of human abdominal aortic tissue was investigated. The results suggested an age-dependent shift in the mechanical response of this tissue.

1.2.3 Bulge Inflation Testing

Bulge inflation test is another type of test to study both hyperelastic and failure behaviors of aortic tissues[27, 28]. In the bulge inflation test, tissue sample is cut into a square-shaped specimen. The specimen is then clamped in an inflation device forming a hermetically sealed cavity in which a fluid (typically water) is injected at a controllable rate. In the meanwhile, the fluid pressure is measured and recorded. Deformation can be obtained by using digital image correlation [17, 29, 30]. The tests provides full-field displacement data and can be used to characterize localized mechanical properties of aortic tissues.

As an example, Duprey et al [31] investigated biaxial rupture properties of ATAA tissues using bulge inflation tests, which demonstrated significantly different rupture stress and stretch compared to those from the uniaxial tests. Specifically, the rupture stretch λ_{rup} in the bulge inflation test is significantly lower than the uniaxial λ_{rup} in both circumferential and axial directions. However, in contrast to planar biaxial tests that has controllable paths of stresses, circumferential and axial stresses are equal in the bulge inflation test.

1.3 Hyperelastic and Failure Modeling of Aortic Tissues

1.3.1 Hyperelastic Modelling

Constitutive modeling of soft tissues is often achieved by specifying the strain energy density W as a function of deformation gradient $W(\boldsymbol{F})$, where $\boldsymbol{F}$ represents the deformation gradient tensor.

Soft biological tissues, such as the aortic wall, comprise bundles of collagen fibers embedded in a ground matrix and can be regarded as fiber-reinforced composites. The deformation gradient $\boldsymbol{F}$ can be multiplicatively decomposed into

$$\boldsymbol{F} = (J^{1/3}\boldsymbol{I})\overline{\boldsymbol{F}} \tag{1.9}$$

where J is the determinant of $\boldsymbol{F}$, and $\boldsymbol{I}$ is the identity tensor. $\overline{\boldsymbol{F}}$ represents the volume-preserving (isochoric) part of the deformation gradient, while $(J^{1/3}\boldsymbol{I})$ represents the volumetric part. The right Cauchy-Green tensor $\boldsymbol{C}$ and its isochoric counterpart $\overline{\boldsymbol{C}}$ is defined as

$$\boldsymbol{C} = \boldsymbol{F}^T\boldsymbol{F}$$

$$\overline{\boldsymbol{C}} = \overline{\boldsymbol{F}}^T\overline{\boldsymbol{F}} \tag{1.10}$$

For nearly incompressible (slightly compressible) material, the total strain energy function W can be additively split into isochoric W_{iso} and volumetric W_{vol} parts, according to

$$W(\boldsymbol{C}, \boldsymbol{a}_{0i}) = W_{iso}(\overline{\boldsymbol{C}}) + W_{vol}(J) \tag{1.11}$$

The strain energy density function W_{iso} is usually formulated based on strain invariants of the isochoric right Cauchy-Green tensor, $\overline{\boldsymbol{C}}$. The first two isochoric strain invariants $\bar{I}_1$ and $\bar{I}_2$ are defined as

$$\bar{I}_1 = tr(\overline{\boldsymbol{C}})$$

$$\bar{I}_2 = \frac{1}{2}\left[\bar{I}_1{}^2 - tr(\overline{\boldsymbol{C}}^2)\right] \tag{1.12}$$

Isotropic hyperelastic model, such as the Demiray model [32], was used to model soft tissues. In the Demiray model, W_{iso} takes the form

$$W_{iso} = D_1\{\exp[D_2(\bar{I}_1 - 3)] - 1\} \tag{1.13}$$

where D_1 and D_2 are material parameters. However, the hyperelastic properties of the aortic wall is anisotropic.

Microstructurally-motivated constitutive models have become increasingly utilized for anisotropic hyperelastic response of soft tissues, in which the contributions of the matrix and collagen fibers to W_{iso} can be modeled separately. Here, we consider a subclass of anisotropic responses, in which the strain energy density depends on four strain invariants: $\bar{I}_1$, $\bar{I}_2$, $\bar{I}_4$ and $\bar{I}_6$. For a fiber-reinforced composite material with two families of fibers, $\bar{I}_4$ and $\bar{I}_6$ are two additional pseudo-invariants that describes deformations in the preferred fiber directions

$$\bar{I}_4 = \boldsymbol{a}_{01} \cdot (\bar{\boldsymbol{C}}\boldsymbol{a}_{01})$$

$$\bar{I}_6 = \boldsymbol{a}_{02} \cdot (\bar{\boldsymbol{C}}\boldsymbol{a}_{02}) \tag{1.14}$$

where unit vectors $\boldsymbol{a}_{01}$ and $\boldsymbol{a}_{02}$ characterize two fiber directions in the reference configuration. These two fiber directions are often assumed to be symmetric about an axis. $\boldsymbol{a}_{01} = (cos\,\theta\,, sin\,\theta\,, 0)$ and $\boldsymbol{a}_{02} = (cos\,\theta\,, -\,sin\,\theta\,, 0)$, where θ is the angle between the fiber direction and the axis of symmetry. Typically, the circumferential axis of the aorta was used as reference. Thus, $\bar{I}_4$ and $\bar{I}_6$ are equal to squares of the stretches in the fiber directions. In the work by Holzapfel et al. [33], the total strain energy density function W can be additively split into isotropic and anisotropic parts. The isotropic matrix material is characterized by strain energy function of the neo-Hookean type. To account for the strong stiffening effect of the collagen fiber recruitment, an exponential function is employed. W_{iso} is given by

$$W_{iso} = \mu(\bar{I}_1 - 3) + \frac{k_1}{2k_2} \sum_{k=4,6} \{\exp[k_2(\bar{I}_k - 1)^2] - 1\} \tag{1.15}$$

where μ is a material parameter to describe the matrix response. k_1 is a positive material parameter that has the same unit of stress, while k_2 is a unitless material parameter. For the volumetric part W_{vol}, the following function is used in Abaqus

$$W_{vol} = \frac{1}{D}[\frac{J^2 - 1}{2} - ln\, J] \tag{1.16}$$

where D is a constant that enforces material incompressibility.

The Holzapfel-Gasser-Ogden model [33] has been extended to other forms. Using the generalized structural tensor (GST), Gasser et al. [34] constructed the following isochoric contribution of the strain energy density function

$$W_{iso} = \mu(\bar{I}_1 - 3) + \frac{k_1}{2k_2} \sum_{k=4,6} [exp\{k_2[\kappa I_1 + (1 - 3\kappa)I_k - 1]^2\} - 1] \tag{1.17}$$

where κ is a parameter describing dispersion of the fiber orientation. This model is known as the Gasser-Ogden-Holzapfel (GOH) model, which has five constitutive parameters, μ, k_1, k_2, κ and θ.

The stress-strain relation can be derived by differentiating the strain energy density W. The Cauchy stress can be calculated using [35]

$$\boldsymbol{\sigma} = \boldsymbol{\sigma}_{vol} + \boldsymbol{\sigma}_{iso} = p\boldsymbol{I} + J^{-1}\overline{\boldsymbol{F}}Dev(\overline{\boldsymbol{S}})\overline{\boldsymbol{F}}^{T} \tag{1.18}$$

where $\boldsymbol{\sigma}_{vol}$ and $\boldsymbol{\sigma}_{iso}$denotes the volumetric and isochoric contribution respectively, p is the hydrostatic pressure $p = dW_{vol}(J)/dJ$, $\boldsymbol{I}$ is the identity tensor. $\overline{\boldsymbol{S}}$ can be expressed by $\overline{\boldsymbol{S}} = 2\partial W_{iso}(\overline{\boldsymbol{C}})/\partial\overline{\boldsymbol{C}}$ and $Dev(\blacksquare) = (\blacksquare) - (1/3)[(\blacksquare):\boldsymbol{C}]\boldsymbol{C}^{-1}$.

In our recent study, we have proposed a physics-informed machine learning (ML) model for constitutive modeling of the aortic tissues (APPENDIX B). Application of ML methods are introduced in Section 1.6.

1.3.2 Failure Modelling

Isotropic failure criteria such as the von Mises stress criterion have been widely adopted in the computational failure analysis of the aortic wall [36-38]. Similar to the maximum shear (Tresca) criterion, the von Mises stress is a classical metric in determining yielding of metal materials due to shear stress in the octahedral plane [39]. The von Mises criterion may not be appropriate for soft biological tissue. The exact failure mechanisms of soft tissue remain unclear and experimental findings suggest that the failure is likely governed by maximum normal stress [27, 40, 41]. The maximum principal stress is another isotropic failure criterion commonly used for the aortic wall [41-43]. However, experimental investigations have demonstrated a significant difference of wall strengths in the circumferential and axial directions of aortic tissues [15-18]. It is impossible to incorporate the anisotropic failure properties into an isotropic failure metric, such as the von Mises stress or the maximum principal stress.

Material failure criteria of engineered fiber-reinforced composites, which are usually made up of unidirectional fiber-reinforced laminae [44-47], have been extensively studied. These composites often exhibit directional-dependent (anisotropic) strength. Among them, the Tsai-Hill criterion [48, 49] and the Hashin-Rotem criterion [50] are two well-known models to characterize anisotropic failure properties of engineered fiber-reinforced composites without fiber dispersion. In these criteria, stress components in the current coordinates need to be transformed onto the material axes to determine failure. Since engineered composites usually undergo non-rotational, infinitesimal deformation before failure, the material axes are often considered to be fixed [45], i.e., independent of deformation. However, the failure criteria assuming fixed material axes may not be valid for the aortic tissues undergoing finite deformation [51]. Recently, Korenczuk et al. [52] applied the Tsai-Hill failure theory to model an anisotropic failure of porcine abdominal aortas. The authors found that the Tsai-Hill criterion, although not able to capture all aspects of tissue failure, performed much better than the von Mises stress criterion [52].

Several anisotropic failure criteria have been utilized for engineered fiber-reinforced composite materials. For the Tsai-Hill criterion [48, 49], the failure metric Λ takes the form of:

$$\Lambda = \left(\frac{\sigma_{\theta\theta}}{X}\right)^2 + \left(\frac{\sigma_{zz}}{Y}\right)^2 - \left(\frac{\sigma_{\theta\theta}}{X}\right)\left(\frac{\sigma_{zz}}{X}\right) + \left(\frac{\tau_{\theta z}}{S}\right)^2 \tag{1.19}$$

where $\sigma_{\theta\theta}$, σ_{zz} and $\tau_{\theta z}$ denotes the normal stress in the fiber direction, transverse normal stress and in-plane shear stress, respectively. X, Y and S are fiber tensile, transverse tensile and in-plane shear strengths, respectively, which are the model parameters to be determined. When $\Lambda = 1$, failure is predicted. The Tsai-Hill criterion is interactive, i.e., it is assumed that all stress components simultaneously contribute to the failure of the composite.

The Hashin-Rotem criterion [50] is another widely used anisotropic failure criterion which incorporates two separate failure modes:

$$\Lambda_f = \frac{\sigma_{\theta\theta}}{X} \qquad \text{fiber failure}$$

$$\Lambda_m = \left(\frac{\sigma_{zz}}{Y}\right)^2 + \left(\frac{\tau_{\theta z}}{S}\right)^2 \qquad \text{matrix failure} \qquad (1.20)$$

The model parameters X, Y and S have similar meanings to those in the Tsai-Hill model. The combined failure metric Λ can be determined by $\Lambda = max\left(\Lambda_f, \Lambda_m\right)$. Failure can be predicted when Λ reaches 1.

For both the Tsai-Hill and the Hashin-Rotem model, X and Y can be determined from uniaxial failure stresses in the fiber and transverse directions, respectively. In order to find S, other mechanical tests, e.g., off-axis tension tests, needs to be performed. Off-axis tests are uniaxial tests along different angles w.r.t to the material axis (i.e., fiber direction). The uniaxial stress in the loading axis needs to be transformed onto the material axis to determine failure using Eqn. (1.19) and (1.20), therefore, a set of transformed stress states can be obtained in the off-axis tension tests. Using the Tsai-Hill model, the off-axis uniaxial strength $X_{\theta\theta}$ can be expressed as

$$X_{\theta\theta}(\theta) = 1\Bigg/\sqrt{\frac{cos^4\,\theta}{X^2} + \frac{sin^4\,\theta}{Y^2} - \frac{sin^2\,\theta\,cos^2\,\theta}{X^2} + \frac{sin^2\,\theta\,cos^2\,\theta}{S^2}} \tag{1.21}$$

where θ is the angle between the fiber direction and the loading axis. Similarly, for the Hashin-Rotem criterion, the off-axis uniaxial strengths for fiber and matrix failure are

$$X_{\theta\theta,f}(\theta) = \frac{X}{cos^2\,\theta} \qquad \text{fiber failure}$$

$$X_{\theta\theta,m}(\theta) = 1\Bigg/\sqrt{\frac{sin^4\,\theta}{Y^2} + \frac{sin^2\,\theta\,cos^2\,\theta}{S^2}} \qquad \text{matrix failure} \tag{1.22}$$

and $X_{\theta\theta}(\theta) = \min\left(X_{\theta\theta,f}(\theta), X_{\theta\theta,m}(\theta)\right)$. Since many soft biological tissues can be considered as fiber-reinforced composites (e.g., collagen fiber in the media layer of the arterial wall are mostly circumferentially oriented), traditional anisotropic failure criteria without fiber dispersion may be directly used to approximate the anisotropic failure properties of soft biological tissues [52].

Micromechanics model, such as the one proposed by Li and Holzapfel [53], may be developed to model hyperelastic and failure properties simultaneously with a common description of fiber dispersion. In this type of model, the failure/damage is related to stress/stretch of each individual fiber using a specific hyperelastic constitutive model, the damage parameters and hyperelastic parameters are coupled, which requires damage and hyperelastic parameters to be identified simultaneously using one set of testing data (e.g. uniaxial data). As shown by experimental works [15, 31], ATAA tissues demonstrate a slightly anisotropic stress-strain response in the elastic deformation region, but the anisotropy in terms of uniaxial strength and failure is much more significant (e.g., circumferential strength is almost double of the axial strength [31]). The slightly anisotropic hyperelastic response may be explained by helically arranged fiber structure in the intima and adventitial layer [54-56], while failure properties of the intact aortic wall may be predominantly determined by the media layer, which has nearly circumferentially-oriented fibers. It could be difficult to consolidate different degrees of anisotropy using the same fiber dispersion pdf. Therefore, failure modeling using such an approach [53] is very challenging and requires more validations, e.g., using off-axis testing data.

1.4 Biomechanical Assessment of ATAA Risk

1.4.1 Biomechanical Risk Assessment is Promising

Biomechanical ATAA risk assessment hold promise. By performing patient-specific finite element analysis (FEA), Martin et al. [57] obtained clinical CT imaging data and tissue mechanical testing data from 27 matching ATAA patients. ATAA inflation and rupture were simulated using FE models of the 27 patients. The aortic size index was sufficient for identifying the patients with the lowest rupture risk, but insufficient for stratifying between patients at moderate and high risk. The results support the use of biomechanical metrics such as peak systolic wall stress and tension-strain modulus for assessment of ATAA rupture risk. Trabelsi et al. [30] conducted a similar study to investigate the patient-specific wall stress distribution of ATAA and the retrospective rupture risk for each patient. Preoperative CT images of 5 ATAA patients were obtained during elective surgeries to generate FE models. Hyperelastic and rupture properties of each patient were obtained using bulge inflation tests. Biomechanical and diameter based rupture risk assessments were found to be weakly corelated.

By comparing the performance of computational fluid dynamics (CFD) and fluid–structure interaction (FSI) simulations with four-dimensional (4D) flow magnetic resonance imaging (MRI) data, Pons et al. [58] evaluated the capability of fluid dynamics predictors to assess risk of aneurysm dilation. Significant difference was found between stable and dilating patients using the FSI-derived predictors.

For abdominal aortic aneurysm (AAA), the benefit of biomechanical risk assessment has been shown using clinical data of ruptured and intact aneurysms. In a multicenter retrospective study by Gasser et al. [59], finite element (FE) models were used to predict peak wall stress (PWS) and peak wall rupture index (PWRI) of 203 non-ruptured and 40 ruptured AAA patients. Significant difference between the non-ruptured and ruptured group was found using PWS- and PWRI-adjusted diameter, which showed that these biomechanical indices are very promising. In a retrospective study, Polzer et al. [60] compared biomechanical indices for 19 ruptured and 24 intact AAA. It was shown that the biomechanical indices are more sensitive than diameter in predicting rupture of asymptomatic AAA. In a prospective multicenter clinical study [61], Doyle et al. followed up 295 AAA patients, rupture occurred in 13 patients and 102 patient underwent repairs. It was found that a biomechanical index is a strong independent predictor of AAA rupture or repair.

Opposite to the promising results, a retrospective study [62] suggested no added value of biomechanical indices for AAA risk assessment. However, in their biomechanical model, the imaged-derived configuration was directly pressurized without proper consideration of zero-pressure configuration and pre-stress, which may result in inaccurate stress calculation.

1.4.2 In Vivo Hyperelastic Properties are the Biggest Unknown

Among the three key components necessary for an engineering stress analysis, i.e., geometries, material properties, and loading/boundary conditions, the *in vivo* material properties are clearly the biggest unknown. Indeed, accurate estimation of *in vivo* mechanical properties of the aortic wall, which is nonlinear and anisotropic, has been a challenging problem in the field of cardiovascular biomechanics for several decades.

It has been shown that high *in vivo* stiffness of ATAA may be correlated with increased rupture risk. Martin et al. [63] proposed a predictive analytical model for ATAA risk on a patient-specific level by analysing planar biaxial and uniaxial testing data of 50 ATAA patients. Based on simplification of ATAA shape and assumptions of circumneutral to axial stress ratio, ATAA pressure-diameter response and the aortic wall yield and failure responses were predicted [63]. No significant corelation was found between systolic diameter and the predicted risk metrics of the ATAA patients. The analysis results indicated that high pressure-strain modulus (decreased tissue compliance) is a significant risk factor for ATAA rupture. Later, Duprey et al. [31] performed a similar study using bulge inflation testing data of 31 ATAA patients. Linearized stiffness in the physiological range was derived from the bulge inflation tests. The authors showed that the stiff aneurysms are prone to rupture, consistent with results of Martin et al. [63].

Since aneurysm rupture/dissection usually occurs under elevated arterial pressures (e.g., about 300mmHg) brought on by extreme emotional or physical stress [64], patient-specific ATAA rupture analysis could benefit from estimating the full *in vivo* hyperelastic properties, which, consequently, can be utilized to predict ATAA mechanical response at various loading conditions.

1.4.3 Failure Metric Plays a Critical Role in Biomechanical Assessment

To assess patient-specific ATAA rupture/dissection risk, numerically computed stresses (circumferential, axial and shear) on the aortic wall need to be converted into a scalar-valued failure metric. Therefore, an accurate failure metric plays a critical role in biomechanical ATAA risk assessment [1].

Isotropic material failure metrics, such as the von Mises stress equivalent stress [36, 37, 65], have been widely adopted in biomechanical risk assessment of aortic aneurysms. Another popular failure metric is the rupture potential index (RPI) [66], which is obtained by dividing an isotropic wall stress (e.g., maximum principal stress [67]) by wall strength. These isotropic criteria may not be appropriate for aortic tissues [52], because the aortic wall strengths in the circumferential and axial directions are significantly different, which has been revealed by many experimental studies [15-17, 21, 68, 69]. To incorporate direction-dependent failure properties, anisotropic failure metric needs to be applied. The Tsai–Hill (TH) criterion [48] is a well-known anisotropic failure model that was originally developed for engineered fiber-reinforced composites. Recently, Korenczuket al. [52] applied the TH failure metric to characterize the failure of porcine abdominal aortas, and the authors found that the anisotropic TH metric performed much better than the isotropic von Mises stress metric [52].

To perform patient-specific biomechanical assessment, parameters of a failure metric (e.g., wall strength in the RPI) need to be determined. However, patient-specific failure properties (i.e., aortic wall strengths) can only be accurately determined using invasive and destructive tests, and these tests clearly cannot be performed for patients whose ATAAs are still intact. Some studies suggested to use deterministic approaches [67, 70-72]. For instance, Geest et al. [73] proposed a linear regression model to estimate wall strength of abdominal aortic aneurysm (AAA) from patient parameters (age, gender, maximum dimeter, family history and smoking status) and local parameters (local intraluminal thrombus (ILT) thickness and local diameter). However, large variability in aortic wall strength has been revealed by many experimental works [15, 17, 21, 68], which indicate that the predictive capability of the deterministic approach is limited [73]. Recently, a probabilistic rupture risk index (PRRI) [74] was proposed for biomechanical risk assessment of AAA leveraging an uncertainty quantification (UQ) framework [75]. The PRRI incorporates a probability distribution of the wall strength, and it offers a physical meaning: PRRI represents the probability of failure. However, the PRRI was developed based on the isotropic maximum principal stress, ignoring the fact that the wall strengths are direction dependent.

Biomechanical assessment using PRRI was referred to as a high-fidelity model [60]. The wall thickness, which is the input to the FE simulations, was treated as a source of uncertainties in their approach [74]. However, in the UQ framework, sampling-based approaches like Monte Carlo are typically needed to quantify the uncertainties of the FE output (i.e. peak wall stress) propagated from the uncertainties of the FE inputs (i.e., wall thickness and material parameters), which often results in high computational cost [76-78].

1.5 Existing Methods for Mechanical Property Identification

1.5.1 Methods to Identify Ex Vivo Material Properties

Identification of the material parameters of a particular constitutive model often employs inverse techniques. In such methods [79, 80], the identification of constitutive parameters of the material is often obtained based on boundary conditions and displacement/strain fields, measured experimentally. An inverse approach, known as the virtual field method [81], has been developed for extracting homogenous [82] and heterogeneous constitutive parameters from *ex vivo* full-field measurement data [83] of blood vessels whose reference configurations are unloaded. However, the configuration of *in vivo* imaging data is always loaded, which makes it challenging to identify the constitutive parameters from *in vivo* loaded geometries.

1.5.2 In Vivo Identification Methods using Simplified Geometries or Material Models

Since the unloaded state of arteries is unknown, it is challenging to inversely estimate hyperelastic constitutive parameters from *in vivo* deformed geometries. To simplify such inverse computation, the geometry of arteries is often assumed as a perfect tube. Based on this assumption, Schulze-Bauer and Holzapfel [84] estimated Fung-type material parameters, Masson *et al*, Olsson and Klarbring, Stålhand [85-88] estimated material parameters using the constitutive model proposed by Holzapfel *et al* [33] and geometrical parameters, Astrand *et al.* [89] and Smoljkić *et al* [90] identified the Gasser–Ogden-Holzapfel (GOH) model [34] parameters.

Recently, some studies [31, 63] derived linearized stiffness from *ex vivo* biaxial tests and showed that the stiff aneurysms are prone to rupture. This linearized metric can provide a simple and clinically-relevant way to roughly predict diameter/stretch-based rupture potential. For instance, Liu *et al.* [91], Zhang *et al.* [92] and Franquet *et al.* [93] developed methods to identify linear elastic material parameters from *in vivo* images. The distribution of linearized stiffness has been measured on ATAA from multiphase CT scans [94, 95].

Other types of simplifications were also used in the literature. For instance, Trabelsi *et al.* [96] proposed a multiple linear regression-based method to estimate the constitutive parameters by assuming a linear relation between the volume of the aorta and the constitutive parameters of the Demiray model. Zeinali-Davarani *et al.* [97] evaluated local wall thickness and material anisotropy of the human aorta, while other constitutive parameters were determined through biaxial tests. However, rupture analysis may benefit more from identification of nonlinear hyperelastic properties.

1.5.3 FE Updating Methods for In Vivo Material Property Identification

To account for the irregularity of patient-specific geometries, inverse FE simulations are often used in the identification of *in vivo* hyperelastic properties from multi-phase clinical images. Optimization-based FE-updating approaches were proposed, in which the optimal set of material parameters is identified by updating the material parameters in the FE simulations to minimize a pre-defined error function. Beefily, *in vivo* material properties are identified by: (1) recovering or estimating the unpressurized geometry, (2) deforming the geometry in FE simulations with *in vivo* loading and boundary conditions with the estimated constitutive parameters, and (3) by using certain optimization methods, the estimated constitutive parameters will be adjusted, and optimal parameters will be identified such that some physical measurements (e.g. strain/displacement) are matched between the simulated, deformed configuration and the *in vivo* loaded configuration.

Using these strategies, Liu *et al* [98] estimated parameters of the modified Mooney-Rivlin model from carotid artery MRI data. The optimization problem can be much more challenging when estimating anisotropic model parameters, since different hyperelastic parameters are coupled nonlinearly in their contributions to the structural response. Wittek *et al* [99, 100] developed two approaches to identify *in vivo* GOH model parameters of the abdominal aorta from 4D ultrasound data based on mixed stochastic-deterministic optimization. A total of 7400 iterations [99] and 43,500–86,900 iterations [100] were needed to reach the optimal set of parameters in their approaches, resulting in a computational time of 1~2 weeks. Such high computational cost could inhibit a practical use of the methods, particularly in a clinical setting requiring fast feedback to clinicians. To expedite the identification process, we have recently proposed the multi-resolution direct search (MRDS) approach [101] (APPENDIX A), which was designed to improve the searching algorithm, and the computation time was reduced to 1~2 days with less than 1000 iterations. However, these studies [99-101] relied on only numerically-generated data to validate the approaches. Experimental validations are needed to verify the assumptions of these approaches.

1.6 Application of Machine Learning (ML) in Biomechanics

Recently, machine learning (ML) techniques, in particular Deep Learning (DL) techniques [102] utilizing deep neural networks (DNN), have garnered enormous attention in the field of artificial intelligence and have led to revolutionary breakthroughs in many applications [102-109]. In the biomechanics field, ML approaches have been used as nonlinear function approximators to establish complex multi-dimensional relationships. ML surrogate models have also been developed to enable fast biomechanical computation.

1.6.1 ML Models as Nonlinear Function Approximators

ML models can be used as nonlinear function approximators to construct complex multi-dimensional dependencies. The applications of machine learning (ML) techniques on the mechanics problems can be traced back to the 1990s [110], when neural networks were first introduced to traditional mechanics fields for constitutive modeling [111] and elastic-plastic fracture mechanics [112]. The pioneering work by Huber and Tsakmakis [113, 114], determined certain constitutive parameters from the spherical indentation data using neural networks. The classical problem can be characterized by the load-depth trajectory, some manually selected features (e.g. depth at a given load level) were sufficient to produce a good predictive capability.

ML approaches have been developed for biomechanical analysis. For instance, Luo and co-workers [115] developed ML classifiers to infer strength of ascending thoracic aneurysm from elastic properties, Cilla and co-workers proposed ML techniques for obtaining the GOH model parameters from uniaxial data [116]. Jiang et al. [117] proposed a DL model to predict the evolution of AAAs by using follow-up dataset.

Our group has been working on applying ML techniques to the field of biomechanics. In our recent work [118], a DL model was developed to estimate the elastic properties of chemically-treated collagenous tissues directly from noninvasive microscopy images. Glutaraldehyde-treated bovine pericardium (GLBP) tissue, widely used in the fabrication of bioprosthetic heart valves and vascular patches, was chosen to develop a representative application. The DL model was designed and trained to process second harmonic generation (SHG) images of collagen networks in GLBP tissue samples, and directly predict the nonlinear anisotropic stress-strain responses of the GLBP tissues. We have proposed a physics-informed ML model for constitutive modeling of the aortic tissues (APPENDIX B). The ML-constitutive model employs a hierarchical learning strategy by following the steps: (1) establishing constitutive laws to describe general characteristic behaviors of a class of materials; (2) determining constitutive parameters for an individual subject. The trained NNMat model may be directly adopted for a different subject without re-training the class parameters, and only the subject parameters are considered as constitutive parameters. The NNMat model was trained, cross-validated and tested using biaxial testing data of 63 ATAA tissue samples, the results demonstrated that the NNMat model has a significantly better performance than the Holzapfel-Gasser-Ogden model.

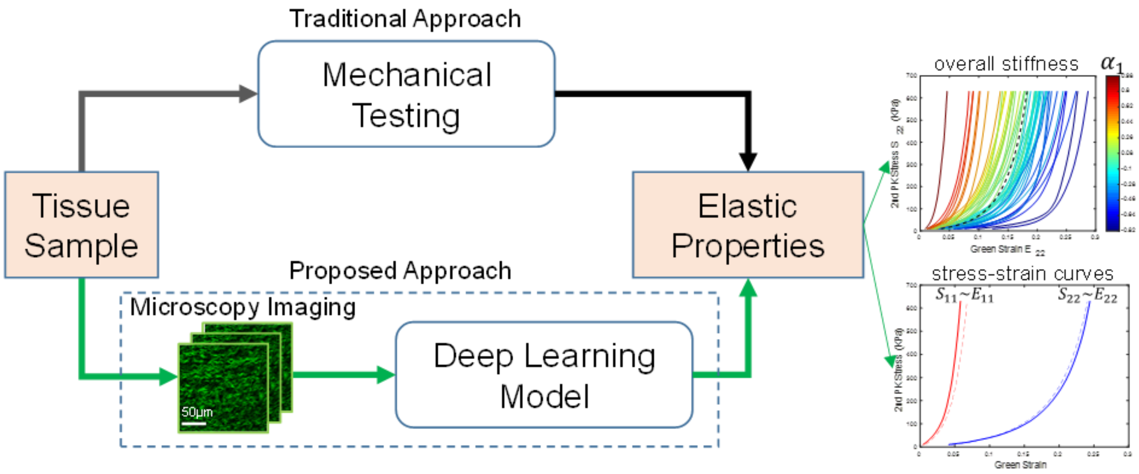
Traditional Approach
Mechanical Testing
Tissue Sample
Elastic Properties
Proposed Approach
Microscopy Imaging
50μm
Deep Learning Model
overall stiffness
α_1
2nd PK Stress S_{22} (KPa)
Green Strain E_{22}
stress-strain curves
$S_{11}{\sim}E_{11}$
$S_{22}{\sim}E_{22}$
2nd PK Stress (KPa)
Green Strain

Figure 1.5 - DL model for estimation of nonlinear anisotropic stress-strain responses of chemically-treated collagenous tissues directly from noninvasive microscopy images [118].

1.6.2 ML Models as Surrogates for Computational Biomechanical Analysis

When trained with sufficient data, ML models may serve as fast surrogates of computational biomechanical models, the latter is often associated with long simulation time and numerical convergence issues.

In a recent study [119], we designed and trained a DL model to take aorta geometry as input and directly output the aortic wall stress distributions, bypassing the FEA calculation process. The trained DL-model can predict the stress distributions in seconds with average errors of 0.492% in the von Mises stress distribution (Figure 1.6). DL model can also be used to learn from CFD results and make fast predictions [120].

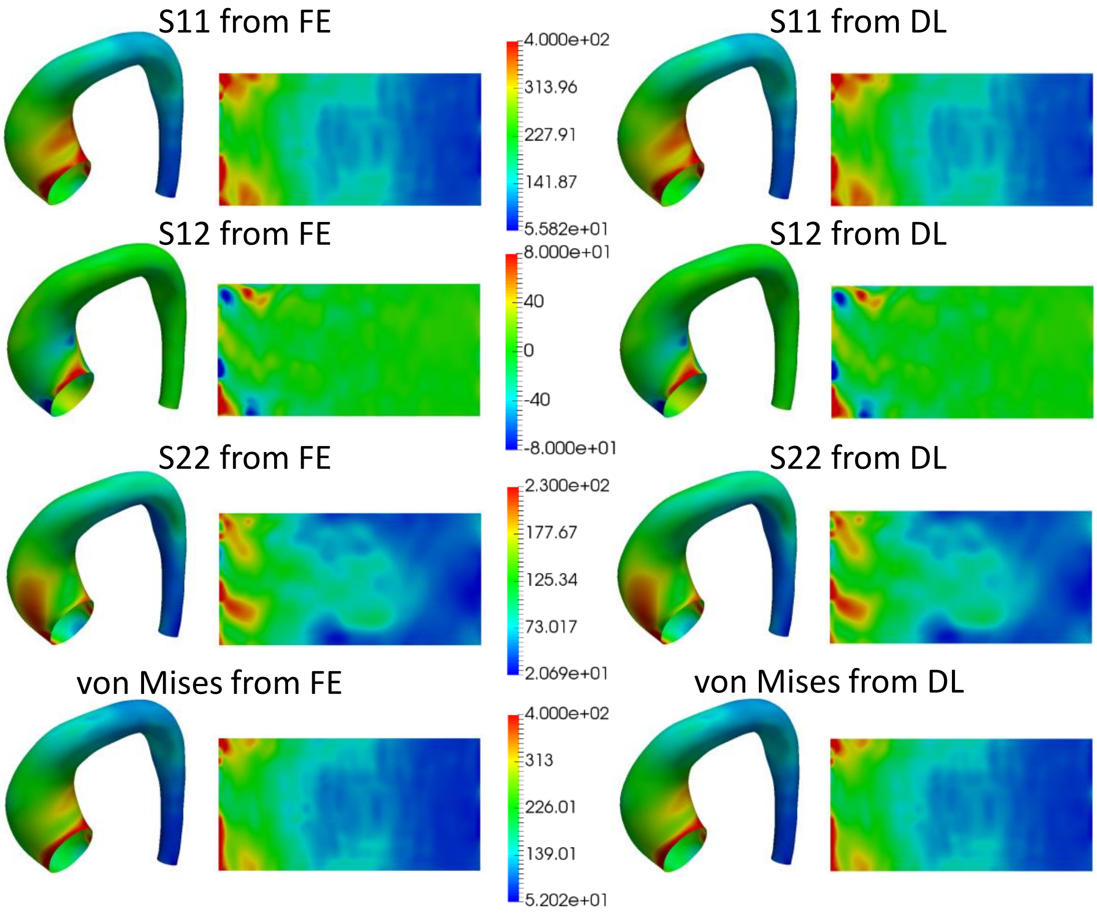

Figure 1.6 - Stress distributions computed from the FE model and DL model [119].

Inverse problems in biomechanics often involve iteratively performing simulations, which are often computationally expensive. ML model can fundamentally change this dilemma by building a direct mapping between inputs and outputs. For instance, the unpressurized geometry is often solved using iterative schemes such as the backward displacement method [121], which has a long computation time and can suffer from numerical convergence issues. We have developed a ML-model [122] to estimate the unpressurized geometry of human thoracic aorta by given two pressurized geometries at two different blood pressure levels.

1.7 Motivation of the Study

Advances in imaging techniques and numerical methods have made it possible to investigate the *in vivo* biomechanics of the cardiovascular system on a patient-specific level. For the four key components in a biomechanical analysis (geometries, loading and boundary conditions, material hyperelastic properties and material failure properties), patient-specific geometries (e.g., anatomic structures of the aorta) and physiological loading conditions (i.e., diastolic and systolic pressures) can be obtained at a high level of spatial and temporal resolutions from clinical diagnostic imaging tools, such as CT scans, and hemodynamic measurements, respectively [123]. However, the *in vivo* material hyperelastic and failure properties, which vary significantly among patients, are clearly the biggest unknown. Indeed, accurate identification of *in vivo* nonlinear and anisotropic hyperelastic properties of the aortic wall has been a challenging problem in the field of cardiovascular biomechanics for several decades. Furthermore, since patient-specific failure properties cannot be obtained noninvasively from clinical images, an accurate failure metric that incorporates uncertainties of failure properties, needs to be developed for patient-specific biomechanical assessment.

1.7.1 Objectives of This Study

The overall goal of this thesis was to develop a novel computational framework to identify *in vivo* patient-specific material properties for biomechanical ATAA risk assessment. To accomplish the goals, the objectives of the thesis are:

1) Develop and validate a novel inverse approach for identification of *in vivo* nonlinear anisotropic hyperelastic properties of thoracic aorta from two-phase 3D CT

images. A new inverse method was developed to identify material properties of the thoracic aorta. Numerical validations were performed using four ATAA patient geometries. Clinical 3D gated CT images and surgically-removed aortic wall tissue samples of two ATAA patients were obtained. Planar biaxial tests were performed on the tissue samples for validation.

2) Investigate machine learning (ML) approach for fast and accurate identification of *in vivo* material hyperleastic properties. A ML approach was developed as a surrogate of the inverse method to rapidly (i.e., within seconds) estimate ATAA material properties. Neural network was designed to take as input two-phase aorta geometries and directly output the material parameters.

3) Develop a probabilistic and anisotropic failure metric for ATAA risk assessment. An anisotropic failure criterion was validated for aortic tissues using off-axis testing data of 4 porcine aortas and 2 human ATAAs. Based on the anisotropic failure criterion, an anisotropic failure probability (FP) metric was developed using uniaxial failure testing data of 84 ATAA patients. Using the identified hyperelastic properties of the two ATAA patients in the 1st objective, FE simulations were performed to estimate the FP under elevated blood pressure.

4) Investigate ATAA risk assessment methods. CT images and matching tissue samples were collected from additional 41 ATAA patients. “Ground-truth” retrospective risk scores were numerically-reconstructed using planar biaxial and uniaxial testing data of the 41 patients. Different risk stratification methods are compared using the “ground-truth” risk data.

1.7.2 Significance of This Study

Current computational models ATAA risk assessment have limited clinical translatability, which can be attributed to one of the major bottlenecks of current technologies: the unknown material hyperleastic properties and material failure properties. It has been shown that these material properties can vary greatly among individuals. Therefore, the unknown *in vivo* patient-specific hyperelastic properties must be noninvasively identified in order to perform accurate patient-specific analysis. Failure properties can only be accurately obtained via invasive and destructive tests; therefore, uncertainties of the failure properties need to be quantified and incorporated in the failure metric for accurate patient-specific ATAA risk assessment.

Fortunately, the *in vivo* aorta deformation under physiological loading conditions can be recorded by multi-phase image modalities such as multi-phase ECG gated CT scans. Two-phase (diastole and systole) aorta geometries and the corresponding blood pressure levels are obtainable. However, direct measurements of *in vivo* aortic wall extensibility can only provide insight on ATAA mechanical responses within the imaged physiologic range [124] (usually between 80mmHg~120mmHg), whereas aneurysm rupture/dissection usually occurs under elevated arterial pressures (e.g., about 300mmHg) brought on by extreme emotional or physical stress [64]. It has been shown that the stress distributions can be significantly altered under supra-physiological pressure [57]. Thus, the full *in vivo* elastic properties need to be noninvasively estimated using a constitutive model, which, consequently, can be utilized to predict patient-specific ATAA mechanical response at various loading conditions.

To facilitate personalized biomechanical analysis of ATAA rupture, a novel efficient inverse method for identification of the *in vivo* patient-specific material parameters is needed without compromising accuracy, and the validity of such method has to be proved by experimental evidences. A potential paradigm-changing solution to the bottleneck associated with the patient-specific modeling is to incorporate ML algorithms to expedite the procedure of *in vivo* material property identification. To accurately and reliably access ATAA risk, anisotropy of the failure properties needs to be taken into consideration, and uncertainty of the failure properties needs to be quantified and incorporated using a probabilistic failure metric. The benefits of identifying patient-specific hyperelatsic properties and using probabilistic failure metric need to be demonstrated by comparing different risk assessment methods.

In this thesis, novel methods were developed to identify *in vivo* tissue mechanical properties from clinical multi-phase CT data in a fast and accurate manner. An anisotropic failure criterion was investigated. Probability distribution of the failure properties was quantified using a probabilistic model. Different risk assessment methods were compared to show promises of the developed computational framework. These methods may enable accurate patient-specific computational analysis of vessel functions, such as ATAA risk analyses for clinical ATAA surgical evaluation. The methods developed in this thesis could be applied to other similar tissue structures (such as veins and lymphatic systems) with modifications.

CHAPTER 2. STATIC DETERMINACY OF THE AORTIC WALL

It is well known that nonlinear material properties and residual deformations/stresses alter the mechanical behavior of arteries, e.g. the pressure-diameter curves. In an effort to enable personalized analysis of the aortic wall stress, nonlinear iterative approaches have been developed to incorporate experimentally-derived material properties and residual deformations into *in vivo* loaded geometries in FE simulations. Yet, the difficulty in obtaining patient-specific material properties and residual deformations has become one of the biggest challenges in the personalized biomechanical analysis. Fortunately, static determinacy offers an appealing prospect that allows for the calculation of arterial wall stress without patient-specific material properties. The aortic wall stress can be computed using forward analysis by enforcing an extremely stiff material property as penalty treatment, which is referred to as the forward penalty approach. However, the effect of the residual deformations on static determinacy is still unclear, which is often stated as a limitation in patient-specific analysis. In this chapter, static determinacy of ATAA is investigated with respect to material properties and residual deformations. By comparing the predicted stresses from 1) a traditional iterative approach with nonlinear material properties and residual deformations and 2) the forward penalty approach, we demonstrate that the transmural mean stress is approximately the same for the two approaches and can be readily obtained from *in vivo* clinical images without knowing the patient-specific material properties and residual deformations. Computation of patient-specific mean stress can be greatly simplified by using the forward penalty approach, which may be clinically valuable. Static determinacy severs as a basis for the development of inverse approach in CHAPTER 3.

The remaining sections are organized as follows. In Section 2.1, the principle of static determinacy is introduced. In Section 2.2, the theoretical arguments are described, and the validity is shown by analytical examples. FE models with patient-specific geometries are demonstrated in Section 2.3. In Section 2.4, discussion are presented. Some of the results of this chapter is published in [125, 126].

2.1 Background

Nonlinear material properties and residual deformations/stresses [127, 128] have been shown to significantly affect the physiological wall stress distributions [33, 129-132]. To incorporate the nonlinear material properties and residual deformations in arteries, traditional forward analysis uses a thick-walled model starting from the stress-free reference configuration. Then deformation relations, constitutive laws and equilibrium equations are utilized to solve the boundary value problem. However, when applying this conventional approach to obtain patient-specific stress fields from the *in vivo* loaded geometries in clinical images, one has to first determine the unknown material parameters and residual deformations, which are required in the thick-walled FE models. Some studies have suggested the use of experimentally-determined material and residual deformation parameters [133, 134]. However, using residual deformations and material properties that are not patient-specific is a clear limitation.

Fortunately, for a specific type of biological membrane structures such as the aorta, the wall stress is nearly insensitive to the variation of material properties. This property is called static determinacy, i.e. the external force (pressure) along the geometry can be used to directly compute the internal tension/stress. This is because the vessel wall can be seen as locally in a plane stress state [135], the solution of the equilibrium is weakly sensitive to the material properties. The aorta is shown to be approximately statically determinate [136]. Thus, its stress distribution can be directly obtained by a forward penalty method [136, 137] which enforces an extremely stiff material property as penalty treatment. The computation of the thin-walled stress can be greatly simplified by this forward approach. However, due to the assumption of no bending stiffness in the membrane elements, the self-equilibrium residual deformations are inadmissible to the thin-walled models, which is often stated as a limitation of such models.

In this chapter, validity of static determinacy for ATAA is examined. By comparing the predicted stresses from 1) a traditional iterative approach with nonlinear material properties and residual deformations (thick-walled model) and 2) the forward penalty approach (thin-walled model), we demonstrate that the transmural mean stress (i.e., averaged stress through the thickness) is approximately the same for the two approaches. Thus, the transmural mean stress can be readily obtained from *in vivo* clinical images using the forward penalty approach without knowing the patient-specific material properties and residual deformations.

2.2 Theoretical and Analytical Arguments

One prominent example of static determinacy is the use of Laplace law to compute the wall hoop stress by assuming a perfect cylindrical shape of the aorta.

$$\sigma_{\theta\theta} = \frac{Pa}{t} \tag{2.1}$$

where $\sigma_{\theta\theta}$ is the hoop stress in the thin-walled tube, P is the pressure, a is the inner radius, and t is the *in vivo* wall thickness. The material properties are not involved in this equation, and stress is directly calculated using the static force equilibrium. Opposite to the middle radius value used in [138], we emphasize that inner radius should be used as the blood pressure is applied to the inner surface of the aorta.

It is well known that material properties and residual stresses alter the mechanical response of arteries, e.g. the pressure-diameter curves [33]. Nonetheless, from the static determinacy prospective, for the *in vivo* loaded configuration, the equilibrium between the resultant force and the external pressure load should always hold, and thus, the stress resultant (tension) should be insensitive to the material parameters and residual deformations. This implies that no matter how the aorta is internally balanced or residually stressed, the wall tension can always be computed only using the static equilibrium. Therefore, when the wall thickness is given, the simple thin-walled model would be sufficient in determining the transmural mean stress.

In the following subsections 2.2.1 and 2.2.2, we demonstrate that the mean hoop stress is independent of material properties and residual deformations (realized by the opening angle method or the layer specific 3D residual deformation).

2.2.1 Different Opening Angles and Material Models

In this subsection, we use an analytical example to demonstrate that the mean hoop stress is insensitive to the change of material properties and opening angles. We assume that the residual stress can be described by the opening angle and that the aorta can be modelled as a perfect tube.

Starting from the cut-open, stress-free configuration, summarizing from [33] and [133], the total deformation gradient tensor of the tube taking into account the residual stress, $\boldsymbol{F}_{total}$, can be obtained as

$$\begin{gathered}\boldsymbol{F}_{total}(r) = \frac{rk}{\left[A^2 + k\frac{l}{L}(r^2 - a^2)\right]^{\frac{1}{2}}}\boldsymbol{e}_\theta \otimes \boldsymbol{E}_\Theta + \frac{l}{L}\boldsymbol{e}_z \otimes \boldsymbol{E}_Z \\ + \frac{L}{rkl}\left[A^2 + k\frac{l}{L}(r^2 - a^2)\right]^{\frac{1}{2}}\boldsymbol{e}_r \otimes \boldsymbol{E}_R\end{gathered} \tag{2.2}$$

where $r \in [a, b]$, a and b are the inner and outer radii of the *in vivo* deformed geometry. k, defined as $k = \frac{2\pi}{2\pi - \alpha}$, is used to describe the opening angle α. A and B are the inner and outer radii of the stress-free geometry. L and l are the axial length of the aorta segment in the stress-free and deformed geometry, respectively. $\boldsymbol{E}_\Theta$, $\boldsymbol{E}_Z$ and $\boldsymbol{E}_R$ and $\boldsymbol{e}_\theta$, $\boldsymbol{e}_z$ and $\boldsymbol{e}_r$ are the unit basis vectors for the stress-free and deformed geometry respectively. To make the solution simple, the constitutive relation of the aorta tissue is first modelled using the isotropic neo-Hookean model. The strain energy function W is

$$W = \frac{1}{2}\mu(I_1 - 3) \tag{2.3}$$

where μ is the shear modulus and I_1 is the first invariant. To solve for the *in vivo* stress when systolic blood pressure ($P = 104mmHg$) [57] is present, we utilize the stress equilibrium equation, which can be expressed in the radial equation

$$\frac{d\sigma_{rr}}{dr} = \frac{1}{r}(\sigma_{rr} - \sigma_{\theta\theta}) \tag{2.4}$$

where $\sigma_{\theta\theta}$ and σ_{rr} are the stresses in the circumferential and radial direction respectively. Eqn. (2.4) can be reduced to $\frac{d\sigma_{rr}}{dr} = \frac{\mu}{r}\left(\lambda_\theta^2 - \lambda_r^2\right)$ [139], with $\lambda_\theta$and λ_r referring to the stretches in the circumferential and radial directions, respectively. By solving the equilibrium Eqn. (2.4), together with the traction continuity condition $\sigma_{rr}(a) = -P$, we are able to obtain the radial stress [139]

$$\sigma_{rr}(r) = -P + \mu\left[\frac{k}{\lambda_z}\log\left(\frac{\lambda_r\lambda_z rk}{A}\right) - \frac{1}{k\lambda_z}\log\left(\frac{r}{a}\right) + \frac{1}{2}\left(\lambda_r^2 - \frac{1}{k\lambda_z}\right)\left(\frac{a^2 - r^2}{a^2}\right)\right] \tag{2.5}$$

where λ_z is the stretch in the axial direction. The hoop stress is then calculated using

$$\sigma_{\theta\theta}(r) = \sigma_{rr}(r) + \mu\left(\lambda_\theta^2 - \lambda_r^2\right) \tag{2.6}$$

The geometry of the aorta in clinical images is always in the *in vivo* deformed state, from which the opening angle is not measurable. To this end, we fixed the inner and outer radii of the *in vivo* deformed geometry, a and b, for all scenarios and vary the opening angle from 0 to 330 degree. For a certain opening angle α, the inner and outer radii A and B of the cut-open sectors are solved using the boundary condition $\sigma_{rr}(b) = 0$ and the assumption of incompressibility $b^2 = a^2 + \frac{1}{k\lambda_z}(B^2 - A^2)$. Related parameters are listed in Table 2.1 and values of A and B are shown in Table 2.2. The transmural mean hoop stress is defined as

$$\overline{\sigma}_{\theta\theta} = \frac{1}{b-a}\int_a^b \sigma_{\theta\theta} dr \tag{2.7}$$

Table 2.1 - The parameters used in the opening angle method.

inner radius a (mm)	outer radius b (mm)	residual axial stretch l/L	systolic pressure (mmHg)	shear modulus μ (kPa)
24.5[a]	26[b]	1.2[c]	104[a]	67.68[a]

[a] from [57], a and systolic pressure are from clinical recorded data, μ was fitted using biaxial experiment of patient "BAV17" with coefficient of determination of 0.8656; [b] based on mean value of deformed wall thickness in [140]; [c] approximated from [141] which refers to the residual axial stretch. We assume there is no axial stretch caused by *in vivo* loading conditions

Table 2.2 - The inner and outer radii A and B of the stress-free configurations corresponding to various opening angles α.

neo-Hookean Model							
$\alpha(°)$	0	60	90	120	180	270	330
$A(mm)$	11.55	14.20	15.96	18.16	24.77	51.23	157.10
$B(mm)$	14.98	17.62	19.39	21.59	28.20	54.67	160.54
Gasser-Ogden-Holzapfel (GOH) Model							
$\alpha(°)$	0	60	90	120	180	270	330
$A(mm)$	18.25	22.12	24.70	27.93	37.63	76.43	231.66
$B(mm)$	20.59	24.46	27.04	30.26	39.97	78.77	234.00

The results are shown in Figure 2.1 (left). The mean hoop stress computed from Eqn. (2.7) is exactly the same as the thin-walled hoop stress calculated using Eqn. (2.1).

Unsurprisingly, if we rewrite Eqn. (2.4) as $\sigma_{\theta\theta} = \frac{d}{dr}(r\sigma_{rr})$ and therefore $\bar{\sigma}_{\theta\theta} = \frac{1}{b-a}\int_a^b d(r\sigma_{rr}) = \frac{b\sigma_{rr}(b)-a\sigma_{rr}(a)}{t} = \frac{Pa}{t}$, which is exactly the same formula as the Laplace law. In addition, as shown in Figure 2.1 (right), the adoption of an anisotropic constitutive model [34] (described in Section 2.3.3, parameters shown in Table 2.3) would not affect the static determinacy. Here, small opening angles may be unusual to observe in experiment [142], they are presented here for illustrative purpose.

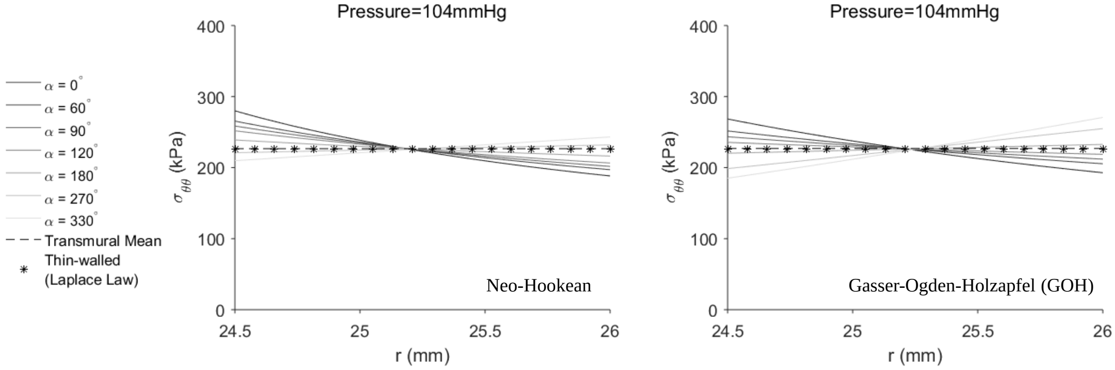

Figure 2.1 - The transmural mean, thin-walled and thick-walled hoop stresses across the wall thickness. In the left figure, thick-walled hoop stresses were computed using neo-Hookean model, while in the right figure, GOH model was used. Transmural mean hoop stress remains the same for all scenarios, thus only one line is plotted.

Table 2.3 - GOH material parameters of the patient "BAV17" extracted from [57]. Coefficient of determination of the curve fitting is 0.9551.

$C_{10}(kPa)$	$k_1(kPa)$	k_2	κ	$\theta(°)$
27.91	512.56	0.00	0.31	90.00

2.2.2 Layer-Specific Three-Dimensional Residual Deformation

As a step forward, Holzapfel and Ogden [139] proposed a layer-specific three-dimensional residual stress model, in which the residual deformations (stretching and bending) of the three layers (intima, media and adventitia) from [143] were encompassed and the residual stresses were calculated using the isotropic neo-Hookean model. In this section, we first replicate the stress distribution in [139] by using the original parameters of geometry, material and residual deformations. Next, physiological pressure is applied to the residually-stressed aorta.

The deformation gradient tensors for intima (I), media (M) and adventitia (A) [133] are

$$
\begin{aligned}
\boldsymbol{F}_{RS}^{(I)}\left(r^{(I)}\right) = {} & \frac{r^{(I)}k^{(I)}}{\left[A^{(I)^2} + k^{(I)}\frac{l}{L^{(I)}}\left(r^{(I)^2} - a^{(I)^2}\right)\right]^{\frac{1}{2}}}\boldsymbol{e}_\theta \otimes \boldsymbol{E}_\Theta + \frac{l}{L^{(I)}}\boldsymbol{e}_z \otimes \boldsymbol{E}_Z \\
& + \frac{L^{(I)}}{r^{(I)}k^{(I)}l}\left[A^{(I)^2} + k^{(I)}\frac{l}{L^{(I)}}\left(r^{(I)^2} - a^{(I)^2}\right)\right]^{\frac{1}{2}}\boldsymbol{e}_r \otimes \boldsymbol{E}_R
\end{aligned}
$$

$$
\begin{aligned}
\boldsymbol{F}_{RS}^{(M)}\left(r^{(M)}\right) = {} & \frac{r^{(M)}\beta}{L^{(M)}}\boldsymbol{e}_\theta \otimes \boldsymbol{E}_Z + \frac{l^{(M)}k^{(M)}}{\pi\left[A^{(M)^2} + \frac{\beta l^{(M)}k^{(M)}}{\pi L^{(M)}}\left(b^{(M)^2} - r^{(M)^2}\right)\right]^{\frac{1}{2}}}\boldsymbol{e}_z \\
& \otimes \boldsymbol{E}_\Theta + \frac{\pi L^{(M)}}{r^{(M)}\beta l^{(M)}k^{(M)}}\left[A^{(M)^2} + \frac{\beta l^{(M)}k^{(M)}}{\pi L^{(M)}}\left(b^{(M)^2} - r^{(M)^2}\right)\right]^{\frac{1}{2}}\boldsymbol{e}_r \\
& \otimes \boldsymbol{E}_R
\end{aligned}
$$

$$
\boldsymbol{F}_{RS}^{(A)}\left(r^{(A)}\right) = \frac{\pi r^{(A)}}{L_2^{(A)}}\boldsymbol{e}_\theta \otimes \boldsymbol{E}_{X_2} + \frac{l}{L_3^{(A)}}\boldsymbol{e}_z \otimes \boldsymbol{E}_{X_3} + \frac{L_2^{(A)}L_3^{(A)}}{\pi r^{(A)}l}\boldsymbol{e}_r \otimes \boldsymbol{E}_{X_1} \tag{2.8}
$$

The definitions and values of the parameters are referred to [139]. Values of the related parameters are listed in Table 2.4.

Table 2.4 - Material and residual deformation parameters from [139, 143]. In addition, $\boldsymbol{l = 2.48mm}$, $\boldsymbol{b^{(I)} = a^{(M)}}$ and $\boldsymbol{b^{(M)} = a^{(A)}}$ can be calculated according to [139].

Intima	Media	Adventitia
$A^{(I)} = 7.50mm$ $B^{(I)} = 7.76mm$ $L^{(I)} = 2.58mm$ $k^{(I)} = 1.19$ $a^{(I)} = 5.61mm$ $\mu^{(I)} = 39.8\text{kPa}$	$A^{(M)} = 8.41mm$ $B^{(M)} = 8.99mm$ $L^{(M)} = 2.52mm$ $k^{(M)} = 2.79$ $\mu^{(M)} = 31.4\text{kPa}$	$L_1^{(A)} = 0.21mm$ $L_2^{(A)} = 18.35mm$ $L_3^{(A)} = 2.29mm$ $b^{(A)} = 7.05mm$ $\mu^{(A)} = 17.3\text{kPa}$

Similar to the procedures for the opening angle method, the hoop stress can be computed using the equilibrium equation and the boundary conditions. Interested readers are referred to [139] for details. A diastolic pressure ($P = 80mmHg$) is applied to the inner surface of the aorta, and we assume no axial stretch caused by *in vivo* loading conditions. The residual axial stretches have been incorporated in the deformation gradient tensors of each layer. The transmural mean hoop stress for the three-layer composite is defined as

$$\bar{\sigma}_{\theta\theta} = \frac{1}{b^{(A)} - a^{(I)}} \sum_{i=I,M,A} \int_{a^{(i)}}^{b^{(i)}} \sigma_{\theta\theta}^{(i)} dr \tag{2.9}$$

As depicted in Figure 2.2, the mean hoop stress is identical to the thin-walled hoop stress.

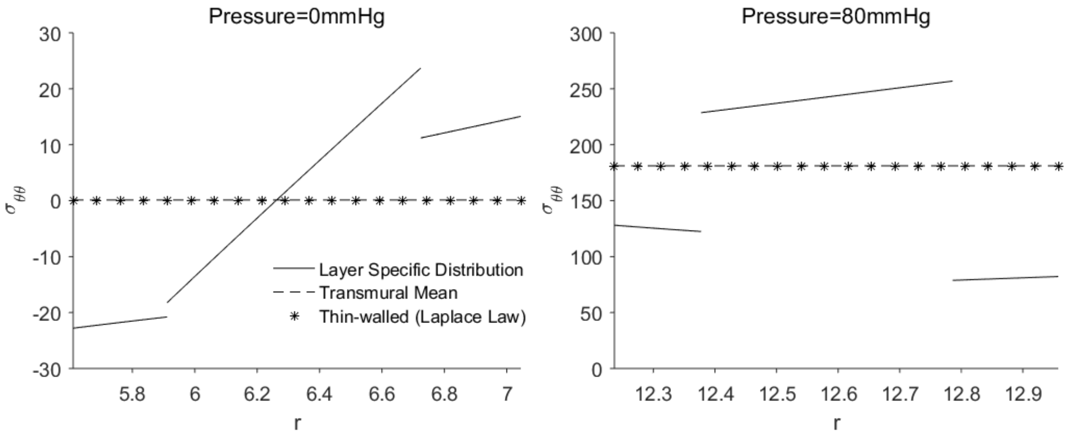

Figure 2.2 - The transmural mean, thin-walled and layer-specific hoop stress distributions in the three layer composite wall when 0 and 80 mmHg pressures are applied.

2.3 Finite Element Analyses Incorporating Patient-Specific Material Properties and Residual Deformations

In this section, irregularities of patient-specific geometries are taken into account using FE analyses. The forward penalty approach is described in Section 2.3.1. In Section 2.3.2, nonlinear FE with patient-specific material properties were performed on 4 ATAA geometries to verify the validity of static determinacy with respect to material properties. Static determinacy with respect to residual deformations was investigated in Section 2.3.3 using a real patient geometry.

2.3.1 The Forward Penalty Approach

The prediction of the *in vivo* stress of the aortic wall has been relied on the recovery of the unloaded state and the incorporation of residual deformations, which requires the use of iterative techniques [134]. A simple and effective forward penalty approach [136, 137] has been recently proposed to predict the *in vivo* thin-walled stress without knowing the material properties. In statically determinate structures, the stress is independent of the material properties, it would be legitimate to assume an extremely stiff property, so that the deformation/change of shape from the unloaded configuration to the loaded configuration is infinitesimal/negligible. This allows us to use the *in vivo* configuration as the unloaded configuration for the forward penalty analysis because the deformation is infinitesimal. Please do not confuse the unloaded configuration for forward penalty analysis with the *actual* unloaded configuration. In our forward penalty approach, an artificially stiff material property (i.e. Young's modulus $E = 2 \times 10^4 GPa$) is assigned to the aortic wall, realizing a penalty treatment to enforce a nearly rigid condition [137]. When the *in vivo* pressure is applied to the *in vivo*, image-derived geometry, the deformation would be infinitesimal due to the high stiffness of the material. The correct *in vivo* thin-walled stress field is readily obtained in this forward analysis due to the fact that the aortic wall is approximately statically determinate. This stress computation approach was shown as effective as iterative approach [137]. Please note that the forward penalty method does not rely on realistic material property or deformation to achieve the correct stress field. Thus the approach cannot be used for predicting material property nor deformation.

2.3.2 Nonlinear FE Simulations with Patient-Specific Material Properties

The aortic tissue is described by the Gasser-Ogden-Holzapfel (GOH) model [34]. In this model, tissues are assumed to be composed of a matrix material with two families of embedded fibers, each of which has a preferred direction. The fiber directions can be mathematically described using two unit vectors. The strain energy function can be expressed by

$$W = C_{10}(\bar{\boldsymbol{I}}_1 - 3) + \frac{k_1}{2k_2}\sum_{i=1}^{2}[exp\{k_2[\kappa\bar{\boldsymbol{I}}_1 + (1-3\kappa)\bar{\boldsymbol{I}}_{4i} - 1]^2\} - 1] + \frac{1}{D}[\frac{J^2 - 1}{2} - \ln J] \tag{2.10}$$

where C_{10}, k_1, k_2, κ and θ are material parameters. C_{10} is material parameter to describe the matrix material. k_1 is a positive material parameter that has the same dimension of stress, while k_2 is a dimensionless parameter. The deviatoric strain invariant $\bar{\boldsymbol{I}}_1$ is used to characterize the matrix material; and the deviatoric strain invariant $\bar{\boldsymbol{I}}_{4i}$ is used to characterize the fiber families. $\bar{\boldsymbol{I}}_{4i}$ is equal to squares of the stretches in the fiber directions. κ is used as a dispersion parameter describing the distribution of fiber orientation. When $\kappa = 0$, the fibers are perfectly aligned. When $\kappa = 0.33$, the fibers are randomly distributed, and the material becomes isotropic. The parameter θ defines the angle between mean local fiber direction and the circumferential axis of the local coordinate system. Please refer to [34, 144] for detailed definitions. The parameter D enforces the nearly incompressibility and is fixed to be 1×10^{-4}.

To examine the validity of static determinacy for ATAA, 4 ATAA geometries from a previous study [57] was used. Patient-specific GOH parameters were determined from biaxial tests [15]. The unpressurized geometries were obtained using the improved backward displacement method [140]. The stress fields can be computed using the unpressurized geometries and nonlinear finite deformation FE with the patient-specific material properties. Using the forward penalty approach with a stiff material ($E = 2 \times 10^4\ GPa$ and $\nu = 0.49$), the stress fields can be obtained on the image-derived geometries. We compared the stress fields computed from nonlinear finite deformation FE with patient-specific material parameters, to the stress fields computed from forward penalty approach. As shown in Figure 2.3, the scalar-valued von Mises stress fields are visualized at the pressure level of 120mmHg. Mean absolute percentage error (MAPE) was calculated for the ATAA patients (named as ATAA1, ATAA2, ATAA3, and ATAA4), which is in the range of 6% ~ 10%. Here, residual deformation was not incorporated in the nonlinear FE models, and the stress fields with transmural variations were directly compared. The MAPE may be reduced by using transmural mean stress for the comparison. The results demonstrate that the forward penalty approach can produce the correct stress field with an acceptable accuracy.

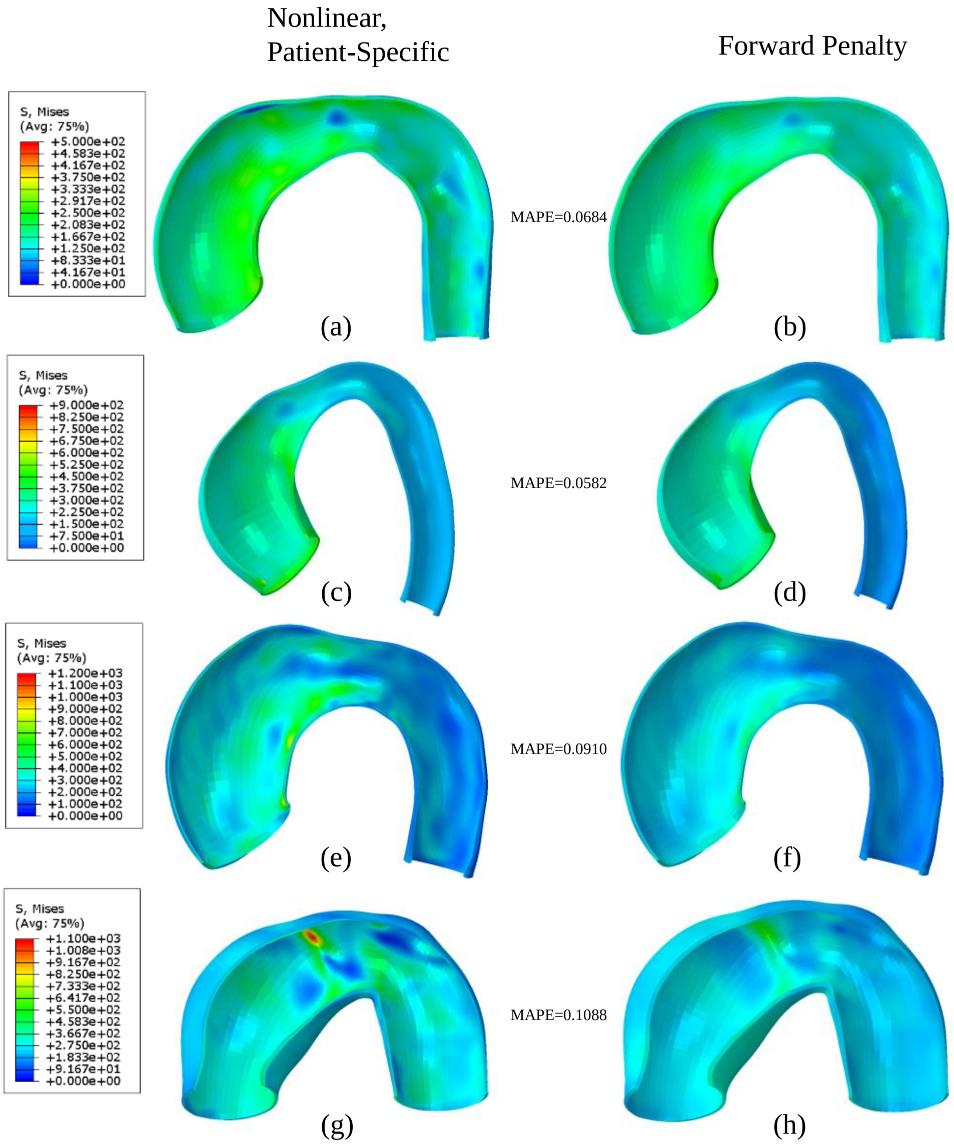

Figure 2.3 - Comparison of von Mises stress computed using nonlinear FE with patient-specific material properties (a), (c), (e) and (g) and that computed from forward penalty approach (b), (d), (f) and (h). Pressure=120mmHg. Mean absolute percentage error (MAPE) for geometries ATAA1 ((a)&(b)), ATAA2 ((c)&(d)), ATAA3 ((e)&(f)) and ATAA4 ((g)&(h)) are obtained by taking the nonlinear FE computed stress as "true" value.

2.3.3 Nonlinear FE Simulations Incorporating Different Opening Angles

A CT-derived geometry from the ATAA patient [57] were used. The inner surface of the aortic wall was divided into 4,950 M3D4 membrane elements in ABAQUS, using our previously developed remeshing algorithm [140]. Mesh sensitivity analysis was performed in previous work [57]. Due to partial volume effect, the wall thickness is difficult to infer from CT images, therefore a constant deformed thickness of 1.5 mm was assumed based on our previous work [140]. Sensitivity analyses with respect to the wall thickness were carried out later in this section. Next, the membrane mesh was extruded outwardly to create two solid meshes (C3D8 elements) with 8 and 9 layers. For the FE models, the axial direction (zz) was defined using the center line of the aorta geometry. Then, the outward normal direction (rr) of each membrane element in the inner surface of the aortic wall was obtained. The hoop direction ($\theta\theta$) was defined by taking cross product of the axial and outward normal directions.

For the forward penalty approach, the same solid meshes were used, the thin-walled stress fields were computed by averaging the stress field across the wall thickness. It is also feasible to directly use membrane elements (inner surface of the aortic wall) for the computation of thin-walled stresses, details are discussed in Section 2.4.

The generalized pre-stressing algorithm (GPA) [133, 145] is implemented in ABAQUS to predict the *in vivo* stress distribution with both the residual deformations and the pre-stresses incorporated. In GPA, the total deformation gradient $\boldsymbol{F}_t$ is stored as a history variable for each integration point. $\boldsymbol{F}_t$ is updated based on the incremental deformation gradient $\Delta\boldsymbol{F}$ resulting from the prescribed load and boundary conditions.

$$\boldsymbol{F}_{t+1} = \Delta\boldsymbol{F}\boldsymbol{F}_t \qquad (2.11)$$

The incremental deformation gradient of the residual stress $\Delta\boldsymbol{F}_{RS}$ is first iteratively applied to the image-derived geometry and stored in $\boldsymbol{F}_t$. Next, the incremental deformation gradient of the pre-stress $\Delta\boldsymbol{F}_{PS}$ resulting from the *in vivo* blood pressure is incrementally applied and stored in $\boldsymbol{F}_t$. Thus, deformation gradient tensors associated with the residual stress $\boldsymbol{F}_{RS}$ and the pre-stress $\boldsymbol{F}_{PS}$ are accounted sequentially. The GPA is implemented in the ABAQUS user subroutine UMAT. The implementation was validated by comparing the analytical and FE results as in [133].

The thick-walled solid elements were first utilized to encompass the opening angle. Various values of the opening angle were incorporated through the GPA. Small opening angles may be unusual to observe in experiments, they are shown here for illustration purposes. The aorta was modelled as a single layer wall. This assumption may be relevant to abdominal aneurysmal tissue since collagen structure becomes nearly homogenous across the entire wall [146]. For ascending aortic aneurysms, collagen organization may be different in different layers [147]. The GOH model (Eqn. (2.10)) was used as the constitutive law, and the material parameters (shown in Table 2.3) were determined from fitting the biaxial data from [57] of the particular patient. The incompressibility parameter D is fixed to be 1×10^{-5}.

Transmural mean hoop stress ($\bar{\sigma}_{\theta\theta}$) was computed using Eqn. (2.7), the remaining in-plane components ($\bar{\sigma}_{zz}$ and $\bar{\sigma}_{\theta z}$) were obtained similarly by taking average with respect to the thickness. Mean absolute error (MAE) and mean absolute percentage error (MAPE) were used to compare the transmural mean stresses of the thin-walled and thick-walled models:

$$MAE(\overline{\sigma}_i) = \frac{1}{N}\sum_{n=1}^{N}\left|\overline{\sigma}_{i,n}{}^{(thin)} - \overline{\sigma}_{i,n}{}^{(thick)}\right|,$$

$$MAPE(\overline{\sigma}_i) = \frac{1}{N}\sum_{n=1}^{N}\left|\frac{\overline{\sigma}_{i,n}{}^{(thin)} - \overline{\sigma}_{i,n}{}^{(thick)}}{\overline{\sigma}_{i,n}{}^{(thick)}}\right| \tag{2.12}$$

where $\overline{\sigma}_{i,n}{}^{(thin)}$ and $\overline{\sigma}_{i,n}{}^{(thick)}$ are the transmural mean stress predicted by the thin-walled and thick-walled models respectively. i denotes a scalar-valued in-plane component ($\theta\theta$ or zz) or an equivalent stress. n is an element index for the thin-walled model and N is the number of elements. Scalar-valued von Mises equivalent stress distributions computed using the in-plane stresses ($\sigma_{\theta\theta}$, σ_{zz} and $\sigma_{\theta z}$) are shown in Figure 2.4 (row 1 and row 4), more detailed views of von Mises stress distributions in a hoop are demonstrated in Figure 2.5. The transmural mean von Mises stress $\bar{\sigma}_{VM}$ was computed using the in-plane mean stresses ($\bar{\sigma}_{\theta\theta}$, $\bar{\sigma}_{zz}$ and $\bar{\sigma}_{\theta z}$). As can be seen in Figure 2.4 (row 2 and row 5), the transmural mean von Mises stress fields are almost identical for various opening angles and the forward penalty approach. The mean values, standard deviations (SD), MAEs and MAPEs of $\bar{\sigma}_{\theta\theta}$, $\bar{\sigma}_{zz}$ and $\bar{\sigma}_{VM}$ are shown in Table 2.5. It can be observed that $\bar{\sigma}_{\theta\theta}$, $\bar{\sigma}_{zz}$ and $\bar{\sigma}_{VM}$ have good agreements for the forward penalty approach and various opening angles.

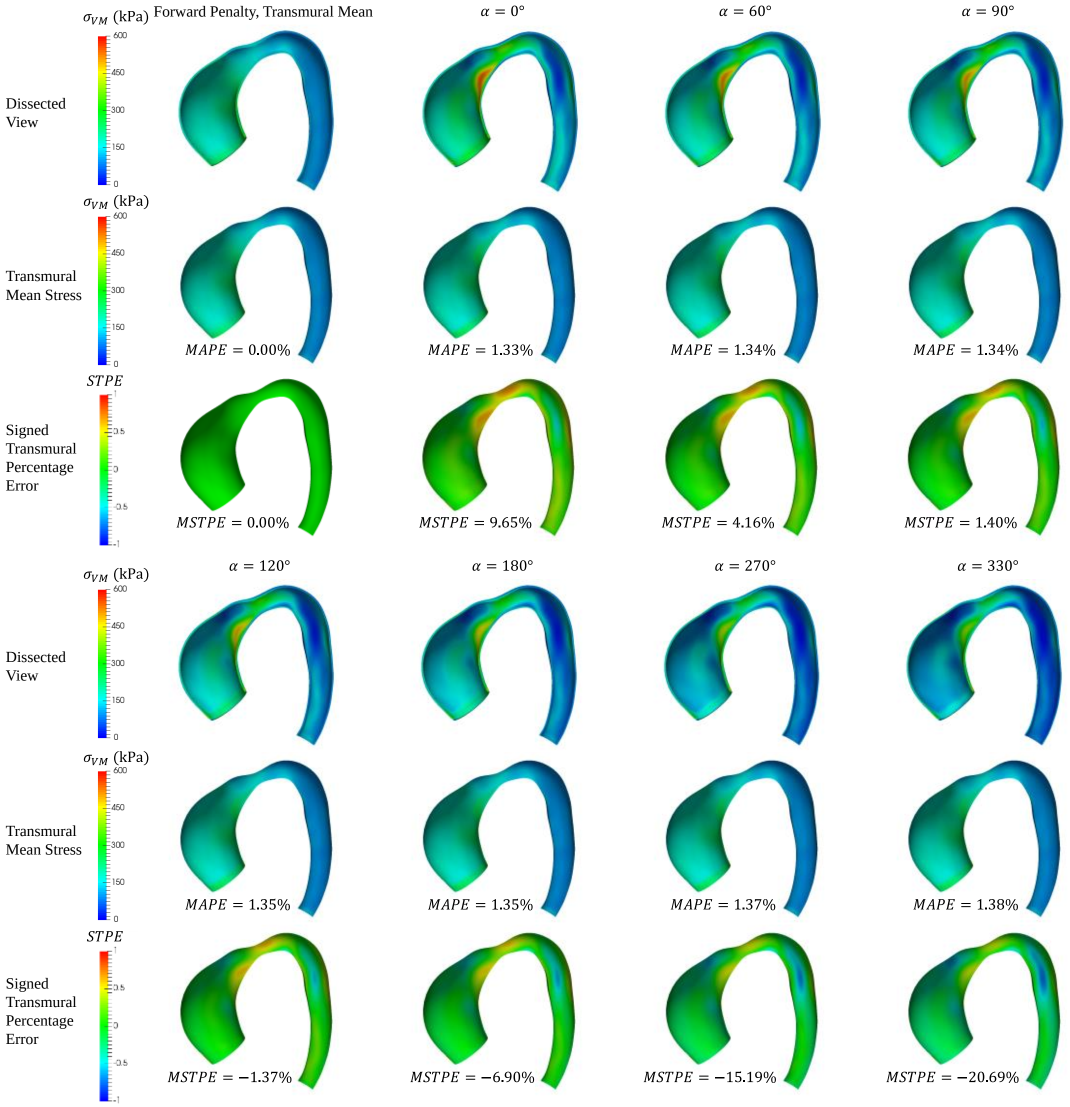
σ_{VM} (kPa)
Forward Penalty, Transmural Mean
$\alpha = 0°$
$\alpha = 60°$
$\alpha = 90°$
600
450
300
150
0
Dissected View
σ_{VM} (kPa)
Transmural Mean Stress
$MAPE = 0.00\%$
$MAPE = 1.33\%$
$MAPE = 1.34\%$
$MAPE = 1.34\%$
$STPE$
1
0.5
0
-0.5
-1
Signed Transmural Percentage Error
$MSTPE = 0.00\%$
$MSTPE = 9.65\%$
$MSTPE = 4.16\%$
$MSTPE = 1.40\%$
$\alpha = 120°$
$\alpha = 180°$
$\alpha = 270°$
$\alpha = 330°$
σ_{VM} (kPa)
Dissected View
σ_{VM} (kPa)
Transmural Mean Stress
$MAPE = 1.35\%$
$MAPE = 1.35\%$
$MAPE = 1.37\%$
$MAPE = 1.38\%$
$STPE$
Signed Transmural Percentage Error
$MSTPE = -1.37\%$
$MSTPE = -6.90\%$
$MSTPE = -15.19\%$
$MSTPE = -20.69\%$

Figure 2.4 - Predicted results using the forward penalty approach and the GPA approach with different opening angles: (1) von Mises stress distribution in the dissected view (row 1 and row 4), (2) the transmural mean von Mises stress (row 2 and row 5), and (3) the signed transmural percentage error (row 3 and row 6).

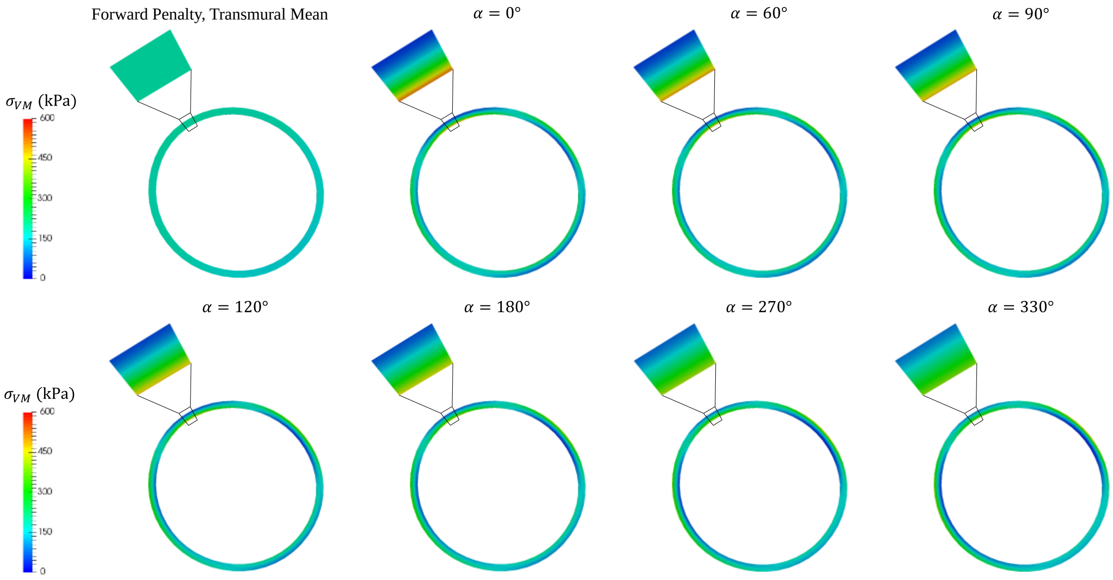

Figure 2.5 - von Mises stress distribution in an aortic hoop using the forward penalty approach and the iterative approach (GPA) with different opening angles.

To study the sensitivity of the MAPE of the transmural mean von Mises stress with respect to the thickness, three representative thickness values (1mm, 2mm and 3mm) were chosen with $\alpha = 120°$. The results are summarized in Table 2.6. Note that this opening angle value is chosen because the corresponding stress distribution is close to homogenized state in the FE simulation, and this value may not be consistent with the average value obtained from experiment [142]. We also notice that opening angle values are widely distributed according to [142], 120 degree can be considered as a feasible value.

In order to quantify the transmural variation, we define a signed transmural percentage error (STPE), corresponding to the nth thin-walled element, as

$$STPE(n) = sign\left[{\sigma_{VM,n}}^{(thick)}(a_n) - {\sigma_{VM,n}}^{(thick)}(b_n)\right] \frac{1}{b_n - a_n} \int_{a_n}^{b_n} \left| \frac{{\sigma_{VM,n}}^{(thick)}(r) - {\bar{\sigma}_{VM,n}}^{(thick)}}{{\bar{\sigma}_{VM,n}}^{(thick)}} \right| dr \tag{2.13}$$

where $\boldsymbol{a_n}$ and $\boldsymbol{b_n}$ represent the inner and outer radii respectively, and $\boldsymbol{r}$ is the radius.

Table 2.5 - The mean values, standard deviations (SD), MAEs and MAPEs in terms of the in-plane mean stresses ($\boldsymbol{\bar{\sigma}_{\theta\theta}}$ and $\boldsymbol{\bar{\sigma}_{zz}}$) and transmural mean von Mises stress ($\boldsymbol{\bar{\sigma}_{VM}}$).

		$\bar{\sigma}_{\theta\theta}$	$\bar{\sigma}_{zz}$	$\bar{\sigma}_{VM}$
forward penalty	mean±SD (kPa)	143.8±50.0	70.0±34.1	128.7±45.4
$\alpha = 0°$	mean±SD (kPa)	143.4±50.1	69.7±31.2	127.4±45.7
	MAE (kPa)	1.1	4.7	1.6
	MAPE	0.73%	9.00%	1.33%
$\alpha = 60°$	mean±SD (kPa)	143.4±50.2	69.6±31.2	127.5±45.8
	MAE (kPa)	1.1	4.8	1.6
	MAPE	0.74%	8.97%	1.34%
$\alpha = 90°$	mean±SD (kPa)	143.4±50.2	69.6±31.2	127.5±45.8
	MAE (kPa)	1.2	4.8	1.6
	MAPE	0.74%	8.96%	1.34%
$\alpha = 120°$	mean±SD (kPa)	143.4±50.2	69.5±31.2	127.5±45.8
	MAE (kPa)	1.2	4.8	1.6
	MAPE	0.75%	8.94%	1.35%
$\alpha = 180°$	mean±SD (kPa)	143.5±50.3	69.3±31.2	127.5±45.9
	MAE (kPa)	1.2	4.8	1.7
	MAPE	0.76%	8.90%	1.35%
$\alpha = 270°$	mean±SD (kPa)	143.5±50.3	69.2±31.2	127.6±46.0
	MAE (kPa)	1.2	4.7	1.6
	MAPE	0.78%	8.83%	1.37%
$\alpha = 330°$	mean±SD (kPa)	143.5±50.4	69.0±31.2	127.6±46.0
	MAE (kPa)	1.2	4.7	1.7
	MAPE	0.79%	8.77%	1.38%

Table 2.6 - Sensitivity of MAPE w.r.t. the thickness.

Wall thickness (mm)	1.0	2.0	3.0
MAPE of $\bar{\sigma}_{VM}$	1.36%	1.31%	1.05%

The sign is given based on the difference between the inner and outer wall von Mises stress. If the inner wall stress is greater than the outer, the STPE is positive, otherwise the STPE is negative.

From Figure 2.4 (row 3 and row 6), with increased opening angle, the mean signed transmural percentage error (MSTPE) changes from positive to negative. The probability density functions (PDFs) of the STPE are plotted in Figure 2.6. The PDFs are fitted using the Gaussian distribution. It can be observed that the PDF shifts leftward with the increase of the opening angle.

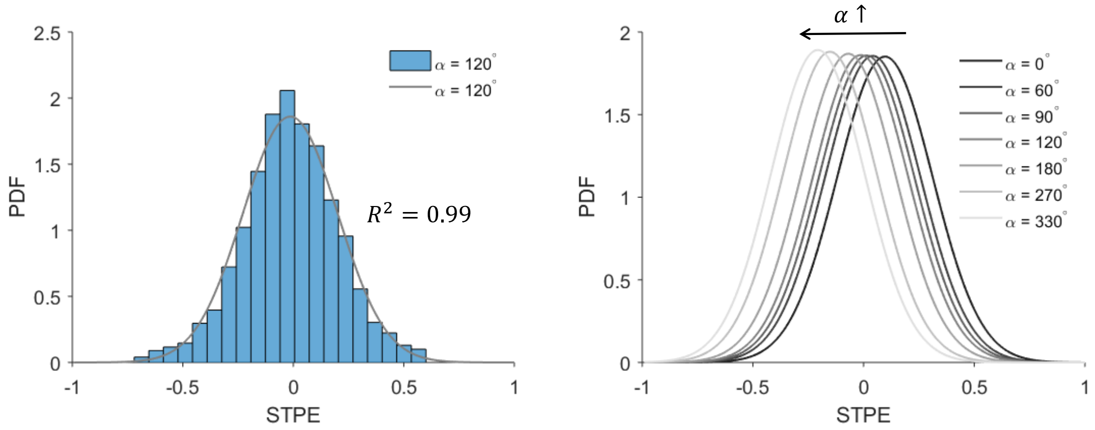

Figure 2.6 - The probability density function (PDF) of the STPE is shown in the histogram and fitted using the Gaussian distribution (left) and fitted PDFs correspond to different opening angles (right).

2.3.4 Nonlinear FE Simulations Incorporating Layer-Specific Three-Dimensional Residual Deformations

For the layer-specific three-dimensional residual deformations, the deformation gradient tensors $\boldsymbol{F}_{RS}^{(i)}\ (i = I, M, A)$ of Section 2.2.2 was incorporated in a FE simulation using the GPA. The ratio of intima, media and adventitia (18.53%, 45.56%, 35.91%) and the layer-specific GOH parameters (shown in Table 2.7) were taken from the median experimental value for human thoracic aortas in [51]. Layer-specific material parameter data for ATAA is also available in [22, 147]. The geometrical parameters determining the residual deformation of abdominal aorta from [139], same as Section 2.2.2 (Table 2.4), were directly used for the ATAA patient. [142] documented layer-specific residual stretch and opening angle data for ATAA. Unfortunately, it is not compatible with the current three-dimensional residual stress model [139]. Specifically, Holzapfel and Ogden [139] considered different geometries of reference configurations for different layers and would need more complicated experimental setups.

Table 2.7 - Layer-specific GOH material parameters from [51].

	$\mathrm{C}_{10}\ (kPa)$	$\mathrm{k}_1 (kPa)$	k_2	κ	$\theta(°)$
Intima	17	4340	13.32	0.20	46.5
Media	14	140	11.90	0.21	38.4
Adventitia	10	390	6.79	0.23	52.3

Regardless of the discrepancy of the von Mises stress in the thickness direction (Figure 2.7, first row), the transmural mean von Mises stress field predicted by the forward penalty approach and the GPA are, again, almost identical, with a MAPE of 5.89% (Figure 2.7, second row). Since the details of transmural distribution of von Mises stress is not clearly shown in the first row of Figure 2.7, we use Figure 2.8 to show von Mises stress distributions in a hoop predicted by method described in Section 2.3.1 (forward penalty) and Section 2.3.3 (opening angle $\alpha = 180°$) and Section 2.3.4 (layer-specific 3D residual deformation), respectively.

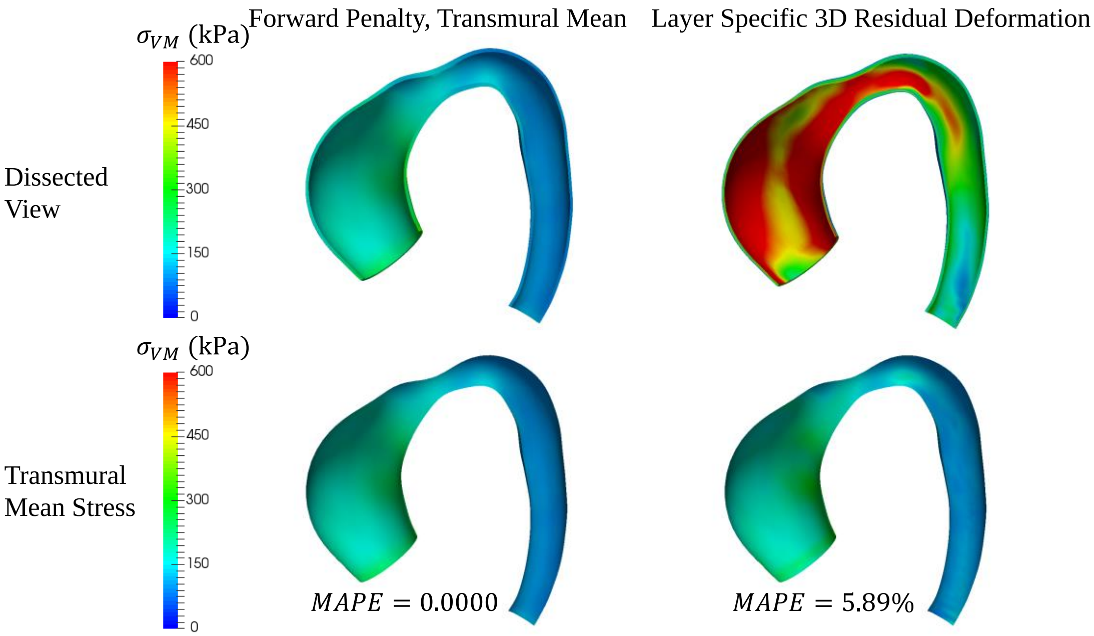

Figure 2.7 - Predicted results using the forward penalty approach and the iterative approach (GPA) with layer-specific three-dimensional residual deformations: (1) the von Mises stress distribution in the dissected view (row 1), (2) the transmural mean stress (row 2).

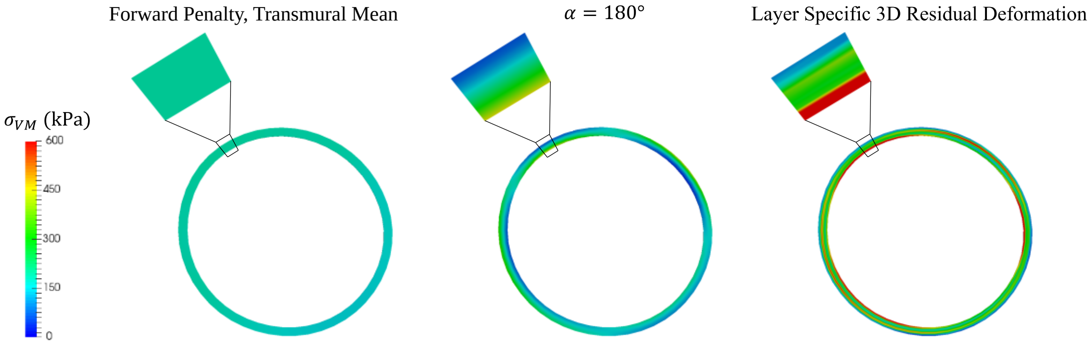

Figure 2.8 - von Mises stress distribution in the aortic hoop using the forward approach, the GPA approach (α=180°) and the layer-specific 3D residual deformation.

2.4 Discussion

One of the biggest obstacles in the field of biomechanical analysis of the aorta is the difficulty in obtaining both the patient-specific material properties and the patient-specific residual deformations from *in vivo* clinical images. This study offers an appealing prospect that the transmural mean stress (or wall tension) of the aortic wall can be computed without knowing the mechanical properties and the residual deformations of the aortic tissue. Computation of patient-specific mean stress can be greatly simplified by using the forward penalty approach, which may be clinically valuable. In some wall strength tests [15, 148], the intact wall is tested without separation of each individual layer, which corresponds to the averaged wall strength across the wall thickness, consistent with the thin-wall assumption. The mean stress may be used together with the experimentally-obtained strength to calculate an approximation of rupture risk such as the rupture potential index (RPI) [149].

2.4.1 Comparison with Traditional Iterative Approach with Nonlinear Material Properties and Residual Deformations

Because of the difference in constituents and thus mechanical properties, stress distribution may not be uniform in multi-layer models. The iterative approaches such as the GPA, may yield detailed results with through-thickness and layer-specific stress distributions using multilayered thick-walled models. Therefore, it would be natural to combine layer-specific wall stress distribution with available layer-specific wall strength data [22] for a more detailed rupture/dissection analysis. Nonetheless, residual deformations are shown to be highly patient-specific and axial location-dependent [142].

Elastic properties also exhibit regional [21, 147] and intra-patient [57] variations. Thus, such complex patient- and layer-specific residual deformation and elastic property fields need to be noninvasively estimated for an accurate modeling prediction of clinical events (e.g. rupture). Currently, it is impossible to estimate the layer-specific and heterogeneous material and residual deformation parameters simultaneously from *in vivo* clinical images. We admit that stresses within each layer may be more useful than the mean stress for predicting some clinical adverse events such as aortic dissection. However, the mean stress is clinically valuable too because it is patient-specific, which does not depend on material parameters and residual deformations.

2.4.2 The Transmural Mean Stress is Consistence with Homogenized Stress State

The inclusion of residual deformation often reduces the hoop stress gradient, and thus tends to homogenize the hoop stress distribution in the *in vivo* deformed configuration [33, 128, 130, 132, 150, 151]. This makes the thin-walled stress, or the mean stress more physiologically relevant in the sense that it represents the ideal homogenized wall stress in single layer models. Homogenized stress state is an assumption for some growth models, e.g., [152], and the method proposed in [153] is based on smoothing the stress gradient. In this study, the incorporation of opening angles also tends to homogenize the hoop stress distribution as shown in Figure 2.1. In Figure 2.4, the MSTPE is close to 0 when 90~180 degree opening angle is incorporated. However, this value seems to be lower than the average value obtained from experiment [142]. This might be due to the assumption of uniform material properties and uniform thickness in the computational model, which could impact the transmural stress distribution. We also notice that a wide range of opening angle is documented in [142], 90~180 degree opening angle can be considered feasible.

For comparison purposes, the same solid meshes in Section 2.3.3 were used when applying the forward penalty approach in Section 2.3.1. The transmural mean stress can also be computed by the forward penalty approach using membrane elements. For various opening angles when using membrane elements, the ranges of MAPEs are $[3.03\%, 3.09\%]$, $[27.37\%, 27.65\%]$ and $[4.44\%, 4.55\%]$ for $\bar{\sigma}_{\theta\theta}$, $\bar{\sigma}_{zz}$ and $\bar{\sigma}_{VM}$, respectively.

2.4.3 Static Determinacy of Axial/Longitudinal Stress

In general, the axial/longitudinal stress $\bar{\sigma}_{zz}$ of a straight tube is statically determinate only when the longitudinal force is known. However, in the present study, the longitudinal force is unknown since a displacement boundary condition was used: the boundary nodes were only allowed to move in the radial directions. Interestingly, as demonstrated in Table 2.5, the transmural mean longitudinal stress $\bar{\sigma}_{zz}$ of the ATAA can also be approximated by the forward penalty approach. This may be due to the fact that the geometry of ATAA is a curved tube, and the longitudinal forces acting on the boundaries are balanced with resultant force from *in vivo* pressure. Longitudinal forces computed using the forward penalty method and various opening angles are demonstrated in Figure 2.9. Because longitudinal forces for various opening angles are almost identical, thus only when $\alpha = 180°$ is plotted. The ascending aorta has *in vivo* longitudinal deformations/stretches due to the heart movements during cardiac cycles. Such boundary condition is very complex and it can be difficult to model in a FE simulation. The *in vivo* longitudinal boundary conditions would significantly impact the longitudinal stress field, which warrants further studies in the future.

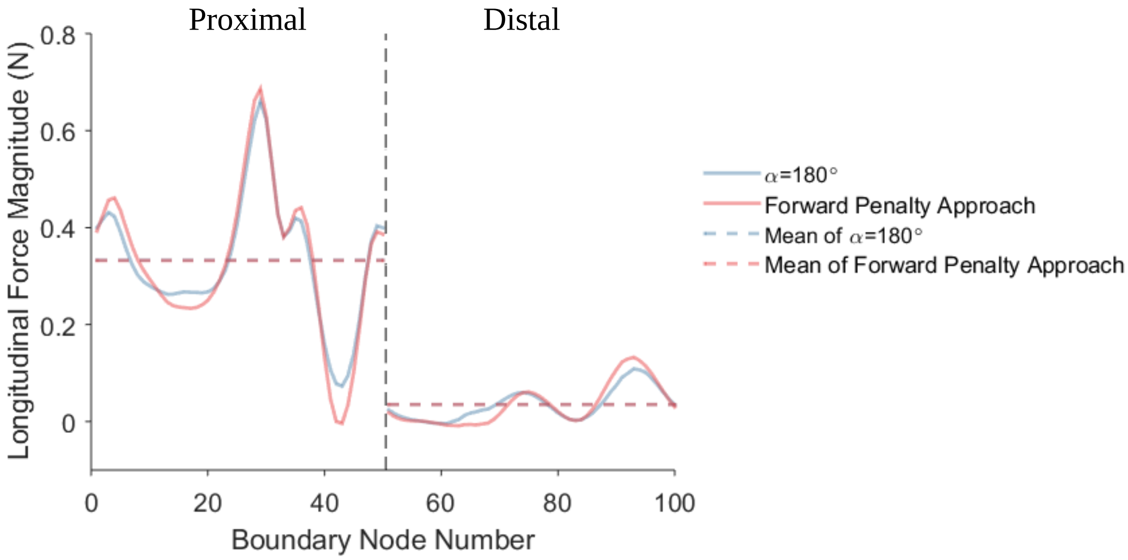

Figure 2.9 - Longitudinal forces computed using the GPA approach (α=180°) and the forward penalty approach on the proximal (nodes 0~50) and distal (nodes 51~100) boundaries of the ATAA model. The longitudinal forces were summed across the wall thickness before plotting. Because longitudinal forces for various opening angles are almost identical, thus only when α=180° is plotted.

2.5 Summary

To summarize, due to static determinacy, the transmural mean stress in the *in vivo* configuration of the aorta is independent of mechanical properties and residual deformations. The forward penalty method, which enforces a rigid condition as the penalty treatment, can greatly simplify the computation of the mean stress for patient-specific geometries.

CHAPTER 3. INVERSE IDENTIFICATION OF IN VIVO HYPERELASTIC PROPERTIES OF THE AORTIC WALL

Accurate identification of *in vivo* nonlinear, anisotropic mechanical properties of the aortic wall of individual patients remains to be one of the critical challenges in the field of cardiovascular biomechanics. Since only the physiologically loaded states of the aorta are given from *in vivo* clinical images, inverse approaches, which take into account of the unloaded configuration, are needed for *in vivo* material parameter identification. Previous inverse methods largely relied on either computationally expensive FE models or simplifications of the geometry or material models. In the previous chapter, the aortic wall was shown to be statically determinate. In this chapter, we investigate a new inverse method based on static determinacy of the aortic wall. This approach consists of the following two steps: (1) computing an "almost true" stress field from *in vivo* geometries and loading conditions using static determinacy, and (2) building an objective function based on the "almost true" stress fields, constitutive equations and deformation relations, and identifying the unknown material parameters by minimizing the objective function. The method was validated through numerical experiments by using the *in vivo* data from four ascending aortic aneurysm (ATAA) patients. The results demonstrated that the method is computationally efficient. Using the novel inverse approach, we identified *in vivo* aortic tissue elastic properties of two ATAA patients from pre-operative gated CT scans. For comparison, corresponding surgically-resected aortic wall tissue samples were obtained and subjected to planar biaxial tests. Relatively close matches were achieved for the *in vivo*-identified and *ex vivo*-fitted stress-stretch responses. This novel approach may facilitate the personalized biomechanical analysis of aortic tissues in clinical applications, such as TAA rupture risk analysis. It is hoped that further development of this inverse approach can enable an accurate identification of the *in vivo* material parameters from *in vivo* image data. Some of the results of this chapter is published in [125, 154].

3.1 Background

Accurate identification of *in vivo* nonlinear, anisotropic mechanical properties of the vessel wall of individual patients has long been regarded as one of the critical challenges in the field of cardiovascular biomechanics [123]. Magnetic resonance imaging (MRI) [155], ultrasound [156, 157] and computed tomography (CT) [124] imaging techniques have been utilized to perform *in vivo* wall motion analyses. For example, MRI [155] and ultrasound [156, 157] studies of ATAA patients have highlighted disparities between the dilated and non-dilated ascending aorta mechanics. However, such direct measurements of *in vivo* aortic wall deformation can only provide insight on ATAA mechanical behaviors within the measured physiologic pressure range [124] (usually between 80mmHg- 120mmHg), whereas aneurysm rupture/dissection usually occurs under elevated arterial pressures (e.g., about 300mmHg) brought on by extreme emotional or physical stress [158]. Thus, patient-specific ATAA rupture analysis could benefit from estimating the full *in vivo* elastic properties using a constitutive model, which, consequently, can be utilized to predict ATAA mechanical response at various loading conditions.

To exploit the 3D geometries obtained from multi-phase clinical image data, previous methods for *in vivo* material parameter identification largely rely on FE updating schemes. Using FE updating methods, Wittek et al. [99, 100] developed two methods to determine GOH material parameters of the human abdominal aorta from *in vivo* 4D ultrasound data [157]. However, numerous iterations were needed to reach the optimal solution with a long computing time of 1~2 weeks. Such high computational cost could inhibit a practical use of these methods, particularly in a clinical setting requiring rapid feedback to clinicians.

In this chapter, we proposed a new inverse approach based on stress computation for the *in vivo* nonlinear material parameter identification of the aortic wall. This method is less computationally expensive. Firstly, we leveraged the fact that the *in vivo* aortic wall stress is approximately statically determinate, which means, for given geometries and loading and boundary conditions under a known blood pressure, different material parameters and constitutive models will give nearly the same stress field. Therefore, the "almost-true" *in vivo* stress field at any cardiac phase can be obtained by using the forward penalty approach with sufficiently stiff material parameters. Secondly, given a constitutive model with an initial guess of the material parameters, by using the constitutive equations and deformation relation between the two loading states (e.g., diastolic and systolic pressures), we applied optimization algorithms to find the "true" material parameters such that the difference between the estimated and the "almost-true" stress fields is minimized. Since FE simulation is not used iteratively in this optimization process, our approach is much faster than the other methods [99, 100] that require numerous iterations of FE simulations. The developed inverse method was applied to identify *in vivo* nonlinear anisotropic material properties from clinical 3D gated CT images of two ATAA patients. For comparison, corresponding surgically-resected aortic wall tissue samples were obtained and subjected to planar biaxial tests to extract their experimentally-derived material properties. The estimated material properties were compared with the experimentally-derived material properties. The proposed approach may facilitate the subject-specific biomechanics analysis of aortic wall stresses in clinical applications, such as TAA rupture risk analysis [57].

3.2 The Inverse Method

3.2.1 Prerequisites and Assumptions

Our method was formulated based on the following assumptions: (1) *In vivo* loaded geometries of the aorta and blood pressure levels are known at 2 phases, e.g., at diastole and systole; (2) Finite element meshes of the geometries at the two phases can be constructed with mesh correspondence, i.e., the displacement field from systole to diastole is obtainable, similar to the full field measurement [83]; (3) the thickness of the aortic wall can be either directly inferred from the clinical images or can be reasonably assumed; and (4) the residual stresses are ignored. In the previous chapter, we showed that the transmural mean stress is independent of residual deformations. The mesh correspondence condition may be satisfied by using 4D (3D+t) ultrasound image data processed with speckle tracking algorithms [159], or ECG-gated CT image data processed with surface tracking algorithms [160]; the heterogeneous thickness of the aortic wall may be extracted by using CT [161-163], MR[164] and ultrasound [165, 166] imaging techniques.

In this thesis, we only considered the homogeneous (average) constitutive behavior of the aortic segment and across the wall thickness. However, our approach can be extended to heterogeneous tissues since it is not based on the assumption of homogeneity.

3.2.2 Constitutive Model

The anisotropic hyperelastic material model developed by Gasser *et al.* (Eqn. (2.10)) [34] was used to model the constitutive response of aortic wall tissue. Thus, the five material parameters, $C_{10}, k_1, k_2, \kappa, \theta$, needs to be identified from *in vivo* geometries and blood pressures. In this chapter, the material incompressibility parameter *D* is fixed to 10^{-4} during all computations.

3.2.3 The Workflow for Constitutive Parameter Identification

The workflow of our material parameter identification process is shown in Figure 3.1. This approach utilizes the static determinacy of the aortic wall: an “almost-true” stress field of the aortic wall can be approximately determined by the geometry and blood pressure load, and only weakly depends on material properties. The static determinacy has been theoretically justified by Miller and Lu [135] and numerically verified by Lu *et al.* [167] and Joldes *et al.*[136]. Therefore, given the deformed configurations at the two cardiac phases, $\boldsymbol{x_a}$ at the diastole phase and $\boldsymbol{x_b}$ at the systole phase, the “almost-true” stress of each element m of the aortic wall at the two phases, $\widetilde{\boldsymbol{\sigma}}_{\boldsymbol{a}}^{m}$ and $\widetilde{\boldsymbol{\sigma}}_{\boldsymbol{b}}^{m}$, respectively, can be calculated by using the forward penalty approach (see Section 2.3.1). In this chapter, we use subscript a and b to denote the diastole and systole respectively, but generally they can represent any two loaded phases as long as the pressure levels and geometries are known**.** The relative deformation gradient $\widetilde{\boldsymbol{F}}_{\boldsymbol{ab}}^{m}$ from the diastolic configuration to the systolic configuration can be calculated using the relative displacement field $\boldsymbol{u_{ab}}$ between the two configurations. As a result, the systolic stress of each element can be estimated by using the constitutive model with the candidate parameters and relative deformation gradient.

The estimated systolic stress, $\widetilde{\boldsymbol{\sigma}}_{\boldsymbol{b}}^{m,\ est}$, which depends on the constitutive parameters $(C_{10},\ k_1,\ k_2,\ \kappa,\ \theta)$, can be compared with the "almost-true" systolic stress $\widetilde{\boldsymbol{\sigma}}_{\boldsymbol{b}}^{m}$, and any discrepancy will indicate that the set of candidate parameters are different from the optimal "true" parameters and hence need to be adjusted by a nonlinear optimization algorithm.

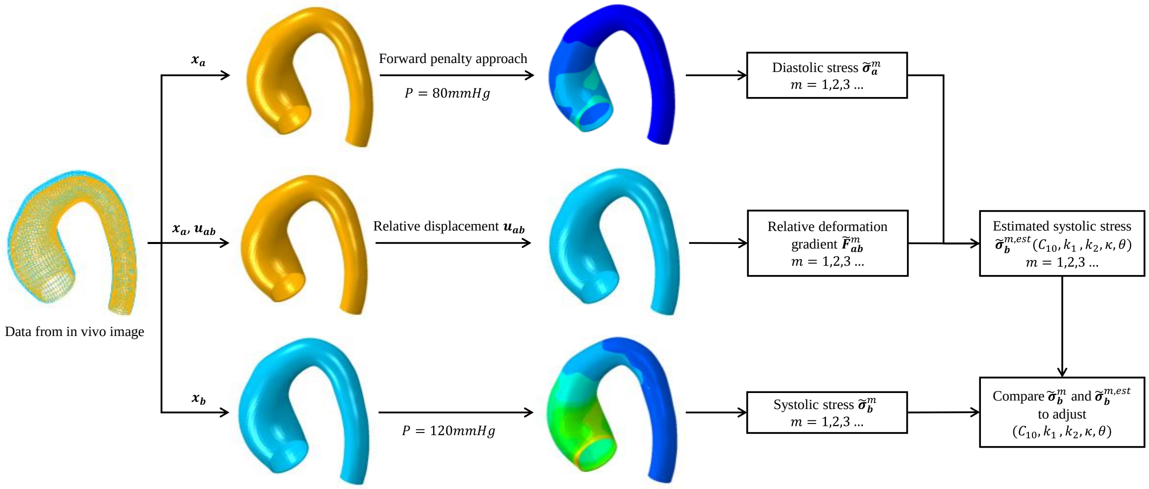

Data from in vivo image
$\boldsymbol{x_a}$
$\boldsymbol{x_a}, \boldsymbol{u_{ab}}$
$\boldsymbol{x_b}$
Forward penalty approach
$P = 80mmHg$
Relative displacement $\boldsymbol{u_{ab}}$
$P = 120mmHg$
Diastolic stress $\widetilde{\boldsymbol{\sigma}}_{\boldsymbol{a}}^{m}$
$m = 1,2,3 \ldots$
Relative deformation gradient $\widetilde{\boldsymbol{F}}_{\boldsymbol{ab}}^{m}$
$m = 1,2,3 \ldots$
Systolic stress $\widetilde{\boldsymbol{\sigma}}_{\boldsymbol{b}}^{m}$
$m = 1,2,3 \ldots$
Estimated systolic stress
$\widetilde{\boldsymbol{\sigma}}_{\boldsymbol{b}}^{m,est}(C_{10}, k_1, k_2, \kappa, \theta)$
$m = 1,2,3 \ldots$
Compare $\widetilde{\boldsymbol{\sigma}}_{\boldsymbol{b}}^{m}$ and $\widetilde{\boldsymbol{\sigma}}_{\boldsymbol{b}}^{m,est}$
to adjust
$(C_{10}, k_1, k_2, \kappa, \theta)$

Figure 3.1 - The flowchart of the material parameter identification process.

This optimization process can be formulated as follows: the objective is to find a set of constitutive parameters $(C_{10}, k_1, k_2, \kappa, \theta)$ that minimize the difference between the "almost-true" systolic tress $\tilde{\sigma}_{b,i}^{m}$ and the estimated systolic tress $\tilde{\sigma}_{b,i}^{m,est}$ for every integration point of each element m, which is defined as

$$g_{err} = \sum_{m=1}^{N} \sum_{i=1}^{6} \left[\tilde{\sigma}_{b,i}^{m} - \tilde{\sigma}_{b,i}^{m,est}(C_{10}, k_1, k_2, \kappa, \theta)\right]^2 \tag{3.1}$$

where N is the number of elements used in the optimization, i is the component index of the stress tensor in Voigt notation. At element m, $\tilde{\sigma}_{b,i}^{m,est}$ is the component of the estimated systolic stress given a set of candidate constitutive parameters $(C_{10}, k_1, k_2, \kappa, \theta)$. For a type of element that has more than one integration point such as C3D8 in the ABAQUS (Simulia, RI), we calculated the squared stress-errors at all integration points and sum them together as the value of the objective function of Eqn. (3.1).

The details of each step in the approach are presented in the following sections. The forward penalty approach (Section 2.3.1) that was used for calculating $\tilde{\boldsymbol{\sigma}}_{\boldsymbol{a}}^{m}$ and $\tilde{\boldsymbol{\sigma}}_{\boldsymbol{b}}^{m}$ is described in Section 3.2.4. The method for estimating $\tilde{\boldsymbol{\sigma}}_{\boldsymbol{b}}^{m,\ est}$ is described in Section 3.2.5. The optimization process and the entire workflow are described in Section 3.2.6. To verify the approach, numerical experiments were carried out on the data from four ascending aortic aneurysm patients in Section 3.3.

3.2.4 "Almost-True" Stress Computation using the Forward Penalty Approach

In the previous chapter, it was shown that the aortic wall is statically determinate, and the forward penalty approach can be used to compute stress on the aortic wall without knowing material properties and residual deformations. Here, the stress computed by static determinacy is considered to be "almost-true", i.e., very close to the true stress in the aortic wall. In this study, we selected a very stiff material ($E = 2 \times 10^4\ GPa$ and $\nu = 0.49$) for the aortic wall to obtain the wall Cauchy stress (Figure 3.1). The static determinacy was numerically validated in Section 2.3.2.

3.2.5 Continuum Mechanics Framework for Systolic Stress Estimation

In this section, we presented a method using the corotational coordinate frame to estimate the systolic stress ($\tilde{\boldsymbol{\sigma}}_{\boldsymbol{b}}^{m,est}$) given the candidate material parameters

$(C_{10}, k_1, k_2, \kappa, \theta)$ of Eqn (2.10). Figure 3.2 illustrates the related variables in the unloaded configurations and the two deformed configurations. The diastolic deformation gradient $\boldsymbol{F_a}$ contains complete information about rotation and stretch that can be uniquely defined via polar decomposition

$$\boldsymbol{F_a} = \boldsymbol{V_a}\boldsymbol{R_a} = \boldsymbol{R_a}\boldsymbol{U_a} \tag{3.2}$$

where $\boldsymbol{V_a}$ is the left stretch tensor, $\boldsymbol{U_a}$ is the right stretch tensor, $\boldsymbol{R_a}$ is the rotation tensor. We defined two coordinate systems *CSYSI* and *CSYSII*, where *CSYSI* refers to a fixed Cartesian coordinate system, and *CSYSII* is the coordinate system corotated with the diastolic rotation $\boldsymbol{R_a}$. Let $\mathit{\Omega}_0$ be the unloaded configuration and $\mathit{\Omega}_0'$ be the corotated unloaded configuration obtained by applying the diastolic rotation $\boldsymbol{R_a}$ on $\mathit{\Omega}_0$. $\mathit{\Omega}_a$ and $\mathit{\Omega}_b$ are the diastolic and systolic configurations respectively.

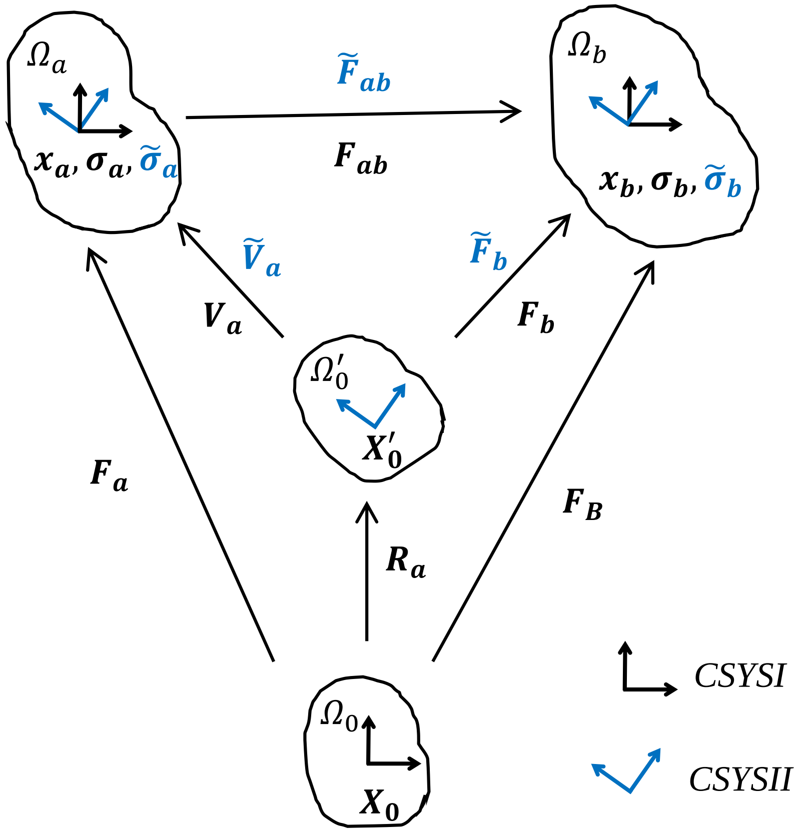
Ω_a
$\widetilde{\boldsymbol{F}}_{ab}$
Ω_b
$\boldsymbol{x_a}, \boldsymbol{\sigma_a}, \widetilde{\boldsymbol{\sigma}}_{\boldsymbol{a}}$
$\boldsymbol{F_{ab}}$
$\boldsymbol{x_b}, \boldsymbol{\sigma_b}, \widetilde{\boldsymbol{\sigma}}_{\boldsymbol{b}}$
$\widetilde{\boldsymbol{V}}_{\boldsymbol{a}}$
$\widetilde{\boldsymbol{F}}_{\boldsymbol{b}}$
$\boldsymbol{V_a}$
$\boldsymbol{F_b}$
Ω_0'
$\boldsymbol{X}_0'$
$\boldsymbol{F_a}$
$\boldsymbol{F_B}$
$\boldsymbol{R_a}$
CSYSI
Ω_0
$\boldsymbol{X_0}$
CSYSII

Figure 3.2 - Deformation measures that map the unloaded configuration $\boldsymbol{\Omega_0}$, the corotated unloaded configuration $\boldsymbol{\Omega_0'}$, the diastolic configuration $\boldsymbol{\Omega_a}$ and the systolic configuration $\boldsymbol{\Omega_b}$.

As shown in Figure 3.2, the diastolic deformation gradient $\boldsymbol{F_a}$, the systolic deformation gradient $\boldsymbol{F_B}$ and the relative deformation gradient $\boldsymbol{F_{ab}}$ in *CSYSI* are defined through:

$$\boldsymbol{F_a} = \frac{\partial \boldsymbol{x_a}}{\partial \mathbf{X_0}}, \qquad \boldsymbol{F_B} = \frac{\partial \boldsymbol{x_b}}{\partial \boldsymbol{X_0}}, \qquad \boldsymbol{F_{ab}} = \frac{\partial \boldsymbol{x_b}}{\partial \boldsymbol{x_a}} \tag{3.3}$$

where $\boldsymbol{X_0}$, $\boldsymbol{x_a}$ and $\boldsymbol{x_b}$ are coordinate vectors of the unloaded, diastolic and systolic configurations respectively, which are defined in *CSYSI*. Similarly, the deformation tensors $\widetilde{\boldsymbol{V}}_{\boldsymbol{a}}$, $\widetilde{\boldsymbol{F}}_{\boldsymbol{ab}}$, $\widetilde{\boldsymbol{F}}_{\boldsymbol{b}}$, are measured in *CSYSII*.

Given the diastolic Cauchy stress, we need to first inversely compute the diastolic deformation gradient $\boldsymbol{F_a}$ in order to obtain the systolic deformation gradient. The main challenge came from the fact that the symmetric Cauchy stress tensor has only 6 independent components, which makes it impossible to get a unique solution of the diastolic deformation gradient $\boldsymbol{F_a}$ that has 9 independent components. To solve this issue, taking advantage of the material objectivity [144, 168], we have the following restriction on the constitutive function h using the corotational frame

$$\boldsymbol{\sigma_a} = \boldsymbol{R_a}\boldsymbol{\widetilde{\sigma}_a}\boldsymbol{R_a^T} = h(\boldsymbol{F_a}) = \boldsymbol{R_a}h\big(\boldsymbol{\widetilde{V}_a}\big)\boldsymbol{R_a^T} \tag{3.4}$$

where $\boldsymbol{\widetilde{\sigma}_a}$ is the diastolic Cauchy stress observed in *CSYSII*. Instead of fully computing the deformation gradient $\boldsymbol{F_a}$, knowing the $\boldsymbol{\widetilde{\sigma}_a}$, the only quantity we need to explicitly derive is the left stretch tensor $\boldsymbol{\widetilde{V}_a}$ in *CSYSII* (the value of $\boldsymbol{\widetilde{V}_a}$ is equal to $\boldsymbol{U_a}$ in *CSYSI*, $\boldsymbol{\widetilde{V}_a} = \boldsymbol{R_a^{-1}}\boldsymbol{V_a}\boldsymbol{R_a} = \boldsymbol{R_a^{-1}}\boldsymbol{F_a} = \boldsymbol{U_a}$). According to the chain rule, we can arrive at the relation among the deformation gradients

$$\boldsymbol{\widetilde{F}_b} = \boldsymbol{\widetilde{F}_{ab}}\boldsymbol{\widetilde{V}_a} \tag{3.5}$$

where $\boldsymbol{\widetilde{F}_{ab}}$ is known. As a result, the systolic Cauchy stress $\boldsymbol{\widetilde{\sigma}_b}$ can be correctly recovered in *CSYSII*.

On account of the nature of strain energy function $\Psi(\boldsymbol{F})$, i.e. $\boldsymbol{\sigma}$ is always expressed in terms of deformation in a forward computation, given a deformation gradient, the Cauchy stress of a hyperelastic material can be calculated using [35]

$$\boldsymbol{\sigma} = \boldsymbol{\sigma}_{vol} + \boldsymbol{\sigma}_{iso} = p\boldsymbol{I} + J^{-1}\overline{\boldsymbol{F}}Dev(\overline{\boldsymbol{S}})\overline{\boldsymbol{F}}^{T} \tag{3.6}$$

where $\boldsymbol{\sigma}_{vol}$ and $\boldsymbol{\sigma}_{iso}$denotes the volumetric and isochoric contribution respectively, p is the hydrostatic pressure $p = dW_{vol}(J)/dJ$, $\boldsymbol{I}$ is identity. $\overline{\boldsymbol{F}}$ is the modified deformation gradient calculated by $\overline{\boldsymbol{F}} = J^{-1/3}\boldsymbol{F}$. $\overline{\boldsymbol{S}}$ can be expressed by $\overline{\boldsymbol{S}} = 2\partial W_{iso}(\overline{\boldsymbol{C}})/\partial\overline{\boldsymbol{C}}$ and $Dev(\blacksquare) = (\blacksquare) - (1/3)[(\blacksquare):\boldsymbol{C}]\boldsymbol{C}^{-1}$, where the modified right Cauchy-Green deformation tensor $\overline{\boldsymbol{C}} = J^{-2/3}\boldsymbol{C}$. For fixed constitutive parameters, the stress $\boldsymbol{\sigma}$ is essentially a function of $\boldsymbol{F}$. If a deformation does not have rotation, we can also compute $\boldsymbol{\sigma}$ using the above formulations by substituting $\boldsymbol{F}$ with left stretch tensor $\boldsymbol{V}$.

An inverse computation scheme was introduced to compute the diastolic left stretch tensor $\widetilde{\boldsymbol{V}}_{\boldsymbol{a}}$ in the *CSYSII*. Nonlinear least square optimization was used for the computation of $\widetilde{\boldsymbol{V}}_{\boldsymbol{a}}$, with 6 unknowns and as many as the number of equations. The objective function was defined by

$$f_{err} = \sum_{i=1}^{6}\left[\tilde{\sigma}_{a,i} - \tilde{\sigma}_{a,i}^{est}(\widetilde{\boldsymbol{V}}_{\boldsymbol{a}})\right]^{2} \tag{3.7}$$

where the stress tensor is represented in Voigt notation. $\tilde{\sigma}_{a,i}^{est}$ represents the components of estimated diastolic stress computed using a guess of $\widetilde{\boldsymbol{V}}_{\boldsymbol{a}}$. The trust region algorithm is used and gradients are estimated using finite differences. The optimization was implemented in MATLAB (Mathworks, MA), and a numerical validation was performed in Section 0.

3.2.6 *Implementation of the Inverse Method*

The FE simulations were performed in ABAQUS/Standard 6.14 using the 3D brick element C3D8. Since the stress of each integration point in an element outputted from ABAQUS is in the local coordinate system associated with the element, the local coordinate system of the output diastolic stress $\widetilde{\boldsymbol{\sigma}}_{\boldsymbol{a}}$ of the element is defined as *CSYSII*. The systolic stress of the same element output from ABAQUS was converted to $\widetilde{\boldsymbol{\sigma}}_{\boldsymbol{b}}$ in *CSYSII*. Here, the forward penalty approach was used to obtain $\widetilde{\boldsymbol{\sigma}}_{\boldsymbol{a}}$ and $\widetilde{\boldsymbol{\sigma}}_{\boldsymbol{b}}$ at the two phases. For convenience, displacement $\boldsymbol{u}_{\boldsymbol{ab}}$ was applied as a boundary condition at every node in ABAQUS to obtain the relative deformation gradient, which is output and converted to $\widetilde{\boldsymbol{F}}_{\boldsymbol{ab}}$ in *CSYSII*.

The workflow of the parameter estimation process is depicted in Figure 3.3. The inner loop is responsible for the inverse calculation of the left stretch tensor $\widetilde{\boldsymbol{V}}_{\boldsymbol{a}}$ at each element, the second loop is repeated for all of the elements, and the outer loop updates candidate material parameters in each iteration. The method was implemented in MATLAB. We used the finite difference and trust-region-reflective algorithm for the optimization, which is "lsqnonlin" in MATLAB.

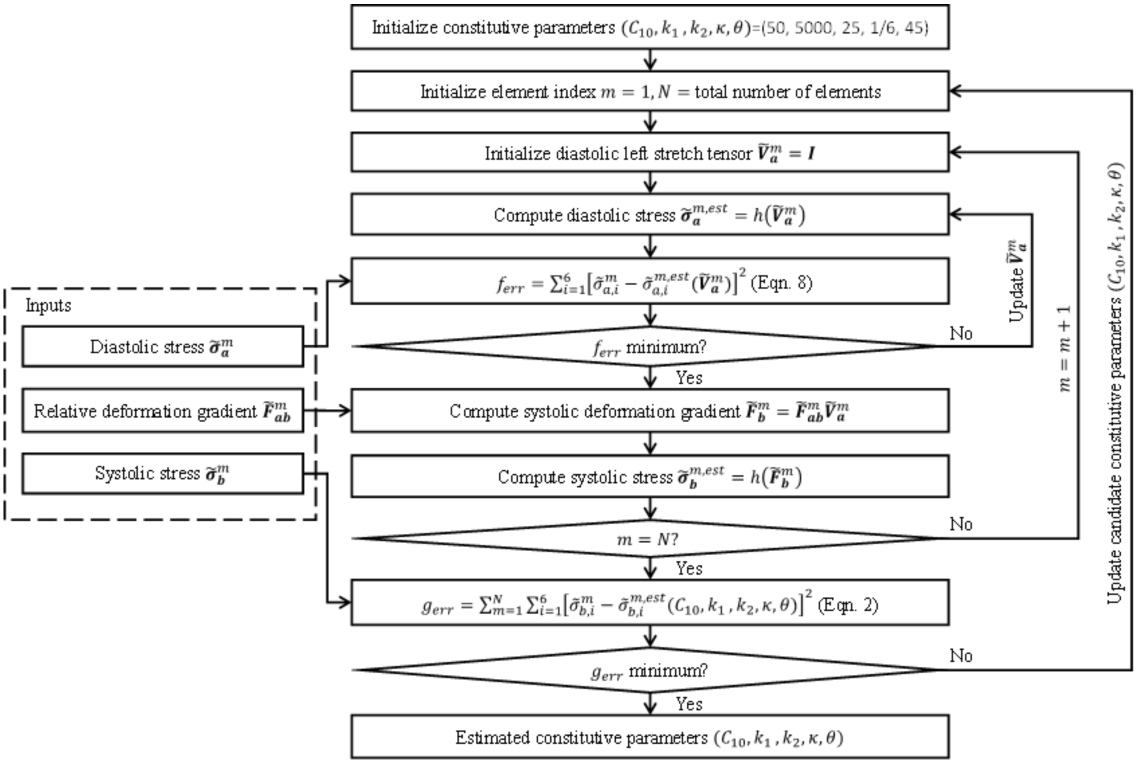
Initialize constitutive parameters $(C_{10}, k_1, k_2, \kappa, \theta)$=(50, 5000, 25, 1/6, 45)
Initialize element index $m = 1, N =$ total number of elements
Initialize diastolic left stretch tensor $\widetilde{\boldsymbol{V}}_{\boldsymbol{a}}^{m} = \boldsymbol{I}$
Compute diastolic stress $\widetilde{\boldsymbol{\sigma}}_{\boldsymbol{a}}^{m,est} = h(\widetilde{\boldsymbol{V}}_{\boldsymbol{a}}^{m})$
$f_{err} = \sum_{i=1}^{6}[\tilde{\sigma}_{a,i}^{m} - \tilde{\sigma}_{a,i}^{m,est}(\widetilde{\boldsymbol{V}}_{\boldsymbol{a}}^{m})]^2$ (Eqn. 8)
Inputs
Diastolic stress $\widetilde{\boldsymbol{\sigma}}_{\boldsymbol{a}}^{m}$
Relative deformation gradient $\widetilde{\boldsymbol{F}}_{\boldsymbol{ab}}^{m}$
Systolic stress $\widetilde{\boldsymbol{\sigma}}_{\boldsymbol{b}}^{m}$
f_{err} minimum?
No
Yes
Update $\widetilde{\boldsymbol{V}}_{\boldsymbol{a}}^{m}$
Compute systolic deformation gradient $\widetilde{\boldsymbol{F}}_{\boldsymbol{b}}^{m} = \widetilde{\boldsymbol{F}}_{\boldsymbol{ab}}^{m}\widetilde{\boldsymbol{V}}_{\boldsymbol{a}}^{m}$
Compute systolic stress $\widetilde{\boldsymbol{\sigma}}_{\boldsymbol{b}}^{m,est} = h(\widetilde{\boldsymbol{F}}_{\boldsymbol{b}}^{m})$
$m = N$?
No
Yes
$m = m + 1$
$g_{err} = \sum_{m=1}^{N}\sum_{i=1}^{6}[\tilde{\sigma}_{b,i}^{m} - \tilde{\sigma}_{b,i}^{m,est}(C_{10}, k_1, k_2, \kappa, \theta)]^2$ (Eqn. 2)
g_{err} minimum?
No
Yes
Update candidate constitutive parameters $(C_{10}, k_1, k_2, \kappa, \theta)$
Estimated constitutive parameters $(C_{10}, k_1, k_2, \kappa, \theta)$

Figure 3.3 - Implementation of the constitutive parameter identification.

3.3 Numerical Validations

The approach was validated by numerical experiments. Clinical cardiac CT image data at the systolic phase (assuming 120mmHg systolic pressure) from four de-identified patients with ascending aortic aneurysms (ATAA) were chosen for the verification (same as Section 2.3.2), whose "true" constitutive parameters were extracted from 7-protocol biaxial tensile tests in a previous study [15, 63] by nonlinear regression. The "true" material parameters are within the upper and lower bounds, which are also comparable to other testing results [51, 169, 170]. The initial value, upper and lower bounds of the constitutive parameters are shown in Table 3.1.

Table 3.1 - Initial value, upper and lower bounds of constitutive parameters.

	$C_{10}\ (kPa)$	$k_1 (kPa)$	k_2	κ	$\theta(°)$
Initial	50	5000	25	1/6	45
Lower bound	0	0	0	0	0
Upper bound	100	10000	50	1/3	90

The geometries of the aorta were reconstructed by using the semi-automatic method developed in our previous study [171]. For simplicity, the branches at the aortic arch were trimmed. We used the following methods to numerically obtain the "true" geometries and stress fields at the diastolic and systolic phases. We assigned experimentally derived material parameters [15] to the corresponding geometries. From CT image data, the unloaded geometries were recovered by the backward displacement method [121], and they were assumed to have a constant wall thickness of 2 mm [57]. The "true" diastolic and systolic geometries were obtained from FE simulations by applying diastolic (P=80mmHg) and systolic (P=120mmHg) pressures on the unloaded geometries. Thus, this only represents an idealized situation where the influence of residual stress is not present in the numerically generated data. Each finite element mesh consists of 10,000 nodes and 4950 elements. Mesh convergence analysis was performed in our previous work [57], and the number of elements is adequate for accurate stress predictions. Mesh correspondence at the two phases was automatically established because the two meshes at the two phases were deformed from the same mesh at the unloaded state.

In all FE simulations, constant pressures were applied uniformly to the inner surface of the FE models, and the boundary nodes of the models, i.e. the proximal and distal ends of the models, were constrained to only allow displacement in the radial direction in the local cylindrical coordinate system. The centerline of the aorta was estimated to define the axial direction of the local coordinate system, and the radial direction was computed using the outward normal direction of the outer surface of the aorta. The local coordinate system followed the average rotation of the element [144], the stress of an element was outputted in the rotated coordinate system. In the parameter estimation procedure, five layers of elements adjacent to the mesh boundaries were excluded in order to avoid the boundary layer phenomenon [135]: the influence of material properties is pronounced only in a thin layer near the fixed edge; and the stress approaches asymptotically a static solution outside the boundary layer.

3.3.1 *Inverse Computation of Diastolic Left Stretch Tensor*

The validation for the inverse computation of $\widetilde{\boldsymbol{V}}_{\boldsymbol{a}}$ was performed by using randomly generated $\boldsymbol{F}_{\boldsymbol{a}}$ and the "true" material parameters of patient ATAA2 ("BAV17" in CHAPTER 2). For the given set of constitutive parameters, the Cauchy stress $\boldsymbol{\sigma}_{\boldsymbol{a}} = h(\boldsymbol{F}_{\boldsymbol{a}})$ was computed and rotated to $\widetilde{\boldsymbol{\sigma}}_{\boldsymbol{a}}$ in *CSYSII* (Figure 3.2). The "true" $\widetilde{\boldsymbol{V}}_{\boldsymbol{a}} = \boldsymbol{R}_{\boldsymbol{a}}^{T}\boldsymbol{V}_{\boldsymbol{a}}\boldsymbol{R}_{\boldsymbol{a}}$ was computed by using polar decomposition and coordinate transformation of $\boldsymbol{F_a}$. Using the inverse computation scheme from Section 3.2.5, we estimated the Cauchy stress and left stretch tensor in *CSYSII* $\widetilde{\boldsymbol{\sigma}}_{\boldsymbol{a}}^{est} = h(\widetilde{\boldsymbol{V}}_{\boldsymbol{a}}^{est})$. The mean errors between the components of the estimated $\widetilde{\boldsymbol{V}}_{\boldsymbol{a}}^{est}$ and "true" $\widetilde{\boldsymbol{V}}_{\boldsymbol{a}}$ were calculated. The procedure was implemented in MATLAB, and it was repeated for numerous randomly generated $\boldsymbol{F_a}$. As shown in Figure 3.4, the result demonstrated that the error of the estimated left stretch tensor was negligible, and the optimization algorithm worked well for the inverse computation.

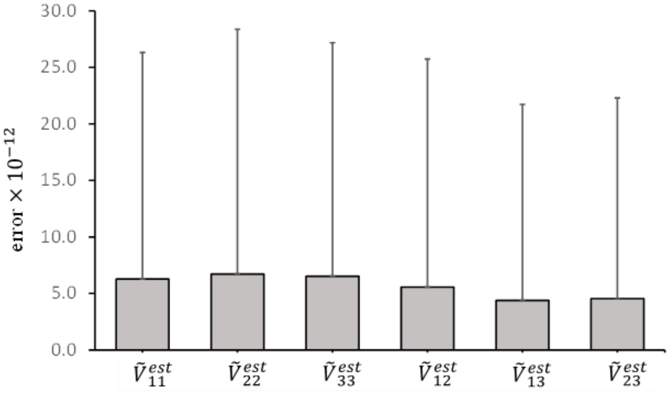

Figure 3.4 - Validation of the inverse computation of left stretch tensor $\widetilde{\boldsymbol{V}}_{\boldsymbol{a}}$ using the constitutive parameters of patient ATAA2 $(\boldsymbol{C_{10}}, \boldsymbol{k_1}, \boldsymbol{k_2}, \boldsymbol{\kappa}, \boldsymbol{\theta}) = (\mathbf{29.91}, \mathbf{512.56}, \mathbf{0.00}, \mathbf{0.3190}, \mathbf{90.00})$. The error is calculated by comparing the estimated $\widetilde{V}_{\boldsymbol{a}}^{est}$ with "true" $\widetilde{V}_{\boldsymbol{a}}$, the error bars represent the standard deviations.

3.3.2 Constitutive Parameters Identification

We applied the method to estimate the material parameters of the four patients (ATAA1, ATAA2, ATAA3, and ATAA4). To evaluate the estimation results, in MATLAB, we simulated biaxial tensile stretches of 3 protocols using the estimated parameters and the "true" parameters, and the stresses and stretches in the circumferential and axial directions were compared. σ_1 and λ_1 denote the circumferential stress and stretch.

σ_2 and λ_2 denote the axial stress and stretch. For each patient, we obtained σ_1 and σ_2 using the following 3 protocols: (1) in the circumferential strip biaxial tension, we fixed $\lambda_2 = 1$ while increasing λ_1; (2) in the equi-biaxial tension, we kept the ratio $\lambda_1/\lambda_2 = 1$; (3) in the axial strip biaxial tension, we fixed $\lambda_1 = 1$ while increasing λ_2.

During the optimization process, the parameters were converged in iterations from the initial values toward the optimal values. An example from patient ATAA2 is shown in Figure 3.5. The optimization started from a set of initial parameters representing a very stiff material, and gradually the stretch-stress curves converged and approached to the "true" curve.

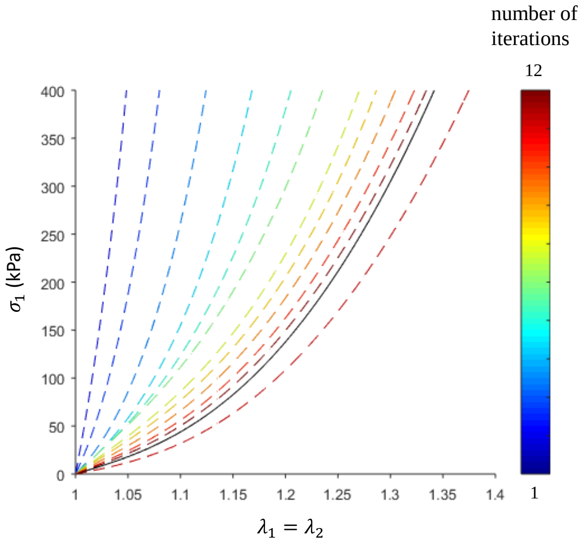

Figure 3.5 - Convergence of the optimization for ATAA2. The solid black line is the "true" curve, and the dashed curves correspond to the estimated parameters in each iteration. Stress in the circumferential direction is plotted.

After running the parameter estimation procedure for each patient, the estimated material parameters were compared with the "true" parameters, and the result is shown in Table 3.2, which demonstrated that the estimated parameters have good agreement with the "true" values, except θ. To evaluate how the difference between the estimated and the "true" parameters affects stress and stretch, we plotted the stretch-stress curves from numerical experiments in Figure 3.6. The coefficient of determination was calculated to measure the discrepancy between the estimated and "true" curves for each patient, as shown in Table 3.3. The mean and standard deviation of the systolic stresses are shown in Figure 3.7. Close agreements can be clearly seen. In addition, it was observed that the stress in the circumferential direction was largest in all cases and approximately twice the axial stress; the stress across the thickness and the shear stress were relatively small.

Table 3.2 - "True" and estimated constitutive parameters of the four patients.

Patient		$C_{10}\ (kPa)$	$k_1 (kPa)$	k_2	κ	$\theta(°)$
ATAA1	"True"	22.91	3622.72	0.00	0.3216	0.00
	Estimated	10.57	3001.25	1.12	0.3079	35.60
ATAA2	"True"	29.91	512.56	0.00	0.3190	90.00
	Estimated	33.52	512.32	0.01	0.3160	86.82
ATAA3	"True"	28.82	222.76	4.37	0.2935	0.00
	Estimated	24.23	196.47	3.67	0.2933	22.79
ATAA4	"True"	25.41	285.19	11.19	0.3284	0.00
	Estimated	28.42	287.96	12.15	0.3260	40.37

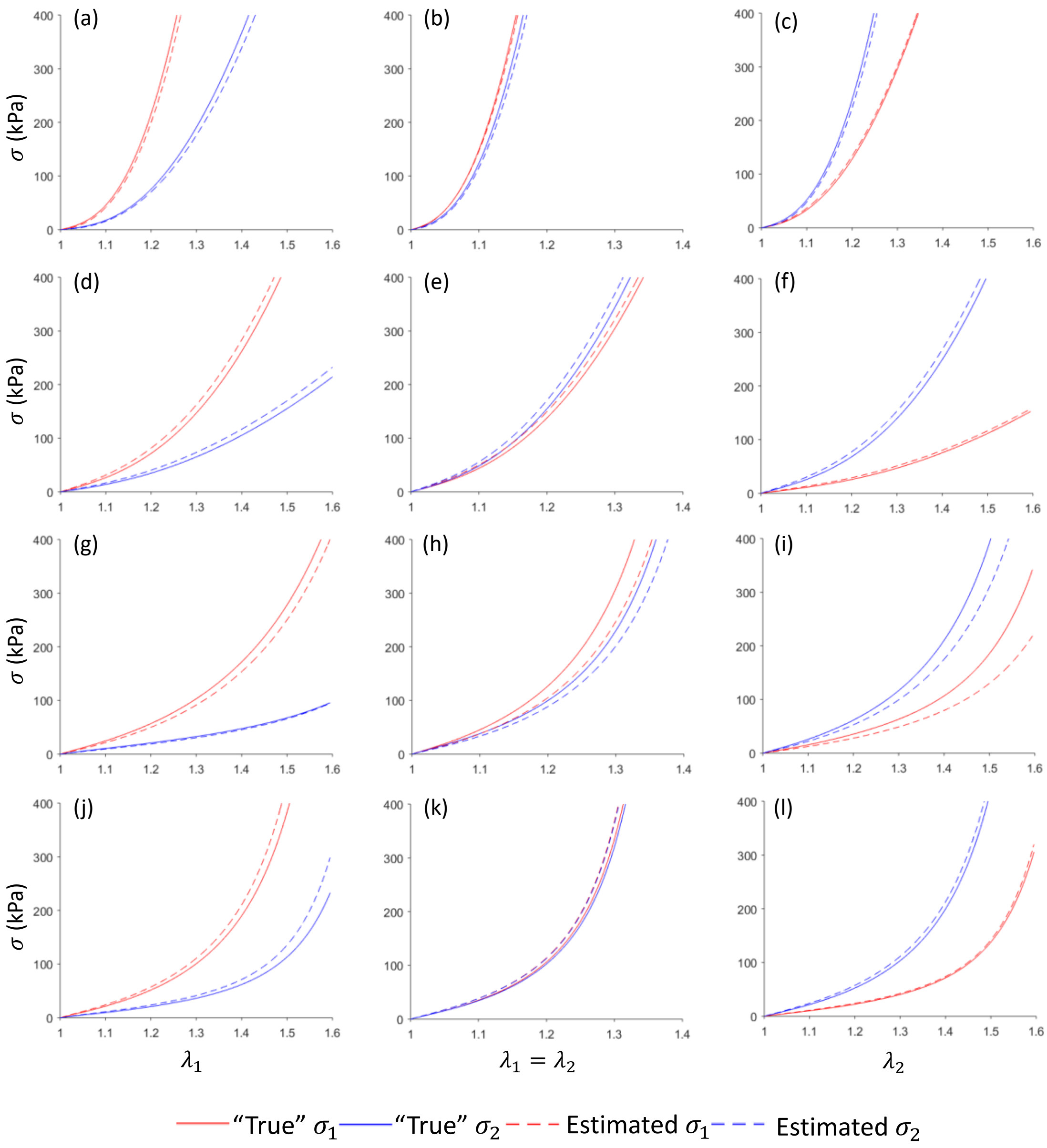

Figure 3.6 - Stretch-stress curves in 3-protocol numerical stretch-controlled tensile experiments for (1) strip biaxial tension in the circumferential direction (a), (d), (g) and (j); (2) equi-biaxial tension (b), (e), (h) and (k); (3) strip biaxial tension in the axial direction (c) (f) (i) and (l). The comparison of "true" and estimated curves for one patient is in the same row, i.e., (a)(b)(c) for ATAA1, (d)(e)(f) for ATAA2, (g)(h)(i) for ATAA3, (j), (k)(l) for ATAA4.

Table 3.3 - Coefficient of determination in the stretch-stress curves for the four patients.

Patient	R^2 in protocol 1		R^2 in protocol 2		R^2 in protocol 3	
	σ_1	σ_2	σ_1	σ_2	σ_1	σ_2
ATAA1	0.987	0.987	0.998	0.988	0.998	0.990
ATAA2	0.981	0.973	0.989	0.981	0.992	0.985
ATAA3	0.974	0.995	0.908	0.959	0.781	0.920
ATAA4	0.968	0.891	0.983	0.967	0.997	0.989

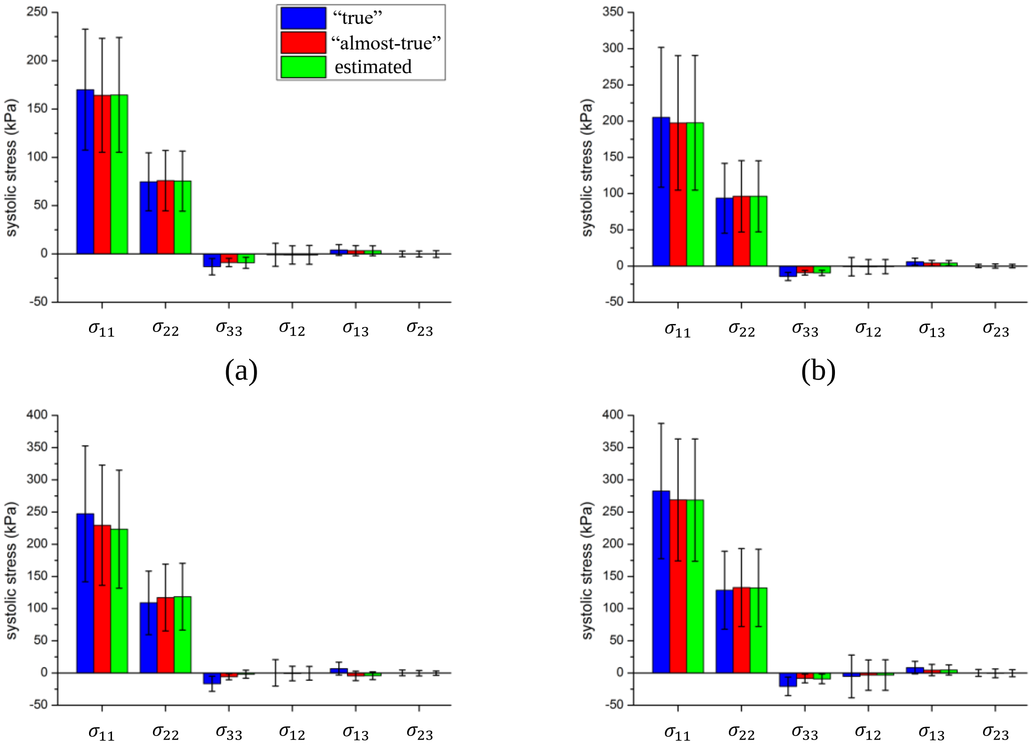

(c) (d)

Figure 3.7 - Comparison of "true", "almost-true" (i.e. computed from the forward penalty approach), and estimated systolic stress from optimization for patient (a) ATAA1, (b) ATAA2, (c) ATAA3 and (d) ATAA4. The error bars represent the standard deviation.

The parameter estimation program was run on a desktop computer with quad-core CPU and 32 GB RAM. Table 3.4 shows the computing time cost for each patient. All of the computations were done within 2 hours, much faster than other methods reported in the literature [99, 100].

Table 3.4 - Time spent for the parameter estimation for each patient.

	ATAA1	ATAA2	ATAA3	ATAA4
Time cost(min)	56	104	117	84

3.4 Experimental Validation

3.4.1 Image Data and Corresponding Tissue Specimens

With Institutional Review Board (IRB) approvals, aortic tissue specimens from two patients (Patient 1: a 67 year-old male; Patient 2: a 68 year-old female) ATAA who underwent surgical repair was obtained from the Emory University Hospital, Atlanta, GA. The 10-phase preoperative ECG-gated CT data and systolic and diastolic blood pressure levels were obtained prior to the intervention. A complete waiver of HIPAA authorization and informed consent was granted by the Emory IRB. All data was collected retrospectively and de-identified and all methods were performed in accordance with the relevant guidelines and regulations. The CT images had a scan matrix size of 256×256, in-plane pixel size of 0.75mm×0.75mm and slice thickness of 1mm. Unfortunately, only part of ATAA of Patient 1 was imaged from the multiphase CT data. For each patient, the systolic and diastolic aorta geometries (Figure 3.8, depicted in red) were reconstructed following our established protocol [171]. Wall thickness of the aorta can be obtained from high resolution CT images according to Shang *et al* [163]. The thickness values were measured at 16 locations (Figure 3.9) from cross-sectional planes of the ATAA segment (Figure 3.8 and Figure 3.9, depicted in yellow) in the systolic phase. For each patient, surgically-excised aneurysmal tissue were dissected into 2~3 square-shaped specimens (2 specimens for Patient 1 and 3 specimens for Patient 2) for biaxial tensile tests. For one square-shaped specimen, the wall thickness values were measured at 3 equally-spaced locations along the diagonal line.

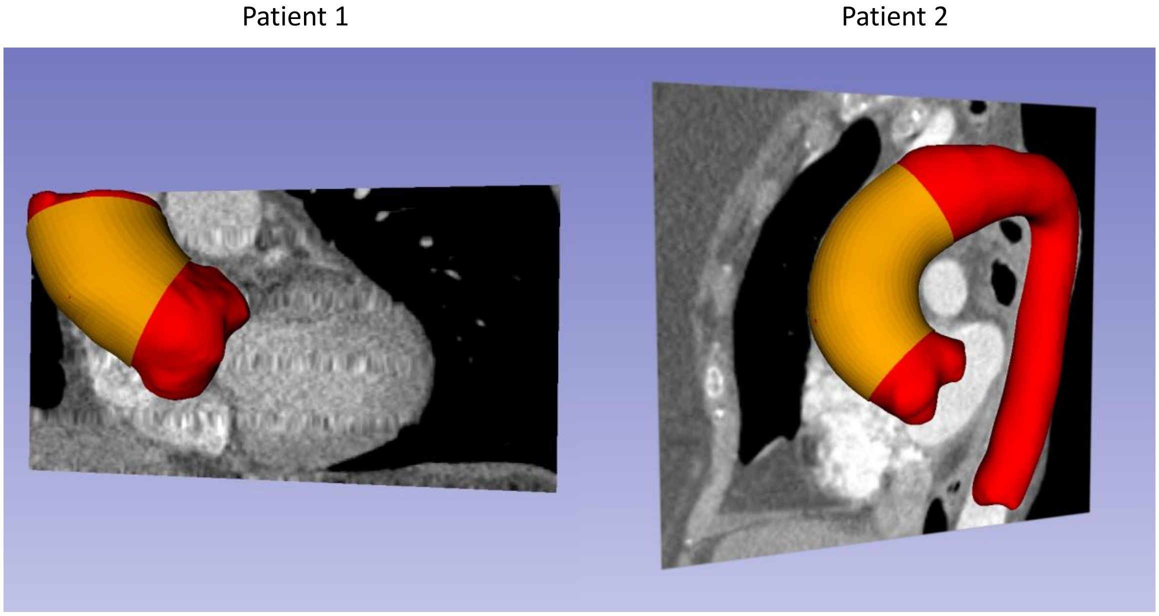

Figure 3.8 - CT image segmentation of the aorta (red) and ATAA segment (yellow) for the two patients.

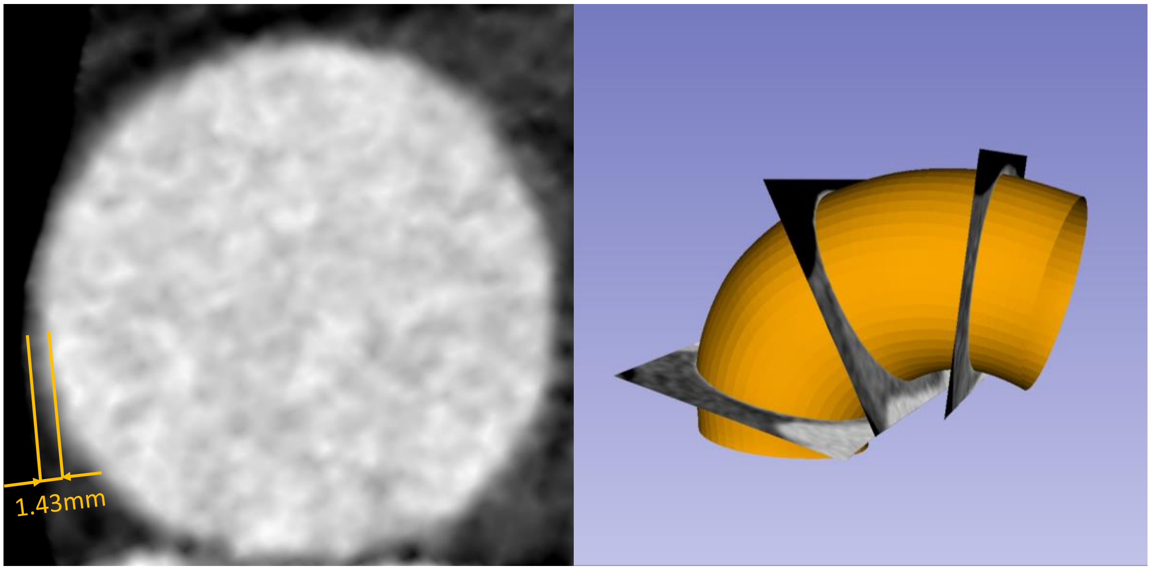

Figure 3.9 - Measuring wall thickness from CT scans.

After image segmentation, each aorta geometry was represented by a triangular mesh. For each patient, since the diastolic aorta geometry Ω_{dia} and systolic aorta geometry Ω_{sys} have different numbers of nodes and elements, the displacement field from diastole to systole cannot be directly calculated. To obtain the displacement field, mesh correspondence between diastolic and systolic phases needs to be established. Herein, non-rigid ICP registration [172] and TPS fitting [173] algorithms were applied to find a nonlinear coordinate transform T from the template geometry Ω_{dia} to the target geometry Ω_{sys}, such that the distance between Ω_{sys} and the transformed template geometry $T(\Omega_{dia})$ is minimized (Figure 3.10 (A)(B)). Please refer to Amberg *et al [172]* for details of the registration method. The geometries of ATAA segment at diastolic phase were remeshed with quadrilateral elements (Figure 3.8, yellow) using our previous remeshing algorithm [140]. Using the transform T, the quad ATAA meshes were transformed onto the surface of the ATAA segment at systolic phase (Figure 3.10 (C)). Thus, we obtained diastolic and systolic quad meshes of the ATAA with mesh correspondence.

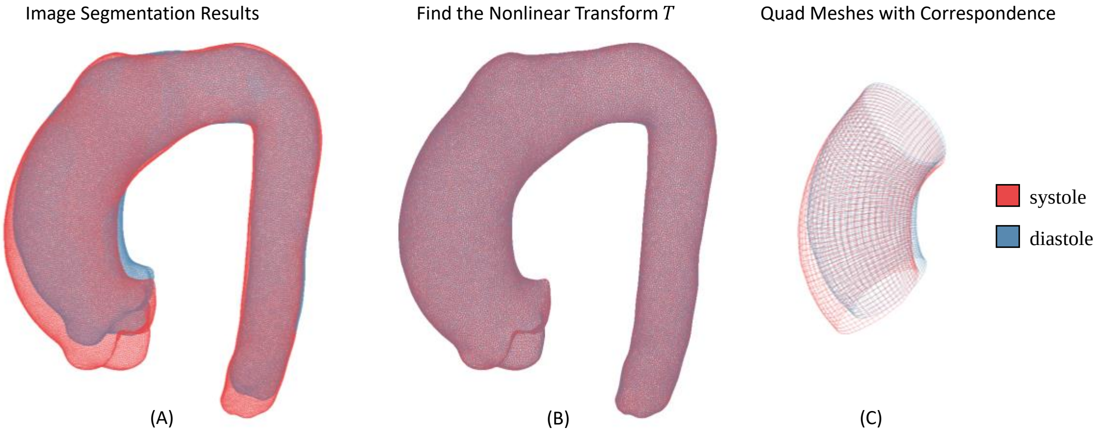
Image Segmentation Results
Find the Nonlinear Transform T
Quad Meshes with Correspondence
🟥 systole
🟦 diastole
(A)
(B)
(C)

Figure 3.10 - Surface registration and transform to establish mesh correspondence. (A) Diastolic geometry Ω_{dia} and systolic geometry Ω_{sys} from image segmentation. (B) A nonlinear transform T from diastolic to systolic phase was obtained using non-rigid ICP registration [172] and thin-plate spline (TPS) fitting [173] algorithms, and therefore the distance between Ω_{sys} and the transformed geometry $\mathrm{T}(\Omega_{\text{dia}})$ is minimized. (C) Diastolic and systolic quad meshes of the ATAA with mesh correspondence.

We assume that the aortic wall is quasi-static at diastole and systole, respectively. Using the CT-derived geometries and corresponding blood pressure levels, the inverse method based on static determinacy (Section 3.2) was applied to identify *in vivo* material parameters.

3.4.2 Biaxial Testing Protocols

Stress-controlled biaxial tensile tests were performed on corresponding surgically-resected tissue samples of the two patients. Frozen tissue samples were submerged in a 37 °C water bath until totally defrosted, following the two-stage slow thawing method to remove the cryopreserving agent [174]. The samples were trimmed into 2~3 square-shaped specimens (2 specimens for Patient 1 and 3 specimens for Patient 2) with a side length of 20~25 mm. Each specimen was subjected to biaxial tension with the circumferential (θ) and longitudinal (z) directions aligned with the primary axes of the biaxial test fixture. A stress-controlled biaxial testing protocol was used [15, 25]. $\boldsymbol{N}$ denotes the nominal stress, and the ratio $N_\theta\colon N_z$ was kept constant. Each tissue specimen was preconditioned for at least 40 continuous cycles with $N_\theta\colon N_z = 1\colon 1$ to minimize tissue hysteresis. Seven successive protocols were performed using ratios $N_\theta\colon N_z = 0.75\colon 1, 0.5\colon 1, 0.3\colon 1, 1\colon 1, 1\colon 0.75, 1\colon 0.5, 1\colon 0.3$. The GOH model parameters for each specimen were obtained by fitting the biaxial stretch-stress response in MATLAB. To obtain material parameters that approximately represent an average response, the stretch-stress data for all specimens from the same patient was fitted simultaneously.

3.4.3 Wall Thickness and Blood Pressures

Table 3.5 - Measured wall thickness (mean ± standard deviation) from CT scans and surgically-resected tissue.

Patient	Source	Wall thickness (mm)
1	*ex vivo*	2.29 ± 0.08
	in vivo	1.57 ± 0.60
2	*ex vivo*	1.95 ± 0.40
	in vivo	1.61 ± 0.37

Table 3.6 - Diastolic and systolic blood pressure for the two patients.

Patient	Phase	Blood pressure (mmHg)
1	diastole	95
	systole	149
2	diastole	80
	systole	156

The wall thickness values from *in vivo* and *ex vivo* measurements are shown in Table 3.5. Diastolic and systolic blood pressures for the two patients are reported in Table

3.6. The blood pressure levels were measured at the time of the patients' visits for CT scans.

3.4.4 In Vivo-Identified and Ex Vivo-Fitted Material Properties

The inverse approach can be completed in about 1 hour with less than 100 FE iterations using a quad-core CPU with 32GB memory. The *in vivo*-identified and *ex vivo*-fitted material parameters are shown in Table 3.7. The coefficient of determination (R^2) values between the *ex vivo*-experimental and *ex vivo*-fitted stress/strain data are also reported in Table 3.7.

Table 3.7 - In vivo-identified and ex vivo-fitted material parameters for the two patients.

Patient	Source	$C_{10}\ (kPa)$	$k_1 (kPa)$	k_2	κ	$\theta(°)$	R^2
1	*ex vivo* all	18.74	100.85	16.67	0.2800	0.00	0.95
	ex vivo 1	19.80	75.40	18.59	0.2809	0.00	0.95
	ex vivo 2	17.44	132.87	13.42	0.2812	0.00	0.96
	in vivo	3.73	429.37	2.81	0.3208	50.54	
2	*ex vivo* all	21.73	669.69	4.97	0.3200	34.28	0.58
	ex vivo 1	16.33	8.05	5.14	0.0000	0.00	0.93
	ex vivo 2	12.78	167.39	0.00	0.3035	90.00	0.96
	ex vivo 3	39.10	1157.64	0.00	0.3199	0.00	0.98
	in vivo	3.49	913.99	1.20	0.2680	77.09	

A more informative way for comparing material properties obtained from the inverse method and experiments, is to plot the stress-stretch curves computed from material parameters. We use σ_θ and λ_θ to denote the circumferential stress and stretch, σ_z and λ_z to denote the longitudinal stress and stretch. Thus, stress-stretch curves are plotted using the *in vivo*-identified *and ex vivo*-fitted material parameters with three λ_θ: λ_z ratios, namely three protocols: (1) in the circumferential strip biaxial protocol, fixing $\lambda_{\mathrm{z}} = 1$ while increasing λ_{θ}; (2) in the equi-biaxial protocol, keeping the ratio $\lambda_{\theta} : \lambda_{\mathrm{z}} = 1 : 1$; (3) in the longitudinal strip biaxial protocol, fixing $\lambda_{\theta} = 1$ while increasing λ_{z}. The stress-stretch curves determined by the estimated parameters were compared with the stress-stretch curves derived from biaxial data. As plotted in Figure 3.11, the two specimens of Patient 1 demonstrate almost identical stretch-stress response, whereas the three tissue specimens of Patient 2 show different stress-stretch responses, which indicate that the material properties are heterogeneously distributed. MAPE is computed to measure the goodness-of-fit between *in vivo*-identified and *ex vivo*-fitted average curve (*ex vivo*-all). For both patients, the average response shows relatively good agreements with the identified stretch-stress curves.

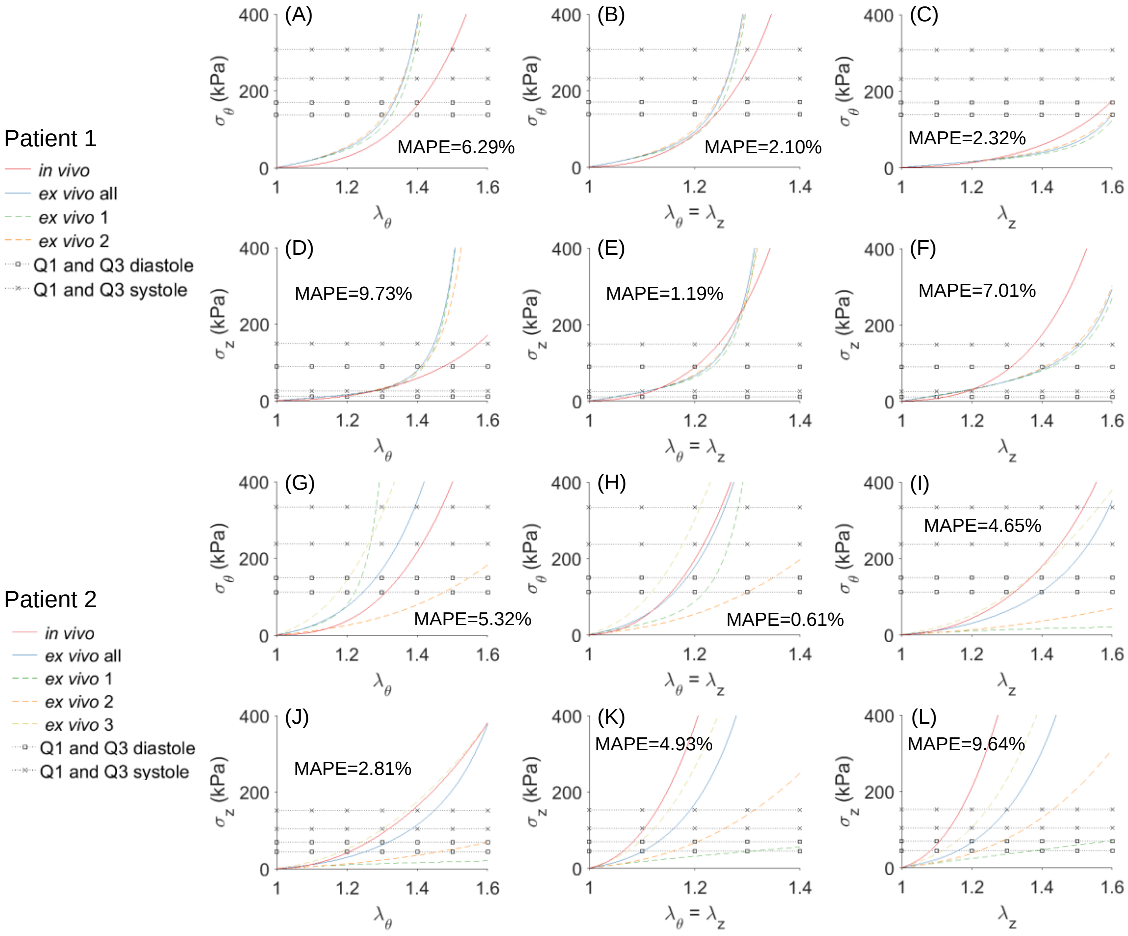

Figure 3.11 - Stress-stretch curves determined from the in vivo-identified material parameters and ex vivo-fitted material parameters for Patient 1 ((A)~(F)) and Patient 2 ((G)~(L)). Left column: strip-biaxial protocol in the circumferential direction; middle column: equi-biaxial protocol; right column: strip-biaxial protocol in the longitudinal direction. First and third rows: circumferential stress, second and fourth rows: longitudinal stress. The average response is indicated by 'ex vivo all'. Q1 and Q3 denote the 25% and 75% interquartile of in vivo stress range.

3.5 Discussion

In this study, we presented a novel inverse method that can estimate the *in vivo* material properties of the aortic wall in a fast and accurate manner. The method utilized the fact that the static determinacy can be used to estimate the *in vivo* stress distributions of the loaded aortic wall, provided the *in vivo* geometry and loading conditions of the aortic wall are known. We built an objective function (Eqn. (3.1)) directly from the constitutive equations to iteratively search for the optimal material parameters. The accuracy of the method was numerically validated by using four ATAA patient data. The constitutive parameters and the aortic wall material responses have been successfully recovered. Despite the discrepancy in numerical values of the constitutive parameters, the inverse method and experiments achieved relatively good agreement in the biaxial stress-stretch curves.

3.5.1 Computational Cost

This approach is much less computationally expensive (1-2 hours) than the iterative FE simulation based approach [99, 100] (1-2 weeks), because It avoids solving finite element problems iteratively. We defined the objective f_{err} and g_{err} in terms of stress, and the analytical expression of the Jacobian (i.e. derivative of the objective function with respect to constitutive parameters) exists, which means the Jacobian can be well approximated by finite difference. This probably helps the optimization to converge in a relatively small number of iterations, e.g., 12 iterations for patient ATAA2.

In general, the constitutive parameter optimization problem is nonlinear, multivariate and non-convex; and such a problem may exhibit several local optima. Jacobian-based optimization methods (e.g. the method used in this approach) may not guarantee a global optimum as shown by the difference in parameters in Table 3.2. However, using the sub-optimal parameters, we obtained very good material responses and wall stress distributions compared to the “true” values, and therefore the sub-optimal parameters are indeed acceptable. Optimization using many initial guesses may improve the results, but it will lead to a much longer computing time.

3.5.2 Discrepancies in Material Properties

In the numerical validations, the largest error can be observed in the constitutive parameter θ, describing the local fiber mean direction, which is possibly caused by the fact that the parameter κ derived from biaxial experiment is close to $1/3$ (isotropic), and therefore θ does not affect the stress computation. The difference between the “true” stress field computed from nonlinear finite deformation FE and the “almost-true” stress field computed from the forward penalty approach is clearly visible in Figure 2.3 and Figure 3.7. This discrepancy probably came from the boundary effects [135]. The restricted boundary nodes limited the axial deformation of the aorta model. Although the “almost-true” stress alone can be used in many applications, such as using the stress-based rupture potential index as an aneurysm rupture risk predictor [149], different tissue damage and failure models exist such as accumulated energy [175, 176], stretch based criterion [31] and distensibility [177] which rely on the deformation and thus depend on patient-specific material properties. Previous works in our group [57] showed that the failure pressure of ascending aortic aneurysm was much higher than the measured systolic pressure, and the failure behavior of the aorta were highly correlated with material properties. Thus, patient-specific material properties enable the analysis of the wall stress at various loading and deformation conditions that cannot be recorded by *in vivo* imaging.

The discrepancies between the *in vivo* identified and *ex vivo* fitted material parameter could be attributed to the following sources. (1) The stretch ratios are different under experimental and physiological (diastolic and systolic) conditions, which indicates that the biaxial experimental data can only partially capture the physiological conditions. A constitutive model that can characterize the biaxial experimental data well may have to extrapolate its predication under some physiological conditions. (2) The aorta may undergoes rhythmic active contraction *in vivo* during the cardiac cycle [178]. However, active contractions generated by the smooth muscle cells are not considered by the constitutive model in this study. The surgically-resected tissues may only demonstrate passive *ex vivo* behavior. This could be a source of discrepancy between the *in vivo* and *ex vivo* properties. (3) The blood pressure levels were measured at the time of the patients' visits for CT scans. Unfortunately, their blood pressures were not obtained simultaneously with the ECG-gated CT scans. (4) The external supports from pulmonary arteries and vena cava could alter the stress distribution within the aorta. Since the supporting forces are unknown, it could be a source of discrepancy between the *ex vivo* and *in vivo* properties. Note that there is no rigid (or high stiffness) structure (e.g. rib cage) that contacts the aorta, it is likely that the external supports from the pulmonary arteries/vena cava would not have significant impact on the loading bearing of the aorta. (5) In the FE simulations, the boundary nodes were only allowed to move in the radial directions. (6) Heart motions could induce unknown axial forces/stresses in the aorta. However, using the current displacement boundary condition, the reaction forces at the proximal and distal ends required for the static equilibrium were calculated by the FEA. Because of different pressure loading conditions, the boundary forces are different for diastole and systole. Therefore, the axial stresses are also different at diastolic and systolic phases and are dependent on the patient-specific geometry and blood pressure levels.

3.5.3 Mesh Correspondence

The diastolic-to-systolic displacement field, which establishes mesh correspondence between diastolic and systolic phases, is often required by the material parameter identification schemes such as the virtual field method [82] and the stress-matching [79] or strain-matching method [99, 100]. This requirement can be satisfied in *ex vivo* experiments by tracking physical markers or tracking speckle patterns in ultrasound images [159]. CT is routinely used for imaging ascending aorta because of its large field of view [179]. However, CT images do not have distinct image texture patterns for tracking individual points on the aortic wall, and therefore the absence of diastolic-to-systolic displacement field poses a critical challenge for material parameter identification using CT data. In this study, mesh correspondence was established using the non-rigid ICP registration [172] and TPS fitting [173] algorithms. Thus, the mesh correspondence can support different identification schemes ([100] and APPENDIX A) and material properties can be estimated from the gated CT data.

The developed inverse method could be applicable to other clinical images with motion tracking. Motion tracking using ultrasound images (known as speckle tracking) has been applied for left-ventricle (LV) motion analysis and strain measurement. The 2D+t (2-dimension plus time) speckle tracking was validated using a rabbit heart model and a simulated heart which shows an average strain error of 0.08% [180]. Automatic algorithms [159, 181-185] for 3D+t LV segmentation and tracking using ultrasound images have been developed over the last eight years. As for ultrasound speckle tracking of vessel wall, Larsson, *et al.* [186] performed validation experiments, in which crystal markers were implanted on the artery wall in order to obtain the "ground truth" strain measurement. 3D+t ultrasound speckle tracking has been applied to study aortic wall strain of healthy and abdominal aortic aneurysms patients *in vivo* by Karatolios, *et al.* [187]. By using this method to obtain *in vivo* strain measurement, Wittek *et al.* [99, 100] developed the FE updating approach for *in vivo* material parameter estimation. For clinical applications, fully automatic segmentation and speckle tracking algorithms for the aortic wall are needed, which can be developed based on the algorithms for LV segmentation and tracking.

Because ECG-gated CT are not routinely performed for ATAA, we only acquired the multiphase CT data and tissue samples of two patients. In addition, only part of ATAA of Patient 1 was imaged from the multiphase CT data, so the identification is restricted on a small segment for Patient 1 (Figure 3.8). Hence, the current inverse approach needs more validation cases before clinical application.

3.5.4 Limitations

In this study, the constitutive parameter identification was based on the following two main assumptions. (1) It is known that the aortic tissue properties are heterogeneously distributed [21, 147], material properties of the inner curvature region may be different from those of the outer curvature region. The wall thickness may also has spatial variation across the ATAA, heterogeneity of wall thickness and material heterogeneity could be correlated [188]. In the current inverse method, we only considered a simplified case, where the averaged *in vivo* wall thickness was used, and the averaged hyperleastic behavior of the aorta segment was identified. The stress-stretch data in this study (Figure 3.11) also suggests material heterogeneity. The approach can be extended to heterogeneous thickness and constitutive parameters by slightly altering the workflow, i.e., evaluating one objective function g_{err} for one element or one group of elements at a time. (2) We assume that residual stresses have minimal impact on the material parameter identification, since a study [189] suggested that the inclusion of residual stress in the model has little effect on estimated material properties. CHAPTER 2 also demonstrated that the transmural mean stress is independent of the residual stress.

3.6 Summary

We proposed a fast and effective method for constitutive parameter estimation of the aortic wall by using the *in vivo* loaded geometries at 2 cardiac phases with known blood pressures. For each patient, the method only needs to run infinitesimal linear elastic FE simulations (the forward penalty approach) twice to obtain the stress fields at the 2 cardiac phases, and the rest of the computation can be run in MATLAB. The inverse computation is mainly dependent on solving nonlinear constitutive equations and optimization algorithms. Good agreement has been achieved between the estimated and “true” material parameters in the numerical verification. The novel inverse approach was applied to pre-operative gated CT scans of two ATAA patients. For comparison, surgically-resected tissue samples were obtained for experimental planar biaxial tests. Relatively close match was achieved in terms of the *in vivo*-identified and *ex vivo*-fitted stress-stretch response. Our results are preliminary but encouraging. It is hoped that further development of this approach can enable an accurate identification of the *in vivo* material properties from gated CT data, which currently is a critical challenge in the field of cardiovascular biomechanics.

CHAPTER 4. MACHINE LEARNING APPROACH FOR FAST IN VIVO HYPERELASTIC PROPERTIES IDENTIFICATION

Patient-specific biomechanical analysis of the aorta requires quantification of the *in vivo* mechanical properties of individual patients. Current inverse approaches have attempted to estimate the nonlinear, anisotropic material parameters from *in vivo* image data using certain optimization schemes. In CHAPTER 3, we also developed an optimization-based inverse method in which the computationally-expensive FE simulations were avoided by building the objective function upon stresses, and the computation time was greatly reduced. However, since optimization-based inverse methods are inherently limited by their iterative nature, any further improvement of computational speed can be difficult. A potential paradigm-changing solution to the bottleneck associated with patient-specific computational modeling is to incorporate machine learning (ML) algorithms to expedite the procedure of *in vivo* material parameter identification. In this chapter, we developed an ML-based approach to estimate the material parameters from three-dimensional aorta geometries obtained at two different blood pressure (i.e., systolic and diastolic) levels. Statistical shape model (SSM) was built by using ATAA geometries of 25 patients to describe the aorta shape probability distribution. The nonlinear relationship between the two loaded shapes and the constitutive parameters are established by an ML-model, which was trained and tested using FE simulation datasets generated from the SSM model. Cross-validations were used to adjust the ML-model structure on a training/validation dataset. The accuracy of the ML-model was examined using a testing dataset. Results of this chapter have been published in [140, 190].

4.1 Background

With advances in medical imaging modalities and computation power, numerical simulations of the cardiovascular structure such as the aorta, which utilizes the patient-specific three-dimensional (3D) geometry, have been increasingly pursued in the past decade [123]. Yet, the difficulty in obtaining *in vivo* patient-specific elastic properties of the aortic wall from clinical cardiac images has been one of the biggest obstacles in patient-specific biomechanical analysis. This has motivated recent efforts to develop inverse methods for estimating the *in vivo* material properties of the aortic wall on a patient-specific basis. In these methods, deformations and boundary conditions are used to inversely estimate the material parameters of a particular constitutive model. However, the complex 3D shapes and nonlinear and anisotropic constitutive behavior make this task challenging.

To fully exploit the 3D geometries reconstructed from medical image data, previous methods for *in vivo* material parameter estimation largely rely on various optimization schemes. In these optimization-based inverse methods, an objective/error function is built upon the difference between predicted and image-derived physical fields (e.g. coordinates of diastolic geometry and diastolic-to-systolic strain field), and then the constitutive parameters are iteratively adjusted until the objective function is minimized. Specifically, starting from an initial guess of the constitutive parameters, the inverse methods usually involve the following steps: (1) recovering an unloaded state from a known loaded state (e.g. systole); (2) predicting the desired physical field of another loaded state (e.g. diastole) through computational analysis, which is referred by numerically-predicted physical field; and (3) the constitutive parameters are iteratively fine-tuned by a nonlinear optimization algorithm until the numerically-predicted physical field matches with the image-derived physical field at the loaded state (e.g. diastole). This optimization process yields the optimal constitutive parameters. Using FE updating schemes, Wittek et al. [99, 100] developed two methods to determine GOH material parameters of the human abdominal aorta from *in vivo* 4D ultrasound data [157] based on stochastic-deterministic optimization. However, numerous iterations were required to find the optimal solution with a long computation time of 1~2 weeks. The high computational cost could inhibit a practical application of these methods, particularly in a clinical setting requiring fast feedback to clinicians. To this end, we have recently proposed two optimization-based methods to expedite the estimation process. The multi-resolution direct search (MRDS) approach (APPENDIX A) was designed to improve the searching algorithm, and the computation time was reduced to 1~2 days with similar CPU and memory. Due to static determinacy, given loading and boundary conditions as well as geometry, stress can also be directly computed from clinical images (CHAPTER 2). Therefore, we developed a stress-based inverse approach (CHAPTER 3), in which the computationally-expensive FE simulations were avoided by building the objective function upon stresses, and the optimization was completed in approximately 2 hours. However, optimization-based inverse methods are inherently limited by their iterative nature, and any further improvement of computational speed can be difficult.

Recently, machine learning (ML) techniques, particularly deep learning (DL) [102, 191, 192], have garnered enormous attention in the field of artificial intelligence, leading to revolutionary breakthroughs in many applications [102-109]. ML-models are capable of establishing complex and nonlinear relationship between inputs and outputs. A potential paradigm-changing solution to the bottlenecks associated with patient-specific computational modeling is to incorporate ML algorithms to expedite the procedure of *in vivo* material parameter identification. By designing and training an ML-model on a large dataset, it may automatically produce the required outputs (constitutive parameters) directly from necessary inputs (multi-phase aorta shapes), without the need for costly iterative schemes. Thus, once trained, the ML-model can instantaneously predict the material parameters.

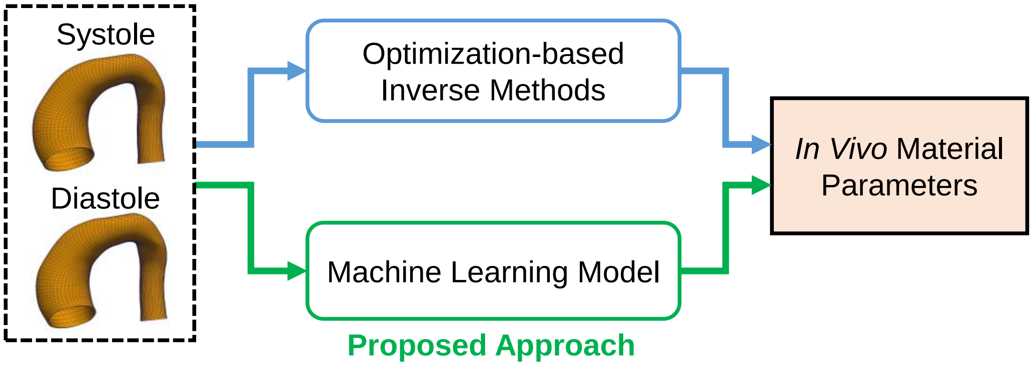
Systole
Diastole
Optimization-based Inverse Methods
Machine Learning Model
Proposed Approach
In Vivo Material Parameters

Figure 4.1 - The proposed machine learning (ML) approach.

In this chapter, we developed an ML-based approach to identify the material parameters of the GOH constitutive model. As depicted in Figure 4.1, the inputs to this ML-model are the aorta geometries at two distinct blood pressure levels, namely the systolic and diastolic geometries, which were also used by our previous optimization-based inverse approaches (CHAPTER 3 and APPENDIX A). Statistical shape model (SSM) was built by using ATAA geometries of 25 patients to describe the aorta shape probability distribution. An ML-model was built to establish the nonlinear relationship between the geometries and the constitutive parameters. The proposed ML-model consists of an unsupervised shape encoding module using principal component analysis and a supervised nonlinear mapping module using a neural network. The datasets for training, validation and testing were generated from FE simulations by sampling SSM parameter space and material parameter space. Cross-validations were used to adjust the neural network structure. The accuracy of the ML-model prediction was examined using a testing dataset.

4.2 Statistical Shape Modeling of the Aorta

4.2.1 Image Data

De-identified clinical cardiac CT scans and resected ATAA tissues were obtained for a total of 25 patients who underwent elective ATAA repair at Yale-New Haven Hospital between the years of 2008 and 2010 [57]. Institutional Review Board approval to review de-identified images was obtained for this study. All patients underwent cardiac CT scans because of suspected ATAA prior to elective repair. The resolution of the images is 0.7x0.7x2.5 mm, and the field of view covers the thoracic and abdominal aorta. The ATAA tissue elastic and failure properties for the same patients were characterized from surgically resected tissues in a previous study [63].

As shown in Figure 4.2, for each patient, the 3D surface of the aorta was semi-automatically reconstructed from the clinical CT image data using Avizo software (Burlington, MA). The surfaces were then trimmed at the ascending aorta just distal to the sinotubular junction on the proximal end and at the descending aorta on the distal end. The branch vessels at the arch were removed. The resulting surfaces were meshed to obtain a total of 25 aorta shapes in the form of triangle meshes with an arbitrary number of nodes and elements.

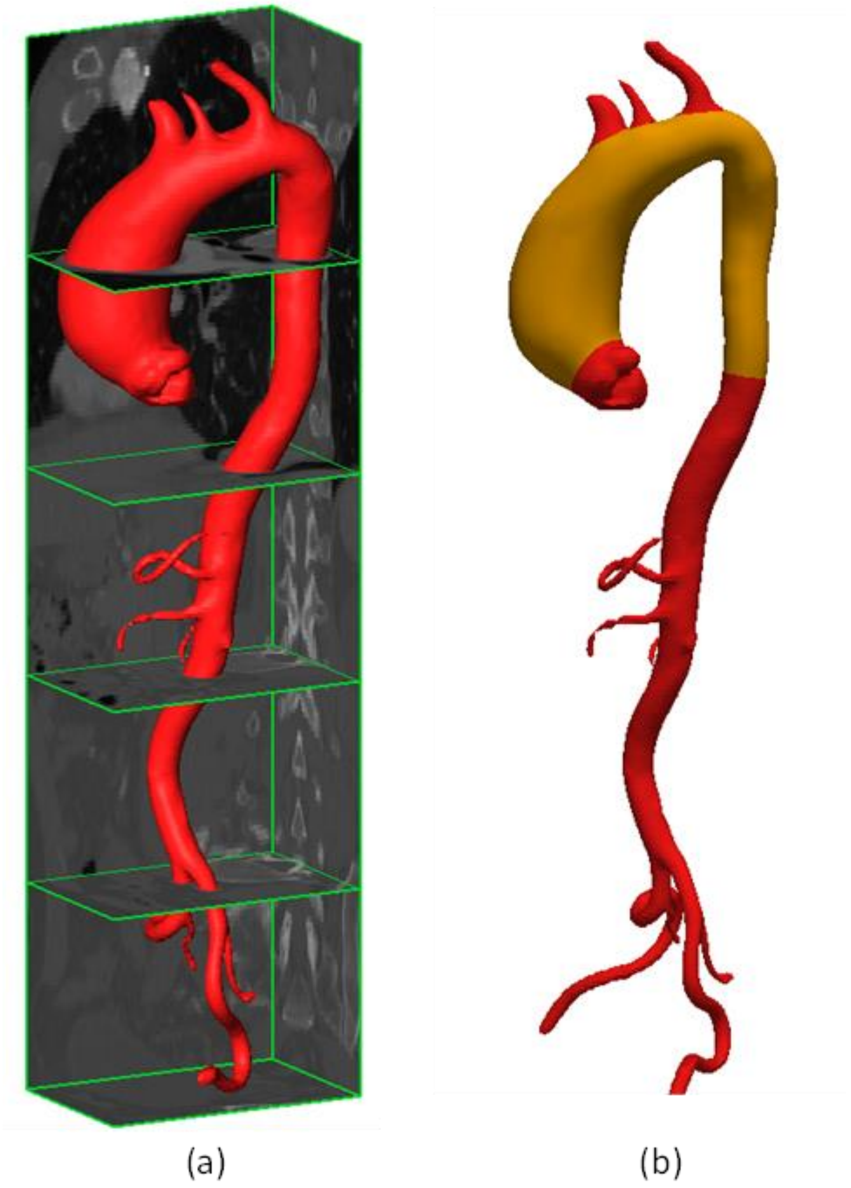
(a)

(b)

Figure 4.2 - (a) The aorta segmented from a 3D CT image. (b) Trimmed aorta surface in gold color.

4.2.2 Aorta Surface Remeshing and Shape Alignment

To establish mesh correspondence between different patients and facilitate SSM and FE analyses, a remeshing method was developed in order to convert the triangle meshes to quad meshes with the same number of nodes and the same nodal connectivity among the elements for all patients. Briefly, given a 3D triangle surface mesh as the input, a minimum-stretch based mesh parameterization was performed, resulting in a 2D triangle mesh in a rectangular shape of a predefined size. The 2D region was then discretized as a 2D quad mesh with 5100 nodes and 4950 elements. By using barycentric interpolation [193] determined by the 3D surface mesh and the 2D triangle mesh, the 2D quad mesh was transformed into the 3D space and the nodes on the top and bottom of the rectangular mesh were merged together to yield a 3D tubular surface mesh with 5000 nodes and 4950 elements.

After remeshing, each shape was aligned to a common coordinate system by Generalized Procrustes Analysis (GPA) [194]. Here, a shape $X^{(k)}$, indexed by $k,$ is a quad surface mesh which can be represented by a vector $X^{(k)} = [\boldsymbol{x}_1^{(k)}, \dots \boldsymbol{x}_n^{(k)}, \dots \boldsymbol{x}_N^{(k)}]$ assembled from the coordinates of each point $\boldsymbol{x}_n^{(k)}$ of the mesh with a total number of N points (i.e. nodes). The alignment process runs in an iterative manner: 1) transform each shape $X^{(k)}$ to the mean shape $\bar{X}$ by the similarity transform, where initially one of the training shapes is randomly chosen as the mean shape; 2) compute the mean shape from all the transformed shapes. Further details on the remeshing algorithms and shape alignment methods are provided in [140].

4.2.3 Statistical Shape Model Construction

Given the aligned shapes $\left\{X^{(1)}, \dots, X^{(k)}, \dots, X^{(K)}\right\}$ $(K = 25)$, a SSM was built by principal component analysis (PCA) [195, 196]. PCA can decompose the shapes into a mean shape and a set of linearly uncorrelated shape variations which are the principal components, also called the modes of shape variations. Standard PCA starts from assembling the covariance matrix $\boldsymbol{C}$, given by

$$\boldsymbol{C} = \frac{1}{K}\sum_{k=1}^{K}\left(\boldsymbol{X}^{(k)} - \overline{\boldsymbol{X}}\right)\left(\boldsymbol{X}^{(k)} - \overline{\boldsymbol{X}}\right)' \tag{4.1}$$

where superscript k represents patient index and K is the total number of patients. In our case, $K = 25$. $\overline{\boldsymbol{X}} = \frac{1}{K}\sum_{k=1}^{K}\boldsymbol{X}^{(k)}$ is the mean shape. Then, the eigenvalues and eigenvectors of the covariance matrix can be calculated via singular value decomposition. For this application, the number of points on each shape, $N = 5000$, is much larger than K and the rank of the matrix $\boldsymbol{C}$ is K. Singular value decomposition was applied to obtain a subset of the eigenvalues and eigenvectors, and the other eigenvalues are all zeros. The SSM was constructed with the mean shape $\overline{X}$ and the modes of shape variation $\left\{V^{(1)}, \ldots, V^{(K)}\right\}$ and the corresponding eigenvalues $\left\{\mu^{(1)}, \ldots, \mu^{(K)}\right\}$ which were sorted from largest to smallest.

4.2.4 Shape Decomposition and Shape Sampling

By using the SSM, a shape $\boldsymbol{X}$ can be decomposed into (i.e., approximated by) the mean shape plus a linear combination of the modes (i.e., shape variation), given by

$$\boldsymbol{X} \approx \overline{\boldsymbol{X}} + \sum_{i=1}^{m} C_i\sqrt{\mu_i}\boldsymbol{V}_i \tag{4.2}$$

where $\boldsymbol{V}_i$ and μ_i are the eigenvectors (i.e. modes of shape variations) and eigenvalues of the covariance matrix, respectively. m is the number of modes used for approximation. Here, the shape $\boldsymbol{X}$ has been aligned to the mean shape $\overline{\boldsymbol{X}}$.

A shape Y can be sampled from the shape distribution, Eqn. (4.2), using a set of SSM parameters $(C_1, \dots, C_m, \dots, C_M)$. A large number of sampled shapes can represent the shape distribution and are more versatile than the original 25 shapes used in the SSM construction. In order to obtain a set of representative shapes, the selected modes must be able to explain a large percentage of the total shape variation, defined by

$$\frac{Explained\ Variation}{Total\ Variation} = \frac{\sum_{m=1}^{M} \lambda^{(m)}}{\sum_{k=1}^{K} \lambda^{(k)}} \tag{4.3}$$

To build the SSM, the first three modes were selected ($m = 3$) which explains 80.1% of the total shape variation. The SSM parameters were standardized by their standard deviations, for example, $(C_1, C_2, C_3) = (0,0,0)$ represents the mean shape and $(C_1, C_2, C_3) = (2,0,0)$ represents a shape that is 2 standard deviations away from the mean shape along the first mode of variation. by using 2 standard deviations, the shapes are, in general, significantly differ from each other. Some representative systolic aorta shapes are plotted in Figure 4.3. The shapes are color-coded with curvature values obtained from Paraview 5.0.0.

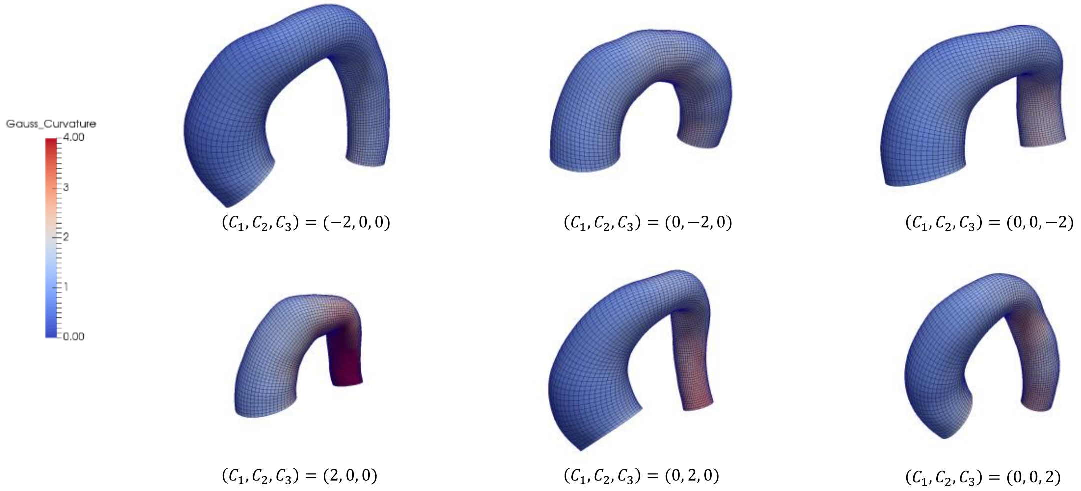

$(C_1, C_2, C_3) = (-2, 0, 0)$ $(C_1, C_2, C_3) = (0, -2, 0)$ $(C_1, C_2, C_3) = (0, 0, -2)$

$(C_1, C_2, C_3) = (2, 0, 0)$ $(C_1, C_2, C_3) = (0, 2, 0)$ $(C_1, C_2, C_3) = (0, 0, 2)$

Figure 4.3 - Systolic aorta shapes corresponding to some representative sets of SSM parameters. The shapes are color-coded with curvature values.

4.3 The ML-Based Inverse Method

4.3.1 Constitutive Model

The fiber reinforced hyperelastic model based on the work by Gasser *et al.* (Eqn. (2.10)) [34] was used to model the constitutive response of aortic wall tissue. In this chapter, the material incompressibility parameter D is fixed to be 5×10^{-4} in the subsequent sections to generate training validation and testing datasets. The task for the ML-model is to identify the five constitute parameters $(C_{10}, k_1, k_2, \kappa, \theta)$ given the two-phase aorta shapes.

4.3.2 Generating the Training/Validation Dataset and the Testing Dataset

The proposed ML model will establish a mapping between the inputs (geometries) to the outputs (material parameters) based on example input-output pairs. Each input-output pair consists of two geometries and the corresponding material parameters. To finetune the ML-model for optimal performance, cross-validation is used in the training phase, where the input-output pairs are partitioned into two subsets, called training set and validation set. The ML-model is trained on the training set, and its performance is assessed using the validation set. After the training phase, the accuracy of the ML-model prediction is evaluated on a new set of input-output pairs, i.e., the testing set.

In this study, the datasets are gathered from FE simulations. Using statistical modeling methods, a large number of material parameter sets are generated from 65 sets of experimentally-derived material parameters, and virtual aorta geometries at one physiological phase (i.e., systole) are generated from the SSM in Section 4.2.4. The diastolic aorta geometries are determined from FE simulations using the virtual systolic geometries and the generated material parameters. Finally, the training/validation dataset and the testing dataset consist of 15366 and 225 input-output pairs, respectively. The detailed procedures to generate the datasets are presented in the following paragraphs.

In previous studies [15, 63], we have collected resected ATAA tissue samples of 65 patients who underwent elective surgeries at Yale-New Haven Hospital, CT, USA between the years of 2008 and 2010, following an IRB-approved protocol. Seven-protocol biaxial tension experiments were carried out on the 65 aneurysmal patients, and five material parameters of the GOH model were determined by fitting the experimentally-obtained stress-strain curves. The material properties of patient i was represented by a vector in $\boldsymbol{y}^{(i)}$ $(i = 1, 2, \ldots, 65)$, with its five components corresponding to five GOH parameters, and the set $\boldsymbol{Y}$ contains the 65 vectors. These vectors are visualized in the material parameter space in Figure 4.4, which shows that these experimentally-derived parameters are highly clustered in certain regions. To uniformly sample the material parameter space, a convex hull of the experimentally-derived parameters was built. The convex hull is essentially a set comprised of convex combinations of all vectors in $\boldsymbol{Y}$,

$$Conv(\boldsymbol{Y}) = \left\{ \boldsymbol{y} = \sum_{i=1}^{65} a_i \boldsymbol{y}^{(i)} \mid \boldsymbol{y}^{(i)} \in \boldsymbol{Y}, i = 1, 2, \ldots, 65, a_i \geq 0 \forall i, \sum_{i=1}^{65} a_i = 1 \right\} \tag{4.4}$$

where $\boldsymbol{y}$ is a vector in the convex hull, and a_i $(i = 1, 2, \ldots, 65)$ are non-negative coefficients that sum up to 1. Next, samples were draw from a uniform distribution inside the convex hull using the Gibbs sampler [197]. 125 and 15 samples were generated for the training/validation set and the testing set, respectively, as shown in Figure 4.4.

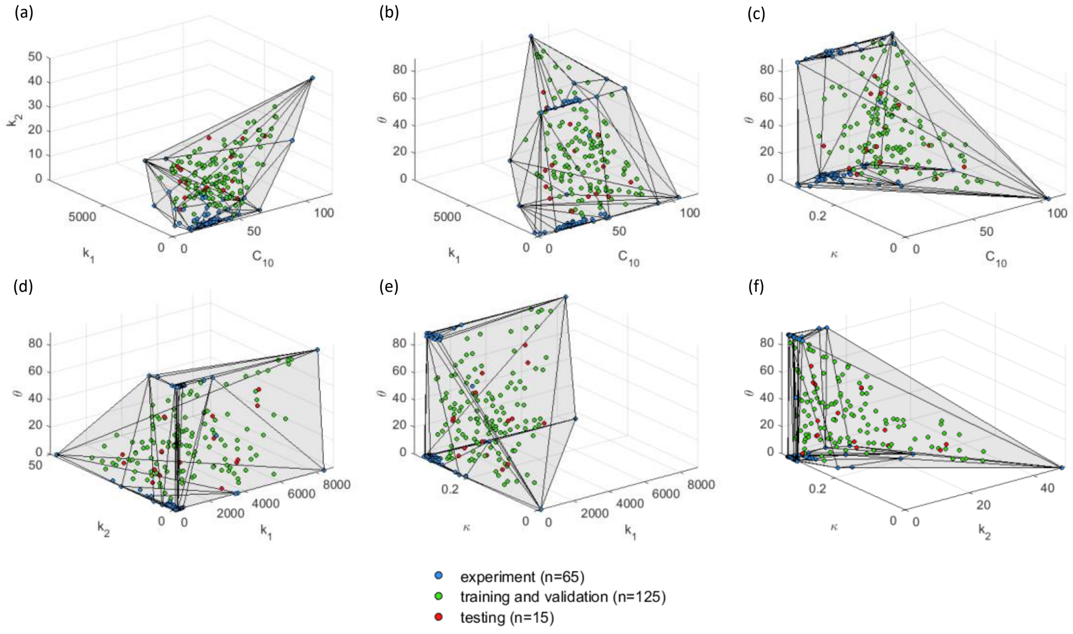

Figure 4.4 - Datasets projected in 3D material parameter subspaces. The convex hull is plotted in the 3D subspaces for illustrative purpose.]

The SSM was built from the 25 real aorta shapes at the systolic phase in Section 4.2.3. The SSM model describes the probability distribution of aorta shapes among the patient population using 3 modes of variations. As a result, a systolic geometry can be represented by a set of SSM parameters (C_1, C_2, C_3) described in detail in Section 4.2.4.

For the training and validation datasets, a total number of 125 virtual aorta shapes at systolic phase were obtained by sampling the SSM parameter space (C_1, C_2, C_3) with equally spaced points in the range of -2 to 2 , i.e., within 2 standard deviations of the mean shape, as shown in Figure 4.5. Similarly, for the testing dataset, the SSM parameter space was sampled within 1.5 standard deviations of the mean shape. Hence, 15 systolic shapes were obtained for the testing dataset. The resulting samples in the SSM parameter space are plotted in Figure 4.5.

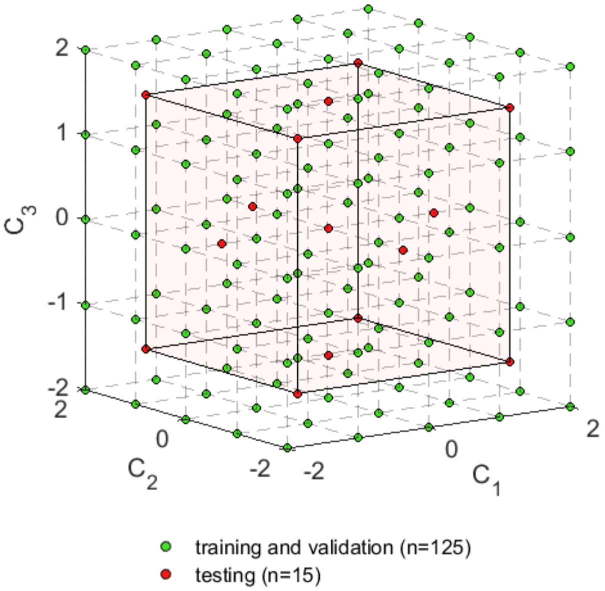

Figure 4.5 - Sampling the SSM parameter spaces.

The virtual aorta geometries obtained from the SSM parameter space were at the systolic phase, which should be in equilibrium with the systolic physiological load.

Therefore, the generalized pre-stressing algorithm (GPA, described in Section 2.3.3) [145] was utilized to incorporate the pre-stress induced by the systolic pressure (16 kPa). In the GPA algorithm, the resulted equilibrium configuration may slightly deviate from the original configuration, depending on the step size [145]. The systolic geometries at the equilibrium configurations were used by the ML-model in the subsequent sections. Next, using a set of material parameters, the virtual aorta geometries at the diastolic phase were determined by depressurizing the systolic geometries to the diastolic phase (10 kPa).

For the training and validation sets, given one of the 125 shapes at the systolic phase and one of the 125 sets of material parameters, the virtual aorta geometry at the diastolic phase was determined through FE simulation. As shown in Figure 4.6, if a FE simulation converges, the input-output pair (systolic and diastolic geometries and a set of material parameters) is collected for training/validation. A total of 15,625 cases (125 materials ×125 shapes) were simulated, out of them, 259 cases were not able to converge. The convergence issues might be due to extreme shapes and/or material properties. As a result, 15366 sets of geometries with known material parameters were obtained. Similarly, for the testing set, 225 input-output pairs were generated from 15 systolic geometries and 15 sets of material parameters (all converged).

The GPA algorithm was implemented in ABAQUS user subroutine UMAT. In the FE simulations, C3D8H solid elements were used, a uniform wall thickness at the systolic phase (1.5 mm) was assumed based on the average value from [140], and pressure was applied uniformly to the inner surface of the aorta models. For the FE models, the longitudinal direction (zz) was defined using the center line of the aorta geometry. Then, the outward normal direction (rr) of each element in the inner surface of the aortic wall was obtained. The circumferential direction ($\theta\theta$) was defined by taking cross product of the longitudinal and outward normal directions. The boundary nodes of the aorta models, i.e. the proximal and distal ends of the model, were only allowed to move in the radial direction defined by the local coordinate system.

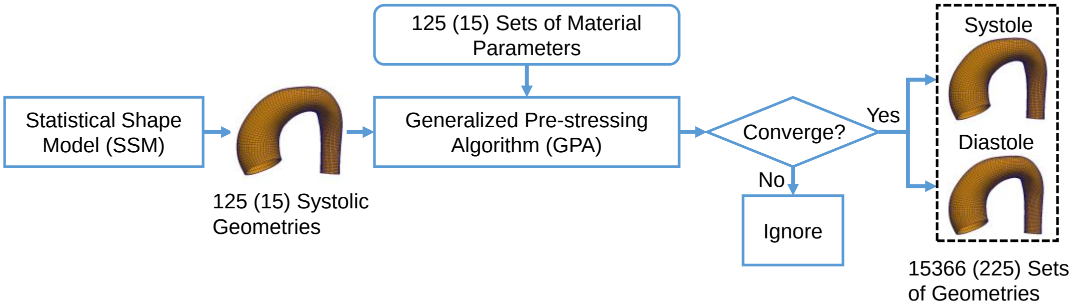
125 (15) Sets of Material Parameters
Statistical Shape Model (SSM)
Generalized Pre-stressing Algorithm (GPA)
Converge?
Yes
No
Ignore
125 (15) Systolic Geometries
Systole
Diastole
15366 (225) Sets of Geometries

Figure 4.6 - The procedure to generate aorta geometries at systole and diastole. The number in the parenthesis indicates the testing dataset.

4.3.3 The Machine Learning Model

The machine learning model consists of an unsupervised shape encoding module and a nonlinear mapping module. The systolic and diastolic shapes are encoded by shape codes. The nonlinear mapping between the shape codes and the material parameters is established by a neural network.

3D geometries are usually represented by FE meshes with a large number of nodes and elements. A shape corresponds to a long vector $\boldsymbol{X}$ of nodal coordinates. However, directly linking the shape $\boldsymbol{X}$ to the material parameters by a neural network, although possible, can lead to a large number of undetermined parameters that require a very large training dataset. A compact representation (i.e. shape code) of a shape can be obtained in a shape encoding procedure. PCA [198] is widely adopted as a shape encoding method and an unsupervised learning technique for dimensionality reduction, in which the original data can be well approximated by a linear combination of a few principal components. Using PCA, the covariance matrix $\boldsymbol{C}$, eigenvalues μ_i and eigenvectors $\boldsymbol{V}_i$ of the training shapes can be obtained using Eqn. (4.1) and Eqn. (4.2). Note that shape encoding module cannot be replaced by the SSM. Here, the systolic and diastolic shapes in the training and validation dataset were encoded by using two shape encoding modules. As mentioned in Section 4.3.2, the systolic geometries from GPA were slightly different from the original configuration from the SSM, and therefore 3 modes, as used in Section 4.2.4, are not enough to capture the shape variations for systolic geometries. For systolic and diastolic geometries, the shape code ($c_i, i = 1, \dots, m$) can be obtained by

$$c_i = \boldsymbol{V}_i^T(\boldsymbol{X} - \overline{\boldsymbol{X}})/\sqrt{\mu_i} \tag{4.5}$$

where $\boldsymbol{V}_i^T$ is the transpose of the column vector $\boldsymbol{V}_i$. The first 12 modes (m=12) were retained for both the systolic and diastolic shape encoding, with the average PCA approximation error being less than 0.1%. We denote the systolic shape code as α_i, diastolic shape code as β_i, $i = 1, 2, \dots, 12$.

The nonlinear mapping module will map the shape codes of the two input shapes to the five material parameters, which is equivalent to establishing five nonlinear functions

$$y_k = g_k(\alpha_1, \dots, \alpha_{12}, \beta_1, \dots, \beta_{12}), k = 1, 2, \dots, 5 \tag{4.6}$$

The inputs are the shape codes α_i and $\beta_i, i = 1, 2, \ldots, 12$, for diastolic and systolic geometries, respectively. The outputs are y_k $(k = 1, 2, \ldots, 5)$, correspond to the five material parameters $(C_{10}, k_1, k_2, \kappa, \theta)$.

Neural network is, in general, flexible and can be used as universal function approximation. As shown in Figure 4.7, a neural network is constructed as the nonlinear mapping module. It consists of feedforward fully-connected units (neurons). Each unit has multiple inputs and a single output. For the jth unit of the ith layer, a linear combination of the input vector $\boldsymbol{z}^i$, with weight vector $\boldsymbol{w}_j^i$ and offset b_j^i, is computed as

$$u_j^i = \boldsymbol{w}_j^{i^T} \boldsymbol{z}^i + b_j^i \tag{4.7}$$

where the superscript i denote the index of layer, and subscript j denote the index of unit in the layer. $\boldsymbol{z}^i$ is a column vector of $\left[z_1^i, z_2^i, \ldots, z_{n_i}^i\right]^T$, and n_i is the number of units in the ith layer. The weighted sum u_j^i is nonlinearly transformed into the output z_j^{i+1} using an activation function.

$$z_j^{i+1} = f(u_j^i) \tag{4.8}$$

The softplus [199] activation function was used, which is given by

$$f(u) = \log(1 + exp(u)) \tag{4.9}$$

This function is a smooth version of the rectified linear unit (ReLU) [200, 201]. As demonstrated in the discussion section, other activation functions can lead to large testing errors in our application. The neural network has two hidden layers with the same number of softplus units, and the output layer has 5 softplus units.

The neural network was implemented using Tensorflow [202]. The inputs and outputs were normalized using the maximum absolute value of each dimension. Consequently, the normalized shape codes are within the range of -1 to 1, and the normalized material parameters are within the range of 0 to 1. The mean squared error (MSE) was used as the loss function

$$MSE = \sum_{k=1}^{5} \frac{1}{N} \sum_{l=1}^{N} \left(\bar{y}_k^{(l)} - \hat{\bar{y}}_k^{(l)} \right)^2 \tag{4.10}$$

where l is the index for an input-output pair, N is the total number of input-output pairs, $\bar{y}_k^{(l)}$ and $\hat{\bar{y}}_k^{(l)}$represent the kth actual and predicted normalized material parameters, respectively. After the nonlinear mapping, the predicted material parameters were rescaled to its original range. The parameters of the neural network were obtained through the Adamax optimization algorithm [203]. For detailed theories, please refer to [204]. The network structure, i.e., number of hidden layers and number of units was determined through cross-validations in Section 4.3.4.

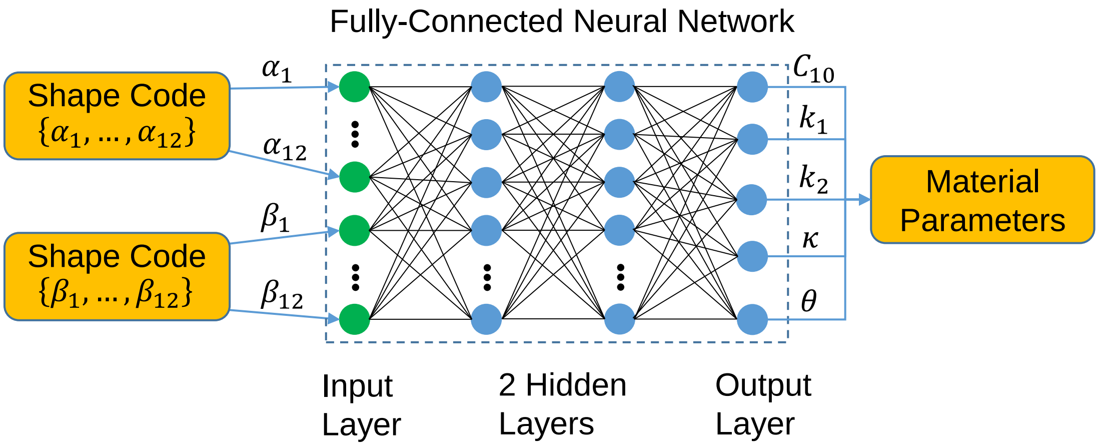
Fully-Connected Neural Network
Shape Code
$\{\alpha_1, \ldots, \alpha_{12}\}$
Shape Code
$\{\beta_1, \ldots, \beta_{12}\}$
α_1
α_{12}
β_1
β_{12}
C_{10}
k_1
k_2
κ
θ
Material Parameters
Input Layer
2 Hidden Layers
Output Layer

Figure 4.7 - The neural network for mapping the shape codes to the material parameters. The green dots represent the input layer, and the blue dots represent the softplus units in the hidden layers and the output layer of the neural network.

4.3.4 Training, Adjusting and Testing the ML-Model

The unsupervised shape encoding module was trained only using the training and validation sets, i.e., the mean shape $\bar{\boldsymbol{X}}$, eigenvectors $\boldsymbol{V}_i$ and eigenvalues μ_i of the covariance were computed only using the training and validation data. Since shapes in the testing set are different from those in the training and validation sets, the testing shape codes were obtained from Eqn. (4.5) using $\bar{\boldsymbol{X}}$, $\boldsymbol{V}_i$ and μ_i computed from the training and validation sets.

Using the training/validation dataset, the performance of the nonlinear mapping module was assessed through leave-one-out (LOO) cross-validation, and the neural network structure was fine-tuned. As depicted in Figure 4.8, in each round of the LOO cross-validation, the data was split into a training set and a validation set, according to the material parameters. We pick one set of material parameters (and its corresponding geometries) from the 125 sets from Section 4.3.2 as the validation set, and train the neural network on the remaining 124 sets (and its corresponding geometries). An averaged error was obtained after repeating this procedure for all the 125 sets of material parameters. Hence, the training set never contains the material information used in the validation. Similarly, ten-fold cross-validation can be performed by splitting the dataset according to sets of material parameters.

The discrepancy between the actual and predicted material parameters was quantified by normalized mean absolute error (NMAE). The absolute error (AE) for the kth material parameter is defined by

$$AE_k^{(l)} = \left| y_k^{(l)} - \hat{y}_k^{(l)} \right| \tag{4.11}$$

where index l and k are the same as Eqn. (4.10), $y_k^{(l)}$ and $\hat{y}_k^{(l)}$ represent the kth actual and predicted material parameter, respectively. The NMAE of the kth material parameter is defined by

$$NMAE_k = \frac{\sum_{l=1}^{N} AE_k^{(l)}}{N\left(\max_l\left(y_k^{(l)}\right) - \min_l\left(y_k^{(l)}\right)\right)} \times 100\% \tag{4.12}$$

where N is defined in Eqn. (4.10). Next, the number of units in each layer was adjusted in the range of 32 to 512 to minimize the averaged NMAE in the LOO and ten-fold cross-validations. Resulting performance for different network structures is summarized in Table 4.1 and Table 4.2. We evaluated neural networks with a single hidden layer (32, 64, 128, 256 number of units), they failed to predict the material parameters with an acceptable accuracy. Thus, network structure with two hidden layers was used. We first kept the number of units in the two hidden layers the same and varied the number of units from 32×32 to 512×512. We found that 256×256 gives the smallest averaged NMAE. Next, we fixed the number of units in a hidden layer and changed the number of units of the other hidden layer. Therefore, we tested 4 additional cases using cross-validations: 128×256, 512×256, 256×128, 256×512. We found that the 256×256 structure offers the smallest averaged NMAE. Therefore, the final network contains 256 units for each of the two hidden layers.

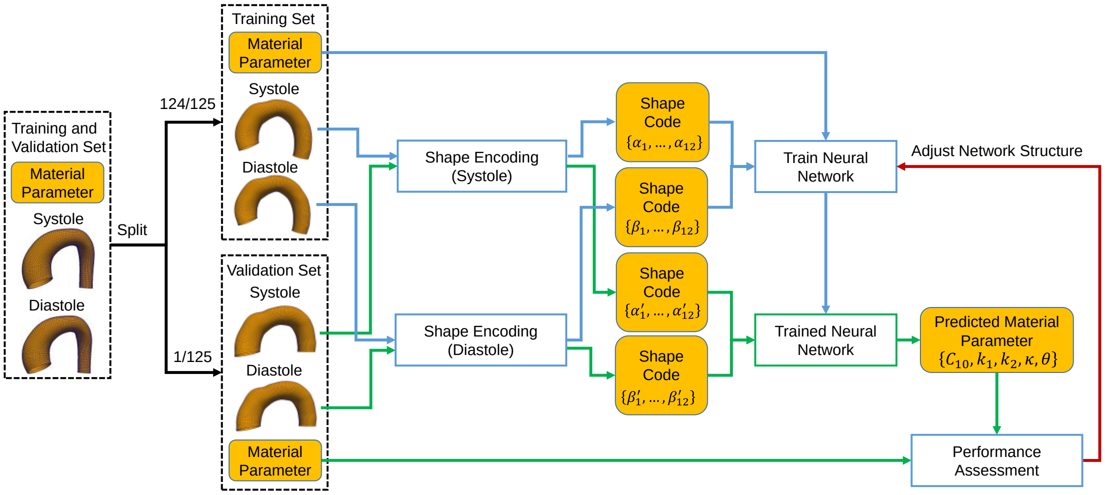
Training and Validation Set
Material Parameter
Systole
Diastole
Split
124/125
1/125
Training Set
Material Parameter
Systole
Diastole
Validation Set
Systole
Diastole
Material Parameter
Shape Encoding (Systole)
Shape Encoding (Diastole)
Shape Code $\{\alpha_1, \ldots, \alpha_{12}\}$
Shape Code $\{\beta_1, \ldots, \beta_{12}\}$
Shape Code $\{\alpha'_1, \ldots, \alpha'_{12}\}$
Shape Code $\{\beta'_1, \ldots, \beta'_{12}\}$
Train Neural Network
Adjust Network Structure
Trained Neural Network
Predicted Material Parameter $\{C_{10}, k_1, k_2, \kappa, \theta\}$
Performance Assessment

Figure 4.8 - Adjusting the network structure using the leave-one-out (LOO) cross-validation.

Table 4.1 - Averaged NMAE (defined in Eqn. (4.12)) of the five material parameters w.r.t. network structure in LOO cross-validation (3,000 epochs).

network structure	C_{10}	k_1	k_2	κ	θ
32	8.47%	4.94%	8.27%	4.92%	9.55%
64	8.08%	4.51%	8.03%	4.36%	9.08%

128	7.90%	4.25%	7.90%	4.12%	8.78%
256	7.99%	4.31%	7.84%	4.12%	8.62%
512	8.00%	4.36%	7.96%	4.23%	8.66%
32×32	8.33%	3.86%	6.84%	4.30%	7.12%
64×64	7.65%	3.41%	6.77%	3.88%	6.96%
128×128	7.58%	3.18%	6.59%	3.60%	6.84%
256×256	6.92%	2.73%	6.35%	3.24%	6.51%
512×512	7.07%	2.81%	6.55%	3.21%	6.81%
128×256	7.60%	3.22%	6.60%	3.58%	7.14%
512×256	7.80%	3.37%	6.68%	3.84%	7.59%
256×128	7.07%	3.10%	6.56%	3.45%	6.70%
256×512	8.72%	8.16%	9.04%	4.30%	10.94%

Table 4.2 - Averaged NMAE (defined in Eqn. (4.12)) of the five material parameters w.r.t. network structure in ten-fold cross-validation (3,000 epochs).

network structure	C_{10}	k_1	k_2	κ	θ
32	8.72%	5.38%	8.57%	5.19%	9.80%
64	8.34%	4.98%	8.24%	4.71%	9.44%
128	8.16%	4.84%	8.13%	4.38%	9.08%
256	8.23%	4.42%	8.16%	4.39%	9.07%
512	8.27%	4.56%	8.21%	4.46%	8.95%
32×32	9.01%	4.25%	7.38%	4.48%	8.32%
64×64	8.04%	3.86%	6.82%	4.04%	7.38%
128×128	7.73%	3.63%	6.75%	3.88%	7.31%
256×256	7.63%	3.14%	6.46%	3.58%	7.43%
512×512	7.24%	3.26%	6.97%	3.53%	7.99%
128×256	7.90%	3.87%	6.92%	3.83%	8.13%
512×256	8.06%	3.45%	6.93%	3.90%	8.08%
256×128	7.76%	3.56%	6.60%	3.92%	7.55%
256×512	8.39%	3.98%	7.06%	4.72%	8.36%

To evaluate the prediction of the ML-model, i.e., to examine how accurate the prediction is compared to FE simulation data, the ML-model was trained on the training/validations set and then the trained ML-model was used to predict the material parameters using shapes in the testing set as the input (Figure 4.9). The predicted material parameters were compared to the actual parameters in the testing set.

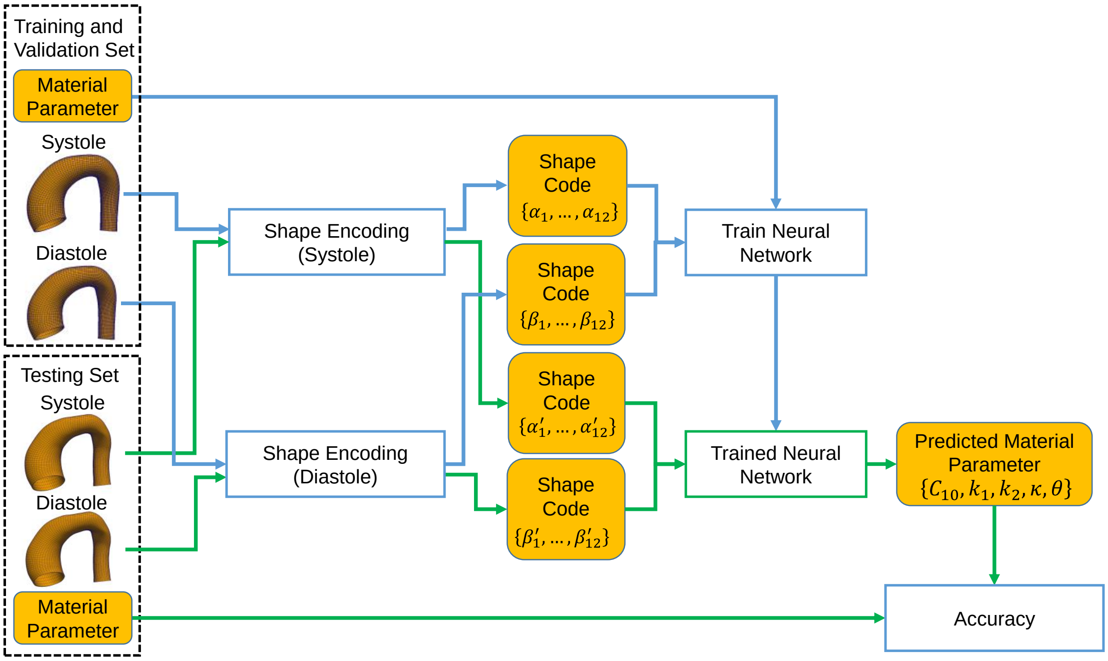
Training and Validation Set
Material Parameter
Systole
Diastole
Testing Set
Systole
Diastole
Material Parameter
Shape Encoding (Systole)
Shape Encoding (Diastole)
Shape Code $\{\alpha_1, \ldots, \alpha_{12}\}$
Shape Code $\{\beta_1, \ldots, \beta_{12}\}$
Shape Code $\{\alpha'_1, \ldots, \alpha'_{12}\}$
Shape Code $\{\beta'_1, \ldots, \beta'_{12}\}$
Train Neural Network
Trained Neural Network
Predicted Material Parameter $\{C_{10}, k_1, k_2, \kappa, \theta\}$
Accuracy

Figure 4.9 - Evaluating the accuracy using the testing dataset.

4.4 Validation and Testing Results

Given a pair of geometries as the inputs, the trained ML-model can output the material parameters within one second on a PC with 3.6GHz quad core CPU and 32GB RAM. The actual versus predicted material parameters in the testing set are shown in Figure 4.10. The ranges of material parameters are resulted from the convex hull in Section 4.3.2, similar ranges of material parameters were reported in the studies [51, 169], which were obtained by fitting the GOH model to uniaxial testing data.

4.4.1 Actual and Predicted Material Parameters

We define the normalized standard deviation of absolute error (NSTAE) of the kth material parameter as

$$NSTAE_k = \frac{1}{\left(\max_l\left(y_k^{(l)}\right) - \min_l\left(y_k^{(l)}\right)\right)} \sqrt{\frac{\sum_{l=1}^{N}\left(AE_k^{(l)} - \overline{AE}_k\right)^2}{N-1}} \times 100\% \qquad (4.13)$$

where $\overline{AE}_k$ is the averaged absolute error for the kth material parameter. The NMAE and NSTAE for each material parameter in the testing set are reported in Table 4.3. The errors indicate that the ML-predicted material parameters are in good agreement with the actual material parameters. The errors might be explained by coupling effect (over-parameterization) of the constitutive model [34], different combinations of material parameters may have similar stress-strain response. This nonlinear coupling has resulted in identification difficulties in the optimization-based inverse approaches ([99, 100], CHAPTER 3, and APPENDIX A).

Table 4.3 - NMAE and NSTAE of the five material parameters in testing set (10,000 epochs).

	C_{10}	k_1	k_2	κ	θ
NMAE	3.75%	1.38%	6.01%	1.88%	3.74%
NSTAE	3.51%	1.59%	4.38%	1.89%	4.56%

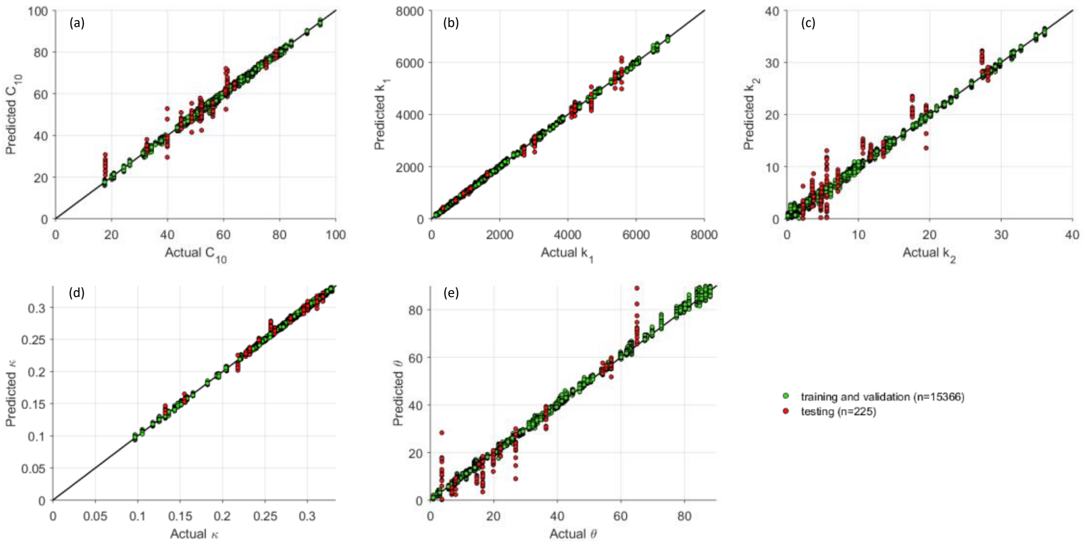

Figure 4.10 - The actual and predicted material parameters. Each point was plotted using its actual value as horizontal x-coordinate and the ML-predicted value as the vertical y-coordinate. A perfect straight line (y=x) indicates perfect prediction, and any deviation from the straight line indicates prediction errors.]

4.4.2 Actual and Predicted Stress-Stretch Curves

To further evaluate the estimation results, stress-stretch curves were plotted by simulating stretch-controlled biaxial tension in MATLAB by assuming the tissue is loaded in the plane stress state and the material is incompressible. We use σ_1 and λ_1 to denote the circumferential stress and stretch, σ_2 and λ_2 to denote the longitudinal stress and stretch. The simulations were based on the following 3 protocols: (1) in the circumferential strip biaxial tension, fixing $\lambda_2 = 1$ while increasing λ_1; (2) in the equi-biaxial tension, keeping the ratio $\lambda_1/\lambda_2 = 1$; (3) in the longitudinal strip biaxial tension, fixing $\lambda_1 = 1$ while increasing λ_2. In total, six stress-stretch curves are generated for each set of constitutive parameters.

Using the testing dataset, the coefficient of determination (R^2) was calculated for each curve, and the averaged coefficient of determination of the six curves for each input-output pair was obtained. The predictions were sorted according to their averaged coefficient of determination. The best, median, worst cases are plotted in Figure 4.11, and the corresponding actual and predicted material parameters are shown in Table 4.4. Nearly matching agreement is achieved for the best cases. For the median case, although the discrepancies in the constitutive parameters seem obvious, the six curves still have close matches. In the worst case, the results are still acceptable in terms of material parameters, and the actual and predicted stress-stretch curves follow the same trends.

Table 4.4 - The actual and predicted material parameters for the best, median, worst cases.

		C_{10} (kPa)	$k_1 (kPa)$	k_2	κ	$\theta(°)$
Best	Actual	63.83	1086.31	28.12	0.1553	7.76
	Predicted	64.66	1091.45	28.08	0.1561	7.55
Median	Actual	48.60	4207.03	4.76	0.2958	16.46
	Predicted	50.59	4325.85	2.20	0.2963	10.16
Worst	Actual	75.15	4683.21	17.53	0.2182	22.05
	Predicted	72.49	4485.17	19.48	0.2096	18.30

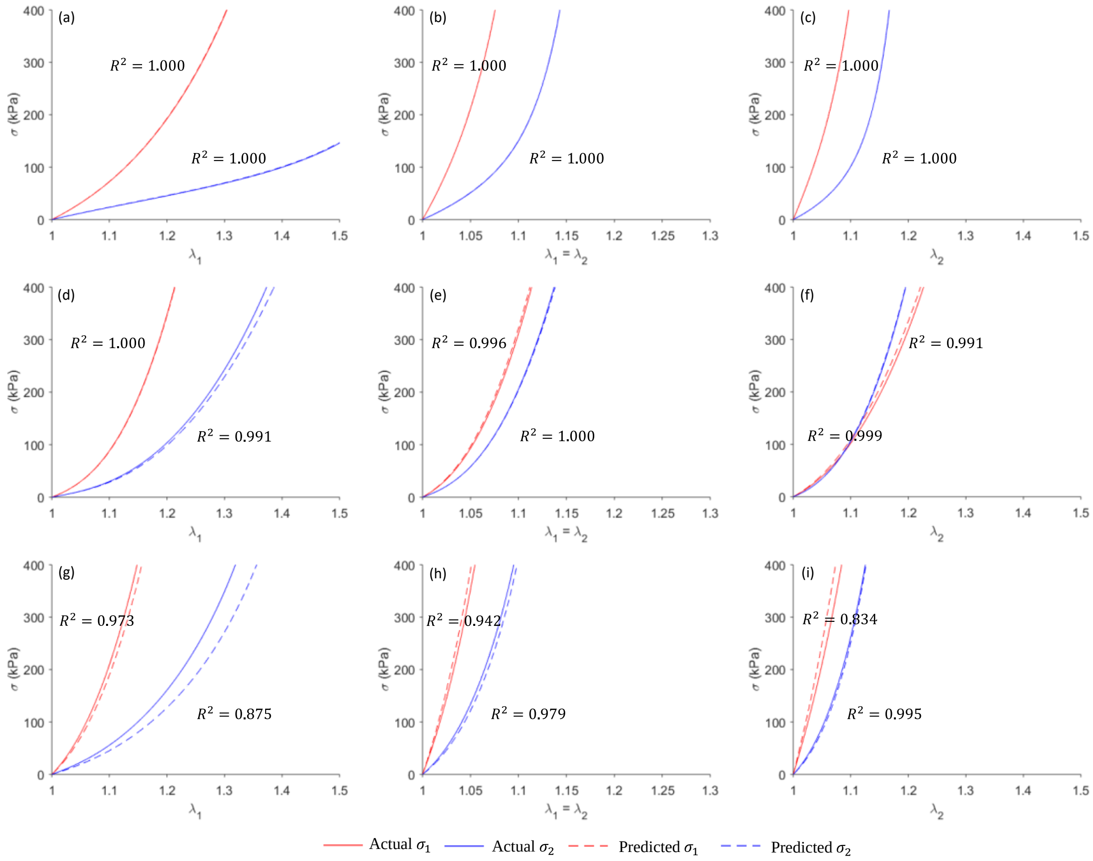

Figure 4.11 - The actual and predicted stress-stretch curves for the best ((a), (b) and (c)), median ((d), (e) and (f)) and worst cases ((g), (h) and (i)).]

4.5 Discussion

Optimization-based inverse methods ([99, 100], CHAPTER 3, and APPENDIX A) have been extensively used for material parameter identification problems. These methods are computationally-expensive. Iterative computations limit the efficiency of these approaches, prohibiting their clinical applications. The proposed ML approach can fundamentally resolve the challenge on computation cost. The ML-model builds a direct linkage between the geometries and the material parameters, bypassing the iterative procedures. Once the ML-model is trained, it can be used to make predictions instantaneously and repeatedly, such that *in vivo* material parameter estimation on any patient in real-time can be possible. Although FE simulations are used to generate training, validation and testing datasets, which takes approximately 10 days in our exemplary application. It should be noted that a similar amount of time is required to find the optimal material parameters for a single patient using nonlinear optimization [99, 100]. The proposed ML-model was evaluated using additional testing data, where minor discrepancies (with NMAE about 1% to 6%) were achieved between the actual and ML-predicted material parameters. The close match between the actual and predicted stress-stretch curves further demonstrates the ML model can predict material constitutive responses with high accuracy. As a rough comparison, the previous approaches ([99, 100], CHAPTER 3, and APPENDIX A) achieved a similar accuracy with deviation from 0% to 6% in terms of material parameters using numerically-generated data. However, it is infeasible to perform a quantitative comparison among different inverse methods ([99, 100], CHAPTER 3, and APPENDIX A) as different datasets were used.

4.5.1 Support Vector Regression (SVR) for Nonlinear Mapping

We chose neural network for the ML-model because it is highly scalable: it can be configured with more layers and units to handle an increasingly large amount of data. Other ML-models can also be used for the material parameter identification problem. For instance, support vector regression (SVR) with radial basis function (RBF) kernel [205] can be applied to our datasets. Utilizing the ν-SVR with fine-tuned parameters ($C = 7, \nu = 0.5, \gamma = 0.3$, definitions referring to [205]), we were able to predict the material parameters with similar accuracy as the neural network. As demonstrated in Table 4.5, the NMAEs of the SVR predictions are slightly higher than those of the neural network.

Table 4.5 - NMAE and NSTAE of the five material parameters in testing set using support vector regression (SVR).

	C_{10}	k_1	k_2	κ	θ
NMAE	4.53%	2.35%	5.16%	1.64%	4.26%
NSTAE	3.35%	2.07%	3.57%	1.57%	5.14%

Our proposed ML model is not tied to the particular form of the constitutive model (Eqn. (2.10)). As long as a constitutive model can be implemented in a FE package, it can be used to generate training and testing data. For example, more advanced fiber dispersion models [206-208] can be used in our future work to handle fiber tension-compression switch.

4.5.2 Training and Testing Loss for Different Activation Functions

To determine material parameters of the aortic wall from medical image data, the 3D geometrical information has to be fully exploited, which cannot be described by using a few intuitive features. In our ML-model, the PCA effectively encodes the input complex geometries into the shape codes. Next, a neural network (24 inputs - 256 hidden units - 256 hidden units - 5 output units) with softplus activation function was utilized to establish the nonlinear mapping between the shape codes and the material parameters. The comparison between the softplus units and other units is illustrated in Figure 4.12. The softplus units outperformed the conventional sigmoid and hyperbolic tangent (tanh) units, the ReLU [209] and its variant SELU [210]. The softplus units lead to the lowest loss in the testing set and thus are more appropriate for this application.

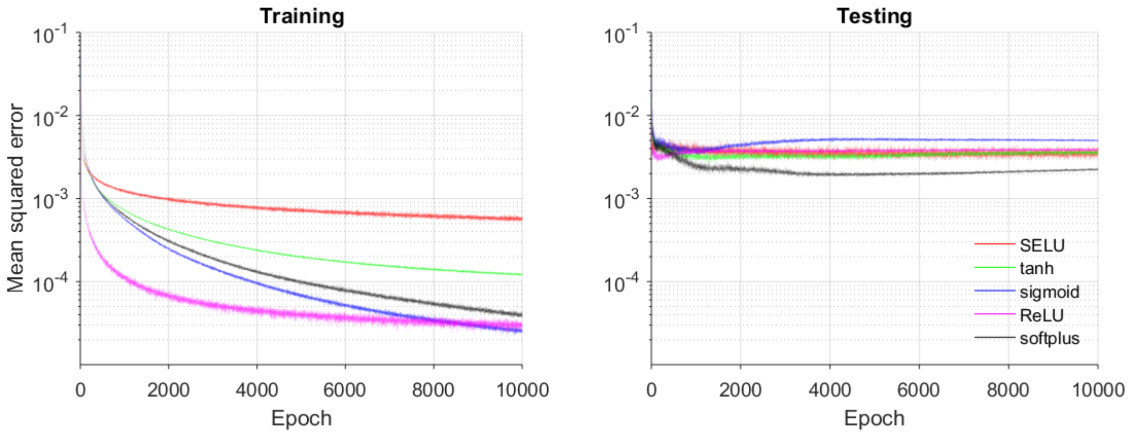

Figure 4.12 - MSE loss function for training and testing using softplus and other units.

4.5.3 Limitations

Since this study only aims to demonstrate the feasibility of the proposed machine learning framework, virtual aorta geometries were used for training and testing our ML-model. We acknowledge that the numerically-generated data may not represent the actual patient geometries and our ML-model has this limitation. Our current ML-model may not be able to handle complex situations such as calcifications in the aorta. The following assumptions and simplifications were used in data generation to expedite the FE simulations: (1) the branches of the aortic arch were trimmed off; (2) a uniform wall thickness at the systolic phase (1.5 mm) was assumed based on the average value from [140]; (3) the systolic and diastolic pressure were assumed to be 120mmHg and 80 mmHg, respectively for all cases; (4) to reduce model complexity, residual stresses were ignored according to a study [189] which shows that the residual stresses have minor effects on the material parameter identification problem; and (5) homogenously distribution of the material properties was assumed, while it is well known that aneurysms have heterogeneously distributed material properties. However, we note that these assumptions and simplifications were also present in the previous optimization-based inverse approaches ([99, 100], CHAPTER 3, and APPENDIX A). The main advantage of the ML-based approach is that it can significantly reduce the computation time. These limitations can be resolved in future work. For examples, the branches can be re-meshed using existing mesh processing method [193], then encoded by additional shape codes. Using MRI [22-25] or high-resolution CT scans [26], the wall thickness may be measurable for individual patient. The full 3D geometries at the two cardiac phases can be encoded using PCA, and therefore the thickness field is naturally accommodated. To handle pressure variations, FE simulation data at a wide range of systolic and diastolic pressure levels can be generated, and the systolic and diastolic pressure can be included as two additional inputs to the neural network. To incorporate the residual stresses, a modified GPA algorithm [133] can be applied to generate training and testing datasets.

Although the feasibility of the ML-model is clearly shown, the model is not ready for clinical application yet until sufficient real patient geometries are available. When a substantial amount of medical image data and experimental testing data are obtained, we can update the SSM space and the convex hull, from which a new large training dataset can be generated using the framework proposed in this study. The updated ML-model will be capable of predicting the material parameters which may provide clinically relevant insights, i.e. serving as a basis for patient-specific rupture risk estimation [57]. In case of a new patient with extreme aorta shape or material properties, which may cause unreliable prediction, a rejection option can be added in the ML-model as in [211]. The enhanced ML-model may avoid making predictions on uncommon cases. Those rare cases can be handled by the optimization-based inverse methods ([99, 100], CHAPTER 3, and APPENDIX A).

4.6 Summary

We have proposed a novel ML approach to estimate the constitutive parameters of the aortic wall from *in vivo* loaded geometries at two cardiac phases with known blood pressures. The ML-model is comprised of an unsupervised shape encoding module and a supervised nonlinear mapping module. FE simulations were used to generate datasets for training, adjusting and testing the ML-model. This novel ML approach can expedite the procedure of *in vivo* material parameter identification: once the ML-model is trained, the material parameters can be estimated within one second.

CHAPTER 5. PROBABILISTIC AND ANISOTROPIC FAILURE METRIC

To noninvasively assess risk of aneurysm rupture and dissection, an accurate material failure metric of the aortic wall is needed. Previously, deterministic or isotropic failure metrics were extensively used for the aortic wall. However, experimental studies have shown that aortic wall tensile strengths in circumferential and axial directions are significantly different (i.e., anisotropic), and vary greatly among patients with aortic aneurysm. In this chapter, we develop a novel probabilistic and anisotropic failure metric for risk stratification of ATAA. A well-studied anisotropic failure criterion, the Tsai–Hill (TH) theory, was explored to model anisotropic failure properties of aortic tissues. To examine fitting capability of the TH criterion, off-axis uniaxial tension tests were performed on aortic tissues of 4 porcine individuals and 18 human ATAA patients. The TH criterion demonstrates a good fitting capability with the off-axis testing data. Next, anisotropic failure property data of 84 ATAA patients was collected from uniaxial tensile tests in the circumferential and axial directions. A joint probability distribution of the anisotropic failure properties was estimated, and the anisotropic failure probability (FP) based on the TH criterion was derived. The novel FP metric, which incorporates uncertainty and anisotropy of failure properties, can be evaluated given wall stresses. To demonstrate application of the FP metric, by using the *in vivo*-identified and *ex vivo*-derived hyperelastic properties of the two patients obtained from CHAPTER 3, the FP metric was computed under elevated blood pressure. Some results of this chapter are published in [69] and available in [212].

5.1 Background

With advances in clinical imaging techniques and computational power in the past decade, numerical simulations have been increasingly pursued to gain a better understanding of the biomechanical events involved in various complex aortic disease conditions, such as rupture and dissection of aortic aneurysm. Using 3D patient-specific aorta geometry and physiological blood pressure, aortic wall stresses can be computed using FEA. To assess patient-specific ATAA rupture/dissection risk, computed stress distributions on the aortic wall are compared with the tensile strengths of the aortic wall, by which a scalar-valued failure metric can be obtained. Therefore, an accurate failure metric plays a critical role in biomechanical ATAA risk assessment [1].

In this work, we developed a novel probabilistic and anisotropic failure metric for ATAA risk stratification. Uniaxial tensile tests were performed using aortic tissue samples from 84 ATAA patients, from which a two-dimensional (2D) probability distribution of the anisotropic wall strengths was obtained. Next, the anisotropic failure probability (FP) based on the TH failure theory was derived from the probability distribution of wall strength. After the aortic wall stresses are computed from patient-specific biomechanical analyses, the novel FP metric can be used for risk classification. Lastly, by using the *in vivo*-identified and *ex vivo*-derived hyperelastic properties of the two patients obtained from CHAPTER 3, the FP metric was evaluated under elevated blood pressure.

5.2 Anisotropic Failure Criterion

5.2.1 The Tsai-Hill (TH) criterion

In this study, the Tsai-Hill (TH) criterion [48] was used for modeling failure properties of the aortic tissues. Applying the TH criterion to the aortic tissue, the failure metric Λ takes the following form:

$$\Lambda = \left(\frac{\sigma_{\theta\theta}}{X}\right)^2 + \left(\frac{\sigma_{zz}}{Y}\right)^2 - \left(\frac{\sigma_{\theta\theta}}{X}\right)\left(\frac{\sigma_{zz}}{X}\right) + \left(\frac{\tau_{\theta z}}{S}\right)^2 \tag{5.1}$$

where $\sigma_{\theta\theta}$, σ_{zz} and $\tau_{\theta z}$ stand for circumferential stress, axial stress and in-plane shear stress, respectively. Cauchy stress is used when the TH criterion is applied for finite deformation. X, Y and S are circumferential, axial and in-plane shear strengths, respectively, which are the model parameters to be determined. Failure happens when Λ reaches 1.

For the TH model, X and Y can be determined from uniaxial failure stresses in the circumferential and axial directions, respectively. In order to find S, off-axis tension tests are typically performed. Off-axis tests are uniaxial tests along different angles w.r.t to the circumferential axis. The uniaxial stress in the loading axis needs to be transformed onto the circumferential/axial direction to determine failure using Eqn. (5.1), therefore, a set of transformed stress states can be obtained in the off-axis tension tests. Using the TH model, the off-axis uniaxial strength $X_{\theta\theta}$ can be expressed as

$$X_{\theta\theta}(\theta) = 1 \Big/ \sqrt{\frac{\cos^4\theta}{X^2} + \frac{\sin^4\theta}{Y^2} - \frac{\sin^2\theta\cos^2\theta}{X^2} + \frac{\sin^2\theta\cos^2\theta}{S^2}} \tag{5.2}$$

where θ is the angle between the fiber (circumferential) direction and the loading axis. Since the collagen fiber direction can rotate due to finite deformation (see Figure 5.1(c)) in an off-axis uniaxial test, one needs to account for the affine rotation of fiber orientations. Hence, θ corresponds to the deformed fiber direction at the moment of failure.

5.2.2 Off-Axis Tension Tests

Porcine and human aortic tissues were utilized for the off-axis tension tests. Fresh descending aortas of 4 porcine were harvested from a local slaughterhouse (Holifield Farms, Covington, GA), ranging between 1 and 5 years of age. Surgically-resected human aortic samples of 18 ATAA patients (13 male, 5 female, age: 66.89 ± 9.26 years) were obtained from the Emory Saint Joseph's Hospital with IRB approval. The porcine and human aorta samples were cryopreserved in 90%/10% RPMI-1640/DMSO solution upon harvest and stored at −80 °C until testing. Frozen tissue samples were slowly defrosted, followed by the multi-stage slow thawing method to remove the cryopreserving agent [15, 174].

The samples were trimmed into 25×13 mm dog bone-shaped specimens using a 3D printed template. Thickness values were measured at three locations in the narrow portion for each specimen with a Mitutoyo 7301 rotating thickness gage (Aurora, IL) with an accuracy of ±0.01 mm. An average thickness was determined and used in the calculation of the undeformed cross-section area. The uniaxial tests were conducted at room temperature using a Test Resources 100Q Universal Testing Machine (Shakopee, MN). Graphite optical markers were placed on the narrow portion of the specimens for optical strain measurements. The axial force was measured by means of a 4.4N load cell (Test

Resources SM-500-294) [213]. Fine grit sandpaper was placed between the tissue and the clamps to avoid slippage during the test. For each porcine individual, 10 aorta specimens with 5 different angles (0°, 45°, 65°, 80° and 90° with respect to the circumferential direction) were obtained and subjected to uniaxial tensile tests until failure, from which failure stress $X_{\theta\theta}$ and failure strain can be extracted. The specimens were quasi-statically stretched to failure at a constant displacement rate of 5mm/min. The specimens were continuously hydrated with 0.9% saline solution to allow for optimal tissue hydration during testing [214]. To minimize the effect of axial position on the failure properties, uniaxial specimens were made according to the pattern shown in Figure 5.1(a) for porcine aortas and Figure 5.1(b) for human samples. The variation of circumferential strength due to change of axial position in porcine samples is small (see Figure 5.2). For surgically-resected human aortic tissue samples, 0°, 45° and 90° uniaxial specimens were obtained for all 18 patients (Figure 5.1(b)). Due to a relatively small size of some human tissue samples, 65° and 80° test specimens were only cut from two patients (patient 1: a 60-year-old male, patient 2: a 51-year-old male).

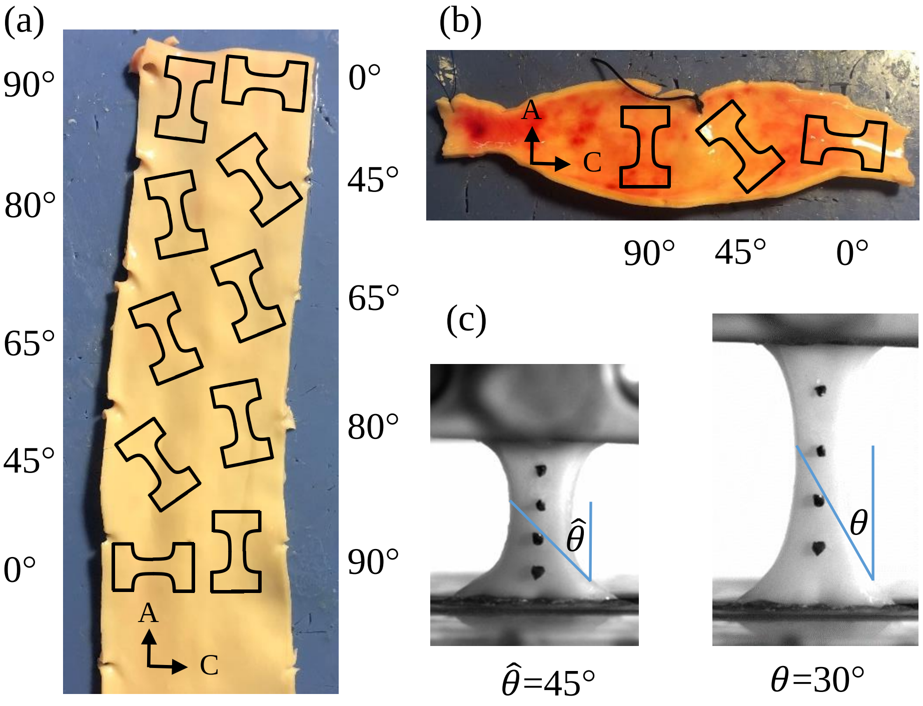

Figure 5.1 - Off-axis tension test of the healthy porcine (a) and human ATAA (b) aortic samples. (a) Outlines of bog-bone shape specimen geometries on a porcine aortic sample. (b) Outlines of bog- bone shape specimen geometries on a human ATAA aortic sample. The 65° and 80° specimens were only obtained from two patients. (c) Screenshots shows the change of fiber direction during the uniaxial test. $\hat{\theta}$ denotes the undeformed fiber orientation and θ is the deformed fiber orientation. A and C represent axial and circumferential directions, respectively.

The testing data were excluded from subsequent analyses if rupture did not occur in the middle of the test specimen [215]. We observed that the aortic wall layers, i.e., media and adventitia layers, may rupture at different times during the uniaxial tests. Therefore, failure was defined by the onset of yielding, i.e., a deviation from the exponential strain-stress curve, which corresponds to a rupture of any layer. It is worth noting that, during the uniaxial test, the fiber directions can affinely rotate due to finite deformation (see Figure 5.1(c)). Hence, the deformed fiber angle θ was used in the TH criterion.

To verify that the axial positions has little effect on the off-axis uniaxial strength $X_{\theta\theta}$, using a descending aorta of another porcine individual (i.e., apart from the 4 porcine individuals used in the off-axis tests), uniaxial tests of circumferential (0°) specimens were performed following the same pattern (Figure 5.1(a)). The results are summarized in Figure 5.2, which shows relatively small deviations from the mean circumferential strength. For resected human ATAA samples, specimens were obtained from approximately identical axial positions, however, material properties could vary in the circumferential direction [21].

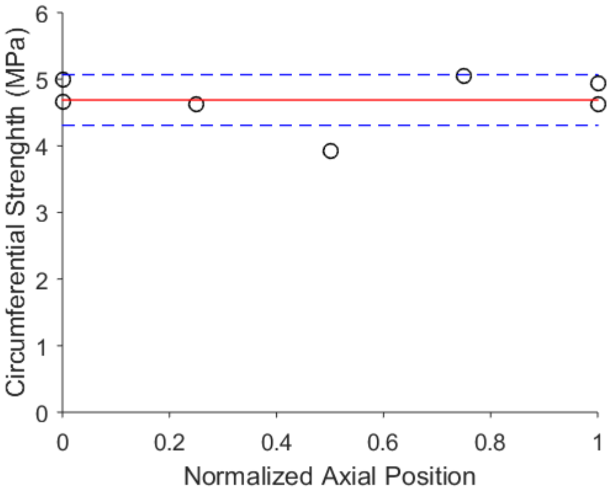

Figure 5.2 - Effect of axial position on the circumferential strength. Solid red line indicates the mean value of circumferential strength. Blue dashed lines indicate the mean ± standard deviation.

5.2.3 Fitting TH Criterion to Off-Axis Testing Data

For the 4 porcine aortas, the uniaxial strengths $X_{\theta\theta}$ versus the deformed fiber orientations θ extracted from the off-axis tests are plotted in Figure 5.3, where the TH criterion fits are also shown. The corresponding failure parameters are listed in Table 5.1.

In general, the TH criterion predicts a smooth trend. All the three models demonstrated good fitting capabilities, as shown by the R^2 values.

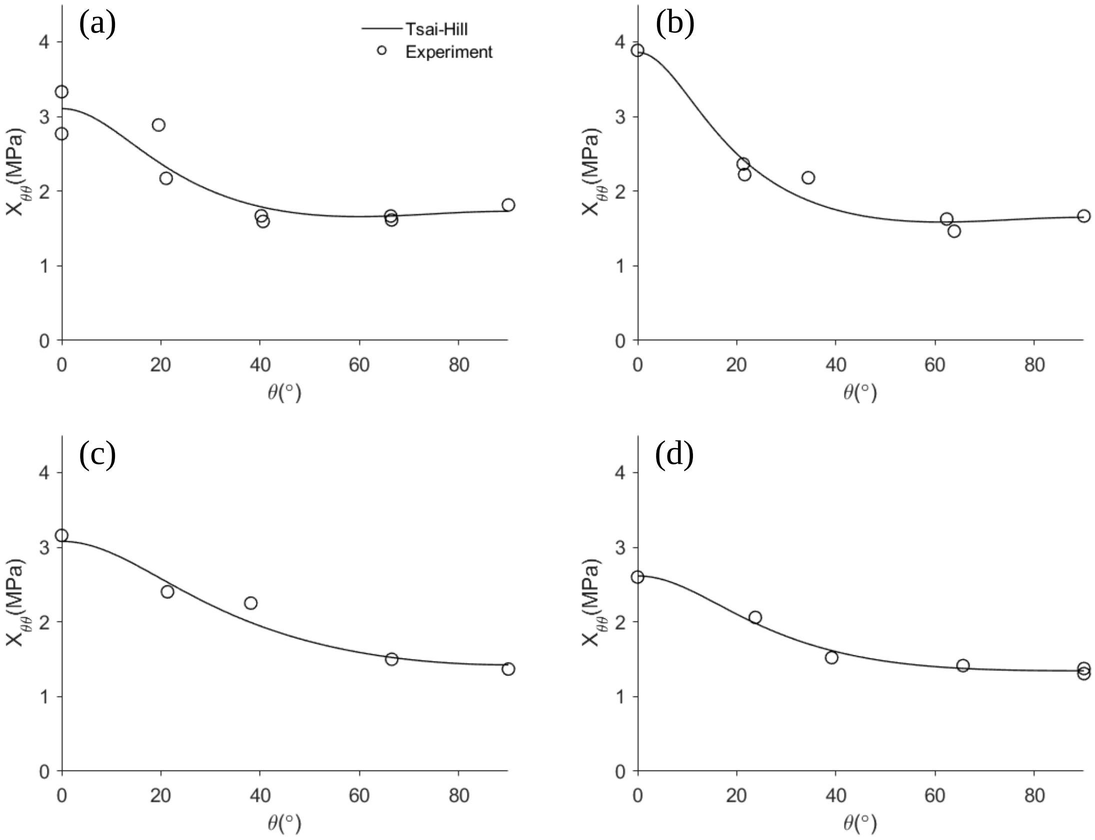

Figure 5.3 - Uniaxial strength obtained from off-axis tests and failure criteria fits for the healthy porcine aortas. (a) to (d) represent porcine individual 1 to 4, respectively.

Table 5.1 - Failure model parameters and corresponding R^2 obtained from fitting off-axis testing data of the healthy porcine aortas.

Porcine #	$X(MPa)$	$Y(MPa)$	$S(MPa)$	R^2
1	3.10	1.73	1.00	0.8580
2	3.86	1.65	0.97	0.9634
3	3.08	1.42	1.20	0.9497
4	2.61	1.35	0.93	0.9856

To demonstrate that the human ATAA tissues also have similar trend with respect to fiber orientation, 0°, 45° and 90° uniaxial specimens of the 18 human ATAA patients were subjected to the off-axis tension tests. Boxplot of uniaxial strength $X_{\theta\theta}$ versus the undeformed mean fiber orientations $\hat{\theta}$ is depicted in Figure 5.4. Using two-sample t-test, we found that the circumferential strength $X_{\theta\theta}(\hat{\theta} = 0°)$ is significantly higher than the axial strength $X_{\theta\theta}(\hat{\theta} = 90°)$ with $p < 0.0001$. The circumferential strength $X_{\theta\theta}(\hat{\theta} = 0°)$ is also significantly higher than the 45° strength $X_{\theta\theta}(\hat{\theta} = 45°)$ with significance $p = 0.0013$. In addition, the 45° strength $X_{\theta\theta}(\hat{\theta} = 0°)$ is significantly higher than the axial strength $X_{\theta\theta}(\hat{\theta} = 90°)$ with $p = 0.0010$.

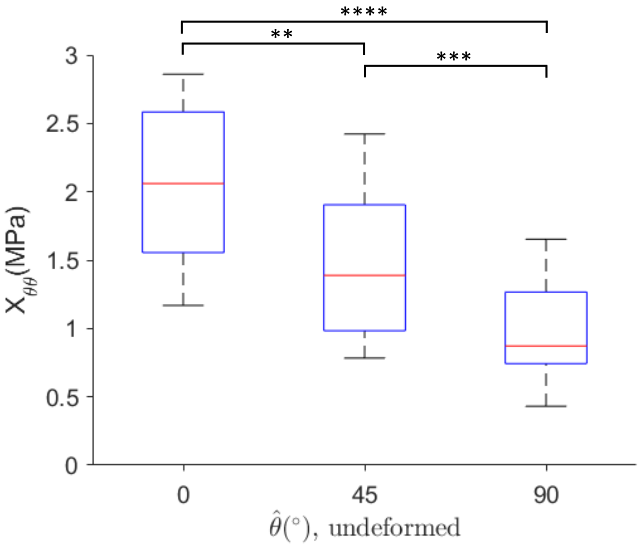

Figure 5.4 - Boxplot of uniaxial strength of human ATAA tissues in off-axis tests. Undeformed mean fiber orientation $\hat{\theta}$ is plotted on the horizontal axis. The red mark indicates the median, and the bottom and top edges of the box indicate the 25th and 75th percentiles, respectively. The whiskers extend to the maximum and minimum of $X_{\theta\theta}$. **, *, **** indicates statistical significance levels of $p \leq 0.01, p \leq 0.001, p \leq 0.0001$, respectively.**

Due to small size of the tissue samples, we were only able to obtain the complete sets of test specimens of all angles (0°, 45°, 65°, 80° and 90°) from two patients. The uniaxial strengths $X_{\theta\theta}$ versus the deformed fiber orientations θ are plotted in Figure 5.5

for the two human ATAA patients, together with the TH criterion fits. The TH failure parameters and corresponding R^2 are shown in Table 5.2. The TH model demonstrated good fitting capabilities to the off-axis testing data.

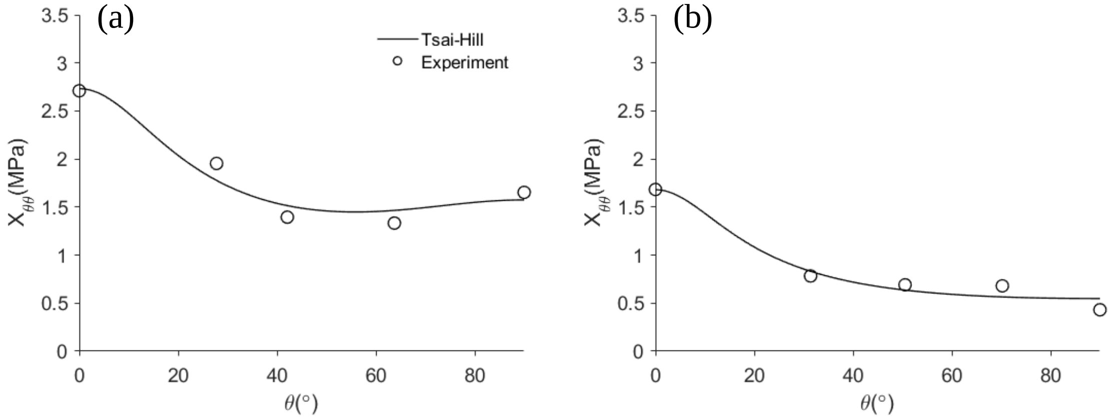

Figure 5.5 - Uniaxial strength obtained from off-axis tests and failure criteria fits for the human ATAA patients. (a) and (b) represent patient 1 and 2, respectively.

Table 5.2 - Failure model parameters and corresponding R^2 obtained from fitting off-axis testing data of the human ATAA tissues.

Porcine #	$X(MPa)$	$Y(MPa)$	$S(MPa)$	R^2
1	2.73	1.57	0.84	0.9443
2	1.68	0.55	0.43	0.9652

5.3 Failure Property Data

In this study, surgically resected human aortic tissues of 98 ATAA patients (72 males, 26 females, age: 62.57 ± 12.42 years) were obtained from the Emory Saint Joseph's Hospital with IRB approval (including the 18 patients in Section 5.2). The tissue samples underwent uniaxial tests (Section 5.3.1) to determine the failure properties. Among the 98 patients, pre-operative 3D CT images of 14 patients were obtained to reconstruct their ATAA geometries. In addition, we obtained surgically resected aortic tissue samples and corresponding CT images of 27 ATAA patients in a previous study [57] from Yale-New Haven Hospital. Uniaxial and biaxial testing were performed for the 27 patients.

The cohort of 125 (98+27) ATAA patients was divided into two groups: (1) 84 patients without CT images; and (2) 41 patients with CT images (including 27 patients from our previous study [57]). In this chapter, failure property data of the 84 patients in Group 1 was used for development of the novel anisotropic and probabilistic failure metric; in CHAPTER 6, Group 2 was used to compute the "ground-truth" risks for validation. Hence, there is no overlapping between the two groups.

5.3.1 Uniaxial Testing in the Circumferential and Axial Directions

Using the similar approach as Section 5.2.2, uniaxial tensile tests were performed in the circumferential and axial directions to extract the TH parameters X and Y of the 98 ATAA tissue samples from Emory (similar uniaxial tests were performed for the 27 patients in our previous study [57]). Definition of failure is the same as that in Section 5.2.2. To demonstrate that the wall strength of the human ATAA tissues is anisotropic, circumferential (X) and axial (Y) strengths of the 125 ATAA patients (Group 1 and Group 2) are depicted in Figure 5.6 using boxplot. By using two-sample t-test, it is shown that the circumferential strength is significantly higher than the axial strength with $p < 0.0001$.

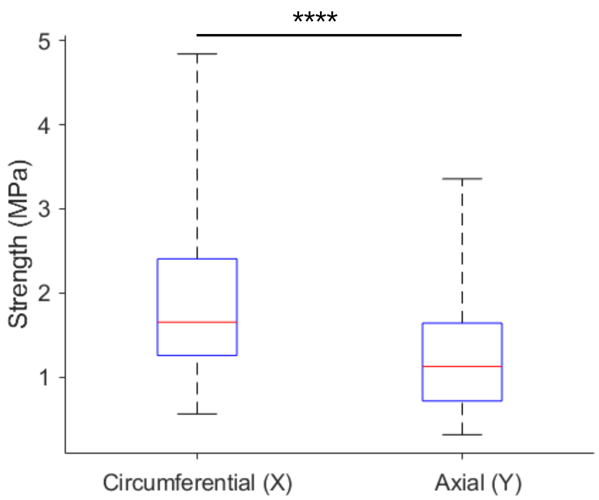

Figure 5.6 - Boxplot of uniaxial strengths of human ATAA tissues. The red mark indicates the median, and the bottom and top edges of the box indicate the 25th and 75th percentiles, respectively. The whiskers extend to the maximum and minimum. ** indicates statistical significance level $p \leq 0.0001$.**

5.3.2 Anisotropic Failure Properties

Results of the uniaxial testing are summarized in Figure 5.7(a) for the two groups. Group 1 was used in the subsequent sections to derive the anisotropic and probabilistic failure metric. For most of human ATAA samples, we were unable to perform off-axis uniaxial tests to obtain S due to the limited size of the tissue samples. An average value ($S = 0.635MPa$) in Section 5.2.3 was used for all patients. The original TH model [48] assumes $X > Y$, which is usually the case for unidirectional fiber-reinforced composite. For the tested aortic tissue samples, $X < Y$ can be observed for a few patents (see Figure 5.7(a)). Therefore, in this study, the TH failure metric is modified as

$$\Lambda = \begin{cases} \left(\frac{\sigma_{\theta\theta}}{X}\right)^2 + \left(\frac{\sigma_{zz}}{Y}\right)^2 - \left(\frac{\sigma_{\theta\theta}}{X}\right)\left(\frac{\sigma_{zz}}{X}\right) + \left(\frac{\tau_{\theta z}}{S}\right)^2, & X \geq Y \\ \left(\frac{\sigma_{\theta\theta}}{X}\right)^2 + \left(\frac{\sigma_{zz}}{Y}\right)^2 - \left(\frac{\sigma_{\theta\theta}}{Y}\right)\left(\frac{\sigma_{zz}}{Y}\right) + \left(\frac{\tau_{\theta z}}{S}\right)^2, & X < Y \end{cases} \tag{5.3}$$

Hence, using the circumferential (X) and axial (Y) strengths determined from uniaxial tests, the TH failure envelopes (contour line defined by $\Lambda = 1$) of the 84 patients in Group 1 can be visualized in Figure 5.7(b) using $\tau_{\theta z} = 0$.

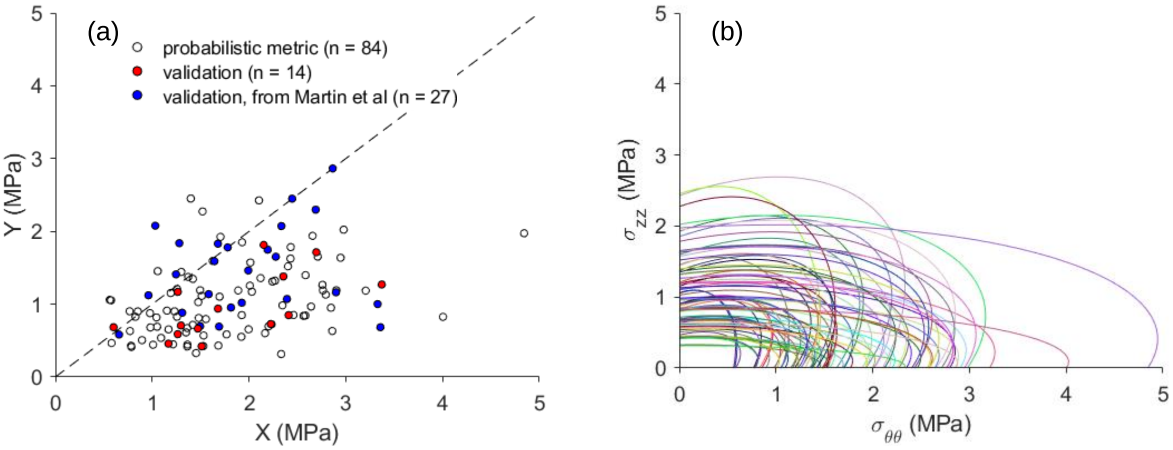

Figure 5.7 - Uniaxial strengths and failure envelopes. (a) Circumferential (X) and axial (Y) strengths of the 125 ATAA patients. Among them, 84 patients were used for developing the probabilistic metric (Group 1), 41 patients were used for validation (Group 2). (b) Tsai-Hill (TH) failure envelopes of the 84 patients in Group 1. $\tau_{\theta z} = 0$ when generating the failure envelopes.

5.4 Anisotropic and Probabilistic Failure Metric

A anisotropic probabilistic failure metric is developed in following the steps: (1) estimating the probability density function (PDF) of failure parameters X and Y (circumferential and axial strengths), f_{XY}, from uniaxial testing data of Group 1; (2) deriving PDF of the failure metric Λ, f_{Λ}, by using the method of random variable transformation (a.k.a. change of variables technique) [216]; and (3) calculating the failure probability (FP), $P(\Lambda > 1)$.

5.4.1 Probability Distribution of Failure Properties

In this study, the joint PDF f_{XY} of the TH model parameters X and Y (circumferential and axial strengths) is obtained using kernel density estimation (KDE) [217, 218], which is a non-parametric model for PDF estimation. The bivariate KDE [219] with diagonal bandwidth matrix takes the following form

$$f_{XY}(x,y) = \frac{1}{nh_1h_2}\sum_{i=1}^{n} K(\frac{x-x_i}{h_1})K(\frac{y-y_i}{h_2}) \tag{5.4}$$

where x_i and y_i are samples of the TH model parameters X and Y, n is the number of samples. h_1 and h_2 represent the bandwidths. $K(\blacksquare)$ is the one-dimensional kernel function. In this study, the normal kernel was selected:

$$K(u) = \frac{1}{\sqrt{2\pi}} exp\,(-\frac{1}{2}u^2) \tag{5.5}$$

To ensure that the support for the PDF is positive, i.e., $\mathbb{R}_+^{\mathbf{2}} = \{(x,y) \in \mathbb{R}^{\mathbf{2}}: x,y > 0\}c$, log transformation was used [220]. h_1 and h_2 were chosen using ten-fold cross validation with likelihood function of the 84 patients data (Group 1) in following the steps: (1) h_1 and h_2 are evenly sampled on a 2D grid from 0.1 to 0.35 with a total of 10,000 points; (2) using a set of h_1 and h_2 values, ten-fold cross validation is performed to evaluate the log-likelihood function; (3) the h_1 and h_2 that lead to the maximum log-likelihood in the ten-fold cross validation were chosen. As a result, $h_1 = 0.2439MPa$ and $h_2 = 0.2237MPa$. In Figure 5.8, the joint PDF f_{XY} and marginal PDFs f_X and f_Y are plotted.

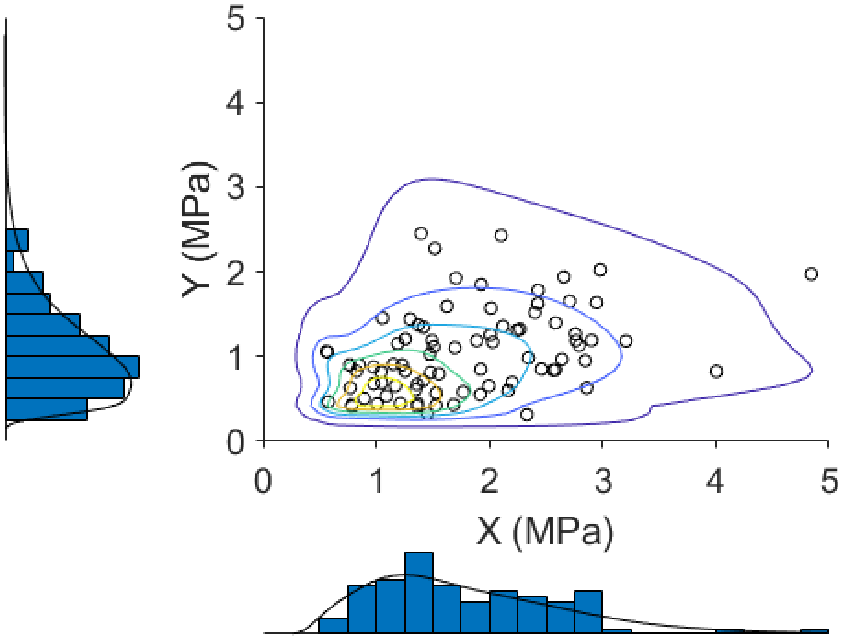

Figure 5.8 - The KDE-estimated joint PDF f_{XY} and marginal PDFs f_X and f_Y. Histograms for marginal distributions are also visualized.

To validate the KDE-estimated distribution, goodness-of-fit tests were performed using the estimated joint PDF f_{XY} and marginal PDFs. The results are summarized in Table 5.3, p =0.9715 was obtained using Chi-square goodness-of-fit test for the joint distribution. The null hypothesis is that the data comes from the KDE-estimated distribution. For all tests, the null hypothesis cannot be rejected, which indicates the PDFs can well describe the data distribution.

Table 5.3 - Goodness-of-fit tests for the joint distribution and marginal distributions. Null hypothesis: the data comes from the KDE-estimated distribution; alternative hypothesis: the data does not come from such distribution.

type of test	joint PDF f_{XY}	type of test	marginal PDF f_X	marginal PDF f_Y
Chi-square	0.9715	Chi-square	0.6481	0.9449
		Kolmogorov-Smirnov	0.5857	0.9346
		Anderson-Darling	0.6432	0.9030

5.4.2 *Failure Probability*

To derive the PDF f_{Λ} of the TH failure metric Λ, the method of direct transformation [216] is employed. Given the stress states ($\sigma_{\theta\theta}$, σ_{zz} and $\tau_{\theta z}$), Λ is a function of the random variables, i.e., $\Lambda = \Lambda(X, Y)$. Since S is a fixed constant in this study, we define a random variable W,

$$W = \Lambda - \left(\frac{\tau_{\theta z}}{S}\right)^2 = g_1(X, Y) = \begin{cases} \left(\frac{\sigma_{\theta\theta}}{X}\right)^2 + \left(\frac{\sigma_{zz}}{Y}\right)^2 - \left(\frac{\sigma_{\theta\theta}}{X}\right)\left(\frac{\sigma_{zz}}{X}\right), & X \geq Y \\ \left(\frac{\sigma_{\theta\theta}}{X}\right)^2 + \left(\frac{\sigma_{zz}}{Y}\right)^2 - \left(\frac{\sigma_{\theta\theta}}{Y}\right)\left(\frac{\sigma_{zz}}{Y}\right), & X < Y \end{cases} \tag{5.6}$$

Therefore, the probability of failure $P(\Lambda > 1)$ is equivalent to $P\left(W > 1 - \left(\frac{\tau_{\theta z}}{S}\right)^2\right)$. We also define a dummy random variable Z

$$Z = g_2(X, Y) = \begin{cases} \left(\frac{\sigma_{\theta\theta}}{X}\right)^2 - \left(\frac{\sigma_{zz}}{Y}\right)^2 - \left(\frac{\sigma_{\theta\theta}}{X}\right)\left(\frac{\sigma_{zz}}{X}\right), & X \geq Y \\ \left(\frac{\sigma_{\theta\theta}}{X}\right)^2 - \left(\frac{\sigma_{zz}}{Y}\right)^2 - \left(\frac{\sigma_{\theta\theta}}{Y}\right)\left(\frac{\sigma_{zz}}{Y}\right), & X < Y \end{cases} \tag{5.7}$$

The two functions $g_1(X,Y)$ and $g_2(X,Y)$ transform X and Y to the space of W and Z. Let $a = \begin{cases} \sigma_{\theta\theta}^2 - \sigma_{\theta\theta}\sigma_{zz}, & X \geq Y \\ \sigma_{\theta\theta}^2 &, X < Y \end{cases}$, and $b = \begin{cases} \sigma_{zz}^2 &, X \geq Y \\ \sigma_{zz}^2 - \sigma_{\theta\theta}\sigma_{zz}, & X < Y \end{cases}$, then we can rewrite the transformation as $w = g_1(x,y) = \frac{a}{x^2} + \frac{b}{y^2}$, and $z = g_2(x,y) = \frac{a}{x^2} - \frac{b}{y^2}$, with support $(x,y) \in \mathbb{R}_+^{\mathbf{2}}$. Hence, the inverse transformation and its Jacobian can be obtained, i.e., $x = g_1^{-1}(w,z) = \left(\frac{2a}{w+z}\right)^{1/2}$, $y = g_2^{-1}(w,z) = \left(\frac{2b}{w-z}\right)^{1/2}$, and $J = \begin{vmatrix} \frac{\partial x}{\partial w} & \frac{\partial x}{\partial z} \\ \frac{\partial y}{\partial w} & \frac{\partial y}{\partial z} \end{vmatrix} = -\left[\frac{(ab)^{1/3}}{(w+z)(w-z)}\right]^{3/2}$.

When $a \neq 0$ and $b \neq 0$, the transformation from (X,Y) to (W,Z) is one-to-one because $J \neq 0$. Using the method of direct transformation [216], the joint PDF of W and Z, f_{WZ}, can be derived using

$$f_{WZ}(w,z) = f_{XY}[g_1^{-1}(w,z), g_2^{-1}(w,z)]|J(w,z)| \tag{5.8}$$

The marginal PDF f_W can be obtained by

$$f_W(w) = \int_{-\infty}^{+\infty} f_{WZ}(w,z)\, dz \tag{5.9}$$

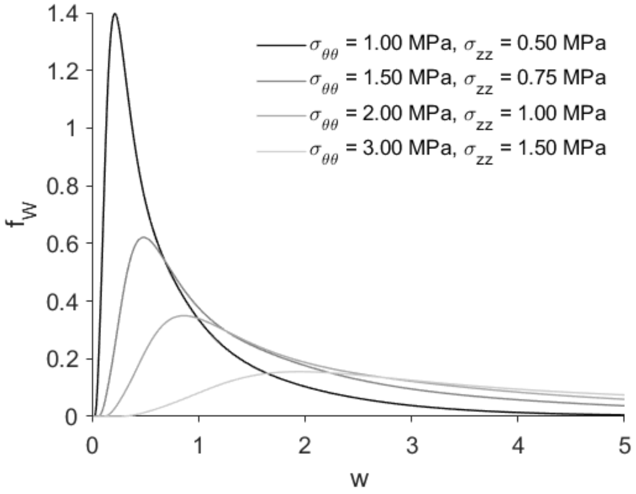

Figure 5.9 - The estimated pdf f_W with given $\sigma_{\theta\theta}$ and σ_{zz} values.

When $a = 0$ or $b = 0$, f_W can be directly obtained using the method of direct transformation for one random variable [216]. If $a = 0$, i.e., $w = g(y) = \frac{b}{y^2}$, PDF f_W can be derived as

$$f_W(w) = f_Y[g^{-1}(w)] \left| \frac{dg^{-1}(w)}{dw} \right| \tag{5.10}$$

Similarly, if $b = 0$, i.e., $w = g(x) = \frac{a}{x^2}$, f_W can be obtained by

$$f_W(w) = f_X[g^{-1}(w)] \left| \frac{dg^{-1}(w)}{dw} \right| \tag{5.11}$$

For illustrative purposes, f_W is plotted in Figure 5.9 by using different values of $\sigma_{\theta\theta}$ and σ_{zz}. Once the PDF f_W is obtained, it is straightforward to compute the failure probability (FP) by integration:

$$FP = P(\Lambda > 1) = P\left(W > 1 - \left(\frac{\tau_{\theta z}}{S}\right)^2\right) = \int_{1-\left(\frac{\tau_{\theta z}}{S}\right)^2}^{+\infty} f_W(w)\, dw \tag{5.12}$$

Given $\tau_{\theta z}$, FP can be visualized on a 2D plot of $\sigma_{\theta\theta}$ and σ_{zz}. In Figure 5.10, 2D contour plots of FP are generated using representative $\tau_{\theta z}$ values.

Given stress states, the value of FP can be obtained via numerical integration. In this study, the FP values were pre-computed in a 3D mesh grid of $\sigma_{\theta\theta}$, σ_{zz} and $\tau_{\theta z}$ prior to FE simulations. FP under specified stress states can be obtained using 3D interpolations from the pre-computed FP values in the grid.

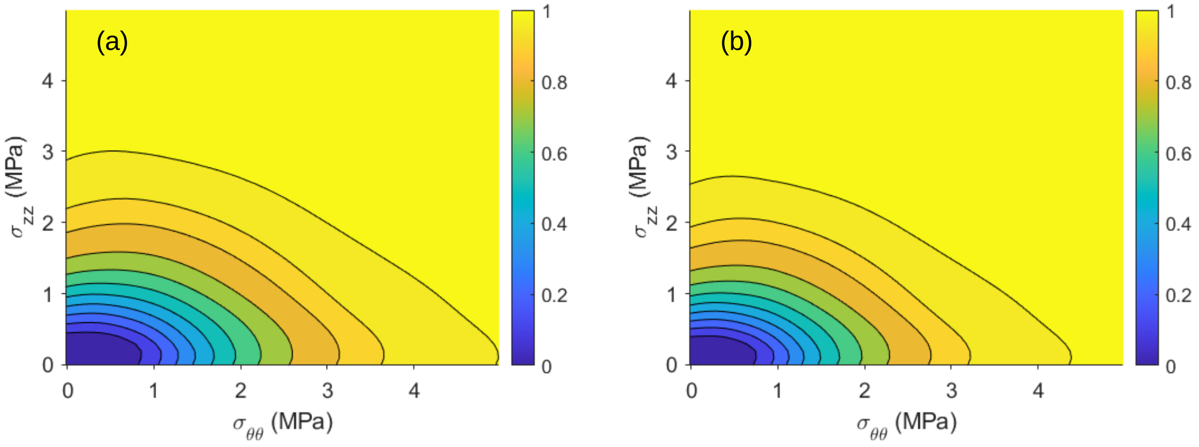

Figure 5.10 - 2D contour of FP in $\boldsymbol{\sigma_{\theta\theta} - \sigma_{zz}}$ plane using (a) $\boldsymbol{\tau_{\theta z} = 0}$ and (b) $\boldsymbol{\tau_{\theta z} = 300kPa}$.

5.5 ATAA Failure Metric under Elevated Pressure using In Vivo-Identified Hyperelastic Properties

In CHAPTER 3, the inverse identification approach was applied to estimate *in vivo* material parameters of the hyperelastic GOH model $(C_{10}, k_1, k_2, \kappa, \theta)$ from ECG-gated CT scans of two ATAA patients. Surgically-resected tissue samples of the same patients were obtained for *ex vivo* biaxial testing. Good agreements were achieved for the *in vivo*-identified and *ex vivo*-derived stretch-stress curves.

Here, systolic geometries of the two patients were reconstructed from the CT images. For Patient 1, a large field of view was recorded; therefore, the aortic arch and descending aorta were included in the analysis. Using the patient-specific ATAA geometries and blood pressures of the two patients, the generalized pre-stressing algorithm (GPA, described in Section 2.3.3) is used to incorporate systolic pre-stress into the aortic wall. Next, by using patient-specific hyperleastic properties (*in vivo*-identified and *ex vivo*-derived), the ATAA stress fields were computed under elevated blood pressure, $1.5P_{sys}$. P_{sys} stands for the systolic blood pressure for each patient. Consequently, the FP metric was evaluated on the ATAA geometries using the *in vivo*-identified and the averaged *ex vivo*-derived properties.

The FP fields on the ATAA geometries are shown in Figure 5.11 for the two patients. It can be observed that the *in vivo*-identified and *ex vivo*-derived properties have resulted in similar distributions of FP metric. For Patient 1, the maximum FP metrics were similar using the *in vivo*-identified and *ex vivo*-derived hyperelastic properties. The slight difference of the maximum FP metrics of Patient 2 may be explained by heterogeneous material properties.

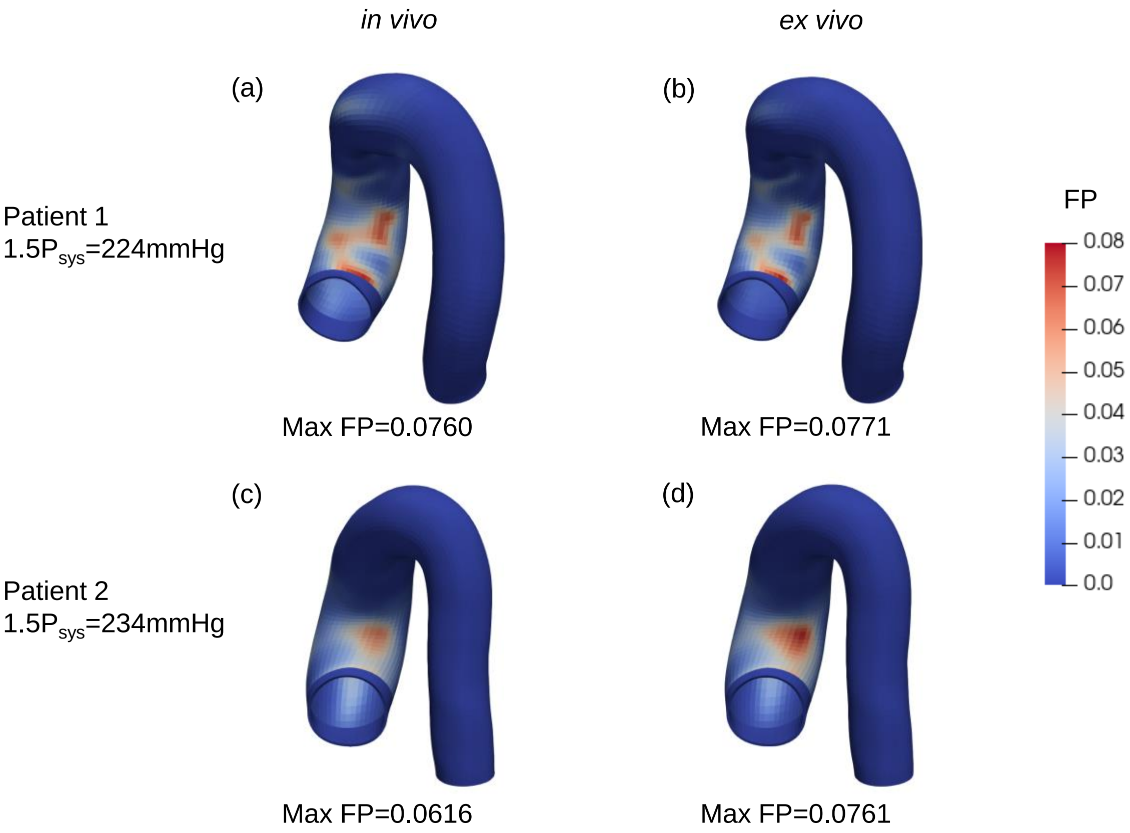
in vivo
ex vivo
(a)
(b)
Patient 1
1.5P$_{sys}$=224mmHg
FP
0.08
0.07
0.06
0.05
0.04
0.03
0.02
0.01
0.0
Max FP=0.0760
Max FP=0.0771
(c)
(d)
Patient 2
1.5P$_{sys}$=234mmHg
Max FP=0.0616
Max FP=0.0761

Figure 5.11 - FP evaluated under elevated blood pressure (1.5P_{sys}) using *in vivo*-identified ((a) and (c)) and *ex vivo*-derived ((b) and (d)) hyperelastic properties. (a) and (b): Patient 1; (c) and (d): Patient 2.

5.6 Discussion

In this study, a probabilistic anisotropic failure metric (FP) is proposed for ATAA risk stratification. Significant anisotropic failure properties of ATAA tissues have been shown in several studies [15, 21, 52, 68, 69], consistent with the testing results obtained in this study (see Figure 5.6). By using the TH criterion, anisotropic failure properties are embedded in FP. Comparing to the standard TH metric, FP incorporates uncertainties of wall strengths, i.e., the distribution of the failure parameters X and Y in the ATAA population. To demonstrate application of the FP metric, by using the *in vivo*-identified and *ex vivo*-derived hyperelastic properties of the two patients obtained from CHAPTER 3, the FP metric was computed under elevated blood pressure. Our results showed that the FP metric distributions are similar by using the *in vivo*-identified and *ex vivo*-derived properties. To our best knowledge, this is the first study that develops a probabilistic and anisotropic failure metric for quantifying failure risk of the aortic wall.

In the off-axis tension tests, porcine aortic tissues exhibit decreasing uniaxial strength from circumferential (0°) to axial (90°) direction, which is in line with a previous study by Korenczuk et al. [52]. Our 0°, 45° and 90° off-axis testing results also indicate anisotropic failure properties of human ATAA tissues differing with statistical significance ($p < 0.05$), which was also observed in many aortic tissue rupture studies [15-24]. It is noted that the 45° uniaxial strength is higher than the axial (90°) strength but lower than the circumferential (0°) strength with statistical significance ($p < 0.05$). The Tsai-Hill anisotropic criterion demonstrates good fitting capabilities with the off-axis tension test data. The fitting capabilities may be further studied using a larger sample size in the future.

5.6.1 Probabilistic Metric and Uncertainty Quantification

Polzer and Gasser [74] proposed a probabilistic rupture risk index (PRRI) based on isotropic wall strength leveraging an uncertainty quantification (UQ) framework [75]. In their work [74], the wall thickness, which is the input to the FE simulations, was treated as a source of uncertainties. However, in the UQ framework, sampling-based approaches like Monte Carlo are typically needed to quantify the uncertainties of the FE output (i.e. peak wall stress) propagated from the uncertainties of the FE inputs (i.e., wall thickness and material parameters), which often results in high computational cost [76-78]. In contrast to PRRI [74] that incorporates uncertainties of both wall strength and wall thickness, the proposed probabilistic failure metric (FP) only considers uncertainties of anisotropic wall strength, and uncertainties from FE inputs are not involved. Therefore, given FE-computed stresses, FP can be derived from experimental uniaxial testing data via simple numerical integration. We have recently developed a deep learning (DL) model [75] as a fast and accurate surrogate of FE simulation, which can replicate the results of FE simulations instantaneously. To incorporate uncertainties originated from FE inputs such as wall thickness into FP, the DL model can be used to accelerate the UQ framework.

5.6.2 Deterministic and Probabilistic Metrics

Deterministic failure metrics [67, 70-72] were extensively used in the literature to assess risk of aortic aneurysms. For example, Geest et al. [73] developed a multiple linear regression method to estimate wall strength of abdominal aortic aneurysm (AAA) from patient parameters (age, gender, maximum dimeter, family history and smoking status) and local parameters (local intraluminal thrombus (ILT) thickness and local diameter). However, since aortic wall strength vary greatly among individuals [15, 17, 21, 68], failure properties are not fully determined by those patient parameters and local parameters. Without incorporation of uncertainties, the predictive capability of the linear regression model is limited [73]. Indeed, patient-specific failure properties (i.e., aortic wall strengths) can only be accurately determined using invasive and destructive tests, and these tests clearly cannot be performed for patients whose ATAAs are still intact.

In contrast, those patient and local parameters were not used in the PRRI [74]. Nonetheless, the PRRI outperformed the deterministic method in a retrospective study [60] of asymptomatic AAA. Therefore, probabilistic metrics, which take into considerations of the uncertainties, may be more promising for risk assessment. With more tissue failure testing data collected, our developed probabilistic metric FP can be updated and improved, e.g., a conditional FP can be built based on patient-specific information (age, gender, family history). The conditional FP, which fully incorporates wall strength data and patient-specific information, combines the merits of both deterministic and probabilistic failure metrics.

5.6.3 Limitations

In this study, the samples were not preconditioned. Preconditioning is commonly performed for biological tissues, which produces repeatable elastic mechanical response [221]. However, the exact mechanisms of preconditioning remain unclear [222], and measured tissue properties are dependent on the preconditioning protocols of interest [223]. In some studies [51, 224], preconditioning was described by the Mullin's effect, and modeled using damage mechanics models. Therefore, it is suggested that preconditioning may not be performed at high loads by which damage could be induced [51]. In addition, the stress softening effects may not be adequately removed if preconditioning is performed at low strain amplitude [222]. Due to directional and subject-specific variability in material properties, e.g. human Patient 2 has a axial failure stress of 0.47 MPa, while porcine subject 2 has a circumferential failure stress of 3.88 MPa, it is difficult to find a consistent preconditioning strain amplitude for all human and porcine samples. Therefore, in this study, we did not apply pre-conditioning protocols for the sake of consistency in failure data collection. The samples were quasi-statically stretched to failure at a constant displacement rate of 5mm/min. It is shown in [225] that, for arterial tissues, the failure properties are independent of the strain rate. We assumed that preconditioning has a negligible effect on failure properties, which needs to be investigated and verified in future studies. For arterial tissues, stress softening effects induced by preconditioning are often small [51] comparing to spinal cord tissues [222]. In this study, the cryopreservation was used for tissue storage, which has been shown to have no significant effect on the material properties of the arterial wall [174].

5.7 Summary

In this chapter, a novel probabilistic and anisotropic failure metric was developed using failure property data from 84 ATAA patients. Off-axis tension tests were performed on aortic tissues of 4 porcine individuals and 18 human ATAA patients. The Tsai-Hill (TH) failure criterion demonstrates a good fitting capability with the off-axis testing data. The novel failure probability (FP) metric, which was derived based on the TH failure criterion, incorporates uncertainties of the anisotropic failure properties. Using the two patients' *in vivo* identification and *ex vivo* testing data obtained in CHAPTER 3, our results showed that the FP metric distributions under elevated blood pressure are similar for the *in vivo*-identified and *ex vivo*-derived properties.

CHAPTER 6. COMPARSION OF RISK ASSESSMENT METHODS

In CHAPTER 5, we developed a novel probabilistic and anisotropic failure metric using uniaxial testing data of 84 ATAA. The anisotropic failure probability (FP) metric, which incorporates uncertainty in the anisotropic failure properties, can be evaluated after the aortic wall stresses are computed from patient-specific biomechanical analysis. In this chapter, to compare different risk assessment methods, "ground-truth" risks of additional 41 ATAA patients were numerically-reconstructed using matching CT images and tissue testing data. Performance of different risk stratification methods (e.g., with and without patient-specific hyperelastic properties) was compared using p-value and receiver operating characteristic (ROC) curve. The results show that: (1) the probabilistic FP metric outperforms the deterministic TH metric; and (2) patient-specific hyperelastic properties can help to improve the performance of probabilistic FP metric in ATAA risk stratification. Some results of this chapter are available in [212].

6.1 Background

TAA is a lethal disease, which may lead to aortic rupture or dissection: the five-year survival in patients left untreated is 54% [5]. Currently, the clinical surgery criterion is primarily based on the aortic size and classifies an ATAA as high risk if the (maximum) diameter is larger than 5.5cm [9, 12], which may not accurately reflect a patient's risk [13, 14]: some aneurysms at smaller diameters (e.g., < 4cm) can and do rupture [13]. As ATAA rupture and dissection are essentially mechanical events, patient-specific biomechanical assessment, such as structural FEA, can provide a more accurate assessment of ATAA rupture/dissection risk [60, 61].

To estimate a patient's risk, patient-specific information (from medical report data or clinical preoperative images) before any adverse event may be used, which may include geometries from images and blood pressure. Patient-specific wall stress can be computed under physiological, hypertensive, or elevated blood pressures. Patient-specific failure properties such as wall strengths are not available for biomechanical assessment, as those can only be obtained using invasive and destructive testing. Without knowing patient-specific wall strengths, an accurate failure metric plays a critical role in biomechanical ATAA risk assessment [1]. In CHAPTER 5, we developed a novel probabilistic and anisotropic failure metric using uniaxial testing data of 84 ATAA. The anisotropic failure probability (FP) metric, which incorporates uncertainty in the anisotropic failure properties, can be evaluated after the aortic wall stresses are computed from patient-specific biomechanical analysis.

In this chapter, CT scans and corresponding surgically-resected tissues samples of additional 41 ATAA patients were obtained. The tissue samples were mechanically tested to obtain the hyperelastic and failure properties (planar biaxial for hyperelastic properties and uniaxial for failure properties). The "ground-truth" risks of 41 ATAA patients were reconstructed from FE simulations using the CT-reconstructed geometries and tissue testing data of the 41 patients. Using the "ground-truth" data, the following risk assessment methods were compared: 1) maximum diameter criterion; 2) maximum failure metric under systolic blood pressure; 3) maximum failure metric under elevated blood pressure evaluated using one set of hyperelastic properties representing the population-mean response; and 4) maximum failure metric under elevated blood pressure evaluated using patient-specific hyperelastic properties. The developed failure probability (FP) metric in CHAPTER 5 and a deterministic Tsai-Hill metric were used as the failure metric and the results were compared.

6.2 CT Image and Tissue Testing Data

In this chapter, the 41 patients in Group 2 were used to numerically reconstruct the risk of ATAA. The tissue samples underwent biaxial tests (Section 6.2.1) to determine hyperelastic properties, and uniaxial tests (Section 6.2.2) to determine the failure properties. Patient characteristics in Group 2 are reported in Table 6.1.

Table 6.1 - Patient characteristics in Group 2 used for validation. The reconstructed failure pressure is obtained in Section 6.3.

Patient #	Age	Gender	Diameter (mm)	Systolic pressure (P_{sys}, mmHg)	Reconstructed failure pressure (P_f, mmHg)
1	76	M	46	130	442
2	52	M	47	101	426
3	69	F	47	150	461
4	66	M	46	131	252
5	73	M	40	147	658
6	73	M	47	178	222
7	69	F	50	138	397
8	59	M	51	128	239
9	60	M	48	128	453
10	59	M	47	119	151
11	45	M	54	144	336
12	48	M	52	119	191
13	48	M	51	105	403
14	59	M	53	131	414
15	64	F	49	104	280
16	62	F	50	75	200

Table 6.1 continued

17	66	M	55	134	272
18	52	M	48	133	201
19	56	M	50	128	208
20	47	M	53	97	202
21	56	M	46	139	191
22	57	M	52	136	428
23	71	M	48	105	242
24	33	M	41	136	145
25	44	M	36	155	408
26	56	F	58	117	262
27	68	M	52	123	295
28	65	M	50	138	377
29	46	F	57	135	190
30	55	M	52	129	191
31	57	M	63	132	153
32	58	M	43	137	267
33	58	M	48	142	316
34	68	M	47	139	214
35	70	M	66	124	141
36	65	M	51	139	320
37	44	M	56	153	302
38	77	F	51	130	195
39	56	M	49	124	379
40	31	F	57	93	274
41	68	M	46	146	286

6.2.1 Biaxal Testing

Seven-protocol biaxial tensile tests were performed on the patient tissues in Group 2. Since the test results for the 27 Yale patients were already available from our previous study [57], in this study, we only performed the tests on the tissues of the 14 patients from Emory. Briefly, cryopreserved tissue samples were slowly defrosted, and the cryopreserving agent was removed using the multi-stage slow thawing method [15, 174]. The samples were carefully trimmed into square-shaped specimens with a side length of

20~25 mm. Thickness was measured at three locations on the diagonal line of the biaxial specimen. An averaged undeformed thickness was recorded. Each specimen was subjected to biaxial tensile loadings which aligned with the circumferential and axial directions. A stress-controlled biaxial testing protocol was utilized [15]. $\boldsymbol{N}$ denotes the first nominal stress, and the ratio $N_\theta\colon N_z$ was kept constant. Each tissue specimen was preconditioned for at least 40 continuous cycles with $N_\theta\colon N_z = 1\colon 1$ to minimize tissue hysteresis. Seven successive protocols were performed using ratios $N_\theta\colon N_z = 0.75\colon 1, 0.5\colon 1, 0.3\colon 1, 1\colon 1, 1\colon 0.75, 1\colon 0.5, 1\colon 0.3$. The GOH model (Eqn. (2.10)) was used as the constitutive law, the incompressibility D is a fixed to be 1×10^{-5}. The five material parameters $(C_{10}, k_1, k_2, \kappa, \theta)$ for an ATAA patient were determined by fitting the GOH model to the biaxial data.

6.2.2 *Uniaxial Testing*

In Section 5.3.1, uniaxial tensile tests were performed in the circumferential and axial directions to extract the wall strengths (X and Y) of the 98 Emory ATAA tissue samples in the two directions (including the 14 Emory patients in Group 2). The testing results for the 27 Yale patients were already available from our previous study [57]. Definition of failure is the same as that in Section 5.2.2. For the 41 patients in Group 2, the Tsai-Hill (TH) model (Eqn. (5.3) was used to describe failure strength using patient-specific parameters X and Y.

6.3 Reconstructing ATAA Risk using Patient-Specific CT Images and Tissue Testing Data

To reconstruct ATAA risk of adverse events (dissection or rupture) for the 41 patients in Group 2, FE simulations were performed using patient-specific information (geometry, blood pressure, experimentally-measured wall thickness, hyperelastic parameters and failure parameters) in Abaqus (Figure 6.1). The patient-specific ATAA geometries were segmented from the patients' pre-operative CT scans using 3D Slicer [226], we assume these geometries are in equilibrium under the systolic blood pressure. Then, the ATAA surfaces were meshed into quadrilateral elements using our remeshing program [140]. Mesh sensitivity analysis was performed in our previous study [57]. To estimate the patient-specific wall thickness in the systolic phase, an analytical procedure [63] was performed using the experimentally-measured undeformed wall thickness assuming $\sigma_{\theta\theta}:\sigma_{zz} = 1:2$ [63]. Solid meshes of the ATAA systolic geometries with C3D8H elements in Abaqus were then obtained by extruding the surface mesh using corresponding systolic wall thickness values.

The generalized pre-stressing algorithm (GPA) [145] was utilized to incorporate the pre-stress induced by the systolic pressure into the patient-specific ATAA systolic geometries.

It is observed that ATAA dissection and rupture usually occurs under elevated blood pressures brought on by extreme emotional or physical stress [64, 158]. To this end, using the patient-specific GOH material parameters, the aorta geometries are pressurized under elevated pressure levels until failure is predicted by the patient-specific TH parameters measured from uniaxial tests (see Figure 6.1). In the FE simulations, the proximal and distal boundaries of the ATAA geometries were only allowed to move in the radial direction. To remove boundary effect, three layers of elements adjacent to the boundaries were excluded from the failure evaluation. For a particular patient, the pressure rupture risk (PRR) [63] is used to quantify the risk revealed by the FE simulation, which is defined as

$$PRR = P_{sys}/P_f \tag{6.1}$$

where P_{sys} stands for the patient's systolic blood pressure and P_f represents the patient's failure pressure. We define high risk as for patient who has a $PRR \geq 0.6$ and low risk as $PRR < 0.6$. According to American Heart Association (AHA)'s blood pressure category [227], if P_{sys} is normal, $P_f = P_{sys}/0.6$ corresponds to the hypertensive crisis (blood pressure higher than 180mmHg). Therefore, using $PRR = 0.6$ as threshold, high risk patients are prone to adverse events under the hypertensive crisis. The numerically-reconstructed risks are considered as "ground-truth" for evaluation of the risk stratification methods in Section 6.4.

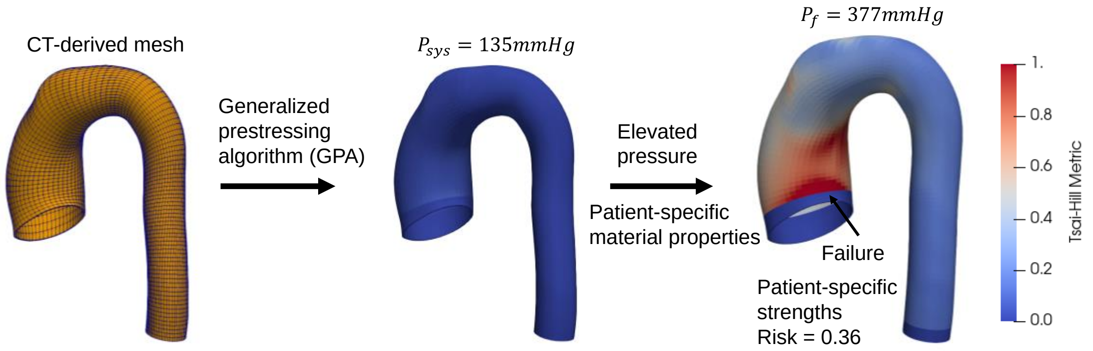
CT-derived mesh
Generalized prestressing algorithm (GPA)
$P_{sys} = 135mmHg$
Elevated pressure
Patient-specific material properties
$P_f = 377mmHg$
Failure
Patient-specific strengths
Risk = 0.36
1.
0.8
0.6
0.4
0.2
0.0
Tsai-Hill Metric

Figure 6.1 - FE simulations to reconstruct ATAA risk.

6.4 ATAA Risk Stratification Methods

To estimate a patient's risk, we can only use information (from medical report data or clinical preoperative images) before any adverse event, which may include geometries from images and blood pressure. We note that patient-specific failure information (wall strengths and failure pressure) cannot be used in the risk stratification, as those can only be obtained using invasive and destructive testing. Using stresses computed from FE simulation, predefined failure metric (FP or TH) can be evaluated on the ATAA wall under a specified pressure for an individual patient. According to several studies, wall thickness may be measured from MRI [228-231] or high resolution CT scans [163]. Hence, in this study, the same 3D aortic geometries from Section 6.3 were used for risk stratification, representing an ideal scenario in which wall thickness can be measured from images.

We apply four different methods to classify high ($PRR \geq 0.6$) and low risk ($PRR < 0.6$) patients, and method performance is evaluated using p-value and receiver operating characteristic (ROC) curve. The following risk stratification methods are investigated:

1. Maximum diameter criterion/metric.
2. Maximum failure metric at P_{sys} (hyperelastic properties are not needed).
3. Maximum failure metric at $1.5P_{sys}$ using one set of hyperelastic properties representing the population-mean response.
4. Maximum failure metric at $1.5P_{sys}$ using patient-specific hyperelastic properties.

The metric in Method 2 to Method 4 is evaluated at a spatial point on the aortic wall. The maximum failure metric is the maximum among the metric values from all spatial points on the aortic wall. By using static determinacy, the transmurally-mean wall stress can be readily obtained from clinical images without knowing the patient-specific hyperelastic properties [135, 136] (thoroughly described in CHAPTER 2). Therefore, in Method 2, patient-specific hyperelastic properties are not needed to compute maximum failure metric at P_{sys}. Failure metric under elevated blood pressure (e.g., $1.5P_{sys}$) may provide more valuable insight on the ATAA risk. However, under supra-physiological pressure loads, failure metric depends on the patient-specific hyperelastic properties. A study [74] suggests to use a population-mean response as a surrogate. Hence, to evaluate this strategy, one representative set of hyperelastic properties is used for all patients in Method 3. Patient-specific hyperelastic properties can be identified from multi-phase clinical images using inverse approaches [99, 100] (our inverse method is developed in CHAPTER 3 and APPENDIX A). Because ECG-gated CT scans were not performed for the 41 patients in Group 2, the inverse method in CHAPTER 3 cannot be applied. To represent an ideal scenario in which the hyperelastic material properties are accurately identified from ECG-gated CT scans, in Method 4, patient-specific GOH parameters fitted from the biaxial tests (Section 6.2.1) are used to evaluate the maximum failure metric at $1.5P_{sys}$.

For comparisons, the probabilistic metric FP (Eqn. (5.12)) and a deterministic TH metric (Λ in Eqn. (5.3) with typical parameters $X = 2.5MPa$ and $Y = 1.2MPa$) are used as the failure metric in Method 2 and Method 4.

3.2 Reconstructed ATAA Risk

Using the patient-specific imaging and tissue testing data, failure pressure (P_f) and risk (PRR) were numerically-reconstructed for the 41 ATAA patients in Group 2 and considered as "ground-truth" for risk stratification. The reconstructed (P_f) is shown in Table 6.1 and the PRR is listed in Table 6.2.

Table 6.2 - Reconstructed risk (PRR) and failure metrics evaluated by different methods (Section 6.4).

Patient #	Method 2 (FP)	Method 3 (FP)	Method 4 (FP)	Method 2 (TH)	Method 4 (TH)	Risk (PRR)
1	0.0054	0.0960	0.0922	0.0519	0.1571	0.2944
2	0.0436	0.1715	0.1412	0.1048	0.2127	0.2373
3	0.0311	0.1310	0.1596	0.0888	0.2139	0.3251
4	0.0385	0.2749	0.3350	0.1012	0.3271	0.5200
5	0.0010	0.0339	0.0224	0.0329	0.0848	0.2236
6	0.1708	0.4672	0.4416	0.2030	0.4658	0.8003
7	0.0022	0.0601	0.0392	0.0434	0.0960	0.3477
8	0.0112	0.1813	0.1750	0.1054	0.2972	0.5366
9	0.0159	0.1325	0.1279	0.0625	0.1595	0.2829
10	0.4105	0.2408	0.6849	0.5012	1.0244	0.7859
11	0.0956	0.3372	0.4444	0.1371	0.4891	0.4290
12	0.0371	0.0329	0.3790	0.1317	0.4837	0.6245
13	0.0104	0.0991	0.1315	0.0671	0.1675	0.2606
14	0.0047	0.1136	0.1449	0.0510	0.1580	0.3167
15	0.0001	0.0093	0.0148	0.0213	0.0637	0.3714
16	0.0038	0.0747	0.1077	0.0500	0.1614	0.3759
17	0.0208	0.2579	0.3149	0.1001	0.3482	0.4926
18	0.0251	0.2182	0.2834	0.0729	0.2723	0.6627
19	0.1310	0.4879	0.5801	0.1748	0.6561	0.6152
20	0.0058	0.1791	0.2325	0.1183	0.3835	0.4796
21	0.0470	0.2843	0.3010	0.1044	0.2890	0.7287
22	0.0100	0.1273	0.1076	0.0657	0.1538	0.3176
23	0.0910	0.2442	0.2884	0.1557	0.3810	0.4330
24	0.0745	0.5103	0.6349	0.2220	0.8389	0.9393
25	0.0116	0.0414	0.0389	0.0626	0.0897	0.3800
26	0.0115	0.1103	0.0969	0.1065	0.2426	0.4473
27	0.0044	0.0914	0.0945	0.0510	0.1341	0.4163
28	0.0254	0.2496	0.2160	0.0828	0.2267	0.3583
29	0.1929	0.0624	0.3067	0.2352	0.3430	0.6792
30	0.0320	0.2833	0.3067	0.0876	0.3073	0.6895
31	0.2592	0.6240	0.8115	0.2884	0.8678	0.8948
32	0.1280	0.4604	0.4085	0.1487	0.3659	0.5327
33	0.1949	0.4687	0.4188	0.2125	0.4203	0.4399
34	0.2138	0.0889	0.4364	0.2870	0.5355	0.5800
35	0.1107	0.3659	0.3301	0.1390	0.3454	0.9478

Table 6.2 continued

36	0.0063	0.0942	0.0902	0.0448	0.1386	0.4346
37	0.0714	0.3635	0.6713	0.1368	0.6630	0.5061
38	0.0322	0.2629	0.4181	0.0978	0.4049	0.6664
39	0.0001	0.0299	0.0102	0.0317	0.0745	0.3268
40	0.0143	0.1643	0.0933	0.1299	0.2784	0.3395
41	0.0023	0.0562	0.0371	0.0375	0.0977	0.5106

6.5 Results

6.5.1 Comparison of Different Risk Stratification Methods

The performance of different risk stratification methods (Section 6.4) is assessed using the "ground-truth" risk data of 41 ATAA patients in Group 2. For Method 1~4, FP of the 41 patients were computed using the patient-specific geometries and systolic blood pressures (see Table 6.2). Using the maximum diameter criterion (Method 1: $p = 0.1677$), no statistical significance was found between the high and low risk groups. Using the maximum FP evaluated at P_{sys}, we found a significant difference between the high and low risk groups (Method 2: $p = 0.0117$). Difference between high and low risk groups is also significant (Method 3: $p = 0.0070$) when using representative hyperelastic properties and the maximum FP at $1.5P_{sys}$. Using patient-specific hyperelastic properties and the maximum FP at $1.5P_{sys}$, the lowest p-value is achieved (Method 4: $p = 0.0001$) to separate the high and low risk groups. The results are shown in Figure 6.2.

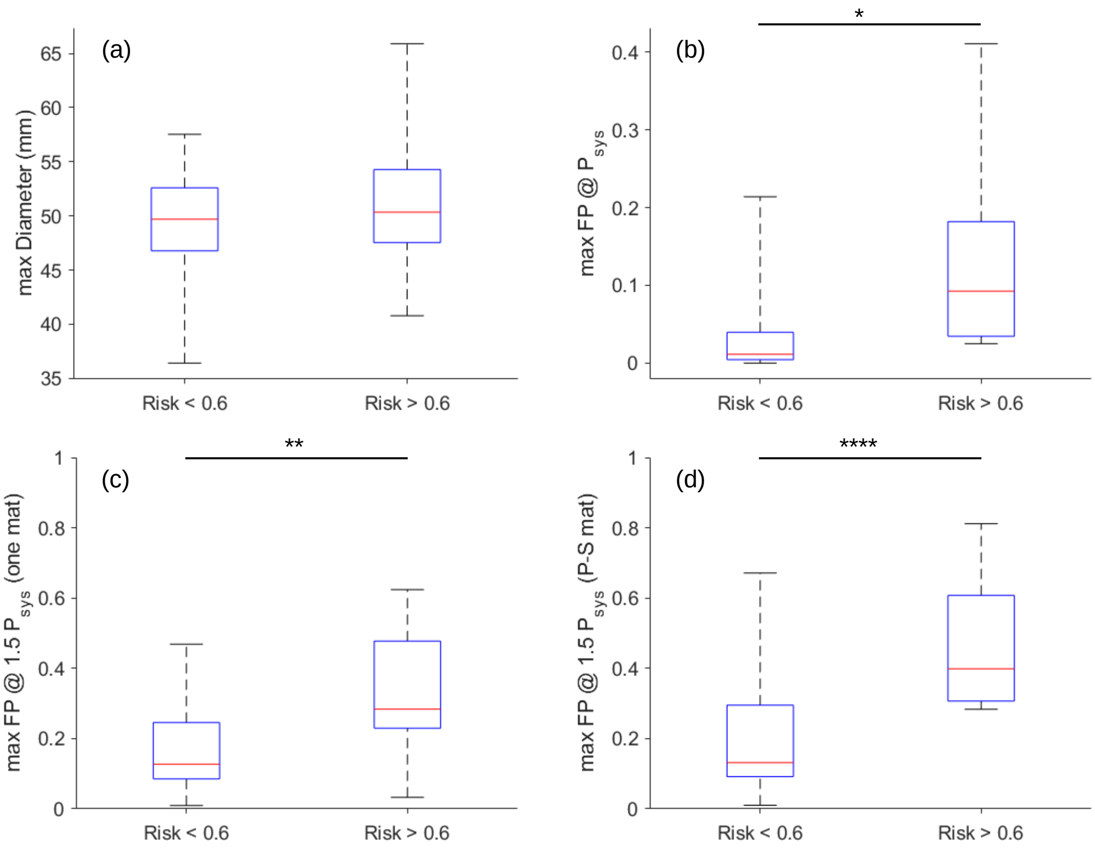

Figure 6.2 - Distribution of failure metrics for high and low risk patients using different stratification methods (Section 6.4). The numerically-reconstructed PRR (Section 6.3) is used as the "ground-truth" risk displayed in the horizontal axis. (a) Method 1: maximum diameter; (b) Method 2: maximum FP evaluated at P_{sys}; (c) Method 3: maximum FP evaluated at $1.5P_{sys}$ using representative hyperelastic properties; and (d) Method 4: maximum FP evaluated at $1.5P_{sys}$ using patient-specific hyperelastic properties. "one mat" stands for representative hyperelastic properties; "P-S mat" stands for patient-specific hyperelastic properties. The red mark indicates the median, and the bottom and top edges of the box indicate the 25th and 75th percentiles, respectively. The whiskers extend to the maximum and minimum. *, **, ** indicates statistical significance levels of $p \leq 0.05$, $p \leq 0.01$, $p \leq 0.0001$, respectively.**

ROC curves of the Method 1~ Method 4 are shown in Figure 6.3. The areas under the curves (AUC), which reflect the discriminative powers of the failure metrics, are 0.5489, 0.8448, 0.7644 and 0.8621, respectively, for Method 1~ Method 4. The diameter criterion has the lowest AUC, while the highest AUC is achieved by FP evaluated under elevated blood pressure using the patient-specific hyperelastic properties, which highlights the potential benefits of incorporating patient-specific hyperelastic properties [99, 100] (our inverse method is developed in CHAPTER 3 and APPENDIX A) in the risk stratification. Comparing to FP at P_{sys} without patient-specific hyperelastic properties, the performance is not improved by evaluating FP under elevated blood pressure by using a representative set of hyperelastic parameters.

In general, to evaluate a diagnostic method, an AUC of 0.5 suggests no discrimination, 0.7 to 0.8 is considered acceptable, and 0.8 to 0.9 is considered excellent [232].

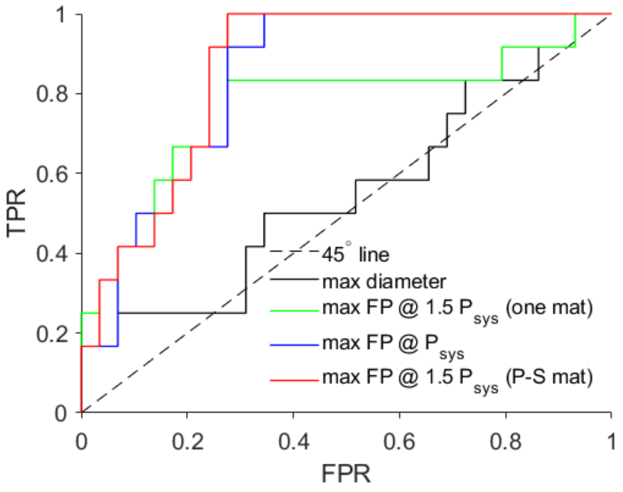

Figure 6.3 - ROC curves of different risk stratification methods. The plots are generated using false positive rate (FPR) versus true positive rate (TPR). "one mat" stands for representative hyperelastic properties; "P-S mat" stands for patient-specific hyperelastic properties. AUC for the diameter (Method 1), FP at P_{sys} (Method 2), FP at $1.5P_{sys}$ using representative hyperelastic properties (Method 3), and FP at $1.5P_{sys}$ using patient-specific hyperelastic properties (Method 4) are 0.5489, 0.8448, 0.7644 and 0.8621, respectively.

6.5.2 Comparison between Probabilistic and Deterministic metrics

Method 2 and Method 4 (Section 6.4) can be equipped with the probabilistic metric (FP in Eqn. (5.12)) or the deterministic TH metric ($\varLambda$ in Eqn. (5.3) with typical failure parameters $X = 2.5MPa$ and $Y = 1.2MPa$). FP and TH of the 41 ATAA patients (Group 2) at P_{sys} and $1.5P_{sys}$ were computed by using the patient-specific geometries and systolic blood pressures. The results are shown in Table 6.2. Difference between high and low risk groups is significant ($p = 0.0099$) using the maximum TH at P_{sys} (Method 2), while $p = 0.0121$ when the same method is used with FP. Using patient-specific hyperelastic properties and the maximum TH at $1.5P_{sys}$ (Method 4), the p-value is low ($p = 0.0017$). The most significant difference was found for FP using Method 4 ($p = 0.0001$). The results are summarized in Figure 6.4.

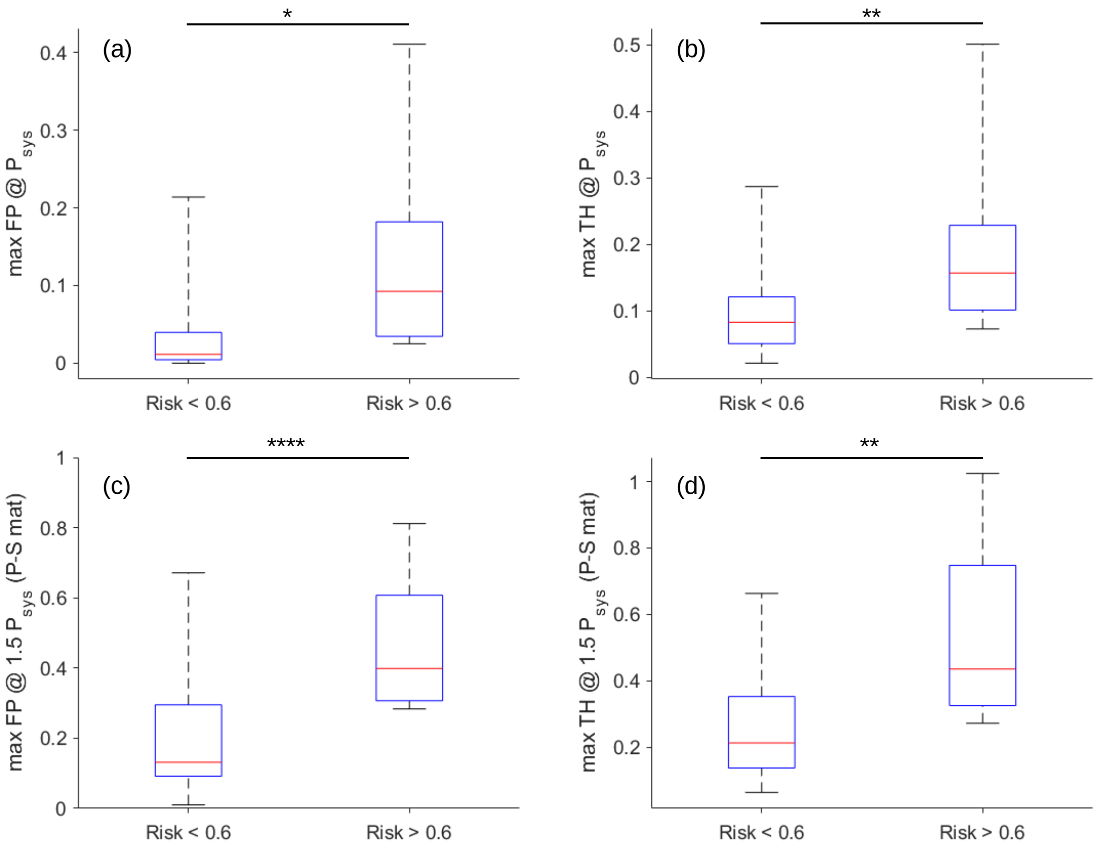

Figure 6.4 - Distribution of probabilistic (FP) and deterministic (TH) failure metrics for high and low risk ATAA. The numerically-reconstructed PRR (Section 6.3) is used as the "ground-truth" risk displayed in the horizontal axis. (a) and (b) Method 2: FP and TH evaluated at P_{sys}; (c) and (d) Method 4: FP and TH evaluated at $1.5P_{sys}$ using patient-specific hyperelastic properties. "P-S mat" stands for patient-specific hyperelastic properties. The red mark indicates the median, and the bottom and top edges of the box indicate the 25th and 75th percentiles, respectively. The whiskers extend to the maximum and minimum. *, **, ** indicates statistical significance levels of $p \leq 0.05$, $p \leq 0.01$, $p \leq 0.0001$, respectively.**

ROC curves of the maximum FP and the maximum TH metrics are demonstrated in Figure 6.5 for failure metrics evaluated at P_{sys} (Figure 6.5(a)) and $1.5P_{sys}$ (Figure 6.5(b), using patient-specific hyperelastic properties). The AUC is 0.8448, 0.8017, 0.8621 and 0.8362, respectively, for FP at P_{sys}, TH at P_{sys}, FP at $1.5P_{sys}$ and TH at $1.5P_{sys}$. The results indicate that the probabilistic metric FP has a better discriminative power comparing to the deterministic metric TH.

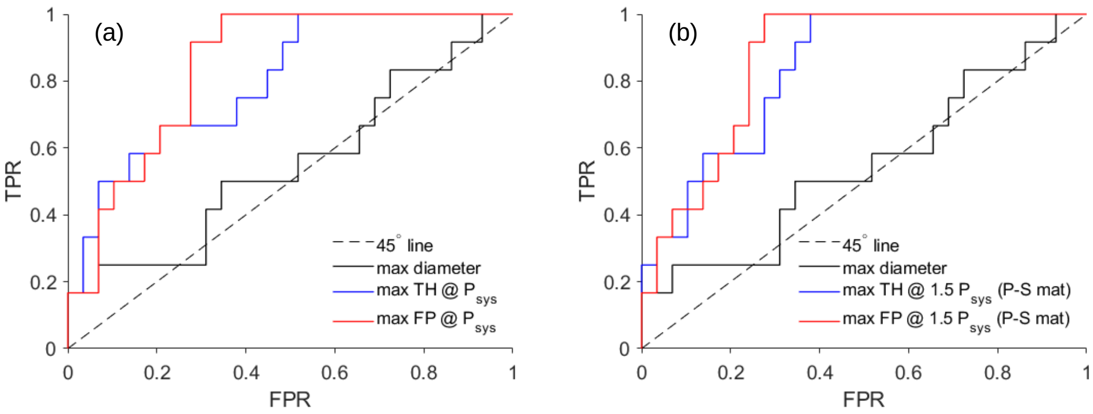

Figure 6.5 - ROC curves of diameter criterion, probabilistic (FP) and deterministic (TH) failure metrics. The plots are generated using false positive rate (FPR) versus true positive rate (TPR). (a) Method 2: FP and TH evaluated at P_{sys}; (b) Method 4: FP and TH evaluated at $1.5P_{sys}$ using patient-specific hyperelastic properties. "P-S mat" stands for patient-specific hyperelastic properties. AUC for the diameter, FP at P_{sys}, TH at P_{sys}, FP at $1.5P_{sys}$ and TH at $1.5P_{sys}$ are 0.5489, 0.8448, 0.8017, 0.8621 and 0.8362, respectively.

6.6 Discussion

Using reconstrued data, this study demonstrated that 1) the performance of FP is superior to the standard TH metric with typical failure parameters; and 2) patient-specific hyperelastic properties can help to improve the performance of probabilistic FP metric in ATAA risk stratification.

6.6.1 Discriminative Power of Different Risk Assessment Methods

Using the reconstructed risk of 41 ATAA patients, we found that the biomechanical failure metrics have more discriminative power (AUC) than the maximum diameter criterion, which is consistent with recent studies [60, 61] investigating real ruptured and intact cases of abdominal aortic aneurysm (AAA). Using patient-specific hyperelastic properties and FP, the highest AUC is achieved (Figure 6.3), which highlights the potential benefit of identifying patient-specific hyperelastic properties ([99, 100], CHAPTER 3, and APPENDIX A) for risk stratifications. When patient-specific hyperelastic properties are not available, no additional benefit was found by assuming representative properties. In this case, failure metric can be evaluated on image-derived geometries using static determinacy ([135, 136] and CHAPTER 2) without the need of patient-specific hyperelastic properties. In this study, an ideal scenario was investigated, in which the wall thickness was assumed to be accurately measured from MRI [22-25] or high-resolution CT scans [26]. Hence, AUCs of the failure metrics could be close to the upper limits.

6.6.2 Limitations

ATAA is a silent killer, the majority of patients remain asymptomatic until rupture or dissection occurs [5], which makes it difficult to obtain clinical CT images of ruptured ATAA. Sample size for ruptured AAA is also a challenge , for instance, a ruptured sample size of 7 was used by Polzer and Gasser [74]. A prospective study [61] collected 13 ruptured cases in about 2~3 years of follow up period. In this study, ATAA risks (PRR) were retrospectively reconstructed by FE simulation using pre-operative images and tissue testing data of 41 patients who underwent elective surgery. These patient-specific images and tissue sample are often more accessible from clinics. We may be able to expand our validation data size once more CT images and tissue samples are collected.

In the current work, reconstruction of ATAA risk (PRR) was based on the following two assumptions: (1) Wall thickness and material properties were assumed to be homogenous across the ATAA geometry. It is known that the hyperelastic and failure properties of aortic wall are regional dependent [21, 147]. The wall thickness may also have spatial variations, and heterogeneity of wall thickness and material heterogeneity could be correlated [188]. In the FE simulations, a simplified case was considered, where the wall thickness was calculated from an averaged experimentally measured value, and the experimentally-derived hyperelastic behavior was used for the entire ATAA geometry. (2) Residual stresses were not incorporated in the FE simulations. In future studies, residual deformation could be taken into considerations by means of the GPA algorithm [133] or volumetric growth approach [152]. However, it is worth noting that the mean wall stress computed by Method 2 (Section 6.4) is independent of residual stresses (CHAPTER 2).

6.7 Summary

In this chapter, numerically-reconstructed risks of additional 41 ATAA patients were used to evaluation different risk assessment methods (diameter, with or without patient-specific hyperelastic properties). Performance of these methods were compared. The probabilistic FP metric outperforms the deterministic TH metric using the reconstructed data. The results also revealed potential benefit of identifying patient-specific hyperelastic properties in ATAA risk stratification.

CHAPTER 7. CONCLUSIONS

In this chapter, the main contributions of this thesis are summarized. Clinical impacts and future directions related to this thesis are briefly discussed.

7.1 Summary

In CHAPTER 1, the ATAA diagnosis and treatment as well as the current diameter criterion were briefly introduced. Next, we introduced experimental biomechanical testing methods of ATAA tissues. Hyperelastic and failure models of aortic tissues were discussed. Biomechanical ATAA risk assessment methods hold promises. Furthermore, we summarized the current state-of-the-art methods to identify material properties. Limitations of existing methods for identification of *in vivo* hyperelastic properties of the aortic wall were discussed. We also introduced some of the applications of machine learning techniques in the field of biomechanics. The objectives and significance of this thesis were outlined.

In CHAPTER 2, we demonstrated that, due to static determinacy, the transmural mean stress in the *in vivo* configuration of ATAA is independent of mechanical properties and residual deformations. The forward penalty method, which enforces a rigid condition as the penalty treatment, can greatly simplify the transmural mean stress computation for patient-specific geometries.

In CHAPTER 3, we developed a novel inverse method for identification of *in vivo* hyperelastic properties of the aortic wall by using *in vivo* geometries at 2 cardiac phases with known blood pressures. This approach leverages the static determinacy of the aortic wall, and forward penalty method validated in CHAPTER 2 was used to compute transmural mean stress in the two phases. Computationally-expensive FE simulations were avoided by building the objective function on stress, the inverse method greatly reduces the computational cost. Good agreements were achieved in the numerical verification. The inverse approach was applied to pre-operative gated CT scans of two ATAA patients. For comparison, surgically-resected tissue samples were obtained for experimental planar biaxial tests. Relatively close match was achieved in terms of the *in vivo*-identified and *ex vivo*-fitted stress-stretch response.

In CHAPTER 4, we proposed a novel ML approach for fast and accurate constitutive parameters of the aortic wall from *in vivo* systolic and diastolic geometries with known blood pressures. The ML-model consists of an unsupervised shape encoding module and a supervised nonlinear mapping module. Numerically-generated datasets were used for training, validating and testing the ML-model. This novel ML approach can expedite the procedure of *in vivo* material parameter identification: once the ML-model is trained, the hyperelastic parameters can be predicted within one second.

In CHAPTER 5, we developed a novel probabilistic and anisotropic failure metric using failure property data from 84 ATAA patients. Off-axis tension tests were performed on aortic tissues of 4 porcine individuals and 2 human ATAA patients. The Tsai-Hill (TH) failure criterion demonstrates a good fitting capability with the off-axis data. The novel failure probability (FP) metric, which was derived based on the TH failure theory, incorporates uncertainties of the anisotropic failure properties. Using the two patients' *in vivo* identification and *ex vivo* testing data obtained in CHAPTER 3, our results showed that the FP metric distributions are similar under elevated blood pressure.

In CHAPTER 6, CT images and matching tissue samples were used to numerically reconstruct “ground-truth” risk of additional 41 ATAA patients The ground-truth risks were used to evaluation different risk assessment methods (diameter, with or without patient-specific hyperelastic properties). Discriminative powers of these methods were compared. The probabilistic FP metric outperforms the deterministic TH metric using the reconstructed data. The results also revealed potential benefit of identifying patient-specific hyperelastic properties in ATAA risk stratification.

The main contributions of this thesis are:

1) The forward penalty approach for computation of transmural mean stress on the aortic wall without knowing patient-specific mechanical properties and residual deformations.

2) A novel inverse method for identification of *in vivo* hyperplastic properties of the aortic wall based on a stress-matching strategy.

3) Validation of the developed inverse approach using ECG-gated CT scans and matching tissue samples.

4) A ML approach for fast and accurate identification of *in vivo* hyperplastic properties.

5) A novel probabilistic and anisotropic failure metric based on the Tsai-Hill failure theory.

5) Comparison of different risk assessment methods using retrospective risks reconstructed from CT image data and matching tissue samples.

7.2 Clinical Relevance

In CHAPTER 2, we have shown that the forward penalty approach can be used for computation of transmural mean stress on the aortic wall without knowing patient-specific mechanical properties and residual deformations. This method greatly simplifies the wall stress computation process, and may enable patient-specific wall stress analysis directly using ATAA geometries constructed from clinical images.

The developed inverse method and ML method in CHAPTER 3 and CHAPTER 4 may be integrated for *in vivo* material hyperplastic property identification using multi-phase clinical images. The ML approach can be applied for fast identification when an ATAA shape is similar to the training data; if not, the inverse method can be invoked for identification without loss of accuracy. The developed identification approaches can be used to evaluate age-dependent *in vivo* hyperleastic response of ATAA. The approaches may facilitate clinical biomechanical TAA risk assessment.

The developed probabilistic and anisotropic failure metric in CHAPTER 5 may facilitate clinical biomechanical ATAA risk assessment since it incorporates uncertainties and anisotropy of the wall strengths. With more data becomes available, the novel failure metric may be updated. The failure metric may be upgraded to reflect failure probability conditioned on patient-specific information (age, gender, familial history, etc.).

Using numerically-reconstructed ATAA risk, the results in CHAPTER 6 showed that the diameter may be an unreliable predictor of ATAA risk. Biomechanical ATAA risk assessment can be benefit from fully exploit the clinically-available image data, which contains information on patient-specific geometry and hyperelastic properties. ATAA risk stratification may benefit from identifying patient-specific hyperelastic properties.

7.3 Future Directions

7.3.1 Refinement of the Computational Framework for ATAA Risk Assessment

Limitations of the current methods may be addressed in future studies. In the developed inverse method, we only considered uniform wall thickness of the aorta segment. However, it is well known that the wall thickness is non-uniform, which can have impact on the wall stress computation. Using MRI [22-25] or high-resolution CT scans [26], the wall thickness may be measurable for individual patient. The non-uniform wall thickness can be measured from non-contrast and contrast CT scans [233]. Joldes et al. [136]combined CT and MRI to extract heterogenous wall thickness of abdominal aorta. In future works, methods can be investigated to construct ATAA geometry with non-uniform wall thickness. In the current work, to generate training data for the ML model, a uniform wall thickness at the systolic phase was used. In future works, using the constructed ATAA geometry with non-uniform wall thickness, the full 3D geometries can be encoded, and therefore the thickness field will be naturally accommodated in the ML approach. It is expected that with the wall thickness accurately determined, the biomechanical ATAA risk assessment can significantly outperform the current diameter criterion.

In the current methods, we assumed that residual stresses have minimal impact on the material parameter identification. In future works, this limitation may be accommodated by developing robust methodologies to incorporate residual stresses into the computational models. The parameters of the residual stresses can also vary greatly among different patients. It might be possible to identify these parameters from clinical images, but they may be nonlinearly coupled with the material hyperelastic parameters. It is unclear whether simultaneous identification of both residual stress and hyperelastic parameters is feasible. The identification of both residual deformation and material parameters warrants further investigations.

In CHAPTER 4, to expedite generation of training, validation and testing data, the systolic and diastolic pressure were assumed to be 120mmHg and 80 mmHg, respectively for all cases. To handle pressure variations, it may be computationally expensive to generate FE simulation data at a wide range of systolic and diastolic pressure levels. In future studies, active learning techniques [234] may be used to reduce the computation cost for dataset generation.

7.3.2 Identification of In Vivo Heterogeneous Hyperelastic Properties

In CHAPTER 3, we developed a novel inverse method for identification of homogenous *in vivo* hyperelastic properties of the aortic wall, while it is well known that ATAA has heterogeneously distributed material properties. The approach can be extended to heterogeneous identification by slightly altering the workflow, i.e., evaluating one objective function g_{err} for one element or one group of elements at a time. However, regularization needs to be added to the objective function to ensure that the identified material parameter field is smooth, which may cause high computational cost using a global optimization method. The regularized optimization problem may be solved using distributed optimization algorithms such as the alternating direction method of multipliers (ADMM) [235].

For the ML approach in CHAPTER 4, homogenous distribution of the material properties was assumed. The ML approach may be improved for heterogenous identification. To encode and decode heterogenous material parameter fields, Low rank approximation (LRA) may be used as in [119].

7.3.3 Develop and Validate Tissue Failure Criteria with Distributed Fiber Orientations

In a recent study [69], we proposed a novel stress-based anisotropic failure criterion with dispersed fiber orientations. In the new failure criterion, the overall failure metric is computed by using angular integration of failure metrics in all directions. Affine rotations of fiber orientations due to finite deformation are taken into account in an anisotropic hyperelastic constitutive model. To examine fitting capability of the failure criterion, the off-axis uniaxial tension testing data (Section 5.2.2) were employed. The dispersed fiber failure criterion demonstrates a good fitting capability with the off-axis testing data. As can be seen in Figure 7.1 under simulated biaxial stress conditions, the dispersed fiber failure criterion predicts a smaller failure envelope comparing to those predicted by the traditional anisotropic criteria without fiber dispersion (Tsai-Hill and Hashin-Rotem), which highlights the potentially important role of fiber dispersion in the failure of the aortic wall. The results suggest that the deformation-dependent fiber orientations may need to be considered when wall strength determined from uniaxial tests are used for in vivo biomechanical analysis. In future works, more investigations are needed to determine biaxial failure properties of the aortic wall.

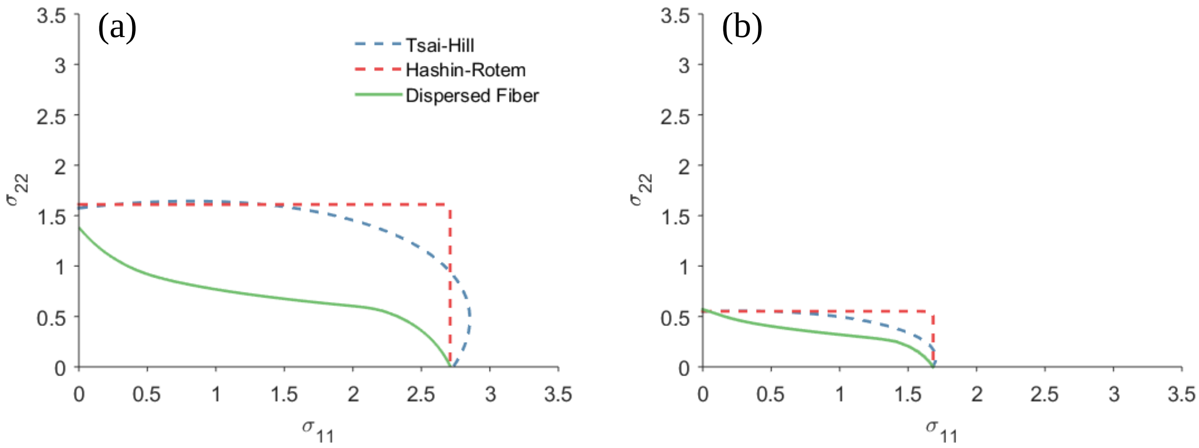

Figure 7.1 - Failure envelopes in the σ_{11}-σ_{22} plane for the human ATAA patients. (a) and (b) represent patient 1 and 2, respectively. Failure parameters are obtained from fitting off-axis testing data.

7.3.4 Evaluate ATAA Risk Assessment Methods using Clinical Data

For abdominal aortic aneurysm (AAA), biomechanical risk assessments were performed using retrospective and prospective clinical data of ruptured and intact aneurysms. For instance, Gasser et al. [59] performed FE simulations to predict biomechanical indices of 203 non-ruptured and 40 ruptured AAA patients. Significant difference between the non-ruptured and ruptured group was found using the biomechanical indices. Polzer et al. [60] compared biomechanical indices for 19 ruptured and 24 intact AAA in a retrospective study. The authors found that the biomechanical indices have more discriminative power than diameter in predicting rupture of asymptomatic AAA. Doyle et al. [61] followed up 295 AAA patients in a prospective study. The authors found that biomechanical index is a strong independent predictor of

AAA events of rupture or repair. For future works, ATAA risk assessment methods can be evaluated retrospectively and prospectively in the same fashion using clinical data. Clinical effectiveness and discriminative power of the biomechanical-based models can be evaluated; therefore, the future retrospective and prospective may facilitate clinical application of biomechanical ATAA risk assessment.

APPENDIX A. ESTIMATION OF IN VIVO MECHANICAL PROPERTIES OF THE AORTIC WALL: A MULTI-RESOLUTION DIRECT SEARCH APPROACH

The patient-specific biomechanical analysis of the aorta requires *in vivo* mechanical properties of individual patients. Existing approaches for estimating *in vivo* material properties often demand high computational cost and mesh correspondence of the aortic wall between different cardiac phases. In this study, we propose a novel multi-resolution direct search (MRDS) approach for estimation of the nonlinear, anisotropic constitutive parameters of the aortic wall. Based on the finite element (FE) updating scheme, the MRDS approach consists of the following three steps: (1) representing constitutive parameters with multiple resolutions using principal component analysis (PCA), (2) building links between the discretized PCA spaces at different resolutions, and (3) searching the PCA spaces in a 'coarse to fine' fashion following the links. The estimation of material parameters is achieved by minimizing a node-to-surface error function, which does not need mesh correspondence. The method was validated through a numerical experiment by using the *in vivo* data from a patient with ascending thoracic aortic aneurysm (ATAA), the results show that the number of FE iterations was significantly reduced compared to previous methods. The approach was also applied to the *in vivo* CT data from an aged healthy human patient, and using the estimated material parameters, the FE-computed geometry was well matched with the image-derived geometry. This novel MRDS approach may facilitate the personalized biomechanical analysis of aortic tissues, such as the rupture risk analysis of ATAA, which requires fast feedback to clinicians. Results have been published in [101].

A.1 Introduction

With the advancement of clinical cardiac imaging modalities and computational tools, patient-specific biomechanical evaluation of aortic disease conditions, such as aortic aneurysm dissection and rupture, is getting closer to reality. Among the three key components necessary for an engineering biomechanics analysis, i.e., geometries, material properties, and loading boundary conditions, the patient-specific *in vivo* material properties is clearly the biggest unknown. Indeed, accurate estimation of *in vivo* mechanical properties of the aortic wall, which is nonlinear and anisotropic, has been a challenging problem in the field of cardiovascular biomechanics for several decades [123].

The methods that use the strain/displacement/stress field measurements to back out the material properties of the aortic wall are collectively referred as the inverse method [81]. Based on the measurement of *in vitro* displacement field from an unloaded configuration to the loaded state [79, 80], an error function is often defined to quantify the discrepancy between the predicted and experimental results. The constitutive parameters, used to define the material properties, are inversely identified by minimizing the error function using certain iterative schemes. Accordingly, the virtual field method [81] has been developed for extracting constitutive parameters from *in vitro* full-field measurement data [82, 83] of blood vessels. However, the unknown unloaded state makes it a challenging task to estimate the constitutive parameters from *in vivo* loaded geometries.

To estimate the *in vivo* mechanical properties, simplifications and assumptions were made in several studies. By assuming linear elastic constitutive relations, [91], [92] and [93] identified linear elastic material parameters from *in vivo* images. By assuming a perfect cylindrical shape of the arteries, [84] identified Fung-type material parameters, [85-88] estimated material parameters using the constitutive model proposed in [33] together with geometrical parameters, [90] estimated the Gasser–Ogden-Holzapfel (GOH) model [34] parameters. [96] proposed a multiple linear regression-based method to estimate the constitutive parameters by assuming a linear relation between the volume of the aorta and the constitutive parameters of the Demiray model.

To account for the patient-specific geometries, the FE updating scheme is typically used to estimate *in vivo* mechanical properties from multi-phase cardiac images, following the steps of: (1) recovering the unpressurized geometry, (2) deforming the geometry with *in vivo* loading and boundary conditions and initial candidate constitutive parameters, and (3) by using certain optimization methods, the estimated constitutive parameters will be iteratively adjusted to ensure certain physical measurements (e.g. strain/displacement) are matched between the FE-deformed configuration and the *in vivo* configuration. This optimization process yields the best set of estimated constitutive parameters. Using such strategies, [98] determined the modified Moony-Rivlin parameters of the carotid artery from 2D slices reconstructed from MRI. [97] evaluated the local wall thickness and material anisotropy of the aorta, while the constitutive parameters were determined through biaxial tests. [99, 100] developed two methods to determine patient-specific GOH material parameters of the human abdominal aorta from *in vivo* 4D ultrasound strain measurements. However, for the FE updating approach, the convexity of the error function is usually not guaranteed, i.e. can have multiple local optima. Different material parameters may be nonlinearly coupled in their contributions to the overall mechanical response. To avoid stuck in the local optima, mixed stochastic-deterministic optimization methods were used by [99, 100]. However, numerous iterations were needed to reach the optimal solution in these methods, often resulting in computing time of 1~2 weeks. The high computational cost could inhibit the practical use of these methods, particularly in a clinical setting requiring rapid feedback to clinicians.

The full-field displacement measurement, which establishes mesh correspondence between different configurations, is often required for the material parameter estimation [79, 82, 99, 100]. The *in vivo* mesh correspondence of the abdominal aorta may be obtained using the 4D ultrasound data [159, 187], for which speckle patterns are used. However, the 4D ultrasound imaging is not routinely used for thoracic aortic wall because of the limited field-of-view [179]. The mesh correspondence can be difficult to obtain from CT and MRI. Thus, the absence of *in vivo* mesh correspondence poses a critical challenge for material parameter identification.

In this study, we proposed a multi-resolution direct search (MRDS) approach for the *in vivo* material parameter estimation of the aortic wall by using *in vivo* loaded geometries at two cardiac phases with known blood pressures. This approach is based on the general framework of FE updating and the objective is to match the FE deformed geometry with the *in vivo* measured geometry by minimizing a node-to-surface error function, which does not require mesh correspondence. The parameter optimization is based on the idea of “coarse-to-fine” search, for which multiple level representations of material parameters with different resolutions are built using principal component analysis

(PCA) prior to the optimization process. The number of FE iterations, compared to previous methods [99, 100], is expected to be significantly reduced. The accuracy of the method was examined by a numerical verification.

A.2 Methods

A.2.1 Prerequisites and Assumptions

The constitutive parameters of homogeneous (average) mechanical properties of the aortic wall segment will be estimated in our approach, which has three main assumptions. (1) *In vivo* loaded geometries of the aorta and blood pressure levels are known at 2 phases, e.g., diastole and systole. However, mesh correspondence between the two phases is not required (i.e. displacement field can be unknown); (2) Wall thickness of the unpressurized geometry is assumed to be a known constant according to our previous experiments [57]; and (3) the residual stresses are ignored. The unpressurized geometry is assumed to be the reference configuration.

A.2.2 Constitutive Model

The Gasser-Ogden-Holzapfel (GOH) model [34] was used to model the mechanical response of the aortic wall tissue. In this model, tissues are assumed to be composed of a matrix material with two families of embedded fibers, each of which has a preferred direction. The fiber directions can be mathematically described using two unit vectors. The strain energy function can be expressed by

$$\Psi = C_{10}(\bar{\boldsymbol{I}}_1 - 3) + \frac{k_1}{2k_2}\sum_{i=1}^{2}[exp\{k_2[\kappa\bar{\boldsymbol{I}}_1 + (1 - 3\kappa)\bar{\boldsymbol{I}}_{4i} - 1]^2\} - 1] \tag{A.1}$$

where C_{10} is a material parameter to describe the matrix material. k_1 is a positive material parameter that has the same dimension of stress, while k_2 is a dimensionless parameter. The deviatoric strain invariant $\bar{\boldsymbol{I}}_1$ is used to characterize the matrix material, and the deviatoric strain invariant $\bar{\boldsymbol{I}}_{4i}$ is used to characterize the fiber families. $\bar{\boldsymbol{I}}_{4i}$ is equal to squares of the stretches in the fiber directions. κ is used as a dispersion parameter describing the distribution of fiber orientation. When $\kappa = 0$, the fibers are perfectly aligned. When $\kappa = 0.33$, the fibers are randomly distributed, and the material becomes isotropic. The mean fiber directions were assumed symmetric with respect to the circumferential axis of the local coordinate system. The parameter θ defines the angle between one of the mean local fiber direction and the circumferential axis of the local coordinate system. Thus, the five material parameters in this model need to be identified, i.e., $(C_{10}, k_1, k_2, \kappa, \theta)$. The constitutive model is a built-in model in ABAQUS 6.14. Shell elements were used to model the aortic wall, by which the incompressibility of the aortic wall is enforced.

A.2.3 Workflow of Constitutive Parameter Estimation

The workflow for constitutive parameter estimation is illustrated in Figure A.1. Briefly, given a set of material parameters, the unpressurized geometry is first recovered from the *in vivo* diastolic geometry using the modified version of backward displacement method [121, 140]; and the systolic pressure is applied to the unpressurized geometry in FE simulation; then the simulated systolic geometry Ω_{sys}^{FE} is compared with the measured systolic geometry Ω_{sys} reconstructed from *in vivo* image. By using the multi-resolution direct search (MRDS) method (to be described below in detail), the constitutive parameters are adjusted to minimize the average node-to-surface distance between the measured systolic geometry Ω_{sys} and FE deformed systolic geometry Ω_{sys}^{FE}.

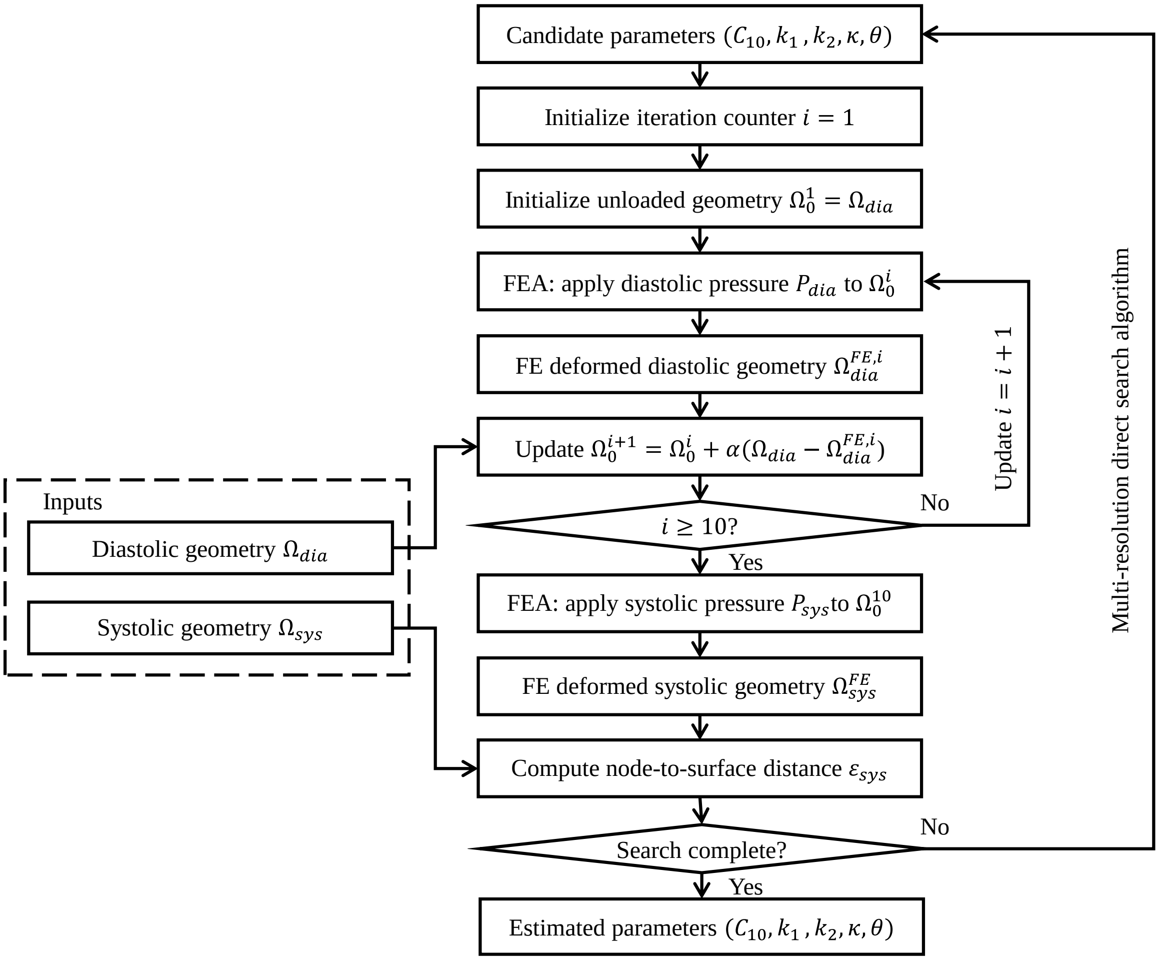

Candidate parameters $(C_{10}, k_1, k_2, \kappa, \theta)$
Initialize iteration counter $i = 1$
Initialize unloaded geometry $\Omega_0^1 = \Omega_{dia}$
FEA: apply diastolic pressure P_{dia} to Ω_0^i
FE deformed diastolic geometry $\Omega_{dia}^{FE,i}$
Update $\Omega_0^{i+1} = \Omega_0^i + \alpha(\Omega_{dia} - \Omega_{dia}^{FE,i})$
$i \geq 10?$
No
Yes
Update $i = i + 1$
FEA: apply systolic pressure P_{sys} to Ω_0^{10}
FE deformed systolic geometry Ω_{sys}^{FE}
Compute node-to-surface distance ε_{sys}
Search complete?
No
Yes
Estimated parameters $(C_{10}, k_1, k_2, \kappa, \theta)$
Multi-resolution direct search algorithm
Inputs
Diastolic geometry Ω_{dia}
Systolic geometry Ω_{sys}

Figure A.1 - Flow chart of the material parameter estimation process. The backward displacement iteration is set to be 10 according to [140]

We define the node-to-surface distance between a node $\boldsymbol{X}$ of a quadrilateral shell mesh surface and a triangulated mesh surface Ω as

$$dist(\boldsymbol{X}, \Omega) = \min_{\boldsymbol{Z} \in \Omega} \|\boldsymbol{Z} - \boldsymbol{X}\| \tag{A.2}$$

where $\boldsymbol{X}$ is the coordinate vector of a node; $\boldsymbol{Z}$ is a point on the triangulated mesh surface Ω (it may be located on a vertex, edge or face). $\|\blacksquare\|$ denotes 3D Euclidean norm. Through optimization, for $\boldsymbol{X}$, the shortest distance to the surface Ω can be obtained. Note that the order of $\boldsymbol{X}$ and Ω matters, i.e., $dist(\boldsymbol{X}, \Omega) \neq dist(\Omega, \boldsymbol{X})$. This distance measure will be used to define an objective function which compares the FE deformed geometry Ω_{sys}^{FE} and the measured geometry Ω_{sys}.

In order to have the symmetric property, the objective function, which measures the average node-to-surface distances between Ω_{sys} and Ω_{sys}^{FE}, is defined as

$$\varepsilon_{sys}\left(\Omega_{sys}, \Omega_{sys}^{FE}\right) = \frac{1}{2N} \sum_{n=1}^{N} \left[dist\left(\boldsymbol{X}_n^{FE}, \Omega_{sys}\right) + dist\left(\boldsymbol{X}_n, \Omega_{sys}^{FE}\right)\right] = \varepsilon_{sys}(\Omega_{sys}^{FE}, \Omega_{sys}) \tag{A.3}$$

where $\boldsymbol{X}_n^{FE}$ is the coordinate vector of the nth node on Ω_{sys}^{FE}, and $\boldsymbol{X}_n$ is the coordinate vector of the nth node on Ω_{sys}; N is the number of nodes. Therefore the mean distance ε_{sys} measures the difference between the measured geometry Ω_{sys} and FE deformed geometry Ω_{sys}^{FE}. For simplicity, within Eqn. (A.3), $dist\left(\boldsymbol{X}_n^{FE}, \Omega_{sys}\right)$ and $dist\left(\boldsymbol{X}_n, \Omega_{sys}^{FE}\right)$ have equal weights, because Ω_{sys} and Ω_{sys}^{FE} have the same number of nodes, which is achieved by using the re-meshing algorithm previously developed in our group [140]. For more general cases, one may modify the weights for geometries with unequal number of nodes.

In practice, the surfaces Ω_{sys} and Ω_{sys}^{FE} are first meshed with quadrilateral shell elements (S4R in ABAQUS) for FE simulations, then, for the node-to-surface distance calculations, triangulation was performed on the surface such that a quadrilateral element is divided into two triangle elements without modifying the nodal coordinates.

In general, the material parameter optimization problem associated with Eqn. (A.3) is nonlinear, multivariate and non-convex; and such a problem may exhibit several local optima. Jacobian-based deterministic optimization methods may not guarantee a global optimum. Mixed stochastic-deterministic methods are usually used in the literature [99, 100], where initial values of the material parameters are assigned randomly as the “seeds” for the deterministic optimization methods. However, by directly searching in the constitutive parameter space, these methods often require numerous iterations and thus demand a huge computing time. In this study, we propose a faster approach using the MRDS strategy, which can significantly speed up the optimization process.

A.2.4 The MRDS Strategy

The key idea of the MRDS approach is to decompose the searching space with multiple resolutions, resulting in multiple level representations of the constitutive parameters, from coarse to fine. For simplicity, throughout this study, we will use the term “level” as the abbreviation of “a level of searching space with a certain resolution”. Rather than searching using the gradient of the objective function in the constitutive parameter space, the MRDS maps the constitutive parameters into a new space using principal component analysis (PCA) and searches in the PCA space at different levels and finds the best one. Therefore, to obtain the multiple level representations, the new PCA space must be discretized into numerous points with multiple resolutions (a point corresponds to a set of material parameters); and the points at one level are sparsely linked to the similar points at adjacent levels; and the links are generated according to the Euclidean distance between points. After a search is performed at the current level, the current best point (i.e. a set of material parameters) is selected; and then following the links associated with the selected point, a new search starts at the next level. As a result, the MRDS method operates on the discrete PCA spaces from the first level with the lowest resolution to the last level with the highest resolution, and the best parameter-candidate will be identified eventually.

A.2.4.1 Constitutive Parameter Representations with Multiple Resolutions Using Principal Component Analysis

Following the procedure shown in Figure A.2, in order to obtain the multiple level representations of material parameters, of which the stress-stretch curves are uniformly distributed, we use stress-stretch curves to represent the constitutive parameters, which map the constitutive parameter space to the “stress-stretch curve space”, and then convert the “stress-stretch curve space” to a PCA space and sample the PCA space uniformly.

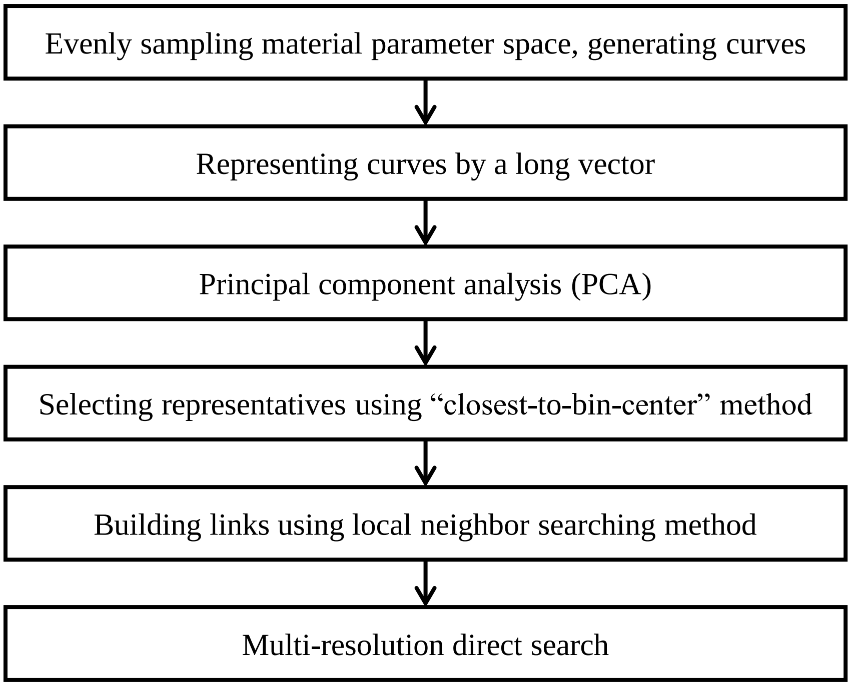
Evenly sampling material parameter space, generating curves
Representing curves by a long vector
Principal component analysis (PCA)
Selecting representatives using “closest-to-bin-center” method
Building links using local neighbor searching method
Multi-resolution direct search

Figure A.2 - Procedures to build resolutions and links.

First, the GOH constitutive parameter space was densely sampled and the corresponding stress-stretch curves were generated. To ensure the constitutive parameters are physiologically possible, i.e. consistent with the experiment data [51, 57, 169], data range constraints were applied on the parameters as shown in Table A.1. Rule-based selection criteria, which were fine-tuned to ensure all the parameters extracted from our previous experiments [57] were included, were applied on the stress-stretch curves. After the sampling and selection processes, a total of 3,409,040 sets of material parameters were obtained. For each set of constitutive parameters, the stress-stretch curves were obtained by simulating stretch-controlled biaxial tension in MATLAB by assuming the tissue is loaded in the plane stress state and the material is incompressible. The simulations were based on 3 protocols: (1) in the circumferential strip biaxial tension, fixing $\lambda_2 = 1$ while increasing λ_1; (2) in the equi-biaxial tension, keeping the ratio $\lambda_1/\lambda_2 = 1$; (3) in the longitudinal strip biaxial tension, fixing $\lambda_1 = 1$ while increasing λ_2. λ_1 and λ_2 is increased gradually by an interval of 0.01. σ_1 and λ_1 denote the circumferential stress and stretch. σ_2 and λ_2 denote the longitudinal stress and stretch. A total of 6 curves from the 3 protocols are generated for each set of material parameters.

Table A.1 - Upper, lower bounds and increment of constitutive parameters for sampling.

	C_{10} (kPa)	$k_1(kPa)$	k_2	κ	$\theta(°)$
Lower bound	0	0	0	0	0
Upper bound	100	10000	50	1/3	90
Increment	5	50	2.5	1/15	15

Furthermore, for each set of material parameters, the stress-stretch curves were sampled at evenly-spaced discrete stress values (21 stress values for the $\sigma_2 \sim \lambda_1$ curve in protocol-1 and the $\sigma_1 \sim \lambda_2$ curve in protocol-3 as the stress level is usually lower in the fixed direction than the tensile direction, 41 stress values for the rest of curves), the corresponding stretch values were recorded and stacked in a vector. Therefore, for each set of material parameters, a vector $\boldsymbol{Y}$ of 206 stretch values is assembled from the 6 stress-stretch curves. Thus, there are one-to-one correspondences between the sets of material parameters and the assembled vectors.

Then, PCA [198] was performed on a total of 3,409,040 vectors to obtain a compact representation of each vector. Briefly, the PCA is a statistical procedure that uses an orthogonal transformation to convert the data to a new coordinate system such that in the new space the first coordinate (principal component) accounts for the largest variability in the data, and each succeeding component in turn has the highest variance. PCA is a standard technique for dimensionality reduction, in which the original data can be well represented (i.e. approximated) by a few principal components in the new space. After applying PCA, each vector $\boldsymbol{Y}$ can be represented by:

$$\boldsymbol{Y} \approx \overline{\boldsymbol{Y}} + \sum_{i=1}^{m} \alpha_i \boldsymbol{PC}_i \tag{A.4}$$

where $\overline{\boldsymbol{Y}}$ represents the population mean of the vectors, and $\boldsymbol{PC}_1, \dots, \boldsymbol{PC}_m$ are the principal components. m is the number of principal components used for the approximation. $\overline{\boldsymbol{Y}}$, m and $\boldsymbol{PC}_i$ are the same for every vector $\boldsymbol{Y}$. $\alpha_1, \dots, \alpha_m$ are the coefficients and different for different vector $\boldsymbol{Y}$, i.e., different material properties, which implies that a set of material parameters is now encoded by a set of coefficients. The first 5 principal components ($m = 5$) are retained to represent the material properties, which accounts for 98.6% of the overall variability, i.e., an approximation error of 1.4%. Therefore each vector $\boldsymbol{Y}$, corresponding to a set of material parameters, can be well represented by a new vector $\boldsymbol{A}$ of only 5 components $\alpha_1, \dots, \alpha_5$. The space of the coefficients is called the PCA space, and an axis in the PCA space is called PC axis. Therefore, sampling the “stress-stretch curve space” is now equivalent to sampling the PCA space.

Next, we obtained multi-level representations of the PCA space by sampling the PCA space with different resolutions (i.e. bin size), from coarse to fine. The “closest-to-bin-center” algorithm was developed to choose the points at a level of the PCA space. Specifically, the PCA space was partitioned into bins (i.e. boxes) with a desirable size at each level. Within a particular bin, the algorithm would search for the closest point to the center of the bin in the PCA space.

$$\boldsymbol{S}_k = \underset{\boldsymbol{A}\in \mathrm{bin}_k}{\arg\min} \|\boldsymbol{A} - \boldsymbol{C}_k\| \tag{A.5}$$

where k stands for the index of the bin, $\boldsymbol{A}$ represents the coordinate vector of a point in the PCA space within the bin_k, $\boldsymbol{C}_k$ is the coordinate vector of the bin center. The closest point to the bin center, $\boldsymbol{S}_k$**,** will be found**.** The PCA space was partitioned at 4 levels also in a coarse-to-fine fashion. For the jth level ($j \leq 4$), the partition was performed only in the sub-space consisting of PC axes from $\boldsymbol{PC}_1$ to $\boldsymbol{PC}_{j+1}$. For example, for the first level, only the $\boldsymbol{PC}_1$~$\boldsymbol{PC}_2$ plane are partitioned, and the bin (i.e. 2D square) center coordinates for higher dimensions are set to zeros (i.e. $C_k(i) = 0\ if\ i > 2$), representing a mean response for the higher dimensions. At each level, sampling the PCA space with certain resolution can be achieved by controlling the bin size. Therefore, by increasing the number of levels, the desired searching accuracy will be achieved. To limit the computing cost, four levels were constructed. At the first level, a total of 12 points were selected from the PCA space, which corresponds to 12 sets of material parameters. Then, a total of 117, 1197 and 10529 points were chosen in the second, third and fourth levels respectively. In Figure A.3, the 4 levels as well as the original 3,409,040 data points are plotted in the projections of the PCA space. For the first and second levels, the stress-stretch curves obtained by using the circumferential strip biaxial protocol are shown in Figure A.4. Therefore, the representation of the material parameter space at a level is a set of points in the PCA space. A level with a higher (or lower) resolution refers to a point-set with a larger (or smaller) number of points, and there are 4 levels, i.e., 4 point-sets, in total.

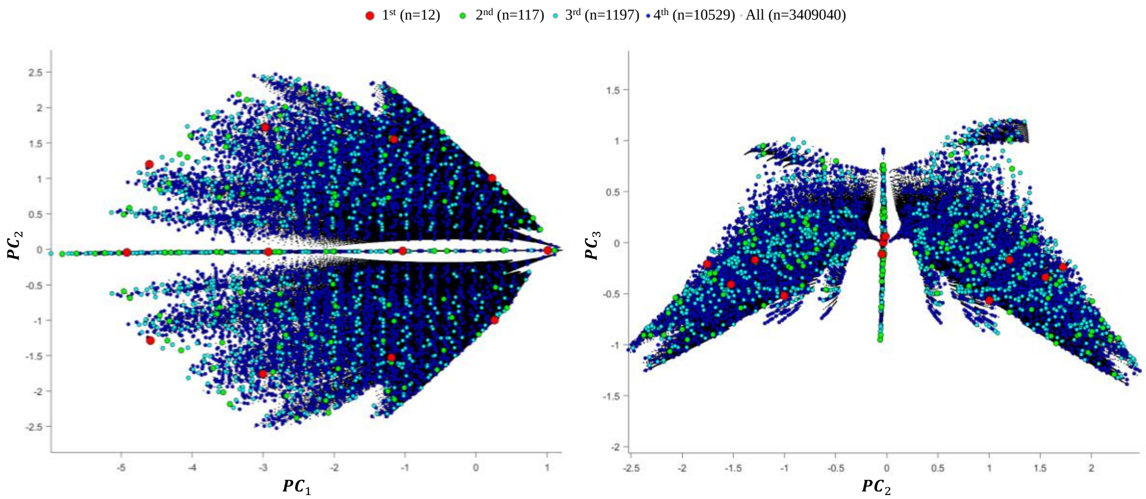

(a) (b)

Figure A.3 - Overlay plots of the 4 levels projected in (a) $PC_1 \sim PC_2$ and (b) $PC_2 \sim PC_3$ plane.

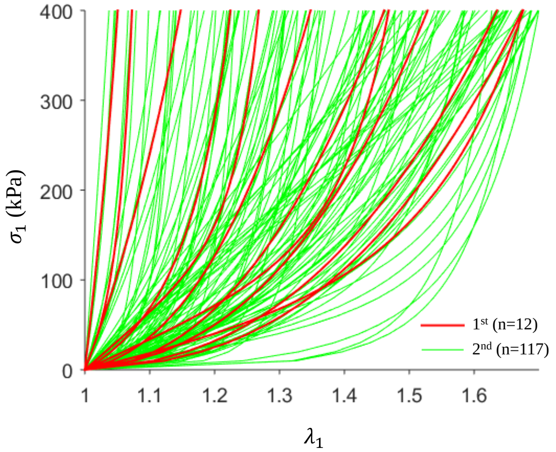

Figure A.4 - The stress-stretch curves in the circumferential strip biaxial protocol for the first and second levels.

Comparison to random sampling in the material parameter space: Although it is much simpler to directly sample the material parameter space with the same range constraints using a uniform random number generator (e.g. “rand” in MATLAB), compared to the procedure in Figure A.2, the resulting stress-stretch curves are distributed randomly as shown in Figure A.5. Our methods ensure that the stress-stretch curves have a nearly uniform distribution at each level.

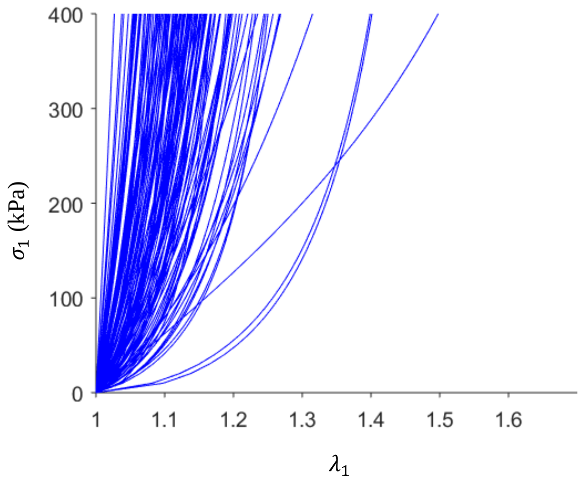

Figure A.5 -The stress-stretch curves in the circumferential strip biaxial protocol obtained by randomly sampling 117 points from the material parameter space.

A.2.4.2 Links between Adjacent Levels

When a point (i.e. a set of material parameters) in the current level is selected by the MRDS (e.g., point A gives a minimum value of Eqn. (A.3) in the current level), further searching needs to be performed at similar points (i.e., with similar material properties) in the next level of a higher resolution. Therefore, hierarchy links between the points at adjacent levels need to be established to guide the MRDS process. To build these links, we followed three intuitive principles: (1) any two points connected by a link should be similar (i.e. similar material properties); (2) every point must have at least one link; and (3) a tradeoff between the total number of links and computational cost should be made: a large number of links can ensure a large search range, but increasing the number of links will lead to the increase of computational cost. To follow the first principle, Euclidean distance in the PCA space was used to measure the distance (i.e. similarity) between two points, and a local neighbor searching method was used to find similar points. For a point A at the current level, the 10 nearest points in the next level with higher resolution (forward linking), and the 2 nearest points in the previous level with lower resolution (backward linking), were identified and linked to point A. Thus, every point in the current level is linked to at least two points in adjacent levels, which satisfies the second principle. By following the first and the second principles, a network of links were built. To reduce the complexity according to the third principle, these links were examined based on the following rule: if the distance between two linked points is larger than a threshold (set to 2), then the link will be removed if not breaking the second principles. After the links are established for all levels, a point at a level will be linked to some points (about 20 on average from forward and backward linking) at the next level with higher resolution. Thus, starting from any point at the first level, the searching can always reach a point at the last level through the links, and for each point at the last level, it can always be traced back through the links to at least a point at the first level. Figure A.6 shows the links between the first two levels in the PCA space.

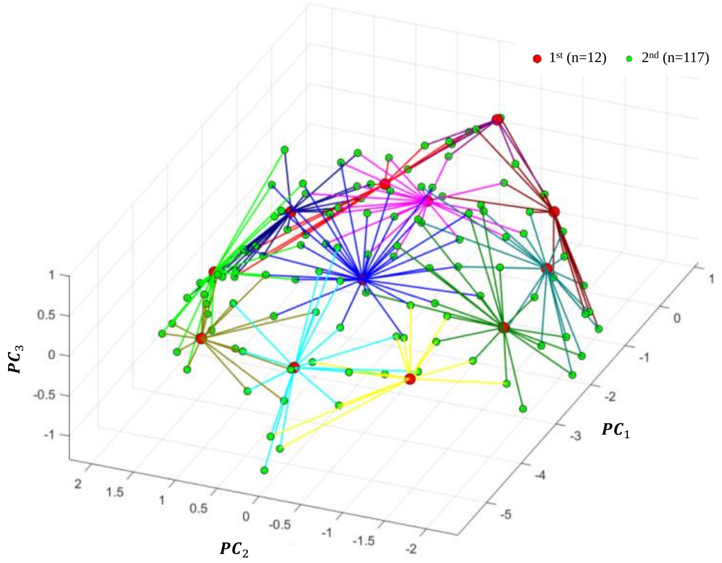

Figure A.6 - Links between the first 2 levels projected in the $PC_1 \sim PC_2 \sim PC_3$ space.

Since MRDS is based on FE updating, searching along a link means performing a series of FE simulations to evaluate the goodness of a set of material parameters (Eqn. (A.3)). Therefore, by controlling the complicity of the link network, we can control the number of FE simulations. Here, the adjustable parameters of the link network are (1) the maximum number of nearest points linked between levels and (2) the distance threshold of each link. In this study, the parameters have been selected such that on average 12(level 1) + 3(level 2~4) × 20 points (i.e. 72 sets of material parameters) will be evaluated by FEA to obtain the final solution, translating to a computational time within 2 days using a quad-core CPU.

A.2.4.3 The Searching Algorithm

The MRDS algorithm starts from the first level by evaluating the 12 points (i.e. parameter-candidates), and the best point will be identified by evaluating the objective function in Eqn. (A.3). The search starts again at the second level by only evaluating the points linked to the best point in the first level. The search will be performed in a similar manner for the third and fourth levels. After the search process completes at the fourth level, the best point will give the final estimation of the constitutive parameters.

A.3 Results

A.3.1 Numerical Validation

The proposed method was validated in a numerical experiment by using a real patient geometry and experimentally-derived material parameters. The clinical cardiac CT image data from a patient with ATAA was obtained at Yale-New Haven Hospital (New Haven, CT). Institutional Review Broad approval to review de-identified images was obtained for this study. The 3D CT image was acquired at the systolic phase, and the systolic pressure was equivalent to 120 mmHg. The patient underwent surgical repair and the ATAA had been excised. The constitutive parameters of the ATAA tissue from this patient were extracted from 7-protocol biaxial tensile tests in a previous study [63]. The geometry of the aorta was reconstructed by using the semi-automatic method developed in our previous study [171], and the branches at the aortic arch were trimmed.

For the validation, the following methods were used to obtain the "measured" geometries at the diastolic and systolic phases. The unloaded geometry of the aortic wall was recovered from the reconstructed geometry from the CT image by using the modified backward displacement method [121, 140], for which the experimentally derived material parameters were utilized and a constant wall thickness of 2 mm at the unloaded state was assumed based on our previous experimental study [57]. The "measured" diastolic and systolic geometries were obtained from FE simulations by applying diastolic (P=80mmHg) and systolic (P=120mmHg) pressures on the unloaded geometry.

In all FE simulations, shell elements S4R in ABAQUS 6.14 and the GOH model were used. Constant pressures were applied uniformly to the inner surface of the FE models, and the boundary nodes of the models, i.e. the proximal and distal ends of the models, were only allowed to move in the radial direction in local cylindrical coordinate systems.

The search process in the validation is shown in Figure A.7. It started from the first level, and the material that led to the minimum objective in Eqn. (A.3) was identified and linked to candidate materials at the second level. Evaluations of the objective were then performed on the linked candidate materials at the second level. The candidate materials gradually clustered together in the subsequent levels, and finally, the estimated curve was very close to the curve corresponding to experimentally-derived material parameters.

The experimentally-derived parameters and the estimated parameters in the numerical validation are shown in Table A.2, and the corresponding stress-stretch curves are depicted in Figure A.8. Although the difference in constitutive parameters is obvious, the biaxial stress-stretch curves have good agreement, which is demonstrated by the coefficients of determination. The results indicate that the estimated mechanical properties resemble the experimentally-derived material response. As shown in Figure A.9, the average of node-to-surface distances between the “measured” and estimated systolic geometries was 0.0818 mm by using Eqn. (A.3), which means the objective function was indeed minimized by the estimated parameters.

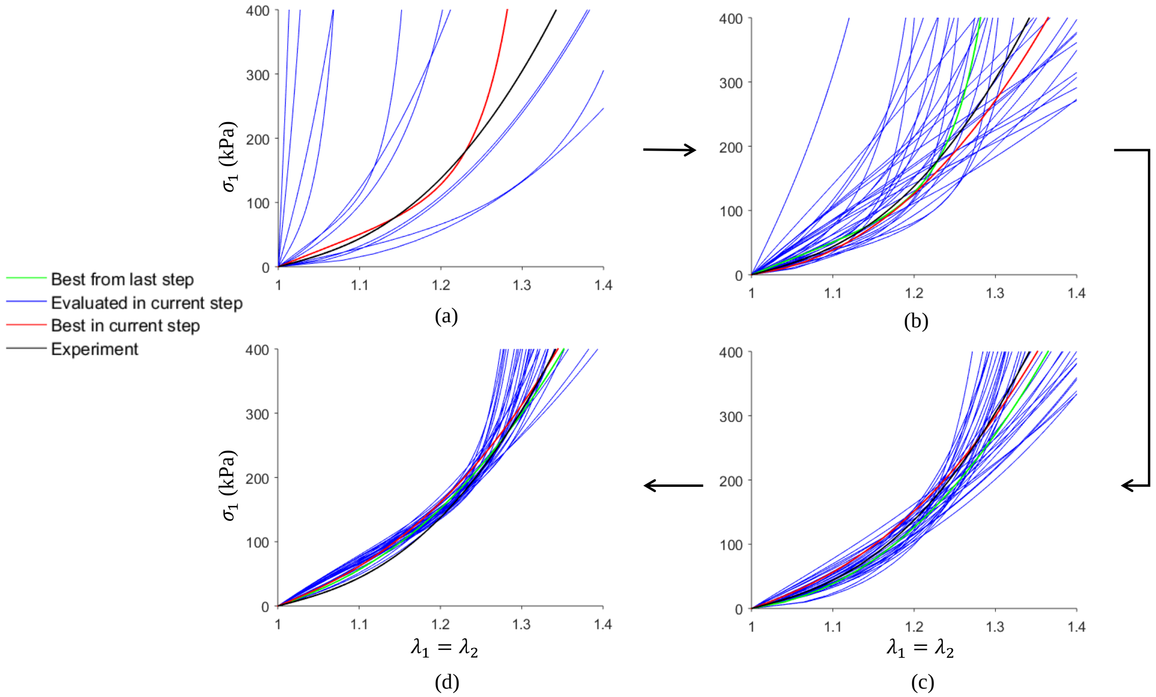

Figure A.7 - Convergence of estimated material parameters to the experimentally-derived material parameters using the MRDS method. The equi-biaxial stress-stretch curves are plotted in each level from (a) to (d).

Table A.2 - Experimentally-derived and estimated constitutive parameters in the numerical validation.

	$C_{10}\ (kPa)$	$k_1 (kPa)$	k_2	κ	$\theta(°)$
Experiment	29.91	512.56	0.00	0.3190	90
Estimated	40	350	0.00	0.2667	60

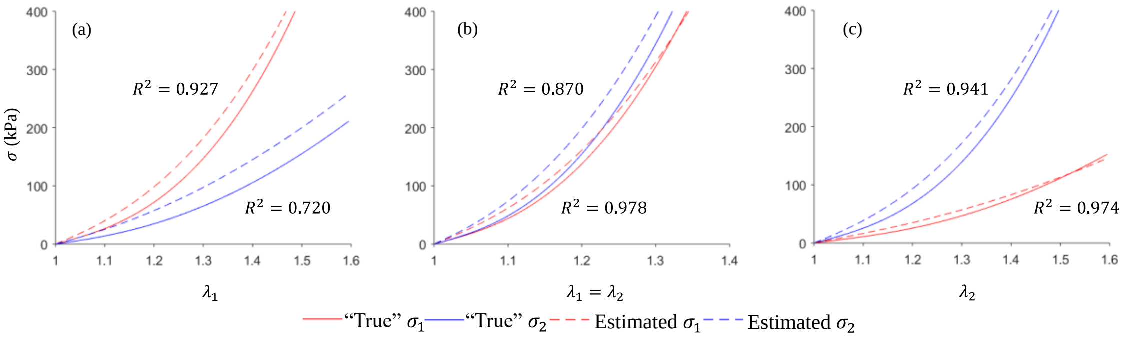

Figure A.8 - Stretch-stress curves in the numerical validation for (a) strip biaxial tension in the circumferential direction; (b) equi-biaxial tension; (c) strip biaxial tension in the longitudinal direction.

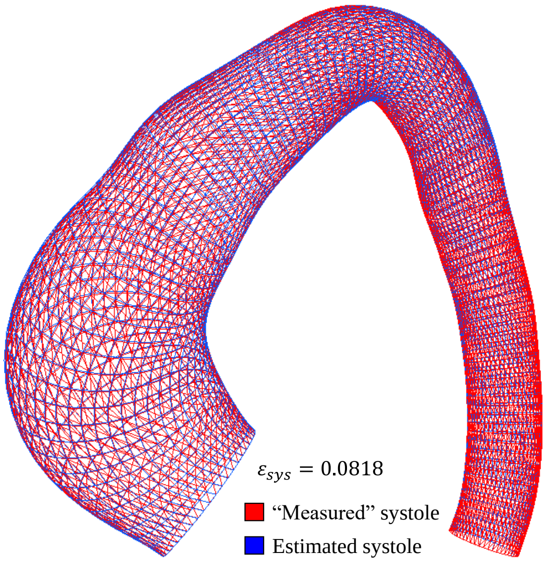

Figure A.9 - Comparison of the "measured" and estimated geometries at the systolic phase in the numerical validation. ε_{sys} is the average of node-to-surface distances between the "measured" and estimated systolic geometries. The "measured" geometry is displayed in triangle mesh, estimated systolic geometry is displayed in quadrilateral shell mesh.

A.3.2 Estimation of In Vivo Mechanical Properties of an Aged Human Healthy Aorta

Full phase cardiac multi-slice CT (MSCT) scans were collected from a patient of age 71 at Hartford Hospital (Hartford, CT). Institutional Review Broad approval to review de-identified images was obtained for this study. The patient did not have TAA, severe aortic stenosis or bicuspid aortic valve. The MSCT examination was performed on a GE LightSpeed 64-channel volume computed tomography scanner. The spatial resolution of the image data was 0.49×0.49×1.25 mm. Images were obtained with helical scanning and ECG gating, encompassing 10 phases over the cardiac cycle. The diastolic and systolic geometries were identified and reconstructed semi-automatically [171]. The iterative closest point (ICP) algorithm [236, 237] was used to rigidly transform the systolic geometry to align with the diastolic geometry. The two geometries were then served as the input to the MRDS method. The MRDS method was then applied to estimate the material parameters for this healthy patient, and the estimated parameters are listed in Table A.3 and the stress-stretch curves are plotted in Figure A.10. Figure A.11 shows the comparison between the estimated, FE deformed systolic geometry and the systolic geometry reconstructed from CT image, and the average of node-to-surface distances was 0.5234 mm by using Eqn. (A.3).

Table A.3 - Estimated constitutive parameters for the healthy aorta.

	C_{10} (kPa)	$\mathrm{k}_1 (kPa)$	k_2	κ	$\theta (°)$
Estimated	30	4750	2.5	0.3333	0

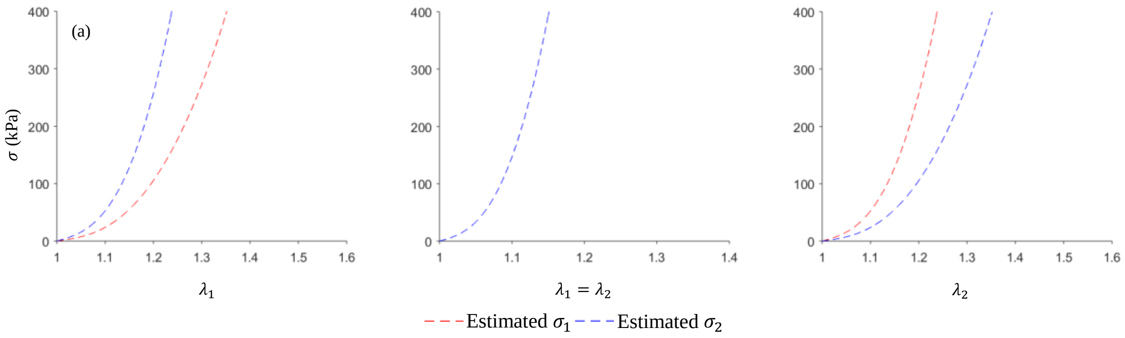

Figure A.10 - Estimated stress-stretch curves for the healthy aorta for (a) strip biaxial tension in the circumferential direction; (b) equi-biaxial tension; (c) strip biaxial tension in the longitudinal direction.

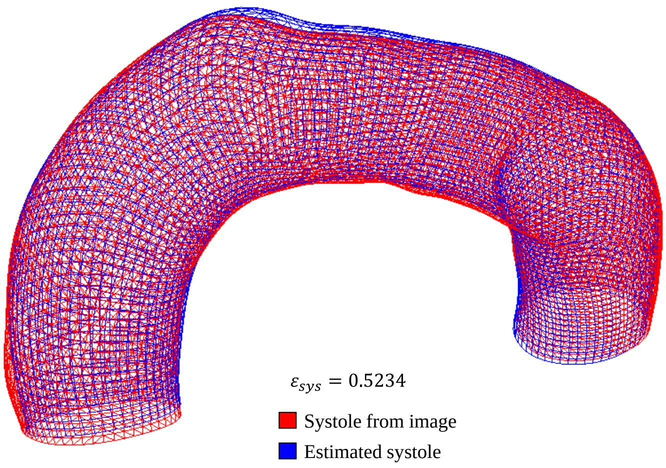

Figure A.11 - Comparison of the estimated systolic geometry and the systolic geometry from CT image for the healthy aorta. ε_{sys} is the average of node-to-surface distances between two geometries. The geometry from CT image is displayed in triangle mesh, estimated systolic geometry is displayed in quadrilateral shell mesh.

A.4 Discussion

Many hyperelastic constitutive models, such as the GOH model [34], have highly coupled material parameters, which cause the parameter estimation difficulty known as the local optima. Not surprisingly, different combinations of C_{10}, k_1, k_2, κ and θ in the GOH model may provide very similar mechanical responses. For the parameter identification methods that search directly on the material parameter space, this coupling among the material parameters will result in numerous local optima. On the contrary, in our proposed MRDS approach, the PCA space derived from the stress-stretch curves, instead of the material parameter space, was used for the search of optimal material properties. Multiple level representations of the PCA space were obtained with different resolutions and with evenly spaced stress-stretch curves. A large set of stress-stretch curves were generated and represented in the PCA space. Candidate material parameters were sampled in the PCA space with multiple bin sizes to achieve multi-resolutions, which was done prior to the MRDS process. The partition of the PCA space may also be achieved by using other clustering methods, such as K-means clustering, but it may not guarantee a uniform partition [238]. In this application, the partition method (section 2.4.1) can produce a nearly-uniformly distributed centers, covering the entire PCA space. The MRDS approach is less computationally expensive than the previous stochastic-deterministic approaches: the MRDS took approximately 1~2 days and less than 1000 FE iterations, using a quad-core CPU with 32GB memory, whereas the previous approaches took about 1~2 weeks and 7400 iterations [99] or 2 weeks and 43500-86900 iterations [100], using similar computing power to ours.

The PCA effectively encodes each set of material parameters as a point in the PCA space, which enables the MRDS approach. Given a new arbitrary set of material parameters, the proposed method can always map it to a point in the PCA space. However, given a new arbitrary point in PCA space, it is difficult to map it back to a set of material parameters. Therefore, a direct search strategy is used in the discretized PCA space instead of gradient-based optimization algorithms which requires the inverse mapping from PCA space to material parameter space. It should be noted that it is possible to use machine learning methods [102] to establish the inverse mapping, enabling gradient-based optimization algorithms in PCA space, which may further improve speed and accuracy and will be our future work.

Despite the discrepancy in constitutive parameters, the biaxial stress-stretch curves have been successfully recovered in the numerical validation. Using the proposed approach, the *in vivo* material parameters of an aged human healthy aorta were estimated, the difference between the FE deformed geometry and the image-derived geometry was about 0.5 mm, approximately the size of a voxel (0.49×0.49×1.25 mm). More accurate solution may be obtained if higher resolution images are available.

A.4.1 Mesh Correspondence

Generally, the mesh correspondence, or full field displacement measurement, is a requirement for both *in vivo* and *in vitro* constitutive parameter estimation. In *in vitro* experiments, this is usually achieved by tracking the markers [82]. It can also be fulfilled by using 4D ultrasound image data processed with speckle tracking algorithms [159]. However, ultrasound imaging has a limited field-of-view [179] and the transthoracic ultrasound signal may be reflected by the rib cage and the sternum [239]. The visualization of the aortic arch may be hampered by the air-filled trachea in the transesophageal echocardiography (TEE) [240]. CT and MRI has been used for imaging thoracic aorta. However, the requirement of mesh correspondence may not be satisfied by using clinical CT or MRI data because there are no image patterns for tracking individual points on the wall, and the performance of surface matching based tracking methods [160] still needs improvement. In the proposed approach, since the objective function is based on the node-to-surface distance, which does not need mesh correspondence, this approach may be suitable for extracting material properties from CT and MRI data.

Our group have previously developed an inverse method (CHAPTER 3) for material parameter identification by using static determinacy [135] and mesh correspondence between two loaded configurations. Under the two assumptions, the stress field on the *in vivo* loaded configuration can be estimated by using infinitesimal linear FEA, and then be used to speed up the parameter identification process. However, the two assumptions of this method significantly limit its potential applications. In this MRDS approach, the two assumptions are no longer needed, which is attractive for many potential applications.

A.4.2 Limitations

CT imaging is usually used for the diagnosis of the aortic aneurysm, especially ATAA, which provides more detailed images and much larger field-of-view than ultrasound imaging. When the contrast agent is used to enhance visualization in cardiac CT imaging, the inner surface of the aorta can be accurately segmented. However, the aortic wall under the loaded state is very thin, about 2 pixels in 64-slice CT, and due to surrounding tissues and partial volume effect (i.e., blurring effect) [241], it is difficult to measure wall thickness field in CT images. Therefore, a constant wall thickness is assumed at the unloaded configuration according to our previous experimental results [57]. The heterogeneity of the wall thickness may have an impact on the estimation of the constitutive behavior. It has been known that the material properties vary at different locations in the thoracic aorta [21, 242, 243]. Indeed, the *in vivo* geometrical difference between systole and diastole may result from either the unknown heterogeneous wall thickness or the unknown heterogeneous material properties, making the material parameter estimation even more challenging. Here we only consider a simplified scenario, where the homogenous wall thickness is assumed, and the constitutive behavior of the aorta segment is investigated in an averaged sense. This simplification could probably explain the relatively large deviation (0.5mm) observed in Figure A.11. To measure the wall thickness field of the aortic wall, it is possible to use the combination of higher resolution CT and MRI as suggested in [136]. The wall thickness field can be incorporated in our future work to improve the accuracy.

To simplify the geometry, the supra-aortic branches were carefully trimmed by human experts. Based on our previous studies, for the particular ATAA patient that was used for numerical validation in this study, the stress and strain results with the branches [57] and without the branches [140] did not differ significantly. For the thoracic aorta, there are limited data on the axial stretch of humans in the literature. For a mouse model study [141], the axial stretch is about 1.1~1.2 for the ascending and proximal thoracic aorta, much lower than the abdominal aorta (~1.6). Furthermore, when prescribing the axial stretch, we encountered severe FE convergence problems, which is being actively investigated in our group. The rigid motion caused by the heart cyclically pulling on the aorta has been removed from FEA by using the ICP algorithm [236, 237] as described in Section 3.2.

The unloaded configuration of the aortic wall is assumed to be stress-free in this approach, and thus residual strain/stress is ignored, which is a limitation of this study.

Several methods have been developed to incorporate residual stress into patient-specific modeling [133, 244, 245]. Typically, the layer-specific material properties are required in these models, which is not the setup for this study. In addition, as reported by [189], the residual stresses may play a minor role in constitutive parameter estimation when a single layer model is used. It is shown in [246] that the residual stretches can vary notably with respect to the axial location and it is also correlated with age and gender. By using certain optimization schemes as proposed in [247], it might be possible to identify the heterogeneous layer-specific residual stress field on a patient-specific basis using *in vivo* images, however, the material properties must have been known as in [247]. In the future work, with the wall thickness measurement incorporated, we will explore the possibility of estimating residual stresses along with the heterogeneous material properties from *in vivo* clinical images.

A.5 Conclusion

We have proposed a novel MRDS approach to estimate the material properties of the aortic wall from *in vivo* loaded geometries at two cardiac phases with known blood pressures, which does not require mesh correspondence. To facilitate the MRDS method, the material parameter space is transformed into a PCA space, and the PCA space is discretized into multiple levels of resolutions. A network of links between adjacent levels is established. The MRDS search is achieved by following the links between adjacent levels, from coarse to fine. The approach was validated in a numerical experiment by using the *in vivo* data from an ATAA patient. It was also applied to estimate *in vivo* material properties of an aged human healthy aorta, and the minimized distance residual reached the image resolution. This novel MRDS approach may facilitate the personalized biomechanical analysis of aortic tissues, such as the rupture risk analysis of ATAA, which requires rapid feedback to clinicians.

APPENDIX B. A GENERIC PHYSICS-INFORMED NEURAL NETWORK-BASED CONSTITUTIVE MODEL FOR SOFT BIOLOGICAL TISSUES

Constitutive modeling is a cornerstone for stress analysis of mechanical behaviors of biological soft tissues. Recently, it has been shown that machine learning (ML) techniques, trained by supervised learning, are powerful in building a direct linkage between input and output, which can be the strain and stress relation in constitutive modeling. In this study, we developed a novel generic physics-informed neural network material (NNMat) model which employs a hierarchical learning strategy by following the steps: (1) establishing constitutive laws to describe general characteristic behaviors of a class of materials; (2) determining constitutive parameters for an individual subject. A novel neural network structure was proposed which has two sets of parameters: (1) a class parameter set for characterizing the general elastic properties; and (2) a subject parameter set (three parameters) for describing individual material response. The trained NNMat model may be directly adopted for a different subject without re-training the class parameters, and only the subject parameters are considered as constitutive parameters. Skip connections are utilized in the neural network to facilitate hierarchical learning. A convexity constraint was imposed to the NNMat model to ensure that the constitutive model is physically relevant. The NNMat model was trained, cross-validated and tested using biaxial testing data of 63 ascending thoracic aortic aneurysm (ATAA) tissue samples, which was compared to expert-constructed models (Holzapfel-Gasser-Ogden, Gasser-Ogden-Holzapfel, and four-fiber families) using the same fitting and testing procedure. Our results demonstrated that the NNMat model has a significant better performance in both fitting (R^2 value of 0.9632 vs 0.9019, p=0.0053) and testing (R^2 value of 0.9471 vs 0.8556, p=0.0203) than the Holzapfel-Gasser-Ogden model. The proposed NNMat model provides a convenient and general methodology for constitutive modeling. Results have been published in [248].

B.1 Introduction

Constitutive modeling is a cornerstone for stress analysis of mechanical behaviors of biological soft tissues [123, 249, 250]. Among the three key components required to solve a continuum biomechanics problem, i.e., the geometry (the domain of interest), the constitutive relations (how the material responds to applied loads under conditions of interest), and the applied loads (or associated boundary conditions), the identification of a robust constitutive model is probably the most challenging one to obtain and the key to success in this approach [251].

Currently, the approach to identify a robust constitutive model follows the DEICE procedure [130]: 1) **D**elineation of general characteristic behaviors, 2) **E**stablishment of an appropriate theoretical framework, 3) **I**dentification of specific functional forms of the constitutive relation, 4) **C**alculation of the values of the material parameters, and 5) **E**valuation of the predictive capability of the final constitutive relation. In this approach, a domain expert, (i.e., a biomechanicist with years of advanced training), plays a central role in the first 3 steps. A classic example is how Dr. Y. C. Fung discovered the famous Green-strain based, exponential form of the strain-energy function for soft tissues, iconized now as the Fung-elastic model [221, 252]. Briefly, Fung showed that preconditioned soft tissue can be considered pseudo-elastic [221, 252], and the slope of load-deflection curve is proportional to the load in uniaxial elongation tests of rabbit mesentery [253]. Consequently, an exponential function was used to account for the nonlinearity of the stress-strain curve for soft tissues. Indeed, the Green-strain based orthotropic form of the strain-energy function constructed by Fung provides excellent fitting capability with experimental data. To study biaxial mechanical properties of myocardial tissues, Humphrey *et al.* [254] performed constant invariant biaxial experiments, in which each of the strain invariant was independently varied, to infer specific functional forms of strain invariant-based constitutive equations. Based on the experimental observations, a polynomial form of the strain-energy function was devised [254]. To formulate a microstructurally-motivated constitutive model, Holzapfel et al. [33] modeled the arterial tissue as bi-layer fiber-reinforced composite, in which the contributions of a ground matrix and collagen fibers can be modeled separately in a strain-energy function.

Constitutive models [32-34, 53, 206-208, 221, 255-257] constructed by biomechanics experts have been widely adopted to model mechanical behaviors of soft tissues. By following the 3rd and 4th steps of the DEICE procedure, the specific formulations of these models usually contain several constitutive parameters that can be adjusted to describe constitutive behaviors of an individual subject (e.g. a tissue sample); therefore, the expert-constructed models can be used to describe constitutive behavior of a new subject (within the same class of materials) without deriving new constitutive equations. In addition, these expert-constructed constitutive models demonstrate excellent in-sample descriptive/fitting capability (e.g., R^2 value is high when fitting to mechanical testing data). However, their out-of-sample predictive capability may be limited when new data (i.e., data that are not used in the fitting) is employed to assess their performance [258].

Recently, machine learning (ML) techniques, especially deep neural networks have led to revolutionary breakthrough in many applications [102-109, 259], including recent works [115, 117, 260-263] in the field of biomechanics. Since ML techniques are capable of automatically discovering and capturing complex multi-dimensional input-output dependencies without the need of manually deriving specific functional forms, we hypothesize that a generic ML-based constitutive model can be developed and can have a similar, if not better, performance compared to the expert-constructed constitutive models.

Based on the universal function approximation theorems, a neural network with adequate capacities can approximate any continuous function with a small error [264-267]. Traditional feedforward fully-connected neural networks (FFNN) have been used to model the strain (input) and stress (output) relations [110, 268]. However, such FFNN-based model use all of its parameters (a.k.a. weights and biases) to construct the constitutive relation for an individual subject, which does not strictly follow the 3rd and 4th steps in the DEICE procedure; therefore, it often contains hundreds to thousands of constitutive parameters. Compared to an expert-constructed model, a FFNN-based constitutive model has three major disadvantages: 1) a large number of constitutive parameters with no physical meanings, in contrast to only a few constitutive parameters in an expert-constructed model. 2) An expert-constructed model can not only delineate and capture the general mechanical behaviors of a class of materials, but also can accurately model an individual subject (e.g. individual material responses) by fine tuning the constitutive parameters. A FFNN-based model, however, cannot capture general characteristic behaviors of a class of materials, i.e., it cannot utilize data from multiple subjects (e.g. tissue samples from many patients) for better modeling of an individual subject (e.g. a tissue sample from a single patient). The model parameters of FFNN-based models for different subjects are completely independent to each other. 3) a FFNN-based model cannot guarantee its convexity, which is important for ensuring the model is physically meaningful with unambiguous mechanical behaviors [33].

In this study, we developed a novel neural network-based material model (NNMat) which employs a physics constraint and a hierarchical learning strategy (Figure B.1): (1) establishing constitutive laws to describe general characteristic behaviors of a class of materials; (2) determining constitutive parameters for an individual subject. These two steps are equivalent to 3rd and 4th steps of the DEICE procedure. The neural network structure consists of two parameter sets corresponding to the two steps: (1) a "class" parameter set for characterizing the general elastic properties of the class of materials; and (2) a "subject" parameter set with three parameters for modeling individual material response. Skip connections are utilized in the neural network structure to facilitate hierarchical learning. Hence, the class parameters can function as the expert-constructed constitutive equations, and the NNMat model has only three constitutive parameters. The trained NNMat model may be directly adopted for a different subject without re-training the class parameters. The predictive capability of the proposed NNMat model is compared with the expert-constructed constitutive models (Holzapfel-Gasser-Ogden [33], Gasser-Ogden-Holzapfel [34], and four-fiber families [257]).

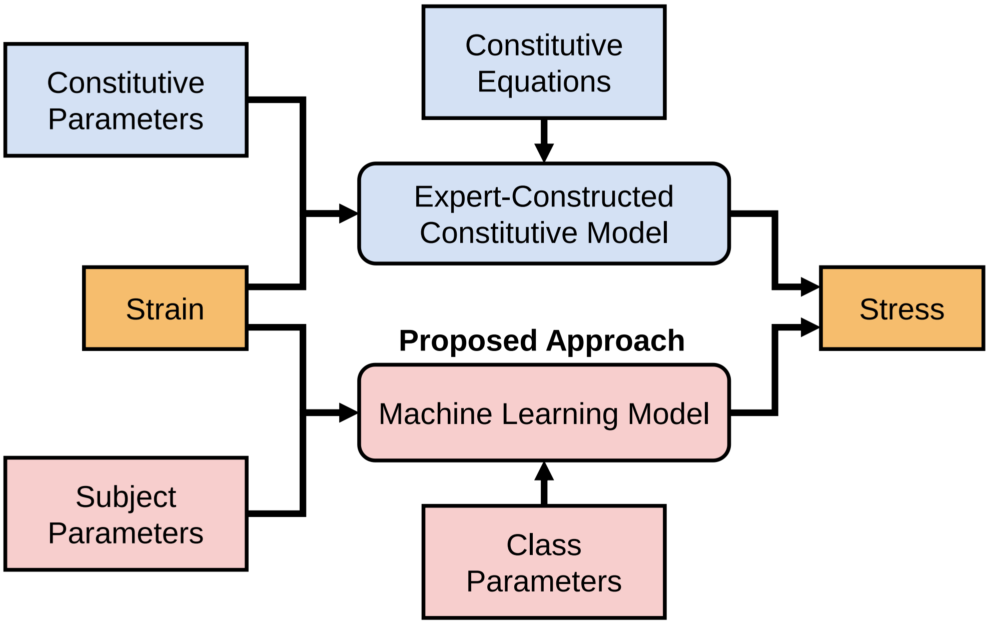
Constitutive Parameters
Constitutive Equations
Expert-Constructed Constitutive Model
Strain
Stress
Proposed Approach
Machine Learning Model
Subject Parameters
Class Parameters

Figure B.1 - The proposed machine learning-based constitutive model.

B.2 Constitutive Modeling of Soft Biological Tissues

Soft biological tissues comprise bundles of collagen fibers embedded in a ground matrix and can be regarded as fiber-reinforced composites. Constitutive modeling of the hyperelastic tissues is often achieved by specifying the strain energy density W as a function of deformation gradient $\mathrm{W}(\mathbf{F})$, where $\mathbf{F}$ represents the deformation gradient tensor. Microstructurally-motivated constitutive models have become increasingly utilized for soft tissues, in which the contributions of the matrix and collagen fibers can be modeled separately. In such models, the strain energy density function W is usually formulated based on strain invariants of the right Cauchy-Green tensor, $\boldsymbol{C} = \mathbf{F}^T\mathbf{F}$. In this study, we consider a subclass of anisotropic responses, in which the strain energy density depends on four strain invariants: I_1, I_2, I_4 and I_6. The first two strain invariants I_1, I_2 are defined as

$$I_1 = tr(\boldsymbol{C}), \quad I_2 = \frac{1}{2}[I_1^2 - tr(\boldsymbol{C}^2)] \tag{B.1}$$

For a fiber-reinforced composite material with two families of fibers, I_4 and I_6 are two additional pseudo-invariants that describes deformations in the preferred fiber directions

$$I_4 = \mathbf{a}_{01} \cdot (\boldsymbol{C}\mathbf{a}_{01}), \quad I_6 = \mathbf{a}_{02} \cdot (\boldsymbol{C}\mathbf{a}_{02}) \tag{B.2}$$

where unit vectors $\mathbf{a}_{01}$ and $\mathbf{a}_{02}$ characterize two fiber directions in the reference configuration. Typically, these two fiber directions are assumed to be symmetric about an axis. $\mathbf{a}_{01} = (\cos\theta\,, \sin\theta\,, 0)$ and $\mathbf{a}_{02} = (\cos\theta\,, -\sin\theta\,, 0)$, where θ is the angle between the fiber direction and the axis of symmetry. In this study, the circumferential axis of the aorta was used as reference. Thus, I_4 and I_6 are equal to squares of the stretches in the fiber directions.

The stress-strain relation can be derived by differentiating the strain energy density W. For incompressible materials, the second Piola-Kirchhoff stress can be derived as [269]:

$$\boldsymbol{S} = -p\boldsymbol{C}^{-1} + 2W_1\boldsymbol{I} + 2W_2(I_1\boldsymbol{I} - \boldsymbol{C}) + 2W_4\mathbf{a}_{01} \otimes \mathbf{a}_{01} + 2W_6\mathbf{a}_{02} \otimes \mathbf{a}_{02} \tag{B.3}$$

where $\boldsymbol{I}$ is the identity tensor, $W_k = \frac{\partial W}{\partial I_k}\,, k = 1, 2, 4, 6$ represent the derivatives of strain energy with respect to the strain invariants. p is the Lagrangian multiplier, which can be determined from boundary conditions. To characterize constitutive behavior, the relationship between strain invariants I_1, I_2, I_4, I_6 and W_1, W_2, W_4, W_6 needs to be established. Four nonlinear functions need to be constructed:

$$W_k = f_k(I_1, I_2, I_4, I_6), k = 1, 2, 4, 6 \tag{B.4}$$

B.2.1 Expert-Constructed Constitutive Equations

Many expert-constructed models are available with specific formulations of W_k [33, 34, 53, 206-208, 256]. For comparison with our ML-based constitutive model, the Holzapfel-Gasser-Ogden (HGO) model [33] with two families of fibers was selected.

In the work by Holzapfel et al. [33], the total strain energy density function W can be additively split into isotropic W_{iso} and anisotropic W_{aniso} parts, according to

$$\mathrm{W}(\mathbf{C}, \mathbf{a}_{01}, \mathbf{a}_{02}) = W_{iso}(\mathbf{C}) + \mathrm{W}_{aniso}(\mathbf{C}, \mathbf{a}_{01}, \mathbf{a}_{02}) \tag{B.5}$$

The isotropic matrix material is characterized by strain energy function of the neo-Hookean type

$$\mathrm{W}_{iso}(\mathbf{C}) = C_{10}(I_1 - 3) \tag{B.6}$$

where C_{10} is a material parameter to describe the matrix response. To account for the strong stiffening effect of the collagen fiber recruitment, an exponential function is employed. The anisotropic contribution is given by

$$\mathrm{W}_{aniso}(\mathbf{C}, \mathbf{a}_{01}, \mathbf{a}_{02}) = \frac{k_1}{2k_2} \sum_{k=4,6} \{exp[k_2(I_k - 1)^2] - 1\} \tag{B.7}$$

where k_1 is a positive material parameter that has the same unit of stress, while k_2 is a unitless material parameter. Hence, in the Holzapfel-Gasser-Ogden model [33], the relationship between strain invariants I_1, I_2, I_4, I_6 and strain energy derivatives W_1, W_2, W_4, W_6 can be obtained as:

$$W_1 = C_{10}$$

$$W_2 = 0$$

$$W_4 = k_1(I_4 - 1)exp[k_2(I_4 - 1)^2]$$

$$W_6 = k_1(I_6 - 1)exp[k_2(I_6 - 1)^2] \tag{B.8}$$

The four constitutive parameters $\{C_{10}, k_1, k_2, \theta\}$ can be determined through curve fitting to describe material properties of an individual subject. Stress-strain relation can be obtained using Eqn. (B.3).

The Holzapfel-Gasser-Ogden model [33] has been extended to other forms. Using the generalized structural tensor (GST), Gasser et al. [34] constructed the following anisotropic contribution of the strain energy density function

$$\mathrm{W}_{aniso}(\mathbf{C}, \mathbf{a}_{01}, \mathbf{a}_{02}) = \frac{k_1}{2k_2}\sum_{k=4,6}[exp\{k_2[\kappa I_1 + (1 - 3\kappa)I_k - 1]^2\} - 1] \tag{B.9}$$

where κ is a parameter describing dispersion of the fiber orientation. This model is known as the Gasser-Ogden-Holzapfel (GOH) model, which has five constitutive parameters $\{C_{10}, k_1, k_2, \kappa, \theta\}$. Hu et al. [257] proposed a four-fiber family model, which makes use of two additional invariants $I_\theta = \mathbf{a}_\theta \cdot (\boldsymbol{C}\mathbf{a}_\theta)$ and $I_\mathrm{z} = \mathbf{a}_z \cdot (\boldsymbol{C}\mathbf{a}_z)$, along the circumferential ($\mathbf{a}_\theta = (1, 0,0)$) and longitudinal ($\mathbf{a}_z = (0, 1,0)$) directions, respectively. The anisotropic part of the strain energy density function is

$$\begin{aligned}
&\mathrm{W}_{aniso}(\mathbf{C}, \mathbf{a}_{01}, \mathbf{a}_{02}) \\
&\qquad = \frac{k_1}{4k_2} \sum_{k=4,6} \{exp[k_2(I_k - 1)^2] - 1\} \\
&\qquad + \frac{k_3}{4k_4} \sum_{l=\theta,z} \{exp[k_4(I_l - 1)^2] - 1\}
\end{aligned} \tag{B.10}$$

Hence, the four-fiber model has six constitutive parameters $\{C_{10}, k_1, k_2, k_3, k_4, \theta\}$. In this study, the fitting and predictive capabilities of the Gasser-Ogden-Holzapfel model and the four-fiber family model are also demonstrated.

B.2.2 ML-Based Constitutive Model

In this study, we developed a generic neural network-based material (NNMat) model (Figure B.2) with a novel neural network structure and a novel hierarchical learning strategy. The goal of the NNMat model is to establish the nonlinear mapping between I_1, I_2, I_4, I_6 and W_1, W_2, W_4, W_6 as described in Eqn. (B.4) (W_2 may be non-zero). A physical constraint is added to the training process to ensure that convexity of the strain energy density is achieved by the NNMat model. Following the 3rd and 4th steps of the DEICE procedure, the NNMat model employs the hierarchical learning strategy: (1) constructing constitutive laws to describe general characteristic behaviors of a class of materials; (2) determining constitutive parameters for an individual subject. Therefore, the NNMat model has two sets of parameters: (1) a “class” parameter set for characterizing hyperelastic properties of the class of materials; and (2) a “subject” parameter set of three parameters for fitting mechanical response of an individual subject. NNMat models of different subjects will share the same class parameter set, but with different sets of subject parameters. In other words, each individual subject has an individual set of subject parameters and shares the same class parameter set with other subjects, assuming these subjects are from the same class of material.

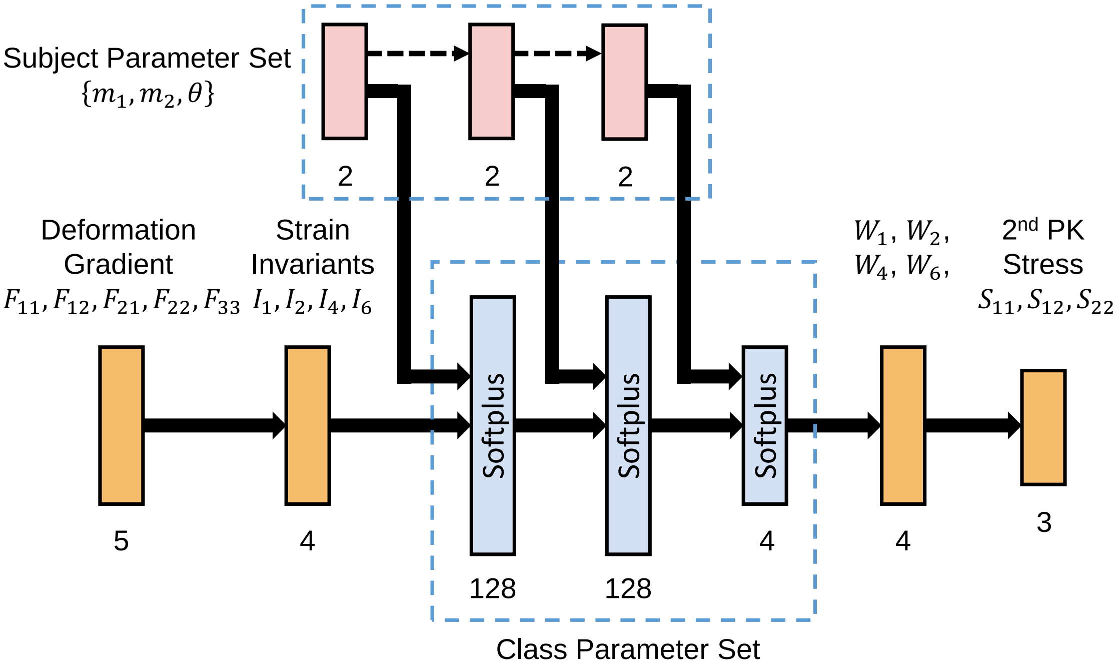
Subject Parameter Set
$\{m_1, m_2, \theta\}$
2
2
2
Deformation Gradient
$F_{11}, F_{12}, F_{21}, F_{22}, F_{33}$
Strain Invariants
I_1, I_2, I_4, I_6
Softplus
Softplus
Softplus
W_1, W_2, W_4, W_6,
2nd PK Stress
S_{11}, S_{12}, S_{22}
5
4
128
128
4
4
3
Class Parameter Set

Figure B.2 - The novel neural network material model (NNMat) with a physics constraint and two parameter-set structures: the class parameter set (blue) and the subject parameter set (red), dashed arrows indicate skip connections. The subject parameter set consist of three constitutive parameters: $\{\boldsymbol{m_1}, \boldsymbol{m_2}, \boldsymbol{\theta}\}$.

Skip connections are increasingly utilized in deep learning research, e.g., additive skip connections in ResNet [270] and concatenative skip connections in DenseNet [271], to skip one or more layers in the neural network and connects the output of a previous layer to the next layers as the input. It can alleviate the vanishing-gradient problem by strengthening feature propagation and encouraging feature reuse [271]. In this study, a novel neural network structure with skip connections are proposed for the NNMat model to facilitate the hierarchical learning strategy.

The structure of the NNMat model is shown in Figure B.2. The class parameter set is processed by a fully-connected neural network, and two subject parameters are connected to each layer via concatenative skip connections, the subject parameter θ is incorporated in the unit directional vectors in Eqn. (B.2). Therefore, the two subject parameters can have contributions to the output of each neuron in the hidden and output layers, which parametrizes the nonlinear mapping between I_1, I_2, I_4, I_6 and W_1, W_2, W_4, W_6. Comparing to only one subject parameter for one layer, skip connections may introduce more interactions between the subject parameters and the hidden/output layers. Specifically, the output of the ith neuron of the jth layer is a weighted sum of the input vector $\boldsymbol{z}^j$, with weight $\boldsymbol{w}_i^j$ and bias b_i^j. In addition, two subject parameters $\boldsymbol{m} = [m_1, m_2]^T$ are also connected (i.e. input) to each neurons with weight $\boldsymbol{p}_i^j$ utilizing concatenative skip connections,

$$u_i^j = {\boldsymbol{w}_i^j}^T \boldsymbol{z}^j + {\boldsymbol{p}_i^j}^T \boldsymbol{m} + b_i^j \tag{B.11}$$

where the superscript j represents the layer index, and subscript i represents the neuron index. $\boldsymbol{z}^j$ represents the input to the neuron $\left[z_1^j, z_2^j, \dots, z_{n_j}^j\right]^T$, and n_j denotes the number of neurons in the jth layer. $\{\boldsymbol{w}_i^j, b_i^j, \boldsymbol{p}_i^j, i, j = 1,2, \dots\}$ is the class parameter set, which is contained in two hidden layers and the output layer, shown in blue color in Figure B.2. The linear combination u_i^j is nonlinearly transformed into the output z_i^{j+1} (the input to layer $j+1$) using the softplus [272] activation function, given by

$$z_i^{j+1} = \log\left(1 + exp\left(u_i^j\right)\right) \tag{B.12}$$

This function is a smooth version of the rectified linear unit (ReLU) [273]. The number of softplus units in the three layers are 128, 128 and 4, respectively. Consequently, in total, there are 18,188 class parameters $\{\boldsymbol{w}_i^j, b_i^j, \boldsymbol{p}_i^j, i, j = 1,2, \ldots\}$ in the NNMat model. The class parameters can function as the expert-constructed constitutive functional forms. Only the subject parameters $\{m_1, m_2, \theta\}$ are considered as constitutive parameters.

After W_k are determined from the neural network, the second Piola-Kirchhoff stress can be computed using Eqn. (B.3). The discrepancy between the experimental and predicted second Piola-Kirchhoff stress was measured by the mean squared error (MSE) loss function,

$$L_S = \sum_{m=1}^{3} \frac{1}{N} \sum_{n=1}^{N} \left(S_m^{(n)} - \hat{S}_m^{(n)} \right)^2 \tag{B.13}$$

where n is the data point index, N is the number of data points in the training dataset, $S_m^{(n)}$ and $\hat{S}_m^{(n)}$denote the kth predicted and experimental second Piola-Kirchhoff stress, respectively. m is the in-plane component index in the Voigt notation.

A physically-relevant strain energy field needs to be convex: the strain energy density should be at minimum (zero) when there is no deformation. In addition, since Newton's iterative method is often employed for solving nonlinear equations in commercial FE packages, convexity of the strain energy density ensures that the material stiffness (Hessian) matrix will be positive definite and well-conditioned, which could stabilize the numerical solution [274]. For in-plane components, the Hessian matrix of the strain energy function can be expressed as:

$$\boldsymbol{H} = \begin{bmatrix} \frac{\partial S_{11}}{\partial E_{11}} & \frac{\partial S_{11}}{\partial E_{12}} & \frac{\partial S_{11}}{\partial E_{22}} \\ \frac{\partial S_{12}}{\partial E_{11}} & \frac{\partial S_{12}}{\partial E_{12}} & \frac{\partial S_{12}}{\partial E_{22}} \\ \frac{\partial S_{22}}{\partial E_{11}} & \frac{\partial S_{22}}{\partial E_{12}} & \frac{\partial S_{22}}{\partial E_{22}} \end{bmatrix} \tag{B.14}$$

For the strain energy function $W = \int \boldsymbol{S}: d\boldsymbol{E}$ to be path independent, it is required that $\boldsymbol{H}$ is symmetric. In the NNMat model, symmetry of $\boldsymbol{H}$ is enforced by a loss function at each data point n:

$$L_{c1}^{(n)} = \left|\frac{\partial S_{11}}{\partial E_{12}} - \frac{\partial S_{12}}{\partial E_{11}}\right| + \left|\frac{\partial S_{11}}{\partial E_{22}} - \frac{\partial S_{22}}{\partial E_{11}}\right| + \left|\frac{\partial S_{12}}{\partial E_{22}} - \frac{\partial S_{22}}{\partial E_{12}}\right| \tag{B.15}$$

Strict convexity requires positive definiteness of $\boldsymbol{H}$ to be satisfied for all possible strain values, which can be shown for expert-constructed model which has closed form solutions [275]. In the NNMat model, convexity of the strain energy density function is enforced by an additional loss function that ensures the positive semi-definiteness of Hessian matrix for all training stress-strain data points: for all $\boldsymbol{x} \in \mathbb{R}^3$, $\boldsymbol{x}^T\boldsymbol{H}\boldsymbol{x} \geq 0$ needs to be satisfied. Using Sylvester's criterion of symmetric matrix, the requirement for positive semi-definiteness is that all of the principal minors must be non-negative [276, 277]. Therefore, the positive semi-definiteness can be quantified by the following loss function for each data point n:

$$L_{c2}^{(n)} = \sum_{p=1}^{3} \sum_{q=1}^{\binom{3}{p}} \max\left(-\Delta_{p,q}, 0\right) \tag{B.16}$$

where $\Delta_{p,q}$ denote the qth principal minor of order p ($p = 1,2,3$) of the Hessian matrix. There are $\binom{3}{p}$ principal minors of order p. Hence, the loss function of the convexity constraints can be obtained by adding $L_{c1}^{(n)}$ and $L_{c2}^{(n)}$ with a weight α:

$$L_c = \frac{1}{N}\sum_{n=1}^{N}\left(L_{c1}^{(n)} + \alpha L_{c2}^{(n)}\right) \tag{B.17}$$

Since the loss functions are based on stress and its derivative, Eqn. (B.3) needs to be included in the NNMat model for backpropagation, which is the last layer shown in yellow color in Figure B.2. The angle θ which defines the two fiber directions is another subject parameter in the NNMat. Hence, three subject parameters $\{m_1, m_2, \theta\}$ in the NNMat model can be adjusted for modeling properties of an individual subject. A bound constraint was imposed on the subject parameters to ensure that m_1, m_2 are in the range of -1 to 1 and θ is within -90° to 90°, which is realized by using the hyperbolic tangent function:

$$\begin{gathered}\widehat{m}_1 = \tanh(m_1) \\ \widehat{m}_2 = \tanh(m_2) \\ \hat{\theta} = 90^\circ \tanh(\theta)\end{gathered} \tag{B.18}$$

where $\widehat{m}_1$, $\widehat{m}_2$ and $\hat{\theta}$ represent the normalized parameters.

Therefore, the combined loss function for training the NNMat model is

$$L(\{m_1, m_2, \theta\}, \{\boldsymbol{w}_i^j, b_i^j, \boldsymbol{p}_i^j, i, j = 1,2, \ldots\}) = L_S + \beta L_c \tag{B.19}$$

where β is another weight parameter. In this study, α and β were chosen using grid search in cross validation (Section 3.3). We note that the result may be refined using adaptive grid search. Other methods may be used for the hyperparameter optimization, e.g., random search [278] and Bayesian optimization [279]. Consequently, the combined loss function is a function of the (unknown) parameters in the NNMat model. The goal of training is to find the optimal values of the parameters in the NNMat model by minimizing the loss function on the training dataset.

We used a novel hierarchical training strategy to find the optimal parameters of the NNMat model. The class and subject parameters are determined in two sequential steps: (1) training and (2) fitting, which is equivalent to the 3rd and 4th steps of the DEICE procedure. During the model training, the class parameter set $\{\boldsymbol{w}_i^j, b_i^j, \boldsymbol{p}_i^j, i, j = 1,2, \ldots\}$ is first optimized across all subjects in the training set, and the subject parameter set $\{m_1, m_2, \theta\}$ is then only optimized for the corresponding subject. During the model fitting, the class parameter set $\{\boldsymbol{w}_i^j, b_i^j, \boldsymbol{p}_i^j, i, j = 1,2, \ldots\}$ is fixed, i.e., it will no longer be updated through backpropagation; only the subject parameters $\{m_1, m_2, \theta\}$ are updated, which is similar to fitting an expert-constructed model. Therefore, the trained NNMat model may be directly adopted to a different subject without re-training the class parameters. When the trained NNMat model is used to characterize constitutive relation of a new subject, only the subject parameters need to be updated/fitted.

The NNMat model was implemented in PyTorch 1.0 [280]. Adam algorithm [281] was used for optimization to obtain the optimal parameters. Training, fitting and validation/testing of the NNMat model was run on a multi-GPU server (10-core CPU with 128GB RAM, 4×NVIDIA GeForce GTX 1080 Ti GPU).

B.3 Cross Validation and Testing

In this study, stress-strain data (63 patients) was split into two sets: a training and validation set (57 patients) and a testing set (6 patients). In the training mode, parameters in both the class set and subject set are updated. While in the fitting mode, the class parameters are fixed and only the three subject parameters are adjusted to optimal for an individual subject. For the testing/validation mode, all the parameters are fixed. The network structure and hyperparameters, e.g., α and β, were determined through cross validation using the training and validation dataset. The performance of the NNMat model was evaluated using the additional testing dataset.

B.3.1 Planar Biaxial Testing Data

In this study, we demonstrate the capability of the proposed NNMat model by using seven-protocol planar biaxial testing data [15] of ATAA tissues from 63 patients/subjects that were published previously by our group [15, 63]. Briefly, before planar biaxial testing, cryopreserved tissue samples were submerged in a 37 °C water bath until totally defrosted, following the two-stage slow thawing method to remove the cryopreservation agent [174]. The samples were trimmed into square-shaped specimens with a side length of 20~25 mm. Each specimen was subjected to biaxial tension with the circumferential (11) and longitudinal (22) directions aligned with the primary axes of the biaxial test fixture. A stress-controlled biaxial testing protocol was used. $\boldsymbol{N}$ denotes the nominal stress, and the ratio $N_{11}: N_{22}$ was kept constant. Each tissue specimen was preconditioned for at least 40 continuous cycles with $N_{11}: N_{22} = 1: 1$ to minimize hysteresis. Seven successive protocols were performed using ratios $N_{11}: N_{22} = 0.3: 1, 0.5: 1, 0.75: 1, 1: 1, 1: 0.75, 1: 0.5, 1: 0.3$. Figure B.3 shows representative biaxial testing results of two ATAA samples. Biaxial testing data was chosen since it contains hyperelastic properties under various in-plane stress ratios, which can be easily split into fitting and testing/validation dataset (i.e., data from six stress protocols for fitting the subject parameters and data from one protocol for testing/validation).

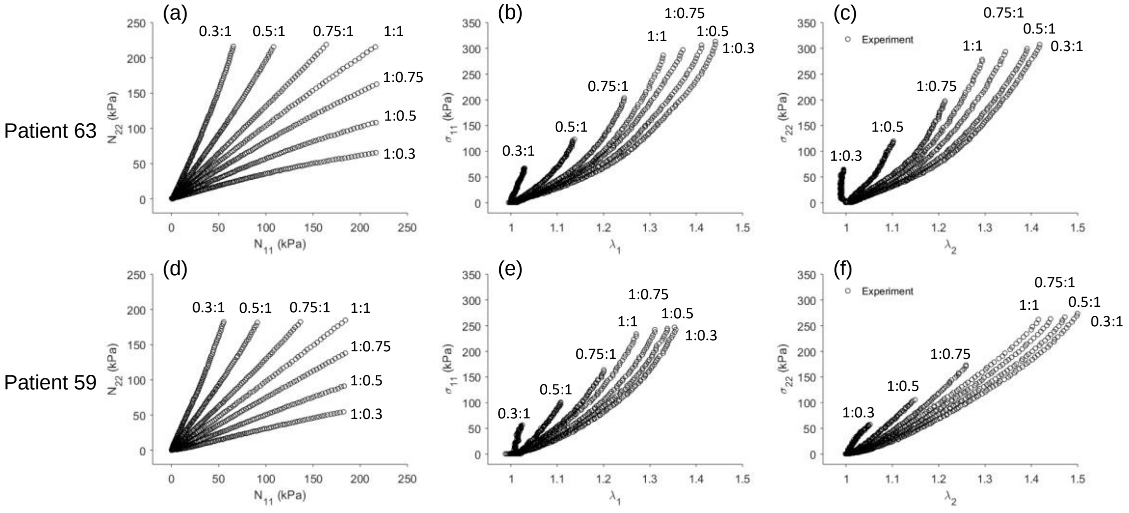

Figure B.3 - Representative stress-stretch results of the seven-protocol planar biaxial testing of two ATAA tissues. Each row represents one patient. (a) and (d): seven successive nominal stress ratios. (b) and (e): circumferential stress-stretch data. (c) and (f): longitudinal stress-stretch data.

B.3.2 Fitting and Testing of the Expert-Constructed Models

Traditionally, for fitting an expert-constructed constitutive model to data, an error function is built based on difference between the experimental data and model predictions, and then constitutive parameters can be determined through nonlinear optimization. Typically, the model fitting process uses all experimental data (i.e. all seven stress protocols), and a coefficient of determination (R^2) as an accuracy metric is reported. However, since this R^2 metric corresponds to the in-sample prediction, the model's ability for out-of-sample prediction cannot be assessed, as shown in Schroeder et al [258]. It is also reported [282] that a Fung-type hyperelastic model [283] with good in-sample fitting could result in erroneous out-of-sample stress predictions. As a consequence, the particular form of the constitutive model [283] needed to be modified by domain experts [282] to achieve a reasonable out-of-sample accuracy.

In this study, the predictive capabilities of the expert-constructed constitutive models in Section 2.1 were evaluated using cross validation. For each subject (i.e. a tissue sample from a patient), leave-one-out cross validation was performed: for each round, data from one stress protocol were selected for testing, and data from the remaining six stress protocols were used for fitting the model to obtain constitutive parameters. The process is repeated seven times for all protocols for each subject/patient in the testing dataset. Therefore, the averaged out-of-sample testing R^2 is used to evaluate the model performance, which provides a baseline to compare with that of the NNMat model. The fitting process was implemented in MATLAB using a nonlinear least square solver.

B.3.3 Cross Validation and Testing of the ML-based Constitutive Model

To assess performance of the NNMat model, cross validation was performed at two levels using the training and validation dataset of 57 patients. As can be seen in Figure B.4, the cross validation procedure consists of an outer loop and an inner loop which correspond to the patient level and stress protocol level, respectively. At the patient level, ten-fold cross validation was performed as follows: (1) split the patient data into ten groups, and each group contains the data from 5~6 patients; (2) in each round of the ten-fold cross validation, select one group for validation and use the remaining nine groups for training. The NNMat model parameters in both the class set and subject set are updated during the training stage. From the cross validation on a patient level, the performance of the NNMat model can be assessed for each individual patient in the training and validation set.

Similar to Section 3.2, leave-one-out cross validation was carried out for each patient on the stress protocol level: data from six protocols were used for fitting the subject parameters $\{m_1, m_2, \theta\}$, and then data from the remaining one protocol were used for assessing the model performance. The capability of the NNMat model to predict stress-strain response under various in-plane stress ratios can be evaluated. The weights α and β, and the number of training epochs were determined during cross validation.

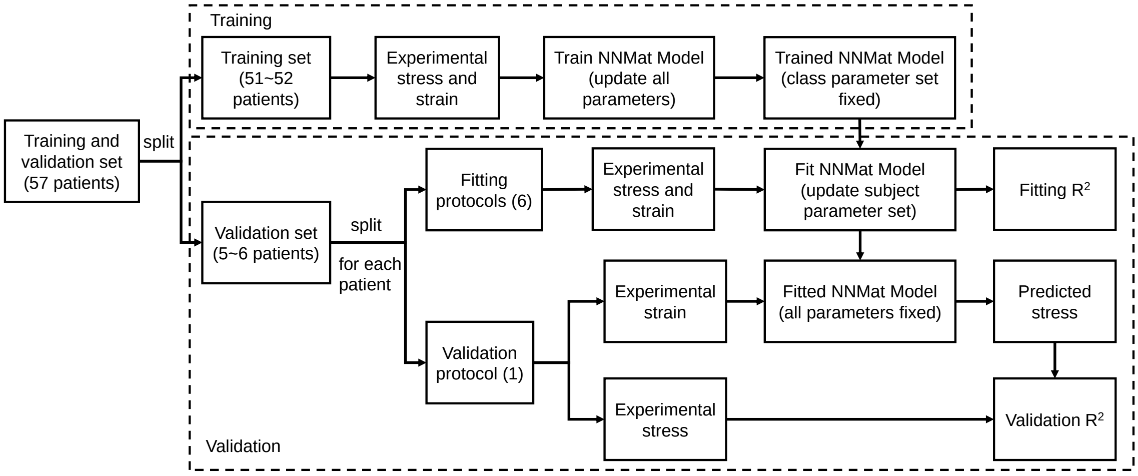
Training
Training set (51~52 patients)
Experimental stress and strain
Train NNMat Model (update all parameters)
Trained NNMat Model (class parameter set fixed)
Training and validation set (57 patients)
split
Validation set (5~6 patients)
split
for each patient
Fitting protocols (6)
Experimental stress and strain
Fit NNMat Model (update subject parameter set)
Fitting R²
Experimental strain
Fitted NNMat Model (all parameters fixed)
Predicted stress
Validation protocol (1)
Experimental stress
Validation R²
Validation

Figure B.4 - Cross validation of the NNMat model on patient level and stress protocol level. Ten-fold cross validation was performed for different patient groups. For each patient, leave-one-out cross validation was performed with different stress protocols.

After the hyperparameters were determined, the NNMat model was trained using the training and validation set (57 patients). Using the additional testing dataset of 6 patients, fitting and testing R^2 were evaluated for each patient using the same leave-one-out fashion on the stress protocol level (see Figure B.5). The averaged testing accuracy was used to evaluate performance of the NNMat model. The computing time for training the NNMat model is approximately 16~18 hours using the training and validation set (73,614 stress-strain data points) with 10,000 epochs on a single GPU. Fitting of subject parameters for one patient can be completed in less than one minute. Using the trained and fitted NNMat model, stress computation can be achieved instantaneously.

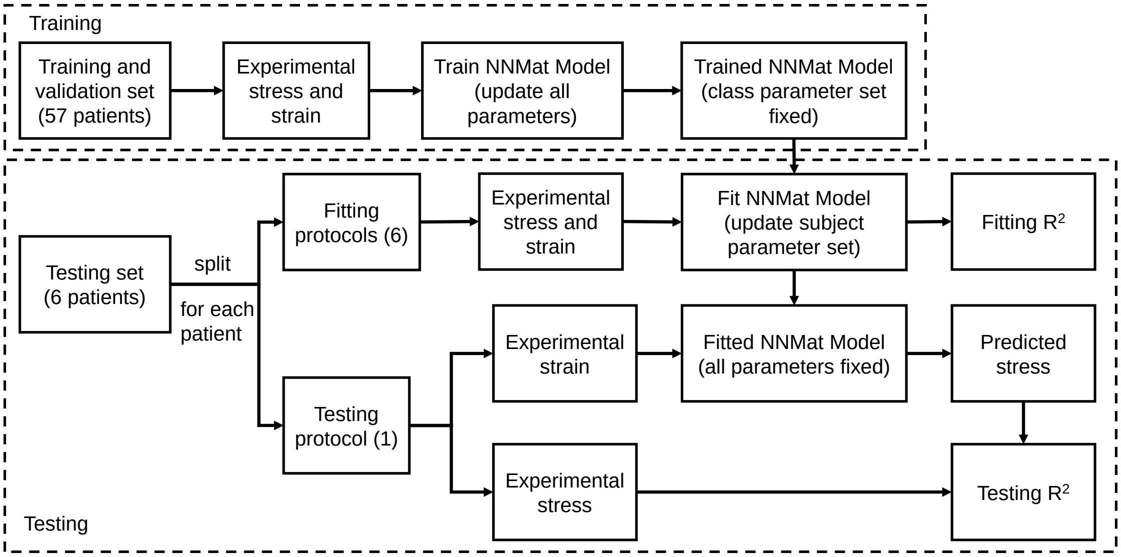
Training
Training and validation set (57 patients)
Experimental stress and strain
Train NNMat Model (update all parameters)
Trained NNMat Model (class parameter set fixed)
Testing set (6 patients)
split
for each patient
Fitting protocols (6)
Experimental stress and strain
Fit NNMat Model (update subject parameter set)
Fitting R^2
Experimental strain
Fitted NNMat Model (all parameters fixed)
Predicted stress
Testing protocol (1)
Experimental stress
Testing R^2
Testing

Figure B.5 - Evaluating accuracy of the NNMat model using an additional testing dataset of 6 patients.

B.4 Results

B.4.1 Cross Validation

Using the training and validation set of 57 patients, grid search was performed to select the weights α and β. To reduce computational cost, the number of training epochs was set to be 1000 for the gird search. It is convenient to examine the convexity of a strain energy density function with respect to two in-plane components of the Green strain E_{11} and E_{22} while the shear component E_{12} is set to zero [274]. To examine its convexity, using the trained and fitted NNMat model, the second Piola-Kirchhoff stress S_{11} and S_{22} can be computed at a series of strain E_{11} and E_{22} values (-0.1 to 0.5). To evaluate whether the convexity condition is satisfied, using Sylvester's criterion [276, 277], we define a convexity criterion Ξ for each pair of E_{11} and E_{22}

$$\begin{aligned}\Xi(E_{11}, E_{22}) = \max\left(-\frac{\partial S_{11}}{\partial E_{11}}\frac{\partial S_{22}}{\partial E_{22}} + \frac{\partial S_{11}}{\partial E_{22}}\frac{\partial S_{22}}{\partial E_{11}}, 0\right) + \max\left(-\frac{\partial S_{11}}{\partial E_{11}}, 0\right) \\ + \max\left(-\frac{\partial S_{22}}{\partial E_{22}}, 0\right)\end{aligned} \tag{B.20}$$

For all strain values, the percentage of convexity criterion equals to zero ($\Xi = 0$) can be used to quantify convexity of the NNMat model. Therefore, we define a convexity index (CI) for a trained and fitted NNMat model

$$CI = \frac{1}{M}\sum_{E_{11}}\sum_{E_{22}} \mathbf{1}_c[\Xi(E_{11}, E_{22})] \tag{B.21}$$

where M represents the total number of E_{11} and E_{22} values. $\mathbf{1}_c(\Xi)$ is an indicator function, $\mathbf{1}_c(\Xi) = 1$ when $\Xi = 0$; otherwise, $\mathbf{1}_c(\Xi) = 0$. Hence, for all fitted NNMat models (using different patients and protocols in the validation set), the mean CI can be used to measure the convexity of the NNMat model. The results of grid search are reported in Table B.1.

The set of weights, $\alpha = 0.1$ and $\beta = 10^{-5}$, was selected because it yields good validation R^2 and an acceptable mean CI. The small α and β values may be explained by the fact that the values of lost terms are orders of magnitude different.

Table B.1 - Fitting and validation results obtained from grid search with different α and β values. The number of training epochs was set to be 1000.

(β, α)	Mean fitting R^2	Mean validation R^2	Mean CI
$(10^{-3},1)$	0.8280	0.7884	99.43%
$(10^{-3},0.1)$	0.8628	0.8310	94.56%
$(10^{-3},0.01)$	0.8603	0.8204	95.40%
$(10^{-5},1)$	0.8668	0.8397	95.93%
$(10^{-5},0.1)$	0.8765	0.8586	96.08%
$(10^{-5},0.01)$	0.8789	0.8564	95.07%
$(10^{-7},1)$	0.8833	0.8620	95.25%
$(10^{-7},0.1)$	0.8865	0.8645	93.84%
$(10^{-7},0.01)$	0.8872	0.8641	92.90%

The number of training epochs was then treated as another hyperparameter. The NNMat model was cross validated using different number of epochs (1000, 5000, 10000, 15000), the results are listed in Table B.2. The number of epochs 10000 was chosen because it resulted in the best performance.

Table B.2 - Fitting and validation results obtained using different number of training epochs.

number of epochs	Mean fitting R^2	Mean validation R^2	Mean CI
1000	0.8765	0.8586	96.08%
5000	0.8998	0.8691	97.40%
10000	0.9359	0.9139	99.10%
15000	0.9192	0.8940	96.24%

B.4.2 Testing

The NNMat model was trained using the training and validation set of 57 patients. The expert-constructed models [33, 34, 257] (Section 2.1) and the trained NNMat model (Section 2.2) were fitted to biaxial data of the 6 ATAA patients in the testing set. Typical stress-strain results of the NNMat and the HGO model for a representative patient are shown in Figure B.6. For comparison, coefficients of determination (R^2) were computed for model predictions in terms of the Cauchy stress. For this particular patient (patient 59), it can be seen that the NNMat model is slightly more accurate than the HGO model. To compare the testing results of the NNMat and expert-constructed models, the fitting R^2 (using six protocols) and testing R^2 (using one protocol) of the four constitutive models for the testing patients are reported Table B.3. The mean and standard deviation of fitting R^2 and testing R^2 are shown in Table B.4. It is demonstrated that the NNMat model significantly outperforms the HGO model in fitting and predicting the ATAA biaxial data (p-value is 0.0053 for fitting and 0.0203 for testing). Power of the t-test is 0.9939 and 0.8329 for fitting and testing, respectively, which represents the probability that the null hypothesis is correctly rejected. The NNMat model has a slightly better performance than the GOH model which employs GST for fiber dispersion, but the result is insignificant.

The NNMat model has a similar performance comparing to the four-fiber model which makes use of two additional invariants.

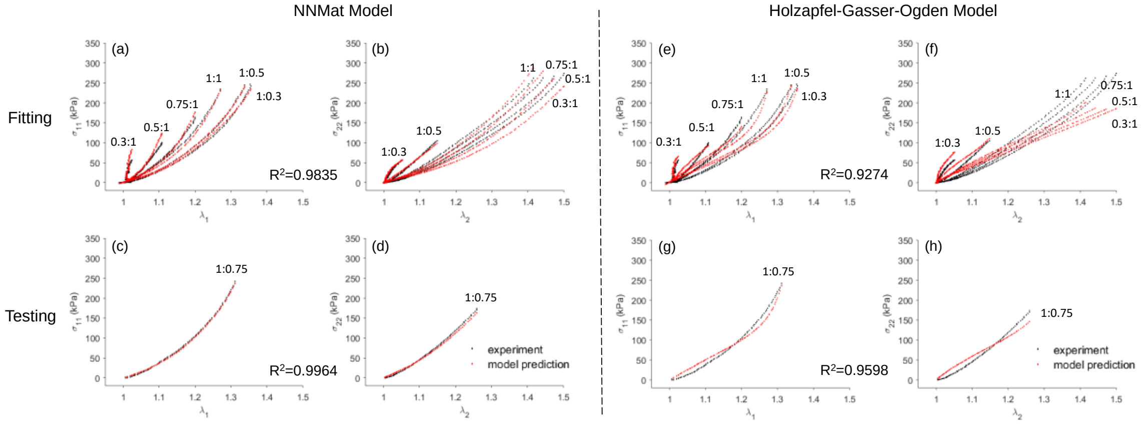

Figure B.6 - Representative Cauchy stress stretch results of the NNMat model and the Holzapfel-Gasser-Ogden model [9] (Section 2.1) in fitting and testing for patient 59.

Table B.3 - Fitting and testing R2 predicted by the NNMat model and expert-constructed models using the testing dataset.

NNMat (3 parameters)			Holzapfel-Gasser-Ogden (4 parameters)		
Patient ID	Fitting R^2	Testing R^2	Patient ID	Fitting R^2	Testing R^2
58	0.9832	0.9747	58	0.9006	0.8737
59	0.9755	0.9749	59	0.9303	0.9197
60	0.9736	0.9511	60	0.9247	0.9171
61	0.9672	0.9658	61	0.8903	0.8094
62	0.8902	0.8272	62	0.8475	0.7297
63	0.9895	0.9891	63	0.9178	0.8838
Gasser-Ogden- Holzapfel (5 parameters)			Four-fiber families (6 parameters)		
Patient ID	Fitting R^2	Testing R^2	Patient ID	Fitting R^2	Testing R^2
58	0.9683	0.9523	58	0.9710	0.9620
59	0.9638	0.9491	59	0.9821	0.9784
60	0.9395	0.9187	60	0.9779	0.9605
61	0.9422	0.9185	61	0.9767	0.9661
62	0.8780	0.8103	62	0.8881	0.7803
63	0.9748	0.9627	63	0.9764	0.9705

Table B.4 - Fitting and testing R^2 (mean ± standard deviation) obtained by the NNMat model and the expert-constructed models. The p-values are computed using Behrens-Fisher two-sample t-test with the null hypothesis that R^2 of the expert-constructed model is great than that of the NNMat model. The results indicate that performance of the NNMat model is much better than the HGO model.

Model	Fitting R^2	p-value	Testing R^2	p-value
NNMat	0.9632±0.0366		0.9471±0.0601	
Holzapfel-Gasser-Ogden	0.9019±0.0306	0.0053	0.8556±0.0735	0.0203
Gasser-Ogden-Holzapfel	0.9445±0.0355	0.1944	0.9186±0.0561	0.2076
Four-fiber families	0.9620±0.0364	0.4782	0.9363±0.0767	0.3956

To visualize the convexity of strain energy density function, similar to Section 4.1, S_{11} and S_{22} were computed at a series of E_{11} and E_{22} values (-0.1 to 0.5). The strain energy density function can be calculated through trapezoidal numerical integration of $W = \int \boldsymbol{S}: d\boldsymbol{E}$. The resulting contours of strain energy function are plotted and examined for each patient. Strain energy functions of four representative patients are shown in Figure B.7, which are approximately convex (strict convexity was not proved). CI values for the fitted NNMat models can be evaluated using Eqn. (B.21), the mean CI in the testing set is 100.00%.

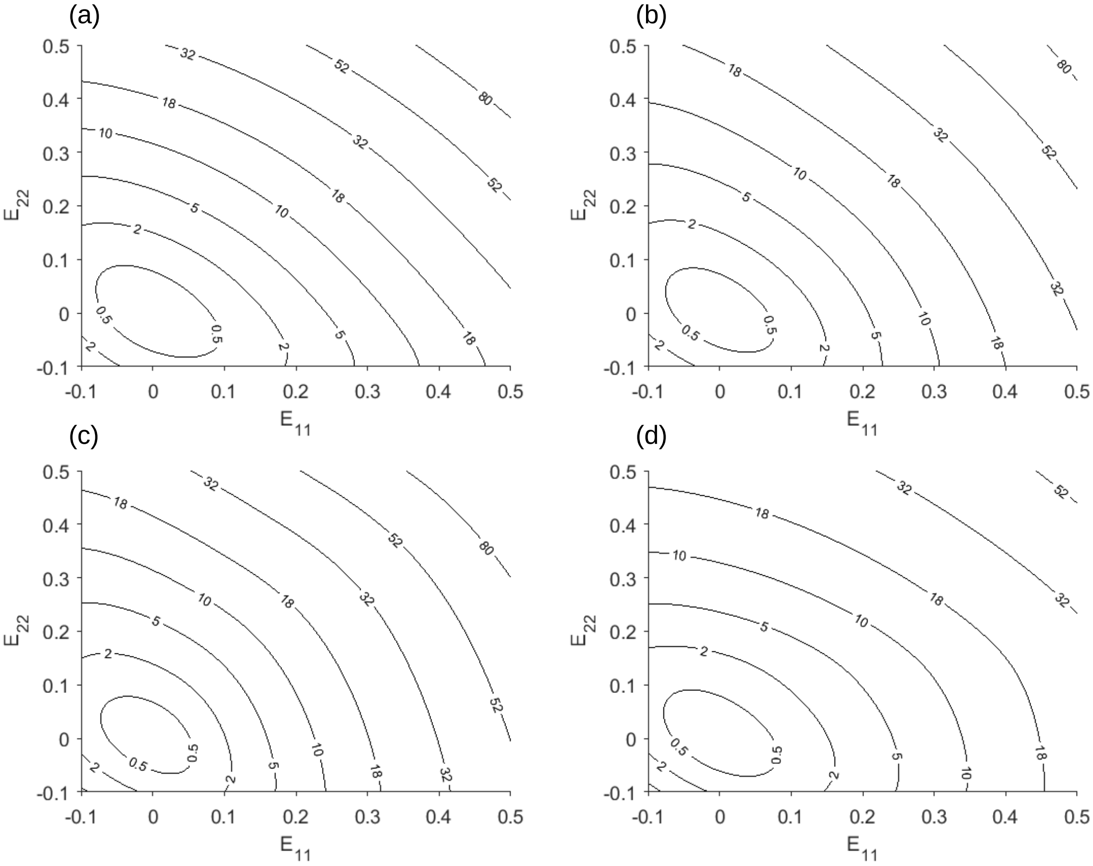

Figure B.7 - Strain energy density function with respect to E_11 and E_22 with E_12=0. Four representative patients are plotted. (a): patient 58, (b): patient 59, (c): patient 60 and (d): patient 62.

B.4.3 Parametric Study

To study the effect of the two subject parameters $\boldsymbol{m} = [m_1, m_2]^T$ on hyperelastic properties of the tissue, a trained NNMat model was employed (trained using the training and validation set) with $\theta = 0^\circ$. The parameter space was sampled at various values of $\widehat{m}_1$ and $\widehat{m}_2$. with an interval of 0.01 in each dimension (from -1 to 1). Note that sampling was performed with the normalized parameters (i.e., $\widehat{m}_1$and $\widehat{m}_2$). We evaluated tangent modulus $T = \frac{\Delta S_{ii}}{\Delta E_{ii}}$ under low strain ($E_{ii} = 0.1$) and high strain ($E_{ii} = 0.5$) in the circumferential (11) and longitudinal (22) directions. The results are shown in Figure B.8.

It can be observed that the high modulus regions are concentrated in the upper right corner of the parameter space, where $\hat{m}_1$and $\hat{m}_2$ are both at maximum. Thus, the larger $\hat{m}_1$and $\hat{m}_2$ are, the higher stiffness the material is, which is physically meaningful.

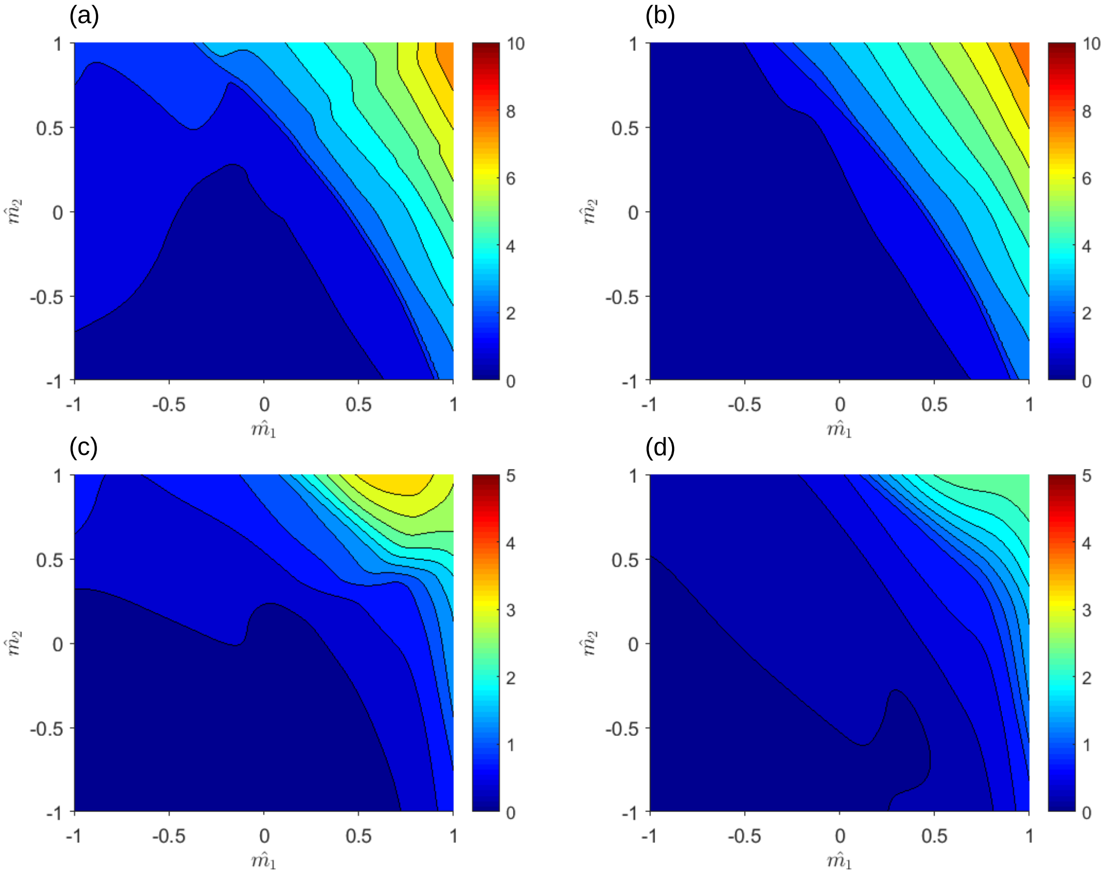

Figure B.8 - Contour plots of tangent moduli in the subject parameter space (θ=0°, trained using patients 7~63). (a) and (b): circumferential; (c) and (d): longitudinal. (a) and (c): tangent modulus at high strain region (0.5); (d) and (d): tangent modulus at low strain region (0.1). Units of tangent moduli are in MPa.

B.5 Discussion

In this study, a novel generic physics-informed machine learning model was proposed for constitutive modeling of soft biological tissues. The proposed NNMat model utilizes a hierarchical learning strategy: it can learn from data of multiple subjects to improve its prediction for individuals. The structure of the NNMat model consists of a class parameter set for characterizing hyperelastic properties of a class of materials and a subject parameter set (three parameters) for fitting mechanical response of an individual subject. In the NNMat model, the subject parameter set is connected to the neural network via skip connections to facilitate hierarchical learning. In addition, a novel hierarchical training strategy was devised to determine the optimal parameters, which involve the determination of common mechanical properties for a class of material (training) and fitting of mechanical response of individual subjects (fitting). The modeling process is analogous to the DEICE procedure for expert-constructed models. Consequently, the NNMat model provides a convenient and general methodology for constitutive modeling of soft biological tissues. It inherits advantages of ML approaches: (1) construction of the NNMat model is an automatic process and does not involve any manual derivations, and (2) predictive capability of the NNMat model with 3 constitutive parameters is, superior to the 4-parameter HGO model; slightly better than the 5-parameter GOH model with consideration of fiber dispersion; and similar to the 6-parameter four-fiber model with two additional invariants. It also shares desired properties with the expert-constructed models: (1) only a few constitutive (subject) parameters $\{m_1, m_2, \theta\}$ are needed for modeling an individual sample response; (2) a physics constraint was enforced for convexity of the strain energy density function, which ensures that the constitutive relation is physically-relevant and numerically stable. Since the NNMat model is differentiable, the elasticity tensor can be numerically computed, which makes the model suitable to be intergraded into a FE solver; (3) physical meanings of the constitutive (subject) parameters can be analyzed. Although training of the NNMat model takes approximately 16~18 hours in our exemplary application. It should be noted that more time and efforts may be required for a domain expert to derive constitutive equations [254].

The current NNMat model was developed for modeling the hyperelastic properties of soft tissues and trained by using planar biaxial data of aortic wall tissues, it may also be extended to model history- or rate- dependent constitutive relations. For materials that exhibit history dependence, stress/strain history and internal state variables may be included as additional input variables. For rate-dependent material behavior, stress/strain rate may be incorporated similar to the traditional FFNN models [284, 285].

B.5.1 Comparison to Traditional FFNN Models

A constitutive model with a large number of constitutive parameters often results in over-parameterization: different combinations of constitutive parameters are nonlinearly coupled which can lead to very similar mechanical response. This is undesirable form a data fitting perspective, in which the optimization problem is highly nonlinear, multivariate and non-convex, which can cause optimization difficulty known as the local optima [99]. In this case, the mechanical properties cannot be unambiguously represented by a set of constitutive parameters. Therefore, a constitutive model with fewer constitutive parameters is always preferred [286, 287]. In contrast to the traditional FFNN models [110, 111, 268, 284, 285] that have hundreds to thousands of parameters, the proposed NNMat model with only three constitutive (subject) parameters is analogous to the expert-constructed models, which may be more suitable for practical applications. The NNMat model may also facilitate inverse estimation of constitutive parameters from *in vivo* clinical data, such as image-derived aortic wall motions ([99, 100], CHAPTER 3, and APPENDIX), for which only the data within the physiological range can be obtained and therefore the identification solution may not be unique if there are too many constitutive parameters in the model.

B.5.2 Standard Regularization Procedures

Classically, the bias–variance trade-off, which implies that the model complexity must be limited to avoid overfitting, is often considered when training a ML model. In many applications, neural network size is significantly larger than data size, and training error approaches zero, which would be traditionally considered overfitted. Therefore, standard regularization procedures, e.g., weight decay and weight pruning, are often employed when training a neural network to prevent overfitting. However, surprisingly, the performance of the over-parameterized network on test set can be excellent [288]. This could be explained by a "double-descent" risk curve [288], which indicates that once the network complexity exceeds a threshold (i.e., being over-parameterized), the test risk starts to decrease (i.e. high performance on test set). The choice of whether to regularize the model can also depend on the available data size. In this study, the NNMat model has 18,188 class parameters and 3 subject parameters. In total, our biaxial data consists of 82,200 strain-stress data points, and there are 73,614 strain-stress data points in the training and validation dataset. In addition, it is shown recently that physics constraint may provide regularization effect in the physics-informed neural network [289], which may significantly reduce the required training data size [290]. Hence, our model may be "underfitting" the data, not complex enough. Nevertheless, the NNMat model has good fitting and testing performance on the testing data without using standard regularization methods. Readers may choose to incorporate standard regularization procedures when implementing their own model, depending on the type of application and available data size.

B.5.3 The NNMat Model is Generic

It is often necessary to modify the general form of the constitutive relation for modeling of a new (structurally different) class of material, e.g. from modeling the arterial wall to the passive myocardium [255]. Although the exponential functional form of strain energy density has been widely adopted in many expert-constructed constitutive models of soft tissues [32-34, 221, 255, 256] to describe the strain stiffening effect due to recruitment of collagen fibers following the work by Dr. Y.C. Fung [253], a number of studies [254, 291, 292] advocated polynomial strain energy functions. In general, the choice of constitutive model should be dependent on the type of tissues and loading ranges in specific applications, e.g., the exponential function without consideration of damage can lead to over-prediction of stress at large strain conditions [51, 53, 169, 293]. Since the proposed NNMat model is generic (i.e., not specifically designed for ATAA tissues), we anticipated that its network structure can be applied to other tissue behaviors and characteristics, and its predictive capability is largely dependent upon the training data provided to it. With abundant training data to be collected (larger population, wider loading range) in the future, the predictive capability of the NNMat is expected to be improved.

B.6 Conclusions

In this study, a physics-informed machine learning model was proposed for constitutive modeling of soft biological tissues. A neural network material model (NNMat) with novel structure and hierarchical learning strategy is proposed. The NNMat model consist of two parameter sets: the class parameter set for characterizing the general elastic properties of a class of materials and the subject parameter set with three parameters for individual material response. Skip connections are utilized in the neural network structure to facilitate hierarchical learning. The proposed NNMat model can learn from the data of multiple subjects to improve its prediction for individuals. Physics constraints were enforced for convexity of the strain energy density function. From the tests we performed, both in-sample and out-of-sample accuracy metrics of the NNMat model are significantly higher than the expert-constructed model.

REFERENCES

1. Sherifova, S. and G.A. Holzapfel, *Biomechanics of aortic wall failure with a focus on dissection and aneurysm: a review.* Acta biomaterialia, 2019. **99**: p. 1-17.

2. Criado, F.J., *Aortic dissection: a 250-year perspective.* Texas Heart Institute Journal, 2011. **38**(6): p. 694.

3. Davies, R.R., et al., *Yearly rupture or dissection rates for thoracic aortic aneurysms: simple prediction based on size.* The Annals of thoracic surgery, 2002. **73**(1): p. 17-28.

4. Elefteriades, J.A., *Natural history of thoracic aortic aneurysms: indications for surgery, and surgical versus nonsurgical risks.* The Annals of thoracic surgery, 2002. **74**(5): p. S1877-S1880.

5. Elefteriades, J.A., *Thoracic Aortic Aneurysm: Reading the Enemy's Playbook.* Yale Journal of Biology and Medicine, 2008. **81**(4): p. 175-186.

6. Coady, M.A., et al., *Familial patterns of thoracic aortic aneurysms.* Archives of surgery, 1999. **134**(4): p. 361-367.

7. Achneck, H., et al., *Ascending thoracic aneurysms are associated with decreased systemic atherosclerosis.* Chest, 2005. **128**(3): p. 1580-1586.

8. Davies, R.R., et al., *Natural history of ascending aortic aneurysms in the setting of an unreplaced bicuspid aortic valve.* The Annals of thoracic surgery, 2007. **83**(4): p. 1338-1344.

9. Coady, M.A., et al., *What is the appropriate size criterion for resection of thoracic aortic aneurysms?* The Journal of Thoracic and Cardiovascular Surgery, 1997. **113**(3): p. 476-491.

10. Kuzmik, G.A., A.X. Sang, and J.A. Elefteriades, *Natural history of thoracic aortic aneurysms.* Journal of vascular surgery, 2012. **56**(2): p. 565-571.

11. Elefteriades, J.A., *Endovascular therapy for thoracic aneurysm diseases: CON.* Cardiology clinics, 2010. **28**(2): p. 413-417.

12. Davies, R.R., et al., *Novel measurement of relative aortic size predicts rupture of thoracic aortic aneurysms.* The Annals of thoracic surgery, 2006. **81**(1): p. 169-177.

13. Elefteriades, J.A. and E.A. Farkas, *Thoracic aortic aneurysm clinically pertinent controversies and uncertainties.* J Am Coll Cardiol, 2010. **55**(9): p. 841-857.

14. Fillinger, M.F., et al., *Anatomic characteristics of ruptured abdominal aortic aneurysm on conventional CT scans: Implications for rupture risk.* J Vasc Surg, 2004. **39**(6): p. 1243-1252.

15. Pham, T., et al., *Biomechanical characterization of ascending aortic aneurysm with concomitant bicuspid aortic valve and bovine aortic arch.* Acta Biomaterialia, 2013. **9**(8): p. 7927-7936.

16. Teng, Z., et al., *Layer-and direction-specific material properties, extreme extensibility and ultimate material strength of human abdominal aorta and aneurysm: a uniaxial extension study.* Annals of biomedical engineering, 2015. **43**(11): p. 2745-2759.

17. Kim, J.-H., et al., *Experimental characterization of rupture in human aortic aneurysms using a full-field measurement technique.* Biomechanics and modeling in mechanobiology, 2012. **11**(6): p. 841-853.

18. Shah, S.B., et al., *Prefailure and failure mechanics of the porcine ascending thoracic aorta: experiments and a multiscale model.* Journal of biomechanical engineering, 2014. **136**(2).

19. García-Herrera, C.M., et al., *Mechanical behaviour and rupture of normal and pathological human ascending aortic wall.* Medical & biological engineering & computing, 2012. **50**(6): p. 559-566.

20. Haskett, D., et al., *Microstructural and biomechanical alterations of the human aorta as a function of age and location.* Biomechanics and modeling in mechanobiology, 2010. **9**(6): p. 725-736.

21. Iliopoulos, D.C., et al., *Regional and directional variations in the mechanical properties of ascending thoracic aortic aneurysms.* Medical Engineering & Physics, 2009. **31**(1): p. 1-9.

22. Sokolis, D.P., E.P. Kritharis, and D.C. Iliopoulos, *Effect of layer heterogeneity on the biomechanical properties of ascending thoracic aortic aneurysms.* Medical & Biological Engineering & Computing, 2012. **50**(12): p. 1227-1237.

23. Forsell, C., et al., *Biomechanical Properties of the Thoracic Aneurysmal Wall: Differences Between Bicuspid Aortic Valve and Tricuspid Aortic Valve Patients.* The Annals of Thoracic Surgery, 2014. **98**(1): p. 65-71.

24. García, A., et al., *Experimental study and constitutive modelling of the passive mechanical properties of the porcine carotid artery and its relation to histological analysis: Implications in animal cardiovascular device trials.* Medical Engineering & Physics, 2011. **33**(6): p. 665-676.

25. Sun, W., M.S. Sacks, and M.J. Scott, *Effects of Boundary Conditions on the Estimation of the Planar Biaxial Mechanical Properties of Soft Tissues.* Journal of Biomechanical Engineering, 2005. **127**(4): p. 709-715.

26. Geest, J.P.V., M.S. Sacks, and D.A. Vorp, *Age dependency of the biaxial biomechanical behavior of human abdominal aorta.* J. Biomech. Eng., 2004. **126**(6): p. 815-822.

27. Mohan, D. and J.W. Melvin, *Failure properties of passive human aortic tissue. II—Biaxial tension tests.* Journal of biomechanics, 1983. **16**(1): p. 31-44.

28. Marra, S.P., et al., *Elastic and rupture properties of porcine aortic tissue measured using inflation testing.* Cardiovascular Engineering, 2006. **6**(4): p. 123-131.

29. Romo, A., et al., *In vitro analysis of localized aneurysm rupture.* Journal of Biomechanics, 2014. **47**(3): p. 607-616.

30. Trabelsi, O., et al., *Patient specific stress and rupture analysis of ascending thoracic aneurysms.* Journal of biomechanics, 2015. **48**(10): p. 1836-1843.

31. Duprey, A., et al., *Biaxial rupture properties of ascending thoracic aortic aneurysms.* Acta Biomaterialia, 2016. **42**: p. 273-285.

32. Demiray, H., *A note on the elasticity of soft biological tissues.* Journal of biomechanics, 1972. **5**(3): p. 309-311.

33. Holzapfel, G.A., T.C. Gasser, and R.W. Ogden, *A New Constitutive Framework for Arterial Wall Mechanics and a Comparative Study of Material Models.* Journal of elasticity and the physical science of solids, 2000. **61**(1): p. 1-48.

34. Gasser, T.C., R.W. Ogden, and G.A. Holzapfel, *Hyperelastic modelling of arterial layers with distributed collagen fibre orientations.* Journal of The Royal Society Interface, 2006. **3**(6): p. 15-35.

35. Holzapfel, G.A., *Nonlinear solid mechanics*. Vol. 24. 2000: Wiley Chichester.

36. Raghavan, M.L., et al., *Wall stress distribution on three-dimensionally reconstructed models of human abdominal aortic aneurysm.* Journal of Vascular Surgery, 2000. **31**(4): p. 760-769.

37. Lu, J., X. Zhou, and M.L. Raghavan, *Inverse elastostatic stress analysis in pre-deformed biological structures: Demonstration using abdominal aortic aneurysms.* Journal of Biomechanics, 2007. **40**(3): p. 693-696.

38. Rissland, P., et al., *Abdominal Aortic Aneurysm Risk of Rupture: Patient-Specific FSI Simulations Using Anisotropic Model.* Journal of Biomechanical Engineering, 2008. **131**(3).

39. Kazimi, S., *Solid mechanics*. 2001: Tata McGraw-Hill Education.

40. Raghavan, M.L., et al., *Regional distribution of wall thickness and failure properties of human abdominal aortic aneurysm.* Journal of biomechanics, 2006. **39**(16): p. 3010-3016.

41. Fillinger, M.F., et al., *In vivo analysis of mechanical wall stress and abdominal aortic aneurysm rupture risk.* Journal of vascular surgery, 2002. **36**(3): p. 589-597.

42. Speelman, L., et al., *Effects of wall calcifications in patient-specific wall stress analyses of abdominal aortic aneurysms.* 2007.

43. Dorfmann, A., et al., *Evaluating patient-specific abdominal aortic aneurysm wall stress based on flow-induced loading.* Biomechanics and Modeling in Mechanobiology, 2010. **9**(2): p. 127-139.

44. Derrien, K., et al., *Prediction of the effective damage properties and failure properties of nonlinear anisotropic discontinuous reinforced composites.* Computer Methods in Applied Mechanics and Engineering, 2000. **185**(2-4): p. 93-107.

45. Sun, C.T., *1.20 - Strength Analysis of Unidirectional Composites and Laminates*, in *Comprehensive Composite Materials*, A. Kelly and C. Zweben, Editors. 2000, Pergamon: Oxford. p. 641-666.

46. Dong, H. and J. Wang, *A criterion for failure mode prediction of angle-ply composite laminates under in-plane tension.* Composite Structures, 2015. **128**: p. 234-240.

47. Dong, H., J. Wang, and B.L. Karihaloo, *An improved Puck's failure theory for fibre-reinforced composite laminates including the in situ strength effect.* Composites science and technology, 2014. **98**: p. 86-92.

48. Azzi, V. and S. Tsai, *Anisotropic strength of composites.* Experimental mechanics, 1965. **5**(9): p. 283-288.

49. Tsai, S.W., *Strength Characteristics of Composite Materials*. 1965, Philco Corp Newport Beach CA.

50. Hashin, Z. and A. Rotem, *A fatigue failure criterion for fiber reinforced materials.* Journal of composite materials, 1973. **7**(4): p. 448-464.

51. Weisbecker, H., et al., *Layer-specific damage experiments and modeling of human thoracic and abdominal aortas with non-atherosclerotic intimal thickening.* Journal of the Mechanical Behavior of Biomedical Materials, 2012. **12**: p. 93-106.

52. Korenczuk, C.E., et al., *Isotropic failure criteria are not appropriate for anisotropic fibrous biological tissues.* Journal of biomechanical engineering, 2017. **139**(7).

53. Li, K. and G.A. Holzapfel, *Multiscale modeling of fiber recruitment and damage with a discrete fiber dispersion method.* Journal of the Mechanics and Physics of Solids, 2019. **126**: p. 226-244.

54. CANHAM, P.B., et al., *Measurements from light and polarised light microscopy of human coronary arteries fixed at distending pressure.* Cardiovascular Research, 1989. **23**(11): p. 973-982.

55. Finlay, H.M., L. McCullough, and P.B. Canham, *Three-dimensional collagen organization of human brain arteries at different transmural pressures.* Journal of vascular research, 1995. **32**(5): p. 301-312.

56. Schriefl, A.J., et al., *Determination of the layer-specific distributed collagen fibre orientations in human thoracic and abdominal aortas and common iliac arteries.* Journal of the Royal Society Interface, 2012. **9**(71): p. 1275-1286.

57. Martin, C., W. Sun, and J. Elefteriades, *Patient-specific finite element analysis of ascending aorta aneurysms.* American Journal of Physiology - Heart and Circulatory Physiology, 2015. **308**(10): p. H1306-H1316.

58. Pons, R., et al., *Fluid–structure interaction simulations outperform computational fluid dynamics in the description of thoracic aorta haemodynamics and in the differentiation of progressive dilation in Marfan syndrome patients.* Royal Society Open Science, 2020. **7**(2): p. 191752.

59. Gasser, T.C., et al., *A novel strategy to translate the biomechanical rupture risk of abdominal aortic aneurysms to their equivalent diameter risk: method and retrospective validation.* European Journal of Vascular and Endovascular Surgery, 2014. **47**(3): p. 288-295.

60. Polzer, S., et al., *Biomechanical indices are more sensitive than diameter in predicting rupture of asymptomatic abdominal aortic aneurysms.* Journal of Vascular Surgery, 2020. **71**(2): p. 617-626.e6.

61. Doyle, B.J., et al., *Biomechanical Assessment Predicts Aneurysm Related Events in Patients with Abdominal Aortic Aneurysm.* European Journal of Vascular and Endovascular Surgery, 2020. **60**(3): p. 365-373.

62. Leemans, E.L., et al., *Additional value of biomechanical indices based on CTa for rupture risk assessment of abdominal aortic aneurysms.* PLOS ONE, 2018. **13**(8): p. e0202672.

63. Martin, C., et al., *Predictive biomechanical analysis of ascending aortic aneurysm rupture potential.* Acta Biomaterialia, 2013. **9**(12): p. 9392-9400.

64. Hatzaras, I.S., et al., *Role of Exertion or Emotion as Inciting Events for Acute Aortic Dissection.* American Journal of Cardiology, 2007. **100**(9): p. 1470-1472.

65. Rissland, P., et al., *Abdominal aortic aneurysm risk of rupture: patient-specific FSI simulations using anisotropic model.* Journal of biomechanical engineering, 2009. **131**(3).

66. VANDE GEEST, J.P., et al., *A biomechanics-based rupture potential index for abdominal aortic aneurysm risk assessment: demonstrative application.* Annals of the New York Academy of Sciences, 2006. **1085**(1): p. 11-21.

67. Joldes, G.R., et al., *BioPARR: A software system for estimating the rupture potential index for abdominal aortic aneurysms.* Scientific Reports, 2017. **7**(1): p. 4641.

68. Angouras, D.C., E.P. Kritharis, and D.P. Sokolis, *Regional distribution of delamination strength in ascending thoracic aortic aneurysms.* Journal of the Mechanical Behavior of Biomedical Materials, 2019. **98**: p. 58-70.

69. Liu, M., et al., *A Novel Anisotropic Failure Criterion With Dispersed Fiber Orientations for Aortic Tissues.* Journal of Biomechanical Engineering, 2020. **142**(11).

70. Gasser, T.C., et al., *Biomechanical rupture risk assessment of abdominal aortic aneurysms: model complexity versus predictability of finite element simulations.* European Journal of Vascular and Endovascular Surgery, 2010. **40**(2): p. 176-185.

71. McGloughlin, T.M. and B.J. Doyle, *New approaches to abdominal aortic aneurysm rupture risk assessment: engineering insights with clinical gain.* Arteriosclerosis, thrombosis, and vascular biology, 2010. **30**(9): p. 1687-1694.

72. Gasser, T.C., *Biomechanical rupture risk assessment: a consistent and objective decision-making tool for abdominal aortic aneurysm patients.* AORTA Journal, 2016. **4**(2): p. 42.

73. Geest, J.P.V., et al., *Towards a noninvasive method for determination of patient-specific wall strength distribution in abdominal aortic aneurysms.* Annals of biomedical engineering, 2006. **34**(7): p. 1098-1106.

74. Polzer, S. and T.C. Gasser, *Biomechanical rupture risk assessment of abdominal aortic aneurysms based on a novel probabilistic rupture risk index.* Journal of The Royal Society Interface, 2015. **12**(113): p. 20150852.

75. Iman, R.L. and J.C. Helton, *An Investigation of Uncertainty and Sensitivity Analysis Techniques for Computer Models.* Risk Analysis, 1988. **8**(1): p. 71-90.

76. Sankaran, S. and A.L. Marsden, *A Stochastic Collocation Method for Uncertainty Quantification and Propagation in Cardiovascular Simulations.* Journal of Biomechanical Engineering, 2011. **133**(3).

77. Biehler, J., M.W. Gee, and W.A. Wall, *Towards efficient uncertainty quantification in complex and large-scale biomechanical problems based on a Bayesian multi-fidelity scheme.* Biomechanics and Modeling in Mechanobiology, 2015. **14**(3): p. 489-513.

78. Boccadifuoco, A., et al., *Uncertainty quantification in numerical simulations of the flow in thoracic aortic aneurysms.* Institute of Structural Analysis and Antiseismic Research, School of Civil Engineering, National Technical University of Athens, NTUA, Athens, Greece, 2016: p. 6226-6249.

79. Zhao, X., X. Chen, and J. Lu, *Pointwise Identification of Elastic Properties in Nonlinear Hyperelastic Membranes—Part II: Experimental Validation.* Journal of Applied Mechanics, 2009. **76**(6): p. 061014-061014.

80. Kroon, M. and G.A. Holzapfel, *Elastic properties of anisotropic vascular membranes examined by inverse analysis.* Computer Methods in Applied Mechanics and Engineering, 2009. **198**(45–46): p. 3622-3632.

81. Grédiac, M., et al., *The Virtual Fields Method for Extracting Constitutive Parameters From Full-Field Measurements: a Review.* Strain, 2006. **42**(4): p. 233-253.

82. Avril, S., P. Badel, and A. Duprey, *Anisotropic and hyperelastic identification of in vitro human arteries from full-field optical measurements.* Journal of Biomechanics, 2010. **43**(15): p. 2978-2985.

83. Genovese, K., et al., *An Improved Panoramic Digital Image Correlation Method for Vascular Strain Analysis and Material Characterization.* Journal of the mechanical behavior of biomedical materials, 2013. **27**: p. 132-142.

84. Schulze-Bauer, C.A.J. and G.A. Holzapfel, *Determination of constitutive equations for human arteries from clinical data.* Journal of Biomechanics, 2003. **36**(2): p. 165-169.

85. Stålhand, J., *Determination of human arterial wall parameters from clinical data.* Biomechanics and Modeling in Mechanobiology, 2009. **8**(2): p. 141-148.

86. Olsson, T. and J.S.A. Klarbring, *Modeling initial strain distribution in soft tissues with application to arteries.* Biomechanics and Modeling in Mechanobiology, 2006. **5**(1): p. 27-38.

87. Masson, I., et al., *Characterization of arterial wall mechanical behavior and stresses from human clinical data.* Journal of Biomechanics, 2008. **41**(12): p. 2618-2627.

88. Masson, I., et al., *Carotid artery mechanical properties and stresses quantified using in vivo data from normotensive and hypertensive humans.* Biomechanics and Modeling in Mechanobiology, 2011. **10**(6): p. 867-882.

89. Åstrand, H., et al., *In vivo estimation of the contribution of elastin and collagen to the mechanical properties in the human abdominal aorta: effect of age and sex.* Journal of Applied Physiology, 2011. **110**(1): p. 176-187.

90. Smoljkić, M., et al., *Non-invasive, energy-based assessment of patient-specific material properties of arterial tissue.* Biomechanics and Modeling in Mechanobiology, 2015. **14**(5): p. 1045-1056.

91. Liu, H. and P. Shi, *Maximum a Posteriori Strategy for the Simultaneous Motion and Material Property Estimation of the Heart.* IEEE Transactions on Biomedical Engineering, 2009. **56**(2): p. 378-389.

92. Zhang, F., et al., *Towards patient-specific modeling of mitral valve repair: 3D transesophageal echocardiography-derived parameter estimation.* Medical Image Analysis, 2017. **35**: p. 599-609.

93. Franquet, A., et al., *Identification of the in vivo elastic properties of common carotid arteries from MRI: A study on subjects with and without atherosclerosis.* Journal of the Mechanical Behavior of Biomedical Materials, 2013. **27**: p. 184-203.

94. Farzaneh, S., O. Trabelsi, and S. Avril, *Inverse identification of local stiffness across ascending thoracic aortic aneurysms.* Biomechanics and Modeling in Mechanobiology, 2019. **18**(1): p. 137-153.

95. Farzaneh, S., et al., *Identifying Local Arterial Stiffness to Assess the Risk of Rupture of Ascending Thoracic Aortic Aneurysms.* Annals of Biomedical Engineering, 2019. **47**(4): p. 1038-1050.

96. Trabelsi, O., et al., *Predictive Models with Patient Specific Material Properties for the Biomechanical Behavior of Ascending Thoracic Aneurysms.* Annals of Biomedical Engineering, 2016. **44**(1): p. 84-98.

97. Zeinali-Davarani, S., et al., *Identification of in vivo material and geometric parameters of a human aorta: toward patient-specific modeling of abdominal aortic aneurysm.* Biomechanics and Modeling in Mechanobiology, 2011. **10**(5): p. 689-699.

98. Liu, H., et al., *Using In Vivo Cine and 3D Multi-Contrast MRI to Determine Human Atherosclerotic Carotid Artery Material Properties and Circumferential Shrinkage Rate and Their Impact on Stress/Strain Predictions.* Journal of Biomechanical Engineering, 2012. **134**(1): p. 011008-011008-9.

99. Wittek, A., et al., *In vivo determination of elastic properties of the human aorta based on 4D ultrasound data.* Journal of the Mechanical Behavior of Biomedical Materials, 2013. **27**: p. 167-183.

100. Wittek, A., et al., *A finite element updating approach for identification of the anisotropic hyperelastic properties of normal and diseased aortic walls from 4D ultrasound strain imaging.* Journal of the Mechanical Behavior of Biomedical Materials, 2016. **58**: p. 122-138.

101. Liu, M., L. Liang, and W. Sun, *Estimation of in vivo mechanical properties of the aortic wall: A multi-resolution direct search approach.* Journal of the Mechanical Behavior of Biomedical Materials, 2018. **77**: p. 649-659.

102. LeCun, Y., Y. Bengio, and G.E. Hinton, *Deep Learning.* Nature, 2015. **521**: p. 436-444.

103. He, K., et al., *Delving Deep into Rectifiers: Surpassing Human-Level Performance on ImageNet Classification.* IEEE International Conference on Computer Vision, 2015.

104. Kokkinos, I., *Pushing the Boundaries of Boundary Detection using Deep Learning.* Int.l Conf. on Learning Representations, 2016.

105. Taigman, Y., et al., *DeepFace: Closing the Gap to Human-Level Performance in Face Verification.* IEEE Conference on Computer Vision and Pattern Recognition, 2014.

106. He, K., et al., *Deep Residual Learning for Image Recognition.* IEEE Conference on Computer Vision and Pattern Recognition, 2016.

107. Krizhevsky, A., I. Sutskever, and G.E. Hinton, *ImageNet Classification with Deep Convolutional Neural Networks.* Neural Information Processing Systems, 2012.

108. Wu, Y., et al., *Google's Neural Machine Translation System: Bridging the Gap between Human and Machine Translation.* Computing Research Repository, 2016. **abs/1609.08144**.

109. Hannun, A., et al., *Deep Speech: Scaling up end-to-end speech recognition.* Computing Research Repository, 2014. **abs/1412.5567**.

110. Yagawa, G. and H. Okuda, *Neural networks in computational mechanics.* Archives of Computational Methods in Engineering, 1996. **3**(4): p. 435.

111. Ghaboussi, J. and D.E. Sidarta, *New nested adaptive neural networks (NANN) for constitutive modeling.* Computers and Geotechnics, 1998. **22**(1): p. 29-52.

112. Theocaris, P.S. and P.D. Panagiotopoulos, *Neural networks for computing in fracture mechanics. Methods and prospects of applications.* Computer Methods in Applied Mechanics and Engineering, 1993. **106**(1): p. 213-228.

113. Huber, N. and C. Tsakmakis, *Determination of constitutive properties fromspherical indentation data using neural networks. Part i:the case of pure kinematic hardening in plasticity laws.* Journal of the Mechanics and Physics of Solids, 1999. **47**(7): p. 1569-1588.

114. Huber, N. and C. Tsakmakis, *Determination of constitutive properties fromspherical indentation data using neural networks. Part ii:plasticity with nonlinear isotropic and kinematichardening.* Journal of the Mechanics and Physics of Solids, 1999. **47**(7): p. 1589-1607.

115. Luo, Y., et al., *Machine learning–aided exploration of relationship between strength and elastic properties in ascending thoracic aneurysm.* International Journal for Numerical Methods in Biomedical Engineering, 2018. **34**(6): p. e2977.

116. Cilla, M., et al., *On the use of machine learning techniques for the mechanical characterization of soft biological tissues.* International Journal for Numerical Methods in Biomedical Engineering. **0**(0): p. e3121.

117. Jiang, Z., et al., *A Deep Learning Approach to Predict Abdominal Aortic Aneurysm Expansion Using Longitudinal Data.* Front. Phys. 7: 235. doi: 10.3389/fphy, 2020.

118. Liang, L., M. Liu, and W. Sun, *A deep learning approach to estimate chemically-treated collagenous tissue nonlinear anisotropic stress-strain responses from microscopy images.* Acta Biomaterialia, 2017. **63**: p. 227-235.

119. Liang, L., et al., *A deep learning approach to estimate stress distribution: a fast and accurate surrogate of finite-element analysis.* Journal of The Royal Society Interface, 2018. **15**(138).

120. Liang, L., W. Mao, and W. Sun, *A feasibility study of deep learning for predicting hemodynamics of human thoracic aorta.* Journal of Biomechanics, 2020. **99**: p. 109544.

121. Bols, J., et al., *A computational method to assess the in vivo stresses and unloaded configuration of patient-specific blood vessels.* Journal of Computational and Applied Mathematics, 2013. **246**: p. 10-17.

122. Liang, L., et al., *A machine learning approach as a surrogate of finite element analysis–based inverse method to estimate the zero-pressure geometry of human thoracic aorta.* International Journal for Numerical Methods in Biomedical Engineering, 2018. **0**(0): p. e3103.

123. Taylor, C.A. and C.A. Figueroa, *Patient-specific Modeling of Cardiovascular Mechanics.* Annual review of biomedical engineering, 2009. **11**: p. 109-134.

124. Martin, C., et al., *Age-Dependent Ascending Aorta Mechanics Assessed Through Multiphase CT.* Annals of Biomedical Engineering, 2013. **41**(12): p. 2565-2574.

125. Liu, M., L. Liang, and W. Sun, *A new inverse method for estimation of in vivo mechanical properties of the aortic wall.* Journal of the Mechanical Behavior of Biomedical Materials, 2017. **72**: p. 148-158.

126. Liu, M., et al., *On the computation of in vivo transmural mean stress of patient-specific aortic wall.* Biomechanics and modeling in mechanobiology, 2019. **18**(2): p. 387-398.

127. Vaishnav, R.N. and J. Vossoughi, *Residual stress and strain in aortic segments.* Journal of Biomechanics, 1983. **20**(3): p. 235-237.

128. Chuong, C.J. and Y.C. Fung, *Residual Stress in Arteries,* in *Frontiers in Biomechanics*, G.W. Schmid-Schönbein, S.L.Y. Woo, and B.W. Zweifach, Editors. 1986, Springer New York: New York, NY. p. 117-129.

129. Matsumoto, T. and K. Hayashi, *Stress and Strain Distribution in Hypertensive and Normotensive Rat Aorta Considering Residual Strain.* Journal of Biomechanical Engineering, 1996. **118**(1): p. 62-73.

130. Humphrey, J.D., *Cardiovascular solid mechanics. Cells, tissues, and organs.* 2002.

131. Delfino, A., et al., *Residual strain effects on the stress field in a thick wall finite element model of the human carotid bifurcation.* Journal of Biomechanics, 1997. **30**(8): p. 777-786.

132. Fung, Y.C., *What are the residual stresses doing in our blood vessels?* Annals of Biomedical Engineering, 1991. **19**(3): p. 237-249.

133. Pierce, D.M., et al., *A method for incorporating three-dimensional residual stretches/stresses into patient-specific finite element simulations of arteries.* Journal of the Mechanical Behavior of Biomedical Materials, 2015. **47**: p. 147-164.

134. Alastrué, V., et al., *Numerical framework for patient-specific computational modelling of vascular tissue.* International Journal for Numerical Methods in Biomedical Engineering, 2010. **26**(1): p. 35-51.

135. Miller, K. and J. Lu, *On the prospect of patient-specific biomechanics without patient-specific properties of tissues.* Journal of the Mechanical Behavior of Biomedical Materials, 2013. **27**: p. 154-166.

136. Joldes, G.R., et al., *A simple, effective and clinically applicable method to compute abdominal aortic aneurysm wall stress.* Journal of the Mechanical Behavior of Biomedical Materials, 2016. **58**: p. 139-148.

137. Lu, J. and Y. Luo, *Solving membrane stress on deformed configuration using inverse elastostatic and forward penalty methods.* Computer Methods in Applied Mechanics and Engineering, 2016. **308**: p. 134-150.

138. Horný, L., M. Netušil, and T. Voňavková, *Axial prestretch and circumferential distensibility in biomechanics of abdominal aorta.* Biomechanics and Modeling in Mechanobiology, 2014. **13**(4): p. 783-799.

139. Holzapfel, G.A. and R.W. Ogden, *Modelling the layer-specific three-dimensional residual stresses in arteries, with an application to the human aorta.* Journal of The Royal Society Interface, 2010. **7**(46): p. 787-799.

140. Liang, L., et al., *A machine learning approach to investigate the relationship between shape features and numerically predicted risk of ascending aortic aneurysm.* Biomechanics and Modeling in Mechanobiology, 2017. **16**(5): p. 1519-1533.

141. Guo, X. and G.S. Kassab, *Variation of mechanical properties along the length of the aorta in C57bl/6 mice.* American Journal of Physiology-Heart and Circulatory Physiology, 2003. **285**(6): p. H2614-H2622.

142. Sokolis, D.P., *Effects of aneurysm on the directional, regional, and layer distribution of residual strains in ascending thoracic aorta.* Journal of the Mechanical Behavior of Biomedical Materials, 2015. **46**: p. 229-243.

143. Holzapfel, G.A., et al., *Layer-Specific 3D Residual Deformations of Human Aortas with Non-Atherosclerotic Intimal Thickening.* Annals of Biomedical Engineering, 2007. **35**(4): p. 530-545.

144. Abaqus, *Abaqus 6.14 Documentation*. 2014.

145. Weisbecker, H., D.M. Pierce, and G.A. Holzapfel, *A generalized prestressing algorithm for finite element simulations of preloaded geometries with application to the aorta.* International Journal for Numerical Methods in Biomedical Engineering, 2014. **30**(9): p. 857-872.

146. Gasser, T.C., et al., *Spatial orientation of collagen fibers in the abdominal aortic aneurysm's wall and its relation to wall mechanics.* Acta Biomaterialia, 2012. **8**(8): p. 3091-3103.

147. Sassani, S.G., S. Tsangaris, and D.P. Sokolis, *Layer- and region-specific material characterization of ascending thoracic aortic aneurysms by microstructure-based models.* Journal of Biomechanics, 2015. **48**(14): p. 3757-3765.

148. Ferrara, A., et al., *Human dilated ascending aorta: Mechanical characterization via uniaxial tensile tests.* Journal of the Mechanical Behavior of Biomedical Materials, 2016. **53**: p. 257-271.

149. Vande Geest, J.P., et al., *A Biomechanics-Based Rupture Potential Index for Abdominal Aortic Aneurysm Risk Assessment.* Annals of the New York Academy of Sciences, 2006. **1085**(1): p. 11-21.

150. Raghavan, M.L., et al., *Three-Dimensional Finite Element Analysis of Residual Stress in Arteries.* Annals of Biomedical Engineering, 2004. **32**(2): p. 257-263.

151. Chaudhry, H.R., et al., *Residual stresses in oscillating thoracic arteries reduce circumferential stresses and stress gradients.* Journal of Biomechanics, 1997. **30**(1): p. 57-62.

152. Polzer, S., et al., *A Numerical Implementation to Predict Residual Strains from the Homogeneous Stress Hypothesis with Application to Abdominal Aortic Aneurysms.* Annals of Biomedical Engineering, 2013. **41**(7): p. 1516-1527.

153. Schröder, J. and S. Brinkhues, *A novel scheme for the approximation of residual stresses in arterial walls.* Archive of Applied Mechanics, 2014. **84**(6): p. 881-898.

154. Liu, M., et al., *Identification of in vivo nonlinear anisotropic mechanical properties of ascending thoracic aortic aneurysm from patient-specific CT scans.* Scientific reports, 2019. **9**(1): p. 1-13.

155. Bieging, E.T., et al., *In vivo three-dimensional MR wall shear stress estimation in ascending aortic dilatation.* J Magn Reson Imaging, 2011. **33**(3): p. 589-97.

156. Koullias, G., et al., *Mechanical deterioration underlies malignant behavior of aneurysmal human ascending aorta.* J Thorac Cardiovasc Surg, 2005. **130**(3): p. 677-83.

157. Wittek, A., et al., *Cyclic three-dimensional wall motion of the human ascending and abdominal aorta characterized by time-resolved three-dimensional ultrasound speckle tracking.* Biomechanics and Modeling in Mechanobiology, 2016. **15**(5): p. 1375-1388.

158. Hatzaras, I., et al., *Weight lifting and aortic dissection: more evidence for a connection.* Cardiology, 2007. **107**(2): p. 103-106.

159. Compas, C.B., et al., *Radial Basis Functions for Combining Shape and Speckle Tracking in 4D Echocardiography.* IEEE Transactions on Medical Imaging, 2014. **33**(6): p. 1275-1289.

160. Pengcheng, S., et al., *Point-tracked quantitative analysis of left ventricular surface motion from 3-D image sequences.* IEEE Transactions on Medical Imaging, 2000. **19**(1): p. 36-50.

161. Kaji, S., et al., *Prediction of Progression or Regression of Type A Aortic Intramural Hematoma by Computed Tomography.* Circulation, 1999. **100**(suppl 2): p. II-281-Ii-286.

162. Slobodin, G., et al., *Increased aortic wall thickness for the diagnosis of aortitis: a computed tomography-based study.* International Journal of Rheumatic Diseases, 2016. **19**(1): p. 82-86.

163. Shang, E.K., et al., *Validation of semiautomated and locally resolved aortic wall thickness measurements from computed tomography.* Journal of Vascular Surgery, 2015. **61**(4): p. 1034-1040.

164. Rosero, E.B., et al., *Agreement between methods of measurement of mean aortic wall thickness by MRI.* Journal of Magnetic Resonance Imaging, 2009. **29**(3): p. 576-582.

165. Åstrand, H., et al., *Noninvasive ultrasound measurements of aortic intima-media thickness: implications for in vivo study of aortic wall stress1.* Journal of Vascular Surgery, 2003. **37**(6): p. 1270-1276.

166. Chiu, K.W.H., et al., *Ultrasound Measurement for Abdominal Aortic Aneurysm Screening: A Direct Comparison of the Three Leading Methods.* European Journal of Vascular and Endovascular Surgery, 2014. **47**(4): p. 367-373.

167. Lu, J., X. Zhou, and M.L. Raghavan, *Inverse method of stress analysis for cerebral aneurysms.* Biomechanics and Modeling in Mechanobiology, 2008. **7**(6): p. 477-486.

168. Belytschko, T., B. Moran, and W.K. Liu, *Nonlinear Finite Elements for Continua and Structures.* John Wiley & Sons, Inc., 2000.

169. Pierce, D.M., et al., *Human thoracic and abdominal aortic aneurysmal tissues: Damage experiments, statistical analysis and constitutive modeling.* Journal of the Mechanical Behavior of Biomedical Materials, 2015. **41**: p. 92-107.

170. Smoljkić, M., et al., *Biomechanical Characterization of Ascending Aortic Aneurysms.* Biomechanics and Modeling in Mechanobiology, 2017. **16**(2): p. 705-720.

171. Wang, Q., et al., *Dimensional Analysis of Aortic Root Geometry During Diastole Using 3D Models Reconstructed from Clinical 64-Slice Computed Tomography Images.* Cardiovascular Engineering and Technology, 2011. **2**(4): p. 324-333.

172. Amberg, B., S. Romdhani, and T. Vetter. *Optimal Step Nonrigid ICP Algorithms for Surface Registration*. in *2007 IEEE Conference on Computer Vision and Pattern Recognition*. 2007.

173. Duchon, J. *Splines minimizing rotation-invariant semi-norms in Sobolev spaces*. 1977. Berlin, Heidelberg: Springer Berlin Heidelberg.

174. Bia, D., et al., *Cryopreservation procedure does not modify human carotid homografts mechanical properties: an isobaric and dynamic analysis.* Cell and Tissue Banking, 2006. **7**(3): p. 183-194.

175. Volokh, K.Y., *Prediction of arterial failure based on a microstructural bi-layer fiber–matrix model with softening.* Journal of Biomechanics, 2008. **41**(2): p. 447-453.

176. Volokh, K.Y. and D.A. Vorp, *A model of growth and rupture of abdominal aortic aneurysm.* Journal of Biomechanics, 2008. **41**(5): p. 1015-1021.

177. Metaxa, E., et al., *The influence of intraluminal thrombus on noninvasive abdominal aortic aneurysm wall distensibility measurement.* Medical & Biological Engineering & Computing, 2015. **53**(4): p. 299-308.

178. Sahibzada, N., et al., *Rhythmic Aortic Contractions Induced by Electrical Stimulation In Vivo in the Rat.* PLOS ONE, 2015. **10**(7): p. e0130255.

179. van Disseldorp, E.M.J., et al., *Influence of limited field-of-view on wall stress analysis in abdominal aortic aneurysms.* Journal of Biomechanics, 2016. **49**(12): p. 2405-2412.

180. Jia, C., et al., *Comparison of 2-D speckle tracking and tissue Doppler imaging in an isolated rabbit heart model.* IEEE Transactions on Ultrasonics, Ferroelectrics, and Frequency Control, 2010. **57**(11): p. 2491-2502.

181. Zhu, Y., et al., *A Dynamical Shape Prior for LV Segmentation from RT3D Echocardiography.* Medical image computing and computer-assisted intervention

: MICCAI ... International Conference on Medical Image Computing and Computer-Assisted Intervention, 2009. **5761**: p. 206-213.

182. Pearlman, P.C., et al., *3D Radio Frequency Ultrasound Cardiac Segmentation Using a Linear Predictor().* Medical image computing and computer-assisted intervention : MICCAI ... International Conference on Medical Image Computing and Computer-Assisted Intervention, 2010. **13**(0 1): p. 502-509.

183. Zhu, Y., et al., *A coupled deformable model for tracking myocardial borders from real-time echocardiography using an incompressibility constraint*. Medical image analysis, 2010. **14**(3): p. 429-448.

184. Pearlman, P.C., et al., *Segmentation of 3D Radio Frequency Echocardiography Using a Spatio-temporal Predictor.* Medical Image Analysis, 2012. **16**(2): p. 351-360.

185. Huang, X., et al., *Contour Tracking in Echocardiographic Sequences via Sparse Representation and Dictionary Learning.* Medical image analysis, 2014. **18**(2): p. 253-271.

186. Matilda, L., et al., *Strain assessment in the carotid artery wall using ultrasound speckle tracking: validation in a sheep model.* Physics in Medicine and Biology, 2015. **60**(3): p. 1107.

187. Karatolios, K., et al., *Method for Aortic Wall Strain Measurement With Three-Dimensional Ultrasound Speckle Tracking and Fitted Finite Element Analysis.* The Annals of Thoracic Surgery, 2013. **96**(5): p. 1664-1671.

188. Bersi, M.R., et al., *Local variations in material and structural properties characterize murine thoracic aortic aneurysm mechanics.* Biomechanics and Modeling in Mechanobiology, 2019. **18**(1): p. 203-218.

189. Labrosse, M.R., et al., *Mechanical behavior of human aortas: Experiments, material constants and 3-D finite element modeling including residual stress.* Journal of Biomechanics, 2009. **42**(8): p. 996-1004.

190. Liu, M., L. Liang, and W. Sun, *Estimation of in vivo constitutive parameters of the aortic wall using a machine learning approach.* Computer methods in applied mechanics and engineering, 2019. **347**: p. 201-217.

191. Litjens, G., et al., *A Survey on Deep Learning in Medical Image Analysis.* arXiv:1702.05747, 2017.

192. Shen, D., G. Wu, and H.-I. Suk, *Deep Learning in Medical Image Analysis.* Annual Review of Biomedical Engineering, 2017. **19**(1): p. 221-248.

193. Botsch, M., et al., *Polygon mesh processing*. 2010: CRC press.

194. Goodall, C., *Procrustes methods in the statistical analysis of shape.* Journal of the Royal Statistical Society: Series B (Methodological), 1991. **53**(2): p. 285-321.

195. Cootes, T.F., et al., *Active shape models-their training and application.* Computer vision and image understanding, 1995. **61**(1): p. 38-59.

196. Heimann, T. and H.-P. Meinzer, *Statistical shape models for 3D medical image segmentation: a review.* Medical image analysis, 2009. **13**(4): p. 543-563.

197. Geman, S. and D. Geman, *Stochastic Relaxation, Gibbs Distributions, and the Bayesian Restoration of Images.* IEEE Transactions on Pattern Analysis and Machine Intelligence, 1984. **PAMI-6**(6): p. 721-741.

198. Webb, A.R. and K.D. Copsey, *Statistical Pattern Recognition*. 2011, Wiley.

199. Dugas, C., et al., *Incorporating second-order functional knowledge for better option pricing*, in *Proceedings of the 13th International Conference on Neural Information Processing Systems*. 2000, MIT Press: Denver, CO. p. 451-457.

200. Glorot, X., A. Bordes, and Y. Bengio, *Deep Sparse Rectifier Neural Networks*, in *Proceedings of the Fourteenth International Conference on Artificial Intelligence and Statistics*, G. Geoffrey, D. David, and D. Miroslav, Editors. 2011, PMLR: Proceedings of Machine Learning Research. p. 315--323.

201. Hahnloser, R.H.R., et al., *Digital selection and analogue amplification coexist in a cortex-inspired silicon circuit.* Nature, 2000. **405**: p. 947.

202. Abadi, M., et al., *TensorFlow: Large-Scale Machine Learning on Heterogeneous Distributed Systems.* http://tensorflow.org/, 2015.

203. Kingma, D.P. and J. Ba, *Adam: A Method for Stochastic Optimization.* the 3rd International Conference for Learning Representations, 2015.

204. Goodfellow, I., Y. Bengio, and A. Courville, *Deep Learning*. Adaptive Computation and Machine Learning series. 2016: The MIT Press.

205. Chang, C.-C. and C.-J. Lin, *LIBSVM: a library for support vector machines.* ACM transactions on intelligent systems and technology (TIST), 2011. **2**(3): p. 27.

206. Li, K., R.W. Ogden, and G.A. Holzapfel, *An exponential constitutive model excluding fibres under compression: Application to extension–inflation of a residually stressed carotid artery.* Mathematics and Mechanics of Solids, 2018. **23**(8): p. 1206-1224.

207. Li, K., R.W. Ogden, and G.A. Holzapfel, *A discrete fibre dispersion method for excluding fibres under compression in the modelling of fibrous tissues.* Journal of The Royal Society Interface, 2018. **15**(138).

208. Li, K., R.W. Ogden, and G.A. Holzapfel, *Modeling fibrous biological tissues with a general invariant that excludes compressed fibers.* Journal of the Mechanics and Physics of Solids, 2018. **110**: p. 38-53.

209. Glorot, X., A. Bordes, and Y. Bengio, *Deep Sparse Rectifier Neural Networks.* Proceedings of the Fourteenth International Conference on Artificial Intelligence and Statistics, 2011.

210. Klambauer, G., et al. *Self-normalizing neural networks*. in *Advances in Neural Information Processing Systems*. 2017.

211. Bartlett, P.L. and M.H. Wegkamp, *Classification with a Reject Option using a Hinge Loss.* J. Mach. Learn. Res., 2008. **9**: p. 1823-1840.

212. Liu, M., et al., *A Probabilistic and Anisotropic Failure Metric for Ascending Thoracic Aortic Aneurysm Risk Stratification.* bioRxiv, 2020.

213. Caballero, A., et al., *Evaluation of transcatheter heart valve biomaterials: Biomechanical characterization of bovine and porcine pericardium.* Journal of the Mechanical Behavior of Biomedical Materials, 2017. **75**: p. 486-494.

214. Pokutta-Paskaleva, A., et al., *Comparative mechanical, morphological, and microstructural characterization of porcine mitral and tricuspid leaflets and chordae tendineae.* Acta Biomaterialia, 2019. **85**: p. 241-252.

215. Sang, C., et al., *A uniaxial testing approach for consistent failure in vascular tissues.* Journal of biomechanical engineering, 2018. **140**(6).

216. Devore, J.L. and K.N. Berk, *Modern mathematical statistics with applications*. 2012: Springer.

217. Davis, R.A., K.-S. Lii, and D.N. Politis, *Remarks on some nonparametric estimates of a density function*, in *Selected Works of Murray Rosenblatt*. 2011, Springer. p. 95-100.

218. Parzen, E., *On estimation of a probability density function and mode.* The annals of mathematical statistics, 1962. **33**(3): p. 1065-1076.

219. Scott, D.W., *Multivariate density estimation: theory, practice, and visualization*. 2015: John Wiley & Sons.

220. Jones, A.T., H.D. Nguyen, and G.J. McLachlan, *logKDE: log-transformed kernel density estimation.* Journal of Open Source Software, 2018. **3**(28): p. 870.

221. Fung, Y.-c., *Biomechanics: mechanical properties of living tissues*. 2013: Springer Science & Business Media.

222. Cheng, S., E.C. Clarke, and L.E. Bilston, *The effects of preconditioning strain on measured tissue properties.* Journal of Biomechanics, 2009. **42**(9): p. 1360-1362.

223. Carew, E.O., J.E. Barber, and I. Vesely, *Role of Preconditioning and Recovery Time in Repeated Testing of Aortic Valve Tissues: Validation Through Quasilinear Viscoelastic Theory.* Annals of Biomedical Engineering, 2000. **28**(9): p. 1093-1100.

224. Calvo, B., et al., *An uncoupled directional damage model for fibred biological soft tissues. Formulation and computational aspects.* International Journal for Numerical Methods in Engineering, 2007. **69**(10): p. 2036-2057.

225. Lee, M.-C. and R.C. Haut, *Strain rate effects on tensile failure properties of the common carotid artery and jugular veins of ferrets.* Journal of Biomechanics, 1992. **25**(8): p. 925-927.

226. Fedorov, A., et al., *3D Slicer as an image computing platform for the Quantitative Imaging Network.* Magnetic resonance imaging, 2012. **30**(9): p. 1323-1341.

227. *Understanding Blood Pressure Readings*. 2020]; Available from: https://www.heart.org/en/health-topics/high-blood-pressure/understanding-blood-pressure-readings?gclid=CjwKCAjwtNf6BRAwEiwAkt6UQttVxmQhyp4eBZh4F5sPrV8OlIyrjPeY62bvcAZa4NmlmWDHd0ZQOxoCrPsQAvD_BwE.

228. Li, A.E., et al., *Using MRI to assess aortic wall thickness in the multiethnic study of atherosclerosis: distribution by race, sex, and age.* American Journal of Roentgenology, 2004. **182**(3): p. 593-597.

229. Liu, C.-Y., et al., *Evolution of aortic wall thickness: long-term follow up from the Multi-Ethnic Study of Atherosclerosis (MESA).* Journal of Cardiovascular Magnetic Resonance, 2013. **15**(S1): p. M14.

230. Ohyama, Y., et al., *Imaging Insights on the Aorta in Aging.* Circulation: Cardiovascular Imaging, 2018. **11**(4): p. e005617.

231. Jarvis, K., et al., *Investigation of Aortic Wall Thickness, Stiffness and Flow Reversal in Patients With Cryptogenic Stroke: A 4D Flow MRI Study.* Journal of Magnetic Resonance Imaging.

232. Mandrekar, J.N., *Receiver operating characteristic curve in diagnostic test assessment.* Journal of Thoracic Oncology, 2010. **5**(9): p. 1315-1316.

233. Elefteriades, J.A., S.K. Mukherjee, and H. Mojibian, *Discrepancies in Measurement of the Thoracic Aorta: JACC Review Topic of the Week.* Journal of the American College of Cardiology, 2020. **76**(2): p. 201-217.

234. Lughofer, E., *Hybrid active learning for reducing the annotation effort of operators in classification systems.* Pattern Recognition, 2012. **45**(2): p. 884-896.

235. Boyd, S., N. Parikh, and E. Chu, *Distributed optimization and statistical learning via the alternating direction method of multipliers*. 2011: Now Publishers Inc.

236. Besl, P.J. and N.D. McKay, *A method for registration of 3-D shapes.* IEEE Transactions on Pattern Analysis and Machine Intelligence, 1992. **14**(2): p. 239-256.

237. Chen, Y. and G. Medioni. *Object modeling by registration of multiple range images*. in *Proceedings. 1991 IEEE International Conference on Robotics and Automation*. 1991.

238. Kerdprasop, K., N. Kerdprasop, and P. Sattayatham, *Weighted K-Means for Density-Biased Clustering*, in *Data Warehousing and Knowledge Discovery: 7th International Conference, DaWaK 2005, Copenhagen, Denmark, August 22-26, 2005. Proceedings*, A.M. Tjoa and J. Trujillo, Editors. 2005, Springer Berlin Heidelberg: Berlin, Heidelberg. p. 488-497.

239. *Echocardiography*, in *Encyclopedia of Heart Diseases*, M.G. Khan, Editor. 2011, Humana Press: Totowa, NJ. p. 431-437.

240. Jansen Klomp, W.W., et al., *Imaging Techniques for Diagnosis of Thoracic Aortic Atherosclerosis.* International Journal of Vascular Medicine, 2016. **2016**: p. 4726094.

241. Barrett, J.F. and N. Keat, *Artifacts in CT: Recognition and Avoidance.* RadioGraphics, 2004. **24**(6): p. 1679-1691.

242. Davis, F.M., et al., *Local mechanical properties of human ascending thoracic aneurysms.* Journal of the Mechanical Behavior of Biomedical Materials, 2016. **61**: p. 235-249.

243. Choudhury, N., et al., *Local mechanical and structural properties of healthy and diseased human ascending aorta tissue.* Cardiovascular Pathology, 2009. **18**(2): p. 83-91.

244. Bellini, C., et al., *A Microstructurally Motivated Model of Arterial Wall Mechanics with Mechanobiological Implications.* Annals of Biomedical Engineering, 2014. **42**(3): p. 488-502.

245. Genet, M., et al., *Heterogeneous growth-induced prestrain in the heart.* Journal of Biomechanics, 2015. **48**(10): p. 2080-2089.

246. Sokolis, D.P., et al., *Regional distribution of circumferential residual strains in the human aorta according to age and gender.* Journal of the Mechanical Behavior of Biomedical Materials, 2017. **67**: p. 87-100.

247. Ares, G.D., et al., *Identification of residual stresses in multi-layered arterial wall tissues using a variational framework.* Computer Methods in Applied Mechanics and Engineering, 2017. **319**: p. 287-313.

248. Liu, M., L. Liang, and W. Sun, *A generic physics-informed neural network-based constitutive model for soft biological tissues.* Computer Methods in Applied Mechanics and Engineering, 2020. **372**: p. 113402.

249. Chabanas, M., V. Luboz, and Y. Payan, *Patient specific finite element model of the face soft tissues for computer-assisted maxillofacial surgery.* Medical image analysis, 2003. **7**(2): p. 131-151.

250. Wittek, A., et al., *Patient-specific model of brain deformation: Application to medical image registration.* Journal of Biomechanics, 2007. **40**(4): p. 919-929.

251. HUMPHREY, J., *INTRODUCTION TO BIOMECHANICS*. Springer.

252. Fung, Y., K. Fronek, and P. Patitucci, *Pseudoelasticity of arteries and the choice of its mathematical expression.* American Journal of Physiology-Heart and Circulatory Physiology, 1979. **237**(5): p. H620-H631.

253. Fung, Y., *Elasticity of soft tissues in simple elongation.* American Journal of Physiology-Legacy Content, 1967. **213**(6): p. 1532-1544.

254. Humphrey, J.D., R.K. Strumpf, and F.C.P. Yin, *Determination of a Constitutive Relation for Passive Myocardium: I. A New Functional Form.* Journal of Biomechanical Engineering, 1990. **112**(3): p. 333-339.

255. Holzapfel, G.A. and R.W. Ogden, *Constitutive modelling of passive myocardium: a structurally based framework for material characterization.* Philosophical Transactions of the Royal Society A: Mathematical, Physical and Engineering Sciences, 2009. **367**(1902): p. 3445-3475.

256. Baek, S., et al., *Theory of small on large: Potential utility in computations of fluid–solid interactions in arteries.* Computer Methods in Applied Mechanics and Engineering, 2007. **196**(31): p. 3070-3078.

257. Hu, J.J., S. Baek, and J.D. Humphrey, *Stress–strain behavior of the passive basilar artery in normotension and hypertension.* Journal of Biomechanics, 2007. **40**(11): p. 2559-2563.

258. Schroeder, F., et al., *Predictive capabilities of various constitutive models for arterial tissue.* Journal of the Mechanical Behavior of Biomedical Materials, 2018. **78**: p. 369-380.

259. He, X., S. Avril, and J. Lu, *Machine Learning Prediction of Tissue Strength and Local Rupture Risk in Ascending Thoracic Aortic Aneurysms.* Molecular \& Cellular Biomechanics, 2019. **16**(Suppl.2): p. 50--52.

260. Dabiri, Y., et al., *Prediction of Left Ventricular Mechanics Using Machine Learning.* Frontiers in Physics, 2019. **7**(117).

261. Romaszko, L., et al., *Direct Learning Left Ventricular Meshes from CMR Images*, G. Ladde and D. Jeske, Editors. 2019. p. 25.

262. Do, H.N., et al., *Prediction of Abdominal Aortic Aneurysm Growth Using Dynamical Gaussian Process Implicit Surface.* IEEE Transactions on Biomedical Engineering, 2019. **66**(3): p. 609-622.

263. Cilla, M., et al., *On the use of machine learning techniques for the mechanical characterization of soft biological tissues.* International journal for numerical methods in biomedical engineering, 2018. **34**(10): p. e3121.

264. Csáji, B.C., *Approximation with artificial neural networks.* Faculty of Sciences, Etvs Lornd University, Hungary, 2001. **24**: p. 48.

265. Leshno, M., et al., *Multilayer feedforward networks with a nonpolynomial activation function can approximate any function.* Neural Networks, 1993. **6**(6): p. 861-867.

266. Cybenko, G., *Approximation by superpositions of a sigmoidal function.* Mathematics of Control, Signals and Systems, 1989. **2**(4): p. 303-314.

267. Hornik, K., *Approximation capabilities of multilayer feedforward networks.* Neural Networks, 1991. **4**(2): p. 251-257.

268. Ghaboussi, J., et al., *Autoprogressive training of neural network constitutive models.* International Journal for Numerical Methods in Engineering, 1998. **42**(1): p. 105-126.

269. Holzapfel, G.A. and R.W. Ogden, *On planar biaxial tests for anisotropic nonlinearly elastic solids. A continuum mechanical framework.* Mathematics and Mechanics of Solids, 2009. **14**(5): p. 474-489.

270. He, K., et al. *Deep residual learning for image recognition*. in *Proceedings of the IEEE conference on computer vision and pattern recognition*. 2016.

271. Huang, G., et al. *Densely connected convolutional networks*. in *Proceedings of the IEEE conference on computer vision and pattern recognition*. 2017.

272. Glorot, X., A. Bordes, and Y. Bengio. *Deep sparse rectifier neural networks*. in *Proceedings of the fourteenth international conference on artificial intelligence and statistics*. 2011.

273. Nair, V. and G.E. Hinton. *Rectified linear units improve restricted boltzmann machines*. in *Proceedings of the 27th international conference on machine learning (ICML-10)*. 2010.

274. Sun, W. and M.S. Sacks, *Finite element implementation of a generalized Fung-elastic constitutive model for planar soft tissues.* Biomechanics and Modeling in Mechanobiology, 2005. **4**(2): p. 190-199.

275. Balzani, D., et al., *A polyconvex framework for soft biological tissues. Adjustment to experimental data.* International Journal of Solids and Structures, 2006. **43**(20): p. 6052-6070.

276. Meyer, C.D., *Matrix analysis and applied linear algebra*. Vol. 71. 2000: Siam.

277. Prussing, J.E., *The principal minor test for semidefinite matrices.* Journal of Guidance, Control, and Dynamics, 1986. **9**(1): p. 121-122.

278. Bergstra, J. and Y. Bengio, *Random search for hyper-parameter optimization.* The Journal of Machine Learning Research, 2012. **13**(1): p. 281-305.

279. Snoek, J., H. Larochelle, and R.P. Adams. *Practical bayesian optimization of machine learning algorithms*. in *Advances in neural information processing systems*. 2012.

280. Paszke, A., et al., *Automatic differentiation in pytorch.* 2017.

281. Kingma, D.P. and J. Ba, *Adam: A method for stochastic optimization.* arXiv preprint arXiv:1412.6980, 2014.

282. Sun , W., et al., *Biaxial Mechanical Response of Bioprosthetic Heart Valve Biomaterials to High In-plane Shear.* Journal of Biomechanical Engineering, 2003. **125**(3): p. 372-380.

283. Sacks, M.S., *A Method for Planar Biaxial Mechanical Testing That Includes In-Plane Shear.* Journal of Biomechanical Engineering, 1999. **121**(5): p. 551-555.

284. Jung, S. and J. Ghaboussi, *Neural network constitutive model for rate-dependent materials.* Computers & Structures, 2006. **84**(15): p. 955-963.

285. Stoffel, M., F. Bamer, and B. Markert, *Neural network based constitutive modeling of nonlinear viscoplastic structural response.* Mechanics Research Communications, 2019. **95**: p. 85-88.

286. Zeinali-Davarani, S., J. Choi, and S. Baek, *On parameter estimation for biaxial mechanical behavior of arteries.* Journal of Biomechanics, 2009. **42**(4): p. 524-530.

287. Guan, D., et al., *On the AIC-based model reduction for the general Holzapfel–Ogden myocardial constitutive law.* Biomechanics and Modeling in Mechanobiology, 2019. **18**(4): p. 1213-1232.

288. Belkin, M., et al., *Reconciling modern machine-learning practice and the classical bias–variance trade-off.* Proceedings of the National Academy of Sciences, 2019. **116**(32): p. 15849-15854.

289. Raissi, M., P. Perdikaris, and G.E. Karniadakis, *Physics-informed neural networks: A deep learning framework for solving forward and inverse problems involving nonlinear partial differential equations.* Journal of Computational Physics, 2019. **378**: p. 686-707.

290. Liu, D. and Y. Wang, *A Dual-Dimer Method for Training Physics-Constrained Neural Networks with Minimax Architecture.* arXiv preprint arXiv:2005.00615, 2020.

291. Vaishnav, R.N., et al., *Nonlinear Anisotropic Elastic Properties of the Canine Aorta.* Biophysical Journal, 1972. **12**(8): p. 1008-1027.

292. Raghavan, M.L. and D.A. Vorp, *Toward a biomechanical tool to evaluate rupture potential of abdominal aortic aneurysm: identification of a finite strain constitutive model and evaluation of its applicability.* Journal of Biomechanics, 2000. **33**(4): p. 475-482.

293. Schmidt, T., D. Balzani, and G.A. Holzapfel, *Statistical approach for a continuum description of damage evolution in soft collagenous tissues.* Computer Methods in Applied Mechanics and Engineering, 2014. **278**: p. 41-61.